Studies on Bulk and Thin Films of $(Zr,Sn)TiO_4$ System

A thesis submitted for the degree of

DOCTOR OF PHILOSOPHY

By

D. PAMU

School of Physics
University of Hyderabad
Hyderabad -500 046
India.

February 2008

To My Family

CERTIFICATE

This is to certify that the work described in this dissertation entitled "**Studies on Bulk and Thin Films of (Zr,Sn)TiO_4 System**" has been carried out by Mr. D.Pamu under our direct supervision for the full period prescribed under Ph.D Ordinances of the University and the same has not been submitted for any other degree or diploma to this or any other University or Institution.

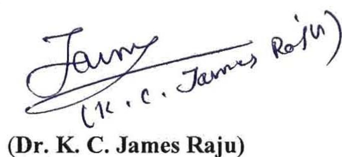

(Dean, School of Physics)

DEAN
School of Physics
University of Hyderabad
Hyderabad-500 046, INDIA

(Dr. K. C. James Raju)

Place: Hyderabad

Date: 5.3.2008

(Thesis Supervisor)

Dr. K.C. JAMES RAJU
READER IN ELECTRONICS
SCHOOL OF PHYSICS
UNIVERSITY OF HYDERABAD
HYDERABAD-500 046, INDIA

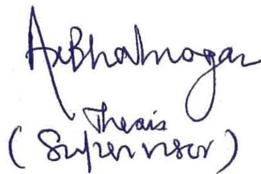

Dr. ANIL K. BHATNAGAR
CSIR Chair Professor
School of Physics
University of Hyderabad
HYDERABAD-500 046, INDIA

Acknowledgements

It is my pleasure to write this part of my thesis to express my gratitude to one and all that have helped me in this long journey of my Research. I thank all of them involved directly or indirectly for the successful completion of this thesis.

I am deeply indebted to **Dr. K. C. James Raju**, for his esteemed guidance throughout my research. The way he inspired, advised and helped me in both academic and personal life is unforgettable. The freedom he has given me is ultimate and unlimited.

I express my sincere thanks to **Prof. A. K. Bhatnagar**, for his initiation in taking me in to the group. It is my privilege to work with him. I thank for all his guidance and help throughout my work. It is my privilege to work with **Dr. M. Ghanashyam Krishna** for his encouragement and guidance in planning experiments and helping me to improve my experimental skills. I thank for all his help in my entire research work.

Several faculty members in the School of Physics have been of immense help providing the constant intellectual insights in to my research. I thank **Prof. Vipin Shrivastava**, Dean School of Physics, as well as **Prof. V. S. S. Sastry** and **Prof. S. N. Kaul**, former Deans of School of Physics for their encouragement and support.

I thank **Dr. M. V. Jacob** from James Cook University, Australia, for providing the low temperature microwave dielectric data for 4 samples, **Dr. A. R. James,** Scientist, DMRL, Hyderabad, for providing Titanium foil and for doing particle size analysis for my samples and **Dr. S. K. Banerjee**, director, BARC, for providing a Zirconium disc. With out their help my work would have been incomplete.

I am grateful to all the Central Instrumentation Laboratory staff, especially **Mr. C. S. Murthy** for helping me with Confocal Microscopy, **Dr. Manjunath** for doing SEM for my samples, **Mr. Nageswara Rao, Mr. Hemanth** for doing XRD and **Mr. Suresh** for doing DSC. At this time it is apt to express my thanks to **Mr. Ravi Shankar** of School of Physics for doing XRD for my samples & **Mr. Vincent** from work shop for his help in designing sample holders for my work.

I thank **Mr. T. Abraham** for his timely help on every occasion and other office staff members of the school for cooperating with me.

It's my great pleasure to acknowledge the financial support of Indian Space Research Organization (ISRO) by providing fellowship for three and half years, National Programme on Smart Materials (NPSM) (6 months) and National Fusion Programme for the present Senior Research Fellowship. Needless to say without these supports this study would not have been materialized. Facilities provided by NPSM, DLRL, ISRO, UGC, UGC-SAP, DST-FIST, DST-ITPAR and UGC-UPE programs are gratefully acknowledged.

All through my six years of research work my colleagues have been a piller of strength for me academically and personally. I deem it a special pleasure to express a big thanks to **Mr. G. Lakshminarayana Rao** for characterizing all my DR samples, **Mr. K. Sudheendran** for doing microwave measurements for my films and impedance measurements, **Mr. K. Venkata Saravanan** for helping me to learn various techniques, **Mr. K. Uma Mahendra Kumar** for helping me in various ways, **Mr. M. S. R. N. Kiran & Mr. P. Prashant Kumar** for their useful discussions, **Mr. Rajeeb Brahma** and **Mr. A. Ram Babu** for their help and co operation, **Mr. T. Anil** and **Mr. Binoy Raphael** for helping me in experiments.

It's my pleasure to remember my other friends in the School of Physics, **Mr. W. D. R. Joseph, N. Srinivasa Rao, Ch. Bheem, P. Suresh. Mr. Swaroop Raju** and others for their help and encouragement.

My special thanks to **Mr P. Steven Raj, K. Anand Dev Paul and K. Satyanarayana** for all their help. I also thank my hostel mates and friends **Mr. M. Arun Kumar, S. Srinivas, G. P. Rattaiah, L. Uday Kumar and Mr. Sudheer Kumar Reddy** for their constant help and guidance.

Special thanks to friendly families of **Mr. Anil Mathews, Mr. Liju Joshua, Mr. M. Kodandaram, Mr. D. Anil Kumar, Dr. Thomas Joseph, Mr. G. Sudhir Kumar, Mr. K. Ganga Raju, Mr. K. Venkateswara Rao, Mr. Nageswara Rao, Mr. U. Nirmal Kumar, Mr. D. John Sundera Rao and Mr. K. Bhushanam** for their spiritual & moral guidance and for their constant prayer support which I received from them. I wish to express my indebtedness to the **HCU, Kukatpally, APAU and**

twin cities (EUs & EGFs) Christian Fellowship for all their encouragement and prayer support.

My special thanks and gratitude to **Mr. G. George's** family for helping me spiritually, morally and financially. My sincere thanks are also due to families of **Mr. G. Sudhir Kumar, Mr. Syam uncle, Jyothi aunty, Swarna madam, Sujatha akka, Mercy akka and Mrs. Lakshmi garu,** for all the inexpressible help I have received, and for taking risk in my life. I thank my uncle **Mr. Y. Chitti Babu and family** for their encouragement and co operation in all the ways of my life. I am deeply indebted to **Ms. Sumana Priya** for her love, care, constant encouragement and prayer support.

It is the endless sacrifice and support of my **Mother and Father** which helped me to realize my goal. I thank my **Sisters and their families (Lakshmi and Krishna Kumari), my brother (Ravi Kumar) and all my relatives** for their love, affection and moral support.

Above all I thank my **Saviour** for being ever present with me, sustaining, strengthening and disciplining me, making me the person who I ought to be.

CONTENTS

Preface I

1 Introduction to Dielectric Resonators and High-k Thin Films 1

1.1 Introduction to dielectric resonators 1
1.2 History of dielectric resonators 1
1.3 Modes in a dielectric resonator 2
1.4a Material requirements of a DR (Dielectric Resonator) 5
1.4b Known dielectric resonator materials 7
1.4c Current state of materials developed for dielectric resonator applications 9
1.4d Future requirements of the DR materials 9
1.5 Physics of DR materials 10
1.6 Electronic applications of high –k (ε_r) materials in thin film form 14
1.7 Characteristics of SiO_2 in MOSFET devices and the difficulties of its Replacement 17
1.8 Efforts to replace SiO_2 18
1.9 Zirconium Tin Titanate (ZST): An interesting system in bulk and thin film form 19
1.10 Motivation of study 22
References 24

2 Preparation and Characterization Techniques Used for Bulk and Thin Films of Compositions in the System (Zr,Sn)TiO_4 27

2.1 Preparation and characterization techniques for bulk (Zr,Sn)TiO_4 27
2.1.1 Solid-state reaction method 27
2.1.2 Stoichiometric weighing of reagents 28
2.1.3 Uniform mixing of reagents 28
2.1.4 Calcination stage 28
2.1.5 Particle size reduction 29
2.1.6 Uniaxial pressing 30
2.1.7 Solid-state sintering 30
2.1.8 Liquid phase sintering 34
2.2 Characterization techniques used for the bulk compositions 34
2.2a X-ray diffraction 34
2.2b Scanning electron microscopy 35
2.3 Microwave measurements 36
2.4 Electrical conductivity measurements 41
2.5 Thin film preparation techniques 45

2.6 Optical properties 52
2.7 Measurement technique used to measure dielectric properties at microwave frequencies 56
2.8 Electrical measurements 57
2.9 Atomic force microscope 58
References 60
3 Preparation and Characterization of Bulk ($(Zr_{0.8},Sn_{0.2})TiO_4$) Ceramics 62
3.1 Preparation of pure ZST 62
3.2 Effect of milling and addition of ZnO on ZST ceramics 66
3.3 Effect of milling and addition of ZnO and CuO on ZST ceramics 79
3.4 Microwave dielectric properties at cryogenic temperatures 92
3.5 Impedance spectroscopy of ZST ceramics 98
References 111
4 Effect of additives on ZST ceramics 112
4.1 Brief literature review of ZST processing 112
4.2 Introduction to the additives that are used with ZST in this study 115
4.3 Properties of ZST ceramics prepared with various additives 116
4.4 Effect of dopants on the structure of ZST ceramics 118
4.5 Effect of additives on the densification of ZST ceramics 125
4.6 The effect of the additives on the microstructure 137
4.7 Microwave dielectric properties 151
4.7.1 Effect of the additives on microwave dielectric constant 151
4.7.2 Effect of the additives on quality factor 157
4.7.3 Effect of the additives on the temperature coefficient of the resonant frequency 165
References 168
5 Preparation, structure and morphology of films in the $(Zr,Sn)TiO_4$ system 170
5.1 Literature review and experimental details of the systems 170
5.2 Structure and morphology of TiO_2 films 186
5.3 Structure and morphology of ZrO_2 films 198
5.4 Structure and morphology of $ZrTiO_4$ (ZT) films 206
5.5 Structure and morphology of $(Zr,Sn)TiO_4$ (ZST) films 211
5.6 Discussion and conclusions 214
References 217
6 Optical and electrical studies of the films in $(Zr,Sn)TiO_4$ system 219
6.1 Optical properties of TiO_2 films 219
6.2 Optical properties of ZrO_2 films 227

6.3 Optical properties of $ZrTiO_4$ films 231
6.4 Optical properties of ZST films 236
6.5 Electrical properties of the films in $(Zr,Sn)TiO_4$ system 240
References 246
7 Dielectric properties of thin films in $(Zr,Sn)TiO_4$ system 247
7.1 Dielectric properties of the films in $(Zr,Sn)TiO_4$ system at low frequencies 247
7.1.1 Low frequency dielectric properties of TiO_2 films 247
7.1.2 Low frequency dielectric properties of ZrO_2 thin films 249
7.1.3 Low frequency dielectric properties of $ZrTiO_4$ thin films 251
7.1.4 Low frequency dielectric properties of ZST thin films 253
7.2 Microwave dielectric properties of the films in $(Zr,Sn)TiO_4$ system 255
7.2.1 Effect of frequency variation on microwave dielectric constant and loss of the films in $(Zr,Sn)TiO_4$ system 255
7.3 Effect of OMP on microwave dielectric constant and tanδ of films in the $(Zr,Sn)TiO_4$ system 260
7.3.1 TiO_2 thin films 260
7.3.2 ZrO_2 thin films 263
7.3.3 $ZrTiO_4$ thin films 266
7.3.4 ZST thin films 267
7.4 Effect of crystallite size and bandgap on microwave dielectric properties of the films in $(Zr,Sn)TiO_4$ system 267
7.4.1 TiO_2 thin films 267
7.4.2 ZrO_2 thin films 270
7.4.3 $ZrTiO_4$ thin films 271
7.4.4 ZST thin films 272
7.5 Effect of strain on microwave dielectric loss of the films in $(Zr,Sn)TiO_4$ system 275
7.6 Effect of processing parameters on dielectric properties 277
References 279
8 Conclusions and future scope of the work 280
8.1 Conclusions 280
8.2 Future scope of the work 282
List of publications

PREFACE

Introduction

Rapid growth of the wireless communication industry in recent years has led to a high demand for microwave ceramic components. Commercial wireless technologies such as cellular phones, direct broadcasting satellite (DBS) and global positioning systems (GPS) have been making rapid progress due to the improved performance of devices like dielectric resonators at microwave frequencies. Dielectric resonators (DRs) are highly densified ceramic bodies of regular geometry which act as resonators at microwave frequencies. They are made of ceramic materials with high dielectric constant (ε_r), low value of tanδ (hence high quality factor, Q value) and low values of temperature coefficient of resonant frequency (τ_f). The same materials are also being used for making substrates for microwave integrated circuits (MICs), ceramic filters and low temperature co- fired ceramic (LTCC) based highly miniaturized microwave systems.

In a similar manner high dielectric constant thin films became important in microelectronics also. This became necessary because for charge storage over an ever decreasing area, materials with higher dielectric constant are essential. As the device dimensions become lower, the frequency of operation of the microelectronic devices goes up and energy dissipation per unit area increases. Hence thin films with high dielectric constant and low dielectric loss even at higher frequencies and with low temperature dependence are important for such microelectronic applications. That means, if one can make thin films of materials for DR application that should serve this purpose.

Therefore a suitable DR composition was identified for this study to make both bulk DRs and thin films. Both the bulk and thin films are characterized in the microwave frequency range to see whether the excellent bulk characteristics are getting retained in thin film form. A composition, which can yield thin films by a simple process is chosen.

Motivation of Study

Among many high-K dielectric materials Zirconium tin titanate (ZST) with composition $(Zr_{0.8},Sn_{0.2})TiO_4$ has been found to be an excellent material for the applications discussed above in bulk. It also has good optical and electrical properties

which could be used for other electronic, photonic and microwave applications. Bulk ZST has a dielectric constant = 38, a high Qxf_o value of ~45,000 (where f is the frequency of measurement in GHz), temperature coefficient of resonant frequency is nearly zero (~0ppm/°C). A disadvantage in preparing this material by the solid state reaction method is the requirement of very high sintering temperatures. Therefore it is interesting to look for ways to reduce its sintering temperature and the effect of such procedures on the microwave dielectric properties. Another important aspect in the study of DR materials is to understand the factors which influence Q value and to look for ways to improve it.

Some aspects are already available on the thin films of the composition $(Zr_{0.8},Sn_{0.2})TiO_4$ prepared by RF sputtering, Pulsed Laser Deposition (PLD) and Chemical Vapor Deposition (CVD). Those reports suggests that these films got lower leakage current compared to SiO_2, making them attractive for CMOS technology. Even though considerable amount of study has gone in to bulk ZST, studies on thin film ZST are rather few. It is noteworthy that ZST is made of oxides of stable metals, making it possible to use reactive dc magnetron sputtering for the growth of ZST films. This work is an attempt in that direction by growing ZST films by a cost effective process and to compare their properties with that of their bulk counterpart.

As a continuing effort in our laboratory on microwave materials, we have chosen to investigate ZST in the bulk form prepared by the solid–state reaction method and in thin film form prepared by the DC reactive magnetron sputtering. We have tried various techniques to reduce the sintering temperature to prepare bulk ZST and have been successful to some extent. To the best of our knowledge, the DC reactive magnetron sputtering has not been used by anyone to prepare ZST films. DC reactive magnetron sputtering technique has been used extensively for preparation of various kinds of films as it gives high deposition rates and is a relatively simple and cheaper technique than the ones like RF sputtering and Pulsed Laser Ablation. One can optimize the deposition parameters resulting in good thickness uniformity of films and their high adhesion to the substrate. We have prepared ZST films from a single cathode consisting of Zr, Sn and Ti metals in appropriate proportions to get the right composition of ZST. This technique avoids the preparation of the ceramic targets which is costly, lengthy and time taking process. Another disadvantage is that the ceramic targets will usually crack after few cycles of sputtering.

The overall main effort in this study was to improve the microwave dielectric properties of the bulk samples by improving the microstructure of this material prepared with different additives and temperature treatments. Another interest was to compare microwave properties of ZST in bulk as well as in thin film form in order to see whether these properties become better or not. In addition, we have also investigated their optical and electrical properties which could not only be useful in other applications but also helps in arriving at a comprehensive picture of the physics of these materials.

In the ZST $(Zr_{0.8}Sn_{0.2})TiO_4$ composition, the sub oxides TiO_2, ZrO_2 and $ZrTiO_4$ are also interesting due to their excellent optical, electrical and dielectric properties. Therefore, we have also undertaken studies of the individual components of ZST films, namely, TiO_2, ZrO_2 and $ZrTiO_4$ films. A systematic preparation effort starting from Ti and Zr metals, proceeding to $ZrTiO_4$ gave confidence to prepare ZST films by simple reactive magnetron sputtering. These investigations also led us to understand the growth of ZST films. Films of TiO_2 and ZrO_2 were deposited from Ti and Zr metal targets and $ZrTiO_4$ using both Ti & Zr targets by the DC reactive magnetron sputtering. These films were characterized by standard methods and their microwave, optical and electrical properties were also studied and results were compared with the existing literature.

The research work described above constitutes the thesis for the award of the Ph.D. degree of the University of Hyderabad. The thesis contains eight chapters. Brief description of the contents of each chapter is given below.

Chapter 1

The first chapter gives a brief introduction to dielectrics, dielectric resonators (DR), ZST and related areas. The historical background and the development of the Dielectric Resonator (DR) from physics and device points of view are presented. Requirements of a material to be used as a DR and a brief overview of bulk DR materials developed are discussed.

The importance of high dielectric constant and low loss films, the characteristics of SiO_2 in MOSFET devices and the difficulties of its replacement are discussed. Then the motivation behind choosing Zirconium Tin Titanate (ZST) as an

interesting system in bulk and thin film form for microwave applications as a DR, for MIC substrate, as a gate oxide and for optical applications are also described.

Chapter 2

Second chapter describes preparation and characterization techniques both for the bulk materials and thin films. The DR materials have been prepared by solid–state reaction method and the sintering mechanisms are discussed in detail. XRD and SEM are used to study the phase composition and microstructure of the DR materials respectively. Dielectric constant (ε_r) and the quality factor values (Q) at microwave frequencies were measured using the Hakki-Coleman dielectric resonator method as modified and improved by Courtney. The temperature coefficient of resonance frequency (τ_f) at microwave frequency was measured in the temperature range 25-80°C. Along with these microwave measurement techniques, the technique of the impedance spectroscopy is described which is used to measure electrical properties of ZST.

An introduction to the DC reactive magnetron sputtering technique, which is used to deposit the films in the $(Zr,Sn)TiO_4$ system has been described. The characterization techniques such as XRD for identification of phases, AFM for microstructure, envelop technique to calculate the optical constants such as refractive index, extinction coefficient and optical bandgap and the packing densities from spectral transmittance spectra are given in detail. Details on the techniques used for electrical and the low frequency dielectric properties of the films using a "Metal-Insulator-Metal (MIM) capacitor structure" and microwave dielectric properties of the films using the cavity perturbation technique are given in this chapter.

Chapter 3

The third chapter describes preparation of ZST ceramics. Since the sintering temperature of the pure ZST ceramics is about 1650°C, the efforts were made to improve the densification by reducing the initial particle size and with the addition of 1wt% ZnO as a sintering aid. With the addition of 1wt% ZnO and reduction of particle size of ZST to 220 nm, the sintering temperature is significantly reduced from 1650 to1350°C and gave improved microwave dielectric properties compared to pure ZST. Further efforts were made to reduce the sintering temperature with the addition of CuO along with 1wt% ZnO as sintering aids using ball-milling time as a variable

parameter. It was found that with these additions sintering temperature of ZST reduced to 1300°C. In addition, the Q factor became better. The impedance spectroscopy of the samples with CuO and without CuO was carried out and it was found that this material does not have any other loss generating mechanism at lower frequencies except the temperature dependant generation of charge carriers.

The microwave dielectric properties of the ZST ceramics were also measured at cryogenic temperatures (15-290K). It was found that the Q factor of the sample without CuO decreased with increase in temperature where as the samples with the addition of CuO up to 1.0wt% showed less dependence on temperature. The Q factor of CuO free ZST is 15000 and that of ZST with 0.5wt% of CuO is 11800 at 15K. The Q factor while measured at room temperature ranged between 2900-7000 at 9.5GHz frequency.

Chapter 4

In the fourth chapter a systematic study of the effect of various additives on the densification, microstructure and on the microwave dielectric properties of ZST are presented. Initially a brief literature review of the additives to ZST is given and then we describe the purpose of additives which were chosen to add to ZST ceramics. The different additives added to ZST are BaO, SrO, MgO, Ta_2O_5, Nb_2O_5, V_2O_5, Sm_2O_3, Nd_2O_3, CeO_2, B_2O_3, ZnO-B_2O_3 and 5ZnO-2B_2O_3. The sintering temperatures and the sintering durations were optimized in each case to get uniform microstructure and higher densities.

All these additives, except glass additives, did not cause any secondary phase formation up to 1.5wt% of the additive concentration; In the case of glass additives, up to 1wt% there is no secondary phases as determined by X-ray diffraction. The addition of BaO and V_2O_5 shows higher densification compared to other additives at 1300°C whereas other additives did not have any effect on lowering the sintering temperature. The addition of glass additives significantly reduced the sintering temperature of ZST ceramic without affecting the microwave dielectric properties. The maximum densities obtained are 98.6%, 98.2% and 98.7% of the theoretical density of ZST for the samples doped with B_2O_3, ZnO-B_2O_3 and 5ZnO-2B_2O_3 sintered at 1150, 1200 and 1250°C, respectively. The microstructures of the ZST ceramics were improved with the addition of these additives.

With the addition of all these additives it was found that there is not much change in the dielectric constant and temperature coefficient of the resonant frequency, whereas the quality factor is found to be a variable. These observations are discussed in this chapter.

Chapter 5

The fifth chapter describes the optimization of processing parameters of the films in the (Zr,Sn)TiO_4 system. The structural and microstructural aspects of the deposited films are also discussed. ZST thin films and the components in the (Zr,Sn)TiO_4 system such as TiO_2, ZrO_2 and $ZrTiO_4$ were deposited on various substrates like, borosilicate glass, quartz and on platinized silicon from the corresponding metal targets Ti, Zr and Sn in the presence of oxygen in the sputter chamber. Initially the growth kinetics of the TiO_2, ZrO_2 and $ZrTiO_4$ films are studied to deposit ZST films from the individual Ti, Zr and Sn metal targets In this thesis deposition of TiO_2, ZrO_2, $ZrTiO_4$ and ZST films deposited in pure oxygen atmosphere in a dc plasma without using argon in the sputter chamber is demonstrated. A study of optimization of various sputtering parameters, including oxygen percentage, was done to get good films.

All TiO_2 films deposited on glass are observed to be crystalline having a mixture of both anatase and rutile phases. It was found that as the oxygen percentage increases the percentage of rutile phase increased. Films deposited on quartz and platinized silicon showed only anatase phase.

ZrO_2 films deposited on glass and with 40-80% of oxygen percentage in sputter chamber exhibited both monoclinic and cubic phases. Films deposited on the same substrate with other oxygen percentages showed only monoclinic phase. However films deposited on quartz exhibited only monoclinic phase at all oxygen percentages.

$ZrTiO_4$ films were deposited from Zr&Ti metal targets and found that films deposited on glass and platinized silicon were partially crystallized in the orthorhombic phase whereas films deposited on quartz were amorphous irrespective of the processing parameters. Similarly ZST films were also deposited from Zr, Sn & Ti metals from a single dc magnetron cathode and found that films deposited on glass were partially crystallized whereas the films deposited on quartz and platinized silicon were amorphous in nature. In all the cases, as deposited films were crystalline without

any external heating. It was observed that the crystal structures and the microstructures of the deposited films were dependent on the processing parameters.

Chapter 6

In this chapter the optical and electrical properties of the films in the $(Zr,Sn)TiO_4$ system were discussed. For all TiO_2, ZrO_2, ZrTiO4 and ZST films it was observed that films deposited at higher Oxygen Mixing Percentage (OMP) showed higher transmittance percentages. The refractive index (n) and the extinction coefficient (k) of the films decreased with increase in OMP. The variation in n values was attributed to variation in the packing densities and partial crystallinity of the films. The extinction coefficients of the films were lower and ranged between 10^{-3} to 10^{-4}.

The optical bandgap values increased with increase in OMP indicating that the films were well oxidized and the films deposited at higher working pressures of O_2 showed higher bandgap values. The films deposited on quartz exhibited higher bandgap values than the films deposited on glass and it is attributed to the fact that the films grown in the amorphous phase exhibits higher bandgap values. It was also found that the bandgap decreases with increase in crystallite size, exhibiting approximately $1/d^2$ dependence where d is the crystallite diameter.

Chapter 7

The dielectric properties of the films in the $(Zr,Sn)TiO_4$ system measured both at lower and at microwave frequencies and the effect of processing parameters, crystallite size and strain on the dielectric properties are discussed in detail in this chapter.

The dielectric properties of TiO_2, ZrO_2, $ZrTiO_4$ and ZST films were measured both at lower (1Hz to 15 MHz) and at microwave (8.2-12.4 GHz) frequencies as a function of OMP. The capacitors (MIM structures) of TiO_2, ZrO_2, $ZrTiO_4$ and ZST films prepared under different OMP were fabricated to measure dielectric properties at low frequencies. All the films deposited at 40% OMP showed highest dielectric constant with low loss both at lower and microwave frequencies; However, ZrO_2 films showed a slightly different behaviour that is, it did not show low loss but showed high dielectric constant. In all the cases (TiO_2, ZrO_2, $ZrTiO_4$ and ZST), the

dielectric constant of each film is close to the bulk value whereas the dielectric loss of the films are observed to be higher than the bulk value.

Interestingly, in all the cases the microwave dielectric loss showed a strong dependence on strain. It is observed that as the strain in the deposited films increases the dielectric loss also increases. In general, reduction in strain and increase in crystallinity occur for the films deposited at higher temperatures but in the present case the films were deposited at ambient temperatures. In all the cases, the reasons for the increase in dielectric loss with increase in OMP could be the partial crystallinity of the films at some OMPs, porosity and the increase in strain in the deposited films with increase in OMP and the decrease in dielectric loss is attributed to the larger uniform grain size.

Detailed observations, their discussion and possible explanations are presented in this chapter.

Chapter 8

This chapter describes an attempt to find correlations between bulk and thin film properties of ZST. Summary of the present work, possible applications and possibilities for further research work are also given.

Chapter-1

Introduction to Dielectric Resonators and High-k Thin Films

1.1 Introduction to dielectric resonators:

Dielectric resonator (DR) is an unmetallized object which functions as a resonant device by means of reflections at the high (ε) dielectric-air interface.

In recent years the rapid growth of the wireless communication industry has created a high demand for microwave ceramic components. Commercial wireless technologies such as cellular phones, direct broadcasting satellite (DBS) and global positioning systems (GPS) have been making rapid progress due to the improved performance of dielectric resonators at microwave frequencies [1,2]. These materials are primarily used in microwave integrated circuits (MIC) as resonator elements, substrates, coaxial resonators and ceramic filters. These unique technologies demand materials, which have their own specialized requirements and functions. The requirements of these materials are high dielectric constant (ε_r), high quality factor (Q) and close to zero value of temperature coefficient of resonant frequency (τ_f). High dielectric constant is important, since it is the key for miniaturization because the size of the resonator depends on the inverse of the square root of the dielectric constant of the material. Higher the quality factor ($Q= 1/\tan\delta$) lower will be the insertion loss and steeper the cut-off frequency. Close to zero ppm/°C value of τ_f ensures temperature stable operation of MICs [1, 2].

The quartz resonators are not attractive at microwave frequencies due to the small signal to noise ratio available with frequency multiplication to microwave frequencies. The metallic cavity resonators are bulky and difficult to integrate with the microwave integrated circuits. The microstrip resonators have emerged but they have high dielectric loss and poor thermal stability.

1.2 History of dielectric resonators:

Lord Rayleigh [3] showed that an infinitely long cylinder of a dielectric material can serve as a guide for electromagnetic waves at certain frequencies, which means that the dielectric has the effect of causing the electromagnetic wave to be confined to the cylinder and its vicinity. In 1939, Ritchmyer [4] proved that

unmetallized dielectric materials could function as electrical resonators, which he called as dielectric resonators (DRs).

The primary reason for confinement of microwaves in and in the vicinity of a DR is its large value of permittivity, ε_r. The dielectric air boundary will be a perfect reflector of microwaves if the angle of incidence is greater than the critical angle $\theta_c = \sin^{-1}(1/\varepsilon_r)$. For large value of ε_r, θ_c is totally internally reflected. Depending on the geometry, the waves will undergo multiple total internal reflections. The reflection coefficient approaches unity as the dielectric constant increases. For this reason, Kajfez [5] considered the dielectric air boundary of a high dielectric material as an interface closer to a perfect magnetic conductor (PMC), in which the magnetic field tangential to its surface is zero. As the dielectric constant increases, the electric and magnetic fields are confined in and near the resonator resulting in small radiation losses.

1.3 Modes in a dielectric resonator:

As in the case of resonant cavities there are many possible resonant modes that can be excited in a DR. The modes are divided in to three main families.

- Transverse Electric Modes (TE)
- Transverse Magnetic Modes (TM)
- Hybrid Electromagnetic Modes (HEM)

The lowest hybrid mode is $HEM_{11\delta}$. Its resonant frequency can come even lower than that of the widely used $TE_{01\delta}$ mode. Its proximity to $TE_{01\delta}$ mode is governed by the aspect ratio of the DR and the proximity of perturbing metallic surfaces to the DR. Proximity of $HEM_{11\delta}$ mode to $TE_{01\delta}$ mode is not preferred as the former got a very low value of Q. The $HEM_{21\delta}$ mode also has lower resonant frequency, which falls right between $TE_{01\delta}$ and $TM_{01\delta}$ modes. Thus, when operating in either of these modes, $HEM_{21\delta}$ modes can cause difficulties. Coupling to TM modes needs different arrangement compared to TE modes. But HEM modes can get coupled to both the TE and TM coupling arrangements, as they have both components. HEM modes are highly leaky (i.e. radiative) and can cause difficulties in using TE and TM modes with their inherent Q values. The complexity of HEM modes increases as the integers m and n take higher values. An aspect ratio of 2.5 makes $TE_{01\delta}$ well separated from all the neighboring modes.

The resonant modes of a cylindrical resonator can be divided in to constituent modes with azimuthal variation given by cos(mφ) or sin(mφ), where m=0, 1,2,3... For m=0 (i.e. axial symmetric modes) the set of modes can be divided in to TE_{mnp} and TM_{mnp}. The first subscript m refers to azimuthal dependence of modes in φ. Second subscript n is radial mode number and the third subscript p denotes the axial mode number. They refer to the field extremes within the DR in the radial and axial directions. Due to the evanescent field effects in a DR, it is customary to replace p with $\ell + \delta$, where ℓ=0, 1, 2, 3... and $0<\delta<\ell$ which means that there are ℓ number of half period variations and a fraction of a period of field variation in the DR along the axial direction.

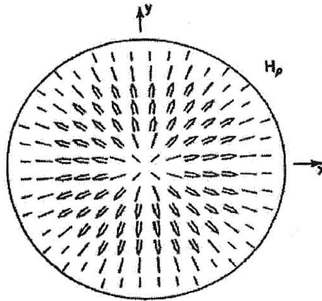

Figure 1.3a: Magnetic field in equatorial plane of the $TE_{01\delta}$ mode [5]

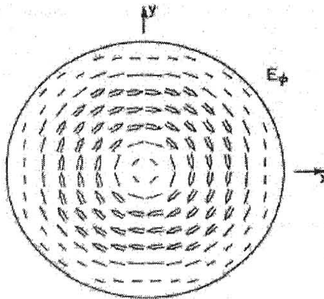

Figure 1.3b: Electric field in equatorial plane of the $TE_{01\delta}$ Mode [5].

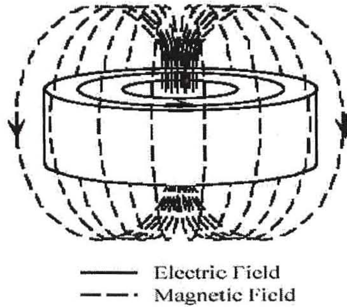

Figure 1.3c: Magnetic and Electric field together in a DR (side view) [3].

The most commonly used mode in the resonator is $TE_{01\delta}$. The magnetic field and electric field lines for this mode are shown in figure 1.3a and 1.3b and the magnetic and electric field together in a DR is shown in figure 1.3c for the $TE_{01\delta}$ mode.

The electric field lines are simple circles concentric with the axis of the cylinder. When the relative dielectric constant is around 40, more than 95% of the electric energy of the $TE_{01\delta}$ mode as well as more than 60% of the magnetic energy is stored inside the DR. The remaining energy is distributed in the air around the DR, decaying rapidly with distance away from the DR vicinity. Although the geometrical form of a dielectric resonator is extremely simple, an exact solution of the Maxwell's equations is considerably more difficult for an isolated DR. To find out the resonant frequencies of a DR with known value of dielectric constant, and having a diameter to height ratio D/L (aspect ratio), standard mode charts are available. Kobayashi and Tanaka [6] reported a mode chart for a dielectric rod resonator short circuited at both ends. Mode chart graphically represents the variation of the factor $\varepsilon_r\,(D/\lambda_o)^2$ as a function of $(D/L)^2$ for all the resonant modes. λ_o is the free space wavelength corresponding to the resonant frequency of the mode. From the mode chart, the resonant frequencies of the all resonant modes of a DR can be found using its ε_r, D and L values. Also one can find out the order in which various modes appear in frequency spectrum using the mode chart. This is important because the proximity of some leaky modes to the mode which is being used can lead to degradation of its performance. From the mode chart, one can find out the aspect ratio which must be used for a DR with given value of ε_r, to get maximum isolation for the mode of

interest. For an approximate estimation of the resonant frequency of the isolated DR, the following simple formula can be used [5].

$$f_{GHz} = \frac{34}{D_{mn}\sqrt{\varepsilon}}\left[\frac{D}{L} + 3\ 45\right] \qquad (1.3.1)$$

where D is the radius and L is the height of the DR.

The size of a DR is considerably smaller than the size of an empty resonant cavity operating at the same frequency. The shape of a DR is usually a cylinder but one can also find tubular, spherical and parallelepiped shapes as shown in figure 1.3d.

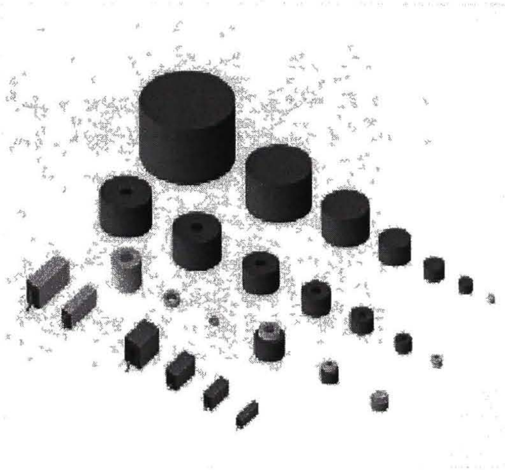

Figure 1.3d: Shapes of DRs commercially available [5].

1.4a Material requirements of a DR:

The important characteristics to be satisfied by a material for DR application are:

(i) High dielectric constant

The dielectric constant of the dielectric resonator material is important because it will ultimately determine the size of the DR. A cylindrically shaped DR sustains an electromagnetic standing wave within its volume because of the reflection at the dielectric air interface. The wavelength of the standing wave is about equal to the diameter of the cylinder and is given by, $D \sim c/f_0\varepsilon_r^{1/2}$ [5] where D is the diameter of the

resonator, c is the velocity of the electromagnetic waves, f_o is the resonant frequency and ε_r is the permitivity of the resonator. Therefore it is more important to have the dielectric constant as high as possible in order to reduce the size of the DR.

(ii) Quality factor (Q)

The quality factor is the figure of merit in assessing the performance of a resonator, which is a measure of the energy loss or dissipation per cycle as with respect to the energy stored in the fields inside the resonator and is defined by

Q = 2π (maximum energy stored)/ (average energy dissipated per cycle)

$$Q= \omega_o W_o/p \qquad (1.4.1)$$

where W_o is stored energy, p is power dissipation and ω_o is the resonant angular frequency.

Perfect dielectrics have no losses since its electrical conductivity is zero, but in real dielectric materials are partially conducting. Therefore the electromagnetic signal looses power as it goes through a dielectric material. For DR applications, Q factor is important and the losses should be minimum. When a DR is coupled to a microwave circuit, from the resonance curve the loaded Q-factor can be calculated as,

$$Q_\ell=f_o/\Delta f \qquad (1.4.2)$$

where f_o is the resonant frequency and Δf is the half power bandwidth at resonant frequency. A higher Q value provides a better signal to noise ratio. This Q-factor is called the unloaded quality factor (Q_u).

$$Q_u=Q_\ell(1+k) \qquad (1.4.3)$$

Where, k is the coupling coefficient. To get accurate value of Q_u, weakly coupled case ($k<1$) is preferred [5]. For a resonator structure there are number of factors that affect the Q_u including: dielectric itself, conduction in the walls of the enclosure and radiation, which are referred to as Q_d, Q_c and Q_r respectively. The losses of the dielectric itself can be divided in to two categories: Intrinsic and extrinsic losses. The intrinsic losses are dependent on the composition and the crystal structure of the material. The extrinsic losses are determined by the microstructure of the material that arises from impurities, vacancies, grain boundaries, porosity, oxygen non-stoichiometry, dislocations etc. The intrinsic losses are arising from the absorption of microwave field by the optical phonons and their eventual degeneration in to thermal phonons [7]. It is well known that the Q-factor of a composition is highest in its single crystal form as it will be free from many of the imperfections of a ceramic.

There are three main mechanisms for microwave absorption: 1) losses in perfect (ideal) crystals because of anharmonic lattice forces which mediate interaction between crystal lattice and phonons 2) losses in real but homogeneous crystals caused by the periodicity defects (isotopes, dopant atoms, vacancies etc) and 3) losses in real inhomogeneous ceramics by extended dislocations, grain boundaries, pores and secondary phases. The first category of loss can be influenced by modifying the composition itself by changing the crystal structure. The other categories of loss depends on many extraneous factors and hence could be influenced by additives and processing conditions.

(iii) Temperature coefficient of the resonant frequency (τ_f)

The temperature coefficient of resonant frequency determines how well a resonator will function when there are fluctuations in temperature. This includes the ambient temperature as well as heating by microwave absorption in the resonator structure. The τ_f is a combination of three independent factors: temperature coefficient of the dielectric constant (τ_ε), thermal expansion of the material (α_L) and the thermal expansion of the environment in which the resonator is mounted. Assuming that the third factor is negligible, the τ_f is given by [5].

$$\tau_f \approx -(\tau_\varepsilon/2+\alpha_L) \qquad (1.4.4)$$

Changes in temperature can cause changes in the dielectric constant and the volume of the resonator and hence the resonant frequency. The acceptable range of values of τ_f for microwave circuit applications is close to zero ppm/°C (±3 ppm/°C). A material with a small positive value of τ_f variation can often be combined with another material with a small negative τ_f variation to make the resonator temperature stable. τ_f is calculated using the relation,

$$\tau_f = \frac{1}{fo} \times \frac{\Delta f}{\Delta T} \text{ ppm/}^{\circ}\text{C} \qquad (1.4.5)$$

where, Δf is the change in resonant frequency over a temperature difference of ΔT, and f_o is the resonant frequency at room temperature (25°C).

1.4b Known dielectric resonator materials:

Various materials are reported for DR applications. These include ceramic mixtures, glass ceramic systems and single-phase compounds. They give the required characteristics by optimizing the processing conditions and in some cases with the

addition of trace quantity of additives. The characteristics of some of these compositions are given in table 1.4b.I. All these compositions have oxygen octahedra as their basic building block. The ions, which occupy the sites inside the octahedra, are indicated separately.

Sl.No	Composition	Structure	ε_r	Qxf$_o$ GHz	τ_f ppm/°C	Ions within the Octahedra	Ref. No.
1	(Mg,Ca) TiO_3	Perovskite	21	56,000	0	Ti	8
2	$Ba(Zn_{1/3}Ta_{2/3})O_3$	Complex perovskite	27-33	1,20,000	2	Zn, Ta	9
3	$Ba(Co,Zn)_{1/3}Nb_{2/3}O_3$	Complex perovskite	34	90,000	0		10
4	$(Zr_{0.8}Sn_{0.2})TiO_4$	α-pbO_2	38	50,000	0	Zr, Sn, Ti	11
5	$Ba_2Ti_9O_{20}$	Perovskite like Hollandite structure	40	32,000	2	Ti	12
6	$ZrTiO_4$-$ZnNb_2O_6$	α-pbO_2	44	48,000	0	Ti, Nb	10
7	$CaTiO_3$-$NdAlO_3$	Perovskite	45	45,000	0		13
8	0.5$BaTiO_3$-0.5 $La(Mg_{1/2}Ti_{1/2})O_3$	Perovskite	61	10,000	-2	Ti, Mg	14
9	$Bi_2(Zn_{1/3}Nb_{2/3})_2O_7$	pyrochlore	76.2	3000		Zn, Nb	15
10	$Ba_4Nd_{9.333}Tu_{18}O_{54}$	Perovskite/ Tetragonal tungsten bronze	80	10000	0	Nd, Ti	16
11	BaO-Pb0-Nd_2O_3-TiO_2	Multiphase system	90	5000	0	Nd, Ti	17

Table 1.4b.I: Some of the DR materials that are known for DR applications

The above-tabulated DR compositions can be classified as

a) Low ε_r and high Q compositions (S.No.1-3)

b) Medium ε_r compositions (S.No.4-7)

c) High ε_r compositions (S.No.8-11)

Some compositions in the first set can be used in millimeter range applications and the second set are utilized in the widely used 4-12GHz range whereas the last group is efficient for use in the lower frequency ranges.

An observation of the structure of these DR compositions reveals that all of them have either perovskite or perovskite related structure. In these structures oxygen octahedra is the basic building block in all the compositions and in all these cases they enclose a highly transition metal ion at their centre. Octahedra share only corners in most of the cases. In most of the cases, the octahedra do not get aligned along a straight line.

Reany et al [10] found that when $\log_{10}Qxf_o$ is plotted against ε_r, it gives a straight line for the commercial DR ceramics. It illustrates the fundamental physical principle that dielectric loss and dielectric constant are not independent parameters.

Colla et al [18] showed that a major factor controlling τ_f was the onset of octahedral tilt transitions. Tilt transitions occur when corner shared oxygen octahedra rotates either in phase or anti phase around the major axes of the perovskite structure. A combination of phase transitions, typically involving rotations of the oxygen octahedra, and modifying permittivity by adjusting the polarizability per unit volume are routinely used to control τ_ε. Maintaining a high Q value while adjusting τ_f is more problematic [10].

For complex perovskites, the order/disorder behavior is important. Complex perovskites that exhibits 1:2 ordered cell usually have highest Q values. To induce 1:2 ordering, the temperature of the order/disorder phase transition needs to be determined and the sample annealed below this value. Optimization of processing parameters to avoid porosity, inhomogeneity, second phases, impurities and pressing defects in general result in increased Q values.

1.4c Current state of materials developed for dielectric resonator applications:

Initially a number of materials have been explored in the attempts to develop suitable microwave dielectric materials. The first generation of ceramic resonators were based on $(Mg,Ca)TiO_3$, $ZrTiO_4$ and $Ba_2TiO_9O_{20}$. In the beginning of the 1990's the ceramic technology for hand sets and base stations diverged. At present $Ba_4Nd_{9.333}Tu_{18}O_{54}$ (BNT) based compounds are used primarily for digital television receivers while $CaTiO_3$-$NdAlO_3$ (CTNA) and $ZrTiO_4$-$ZnNb_2O_6$ (ZT-ZN) based ceramics dominates the base station resonator market. $Ba(Co,Zn)_{1/3}Nb_{2/3}O_3$ (BCZN) based ceramics are a recent entrant and they are cheaper replacement for the more expensive materials [10].

1.4d Future requirements of the DR materials:

In order for microwave dielectric ceramics to be used in base stations, they must inevitably offer a commercial advantage over competing technologies. In particular metal cavities offer an alternative to ceramic resonators. Qxf_o factors of metal cavities are considerably lower (~6000 GHz) but they are two orders of magnitude cheaper. The high cost of ceramics comes from the often-expensive raw

materials such as Nb_2O_5 and Ta_2O_5, and the complex manufacturing process necessary to ensure optimum properties. Therefore, ceramics are only used where high Q is paramount and miniaturization is necessary. At the same time, the efforts are focused on to improve Q particularly by minimizing the extrinsic losses.

Ceramics offer a distinct advantage over competing technologies in the use of unusual geometries to induce multimode resonance, by reducing cost and space. The unusual shapes and designs lay down new challenges to ceramists to control τ_f, ε_r and Q, despite the processing stages required [10].

The microwave ceramic resonator market for base station technology has matured and industry is focusing primarily on improvement on Q and its cost [10]. New applications for low loss microwave ceramics are constantly emerging such as global positioning systems, low temperature co-fired ceramics for embedded microwave circuitry, tunable filters and applications in advanced radar technology [10].

1.5 Physics of DR materials:

1.5a Polarization mechanisms in dielectrics

Polarization is an ordering in space of electrically charged unit under the influence of an external electric field. This causes the formation of an electric moment in the entire volume of the dielectric and in each separate polarizing unit (atom, ion or molecule). Linear dielectrics show a direct proportionality between the induced electric dipole moment p acquired by the polarizable unit during the process of polarization and the intensity E of the field acting on it as given by $p=\alpha E$. Where α is known as the polarizability. Polarizability reflects the properties of individual polarizable unit and not of a certain volume of matter and is the most important microscopic electrical parameter of a dielectric. During polarization the charges that are displaceable will be brought in to motion. Piling up of mobile charge carriers at physical barriers such as grain boundary causes interfacial polarization or space charge polarization. At low frequencies (~1 KHz) this mechanism gives rise to a high dielectric constant. Dipolar polarization occurs due to the molecules containing permanent dipole moment or by the rotation of dipoles between two equilibrium positions and this relaxes around 10^3 to10^6 Hz. The ionic polarization occurs due to the displacement of the positive and negative ions against each other and it relaxes in

the frequency range of 10^{12} to 10^{13} Hz. Electronic polarization occurs due to the displacement of electrons with respect to the atomic nucleus and it relaxes at high frequencies ~10^{15}Hz. The mechanisms of these four polarizations are shown schematically in figure 1.5a. Each of these involves a short–range motion of charge and contributes to the total polarization of the material, and at microwave frequencies ionic and electronic polarizations contribute to the dielectric properties [19].

1.5b Dielectric losses

According to the material requirements for DRs the dielectric losses and temperature dependence of dielectric properties assumes more significant.

Generally, three mechanisms can be distinguished for dielectric losses at microwave frequencies [7].

The dielectric losses related to phonon damping are usually described in the framework of classical dielectric function

$$\varepsilon(\omega)=\varepsilon_{\infty}+\sum_{J}\frac{J}{\omega_{J}^{2}{}_{TO}-\omega^{2}+\iota\gamma_{J}\omega} \tag{1.5.1}$$

where, ε_{∞} is the permittivity at optical frequencies, ω_{JTO} are the frequencies of the transverse optical (TO) lattice modes, and f_J and γ_J are their oscillator strengths and damping constants respectively. The dielectric loss at microwave frequencies ($\omega \ll \omega_{J\ TO}$, i.e. ω=0) can be calculated from equation (1.5.1) as

$$\tan\delta=\omega\sum_{J}\frac{J}{\varepsilon(O)}\frac{\gamma_{J}}{\omega_{JTO}^{4}} \tag{1.5.2}$$

For the practically important case of kT being larger than the phonon energy, the anharmonic interactions between phonons caused by the third and fourth order terms of the lattice potential lead to $\gamma_J \propto T$ and $\gamma_J \propto T^2$ respectively [20]. The dominating dampening process among these is the decay of one TO phonon in to two acoustical (thermal) phonons [21]. Equation 1.5.2 shows that, in cases of dominating intrinsic losses, the product of quality factor (Q=1/tanδ) and frequency f (ω=2πf) is expected to be constant, a rule which holds, at least approximately for many ceramics. Recent days, it is widely accepted that intrinsic losses can be determined by far-infrared (FIR) spectroscopy, and therefore this method is now often is used for the characterization of classical microwave ceramics and related compounds [22]. FIR spectroscopy greatly simplifies the search for new low loss ceramics because in the

FIR frequency range, intrinsic losses out number extrinsic ones, and thus FIR data are much less sensitive to processing than the losses measured at microwave frequencies.

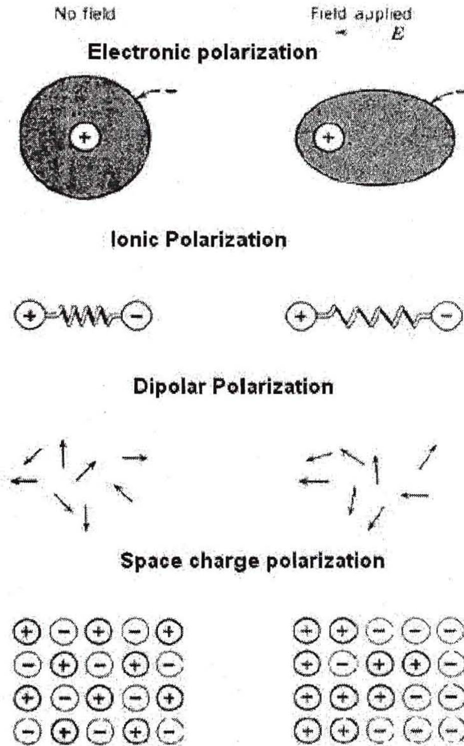

Figure 1.5a: Different types of polarization in a dielectric [19].

Knowledge of the intrinsic losses is useful to examine the extent to which the losses of microwave ceramics can be reduced to the small intrinsic values by using advanced processing methods [23]. It is also interesting to note that the intrinsic losses are closely related to the value of permittivity a power law, $\tan\delta \propto \varepsilon^{a}$ with a=4 [7].

1.5c Temperature coefficients

To obtain temperature stable oscillators and filters, it is necessary that the resonant frequency (f_r) of a resonator does not change much over a large temperature

range (generally in the range of -20 to +80°C). The temperature coefficient of resonant frequency τ_f is given by [7]

$$\tau_f = \frac{1}{f_r} \cdot \frac{\partial f}{\partial T} \approx \frac{1}{f_r} \cdot \frac{\Delta f_r}{\Delta T} \qquad (1.5.3)$$

where T is the temperature. Because the resonant frequency of a resonator depends on its size and on ε, the following equation holds true [7].

$$\tau_f \approx -(\tau_\varepsilon/2 + \alpha_L) \qquad (1.5.4)$$

Where τ_ε is defined according to τ_f in equation (1.5.3) and α_l is the linear thermal expansion coefficient, i.e. the temperature coefficient of one of the resonator dimensions (eg. length, l). The requirement that $\tau_f = 0$ translates then in to $\tau_\varepsilon \approx -2\alpha_l$. In addition, it is often necessary that the τ_f in a material system be variable between positive and negative values by virtue of variation of the materials composition. This enables one to set the temperature drift of the composite element containing a resonator equal to zero [7].

From the equation 1.5.4, the discussion on temperature coefficients can be restricted to consider only the temperature coefficient of permittivity τ_ε and τ_ε is defined as [7]

$$\tau_\varepsilon = \frac{(\varepsilon_r - 1)(\varepsilon_r + 2)}{\varepsilon_r} \left[\frac{\upsilon}{\alpha} \left(\frac{\partial \alpha}{\partial \upsilon} \right)_T \alpha_l + \frac{1}{3\alpha} \left(\frac{\partial \alpha}{\partial T} \right)_\upsilon - \alpha_l \right] \qquad (1.5.5)$$

The above equation directly follows from the Clausius-Mosotti equation, which takes the long-range coulomb interactions in to account. From the equation 1.5.5 it is important to note that the polarizability α equals the sum of polarizabilities of all atoms in a unit cell with volume υ only if all the atoms in the structure have a cubic environment. This is the case for alkali halides but not for complicated structures. However, the additional dipole fields can be taken in to account by an effective polarizability α so that both the Clausius-Mosotti equation and equation 1.5.5 are valid. In the case of perovskites, for example, the effective polarizabilty α is obtained by adding an additional ionic polarizabilty $\Delta\alpha^1$ to the electronic and ionic polaraizabilities of all atoms in the unit cell. This additional polarizability $\Delta\alpha'$ caused by the structure contributes an additional term proportional to $-\alpha_l \Delta\alpha'$ in equation 1.5.5 [7].

In materials with more complicated structures, the additional ionic polarizabilty $\Delta\alpha'$ is not only raises ε_r value but also shifts τ_ε to negative values [7].

Both strong electronic polarizabilities and $\Delta\alpha'$ also give rise to a softening of the lattice modes [7]. Thus the anharmonic contribution $\left(\frac{\partial\alpha}{\partial T}\right)_{\upsilon}$ to τ_{ε} increases and makes τ_{ε} more negative. In the case of microwave dielectrics, ionic polarizabilitiy dominates ε_r and thus τ_{ε} is affected [7].

1.6 Electronic applications of high –k (ε_r) materials in thin film form:

Thin film science and technology plays an important role in the present day industries. Thin film technology has been developed primarily for the need of the integrated circuit industry. The demand for development of smaller and smaller devices with higher speed especially in new generation of integrated circuits requires advanced materials and new processing techniques suitable for future giga scale integration (GSI) technology. In this regard, physics and technology of thin films can play an important role to achieve this goal. The production of thin films for device purposes has been developed over the past 40 years. Thin films as a two dimensional system are of great importance to many real-world problems. Their material costs are very small as compared to the corresponding bulk material and they perform the same function when it comes to surface processes. Thus, knowledge and determination of the nature, functions and properties of thin films can be used for the development of new technologies for future applications.

Thin film technology is based on three foundations: fabrication, characterization and applications. Some of the important applications of thin films are in microelectronics, communication, optical electronics, catalysis, surface coating of all kinds and in energy generation and conservation strategies.

Since 1997, a consortium of industry representatives has developed and customized the International Technology Roadmap on Semiconductors (ITRS): a publication on the projected equipment, design, and material requirements needed to maintain the rapid evolution of integrated circuit (IC) technology. The 1999 ITRS publication projected the need for superior high dielectric constant (ε_r), low leakage current materials to replace SiO_2 in gate stacks in complementary metal-oxide semiconductor (CMOS) and dynamic random access memory (DRAM) devices by the year 2005. Since then, it has become apparent that advanced high speed IC's are being developed much faster than the ITRS forecasts. The revised 2000 roadmap stated that,

"while developmental progress in this area has been significant, it becomes increasingly probable that chip production with high–ε_r gate stacks will be very difficult to achieve (even) in the 2005 time frame, and therefore appears unlikely in the more accelerated time frames suggested by the new proposed gate length scaling forecasts. Consequently a major 2001 task is the analysis of the current accelerated trend, and the identification of design, device and material alternatives imposed by the difficulties of accelerated high ε_r/dual metal gate CMOS integration" [24].

For 40 years, SiO_2 has been used as the gate dielectric material in silicon based CMOS devices. Demand for greater speed and increased storage capacity has driven the feature size shrinkage of CMOS-based circuits and storage devices. With the shrinkage of metal-oxide semiconductor field effect transistor (MOSFET) devices, channel lengths and gate dielectric thickness have been scaled to maintain performance and turn-on voltage characteristics. SiO_2 has been scaled down to attain the desired capacitance, but a roadblock exists in how thin the SiO_2 layer can be made without exceeding the leakage current requirements. Below~0.7nm the leakage current of SiO_2 through electron tunneling becomes too high, to maintain device requirements. The leakage current is particularly important for logic devices, which must maintain tightly controlled turn-on and turn-off voltages. The leakage current, although important for storage devices, does not require a stringent design rule for dynamic memory devices since the data must be periodically re-written to the bit in the operation. Data is re-written on the order of every two to three hundred milliseconds. [25] Leakage current is considerably more important for static memory devices. New high ε_r materials that meet varying requirements are fervently being sought to replace SiO_2 by the projected timeframes for the production of future generation devices. With higher dielectric materials, the required capacitance can be maintained with thicker gate layers thereby keeping leakage current under control.

The equation for capacitance is typically written in terms of t_{eq}, the Equivalent Oxide Thickness (EOT). EOT represents the theoretical thickness of SiO_2 required to achieve the same capacitance as the high ε_r replacement material. If the dielectric material is SiO_2 (ε=3.9), then

$$t_{eq}=3.9.\ \varepsilon_o.\left[\frac{A}{C}\right] \qquad (1.6.1)$$

Assuming a capacitance density (C/A) = 34.5 fF/μm^2, then t_{eq} = 1nm. For an alternative dielectric material to achieve the same capacitance density equivalent to t_{eq} =1nm,

$$t_{high\text{-}k} = \frac{\varepsilon_{high-k}}{3.9} t_{eq} \quad (1.6.2)$$

A material with dielectric constant ε = 25 would require a physical thickness of 6.4 nm to achieve the same capacitance density as SiO_2 with t_{eq} = 1nm. Often, a thin SiO_2 interfacial layer is produced either during the deposition of the higher ε_r material or during post deposition annealing treatments. The incorporation of interfacial layers between the silicon substance and the high-ε_r material effectively reduce the overall dielectric constant of the material. The series capacitance of two dielectrics in contact is given by,

$$\frac{1}{C_{total}} = \frac{1}{C_1} + \frac{1}{C_2} \quad (1.6.3)$$

where C_1 and C_2 are the capacitances of the two dielectric materials present. The equivalent oxide thickness can then be given by

$$t_{eq} = t_{SiO_2} + \left(\frac{3.9}{\varepsilon_{high-k}}\right) t_{high-k} \quad (1.6.4)$$

From equation 1.6.4, it can be seen that when an interfacial SiO_2 layer is present, the minimum achievable EOT is that of the lower dielectric constant material. This is true whether the dielectric material is SiO_2, a silicide, or a silicate.

Table of EOT comparison for different films is tabulated in table 1.6.I

Name of the Material	ε_r	**EOT (nm)**	**Name of the Material**	ε_r	**EOT (nm)**
Si_3N_4	7.5	1.79	Ta_2O_5	25	6.66
Al_2O_3	9.1	2.3	La_2O_3	28	7.69
$HfSiO_x$	10	2.82	Pr_2O_3	30	7.94
Y_2O_3	16	3.84	$ZrTiO_4$	38	9.74
HfO_2	18	5.38	$(Zr,Sn)TiO_4$	38	9.74
ZrO_2	22	6.4	TiO_2	100	20.51

Table 1.6.I: Comparison of EOT for different materials.

From the above table it is clear that, higher the dielectric constant, higher is the EOT.

1.7 Characteristics of SiO_2 in MOSFET devices and the difficulties of its replacement:

The use of SiO_2 on silicon for producing MOSFETs offers several key advantages that can be split between two categories: (1) fundamental properties and (2) device properties. The fundamental properties of SiO_2 include dielectric constant, barrier height, stability in contact with silicon, and morphology. Device properties include: processing, integration and performance issues such as interface quality, process compatibility, device lifetime and reliability [26]. SiO_2, the current gate dielectric material in FET devices has proven to be an extremely difficult material to replace, since it has several characteristics that make it advantageous as the gate dielectric for silicon based FET devices. Among them, SiO_2 is a thermodynamically stable, self-passivating, amorphous oxide that acts as a water insoluble barrier. The density of the oxide can be tailored such that it effectively impedes the diffusion of contaminants and impurities to the underlying silicon. Growth of SiO_2 is so thermodynamically favorable that growth of SiO_2 on pristine silicon surfaces in ambient conditions is impossible to avert. Thick, high purity films have been thermally grown on silicon substrates with a low fixed charge density ($< 5x10^{10}$ cm^{-2}) and an interface with silicon that exhibits a low density of states ($<5x10^{10}$ cm^{-2}-eV) reproducibly. While SiO_2 is one of the thinnest components of the device, it routinely and reliably withstands the highest electric field (~1MV/cm). Additionally, it exhibits a small amount of low-frequency C-V hysteresis and frequency dispersion (<10mV). Furthermore, the dielectric exhibits small amounts of stress-induced leakage currents (SILC) resulting from voltage stress, high surface mobility at the interface, and is highly reliable after years of high-field stress (~10 years). SiO_2 is thermally, chemically and mechanically compatible with Si and heavily doped poly-Si doping, and anneals at 950-1050°C, without noticeable loss of the intrinsic properties noted above. For SiO_2, the leakage current changes from $1x10^{-12}$ A/cm^2 at 3.5 nm to 10 A/cm^2 at 1.5 nm. The band gap of SiO_2 is 8.9 eV with band offsets relative to Si greater than 1 eV. Today, the silicon oxide layer is doped with nitrogen to form silicon oxynitrides SiO_xN_y, to prevent diffusion of boron dopants in adjacent poly-Si layers and to increase the dielectric constant to ~6.5 [27-29]. Achievement of all these characteristics with another dielectric layer of comparable or better properties is an extremely difficult task.

1.8 Efforts to replace SiO_2:

Table 1.8.I lists several materials and their properties including dielectric constant that have been studied as possible replacement for SiO_2. Before the discussion begins, it is important to understand the requirements for differing device applications. For memory/storage applications, significant attention has been focused on Ta_2O_5, $SrTiO_3$ and Al_2O_3. Static memory applications require a very low leakage current ($J<10^{-8} A/cm^2$) and high charge storage density. In this case, thermodynamic stability of the high-ε_r materials on silicon is not as critical since the dielectric material is sandwiched by the electrodes, poly-Si or metal. Attempts to minimize interfacial reactions are solely to maximize charge density storage capacity [30]. Additionally, unlike MOSFET applications, no electric field penetration below the bottom electrode is required allowing the use of metal or heavily doped poly-Si as the bottom electrode. Also, current transport along the dielectric interface is not important as in MOSFET applications. Ultimately, the bottom dielectric interface is not as critical in storage applications.

Material	ε_r	Bandgap (eV)	Crystal Structure
TiO_2	100	3.4	Tetragonal (Rutile, Anatase)
La_2O_3	30	4.3	Hexagonal, Cubic
Ta_2O_5	26	4.5	Orthorhombic
HfO_2	25	5.7	Monoclinic, Tetragonal, Cubic
ZrO_2	25	5.9	Monoclinic, Tetragonal, Cubic
Pr_2O_3	26	3.5	Amorphous
Y_2O_3	15	5.6	Cubic
Al_2O_3	9	8.7	Amorphous
Si_3N_4	7	5.1	Amorphous
SiO_2	3.9	8.9	Amorphous

Table 1.8.I: List of high-ε_r material candidates.

A significant research has been done on the materials listed in table 1.8.I, but these materials don't possess all the requirements needed for the replacement of SiO_2. Studies of ternary and quaternary oxides and silicates have been the next frontier for

finding an adequate replacement. It is well understood that transition metal oxides can offer higher dielectric constants due to their higher polarizabilities. The use of mixed transition metal oxides have been studied as an approach to acquiring higher dielectric constants while attaining other required properties such as low leakage current and high stability.

In 1998, Van Dover et al. at Bell Laboratories [31] used a composition – spread approach to explore the dielectric constant of a wide range of zirconium tin titanate (ZST) compositions. They used RF magnetron sputtering to deposit different compositions of the $(Zr_xSn_yTi_Z)O_4$ system. A region of the ternary phase diagram was discovered where amorphous films exhibited ε_r of two to three times larger than those of Ta_2O_x films (ε_r = 50 to 70). In addition, the same region showed leakage currents from 10^{-9} to 10^{-7} A/cm^2 at 1 MV/cm. Based on these criteria, ZST appear to be a possible solution to the growing need for high-ε_r materials in IC devices.

1.9 Zirconium Tin Titanate (ZST): An interesting system in bulk and thin film form:

1.9a Bulk ZST for microwave applications

Dielectric materials based on the ZrO_2-SnO_2-TiO_2 ternary system are attractive for applications in the microwave domain due to their high dielectric constant, low loss, and controlled temperature coefficient of the permittivity. $(Zr_{0.8},Sn_{0.2})TiO_4$ (ZST) exhibits a near zero temperature coefficient of resonance frequency and hence offers a great stability to specific applications such as frequency discriminators, low phase-noise dielectric resonator oscillators, duplexers and filters and other applications. They are also useful as a substrate for microwave integrated circuit (MIC) substrates.

1.9b ZST thin film as a possible gate oxide in electronic applications

The search for materials with high dielectric constant as an alternative to SiO_2 in CMOS gate oxide and ULSI (Ultra Large Scale Integrated) dynamic random access memory (DRAM) applications have been the subject of intense research in recent years as described in the previous section.

As mentioned in the previous section, the physical and electrical properties of $(Zr,Sn)TiO_4$ thin films as reported by other researchers has good characteristics such as high dielectric constant, low dielectric loss and high temperature stability. These

properties make ZST thin film a noteworthy material in integrated electronics as well as in high frequency applications.

1.9c Structure of ZST

The crystal structure of $ZrTiO_4$ is orthorhombic α-PbO_2 type, shown in figure 1.9a and 9b, based on columns of zigzag chains of edge shared metal oxygen octahedral, two octahedra wide. These columns share corner oxygens with columns in the next metal plane in a close packed oxygen lattice [1]. For material heated at 1200°C and higher, the entropic contribution to the total energy of the crystal is dominant, and Zr and Ti are fully disordered and randomly mixed on the octahedral metal sites. At low temperatures, however the differences in co-ordination environments expected from Pauling rules that Ti should have octahedral coordination to oxygen and Zr cubic coordination to overcome entropy, and an ordered crystal structure is formed. In the ordered structure, the columns of edge shared metal oxygen polyhedra are either exclusively TiO_6 octahedra or distorted ZrO_8 cubes formed by slight local shift of the close packed oxygens [1]. The Ti and Zr edge shared columns alternatively. The distortion of the close packed oxygen lattice which occurs during the cation ordering results in the shortening of the crystallographic axes, an easily observable change often taken as the primary indicator that such an ordering has occurred. The ordering transition is sluggish, occurring on the same scale of ceramic processing and therefore the processing parameters such as cooling rate can have an important influence on the exact nature of the phase. Further it has been shown that there are more complex partially ordered sites between the fully ordered and disordered variants involving different TiO_6-ZrO_8 column sequences dependent on cooling rate and exact Zr/Ti ratio.

The effect of Sn substitution in the crystal structure has been studied in an attempt to correlate the structure and the dielectric properties [1]. In general, the addition of a third metal element to a material like $ZrTiO_4$ would expect to facilitate the occurrence of the disordered state, as partial mixing increases entropy and therefore stabilize the more disordered phase. This is true for this system on averaging over many unit cells, but the true microscopic structure is much more complex. The Sn substitution at temperatures which usually result in the ordered structure actually causes a mixing of ordered chain fragments of TiO_6 octahedra with ordered chain fragments of double ZrO_8 cubes along single columns, which in the fully ordered

structure would contain only octahedra or cubes. It has been reported that the Sn substitutions occur at the exact locations of the switching from TiO_6 octahedra to ZrO_8 cubes along the chains, thus resulting in more switching in the columns with increasing Sn content. This decrease in the correlation lengths of the ordered regions occurs with the increasing Sn content, as does the increase in Q and decrease in the temperature coefficient of the resonant frequency. Though the effect of Zr/Ti disorder is significant, it is not as dramatic as partial Sn substitution for Zr. The best properties were obtained for materials with pure Zr substitution as $Zr_{1-x}Sn_xTiO_4$ where the solid solution range is approximately $0.0<x<0.4$. At compositions between $x=0.2$ and 0.3 the best microwave dielectric properties of this composition are obtained [1].

Below 1200°C, the high-temperature phase, transforms to a low-temperature phase characterized by a small decrease in the longest unit cell dimension. It has been demonstrated that the transformation from the high-temperature to the low-temperature phase is marked by a reduction in the c-axis length from 0.55 to 0.535nm [32-35]. The transformation is indicative of an order-disorder transition. The high-temperature phase exhibits a disordered positioning of cations in the octahedral sites. As the temperature is reduced below 1200°C, the reduction of the c-axis length, as well as cation ordering, marks the phase transformation.

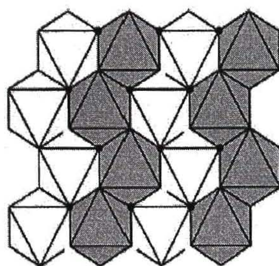

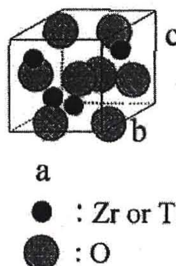

Figure 1.9a

Figure 1.9b

Figure 1.9a &b: Structure of $ZrTiO_4$. [1,36].

For figure 1.9a, the shaded and un shaded metal–oxygen octahedra are above and below the close packed plane of oxygen atoms in the plane of the paper. In the

disordered state, Zr and Ti are mixed on all metal sites. In the ordered state, columns of octahdra are occupied by either Zr or Ti with an accompanying distortion of the oxygen array.

Apart from the high-ε_r applications the films of $(Zr_{0.8},Sn_{0.2})TiO_4$ and the sub oxides of it such as TiO_2, ZrO_2 and $ZrTiO_4$ are suitable for application in interference coatings [37], optical wave guides [38], gas sensors [39], solar cells [40], for tribological applications [41], prostheses for the human body parts substitution [42], buffer layers for growing superconductors [43], oxygen sensors [44], heat resistant coatings [45] and ionic conductors [46].

1.10 Motivation of study:

Among many high- ε_r dielectric materials zirconium tin titanate (ZST) with composition $(Zr_{0.8},Sn_{0.2})TiO_4$ has been found to be an excellent material for the applications discussed above in bulk. It also has good optical and electrical properties which could be used for other electronic, photonic and microwave applications. Bulk ZST has a dielectric constant of 38, a high Qxf_o value of ~45,000 (where f_o is the frequency of measurement in GHz) and a temperature coefficient of resonant frequency nearly zero (~0ppm/°C) [47]. A disadvantage in preparing this material by the solid state reaction method is the requirement of very high sintering temperatures. Therefore it is interesting to look for ways to reduce its sintering temperature and the effect of such procedures on the microwave dielectric properties. Another important aspect in the study of DR materials is to understand the factors which influence Q value and to look for ways to improve it.

Some studies are already available on the thin films of the composition $(Zr_{0.8},Sn_{0.2})TiO_4$ prepared by RF sputtering [48], Pulsed Laser Deposition (PLD) [36] and Chemical Vapor Deposition (CVD) [49]. Those reports suggests that these films got lower leakage current compared to SiO_2, making them attractive for CMOS technology. Even though considerable amount of study has gone in to bulk ZST, studies on thin film ZST are rather few. It is noteworthy that ZST is made of oxides of stable metals, making it possible to use reactive dc magnetron sputtering for the growth of ZST films. This work is an attempt in that direction by growing ZST films by a cost effective process and to compare their properties with that of their bulk counterpart.

As a continuing effort in our laboratory on microwave materials, we have chosen to investigate ZST in the bulk form prepared by the solid–state reaction method and in thin film form prepared by the DC reactive magnetron sputtering. We have tried various techniques to reduce the sintering temperature to prepare bulk ZST and have been successful to some extent. To the best of our knowledge, the DC reactive magnetron sputtering has not been used by anyone to prepare ZST films. DC reactive magnetron sputtering technique has been used extensively for preparation of various kinds of films as it gives high deposition rates and is a relatively simple and cheaper technique than the ones like RF sputtering and Pulsed Laser Ablation. One can optimize the deposition parameters resulting in good thickness uniformity of films and giving high adhesion to the substrate. We have prepared ZST films from a single cathode consisting of Zr, Sn and Ti metals in appropriate proportions to get the right composition of ZST. This technique avoids the preparation of ceramic targets which is costly, lengthy and a time taking process. Another disadvantage is that the ceramic targets will usually crack after a few cycles of sputtering.

An important effort in this study was to improve the microwave dielectric properties of the bulk samples by improving the microstructure of this material prepared with different additives and temperature treatments. Another interest was to compare microwave properties of ZST in bulk as well as in thin film form in order to see whether the good bulk microwave properties are getting retained in thin film form. In addition, their optical and electrical properties are also investigated to arrive at a comprehensive picture of the physics of these materials.

In the ZST $(Zr_{0.8}Sn_{0.2})TiO_4$ composition, the sub oxides TiO_2, ZrO_2 and $ZrTiO_4$ are also interesting due to their excellent optical, electrical and dielectric properties. Therefore, we have also undertaken studies of the individual components of ZST composition, namely, TiO_2, ZrO_2 and $ZrTiO_4$ films. A systematic preparation effort starting from Ti and Zr metals, proceeding to TiO_2, ZrO_2 and $ZrTiO_4$ films gave confidence to prepare ZST films by simple reactive magnetron sputtering. These investigations also led us to explore the growth of these films in 100% oxygen in the sputtering atmosphere. Films of TiO_2 and ZrO_2 were deposited from Ti and Zr metal targets and $ZrTiO_4$ using both Ti & Zr targets by the DC reactive magnetron sputtering. These films were characterized by standard methods and their microwave, optical and electrical properties were studied and results compared with the existing literature.

References:

[1] R.J.Cava, J.Mater.Chem., **11**, 54 (2001).

[2] A.Ioachim, M.G.Banciu, M.I.Toacsen, L.Nedelcu, D.Ghetu, H.V.Alexandrau, C.Berbecaru, A.Dutu and G.Stoica, Appl.Surf.Sci., **253**, 335 (2006).

[3] Rayleigh, Phil.Mag., **43**, 123 (1892).

[4] R.D.Richtmeyer, J.Appl.Phys., **10**, 359 (1939).

[5] D.Kajfez "Dielectric resonators" D.Kajfez and P.Guillon (Eds.), (Artech House, Norwood) 1986.

[6] Y.Kobayashi and S.Tanaka, IEEE Trans. Microwave Theory Tech., **28**, 1077 (1980).

[7] W.Wersing, "High Frequency Ceramic Dielectrics and Their Applications for Microwave Components" In Electronic Ceramics, (Elsevier Applied Science, London U.K) 1991.

[8] K.Wakino, Ferroelectrics, **91**, 69 (1989).

[9] S. Kawashima, M. Nishida, I. Ueda and K. Wakino, J. Am. Ceram. Soc., **66**, 421 (1983).

[10] I.M.Reaney and D.Iddles, J. Am. Ceram. Soc., **89**, 2063 (2006).

[11] R.B.Von Dover, L.F.Schneemeyer and R.M.Fleming, Nature, **392**, 162 (1998).

[12] H.M.O'Bryan and J.Thomson, J. Am. Ceram. Soc., **66**, 66 (1983).

[13] B. Jancar, D. Suvorov, M. Valan, G. Drazic, J. Euro. Ceram. Soc., **23**, 1391 (2003).

[14] M.P. Seabra, M. Avdeev, V.M. Ferreira, R.C. Pullar, N. Mc N Alford, I.M. Reaney, J. Am.Ceram.Soc., **87**, 584 (2004).

[15] S.Y. Wu, Y. Li and X.M. Chen, J. Appl. Phys., **96**, 5683 (2004).

[16] J.M.Durand and J.P.Boilot, J.Mater.Sci.Lett., **6**, 134 (1987).

[17] K.Wakino, K.Minai, and H.Tamura, J. Am. Ceram. Soc., **67**, 278 (1984).

[18] E.L.Colla, I.M.Reaney and N.Setter, J.Appl.Phys., **74**, 3414 (1993).

[19] B.Tareev, "Physics of dielectric materials" (Mir Publishers, Moscow) 1975.

[20] V.L.Gurevich and A.K. Tagantsev, Sov.Phys. JETP, **64**, 142 (1986).

[21] F.Gervais and B.Piriou, Phys.Rev.B, **10**, 1642 (1974).

[22] R.Kudesia, A.E.Mc Hale R.A.Condrate, and R.L Synder, J.Mater.Sci., **28**, 5569 (1993).

[23] K.Fukada and R.kitoh, J.Am.Ceram.Soc., 77, 149 (1994).
[24] Semiconductors Industry Association, "International Technology Roadmap for Semiconductors", 2001.
[25] A.I. Kingon, J.P. Maria, and S.K. Streiffer, Nature, **406**, 1032 (2000).
[26] R.M. Wallace and G. Wilk, Mater. Res. Bull., **27**, 192 (2002).
[27] D.A. Buchanan, IBM Journal of Research and Development, **43**, 245 (1999).
[28] H.R. Huff, A. Hou, C. Lim, Y. Kim, J. Barnett, G. Bersuker, G.A. Brown, C.D. Young, P.M. Zeitzoff, J. Gutt, P. Lysaght, M.L. Gardner and R.W. Murto, Proceedings of the Conference of Nano and Giga Challenges in Microelectronics, Moscow, pp 1-18 (2002).
[29] D.G. Schlom and J.H. Haeni, Mater. Res. Bull., **27**, 198 (2002).
[30] G.D. Wilk, R.M. Wallace, and J.M. Anthony, J. Appl. Phys., **89**, 5243 (2001).
[31] R.B.V. Dover, L.F. Schneemeyer, and M. Fleming, Nature, **392**, 162 (1998).
[32] L.W. Caughanour, R.S. Roth, and M. Fleming, Journal of Research of the National Bureau of Standards, **52**, 37 (1954).
[33] R.E. Newnham, J.Am. Ceram. Soc., **50**, 216 (1967).
[34] R.W. Lynch and B.Morosin, J.Am. Ceram. Soc., **55**, 409 (1972).
[35] A. McHale and R. Roth, Communications of the J.Am. Ceram. Soc., **C18-C20**, (1983).
[36] O. Nakagawara, Y. Toyota, M. Kobayashi, Y. Yoshino, Y. Katayama, H. Tabata, and T. Kawai, J. Appl.Phys., **80**, 388 (1996).
[37] H.K.Pulker " Coatings on glass" (Elsevier Science Publishers B.V) 1984.
[38] Zhai Jiwei, Yang Tao, Zhang Liangying and Yao Xi, Ceramics International, **25,** 667 (1999).
[39] R. Zhang, M.I.Tejedor, M. A.Anderson, M. Paulose and Craig A.Grimes, Sensors, **2**, 331 (2002).
[40] U.Bach, D.Lupo, P.Comle, J.E.Moser, F.Weissortel, J.Salbeck and H.Spreitzer, Nature, **395**, 583 (1998).
[41] S.Lang, T.Beck, A.Schattke, C.Uhlaq and A.Dinia, Surf.Coat.Technol., **180-181**, 85 (2004).
[42] M.Ferraris, E.Verne, P.Appendino, C.Moisescu, A.Krajewski, A.Ravaglioli, and A.Piancastelli, Biomaterials, **21**, 765 (2000).
[43] Y.Komatsu, T.Sato, S.Ito and K.Akadi, Thin Solid Films, **341**, 132 (1999).

[44] G.L Tan and X-J Wu, Thin Solid Films, **330**, 59 (1998).

[45] K.Izumi, M.Murakami, T.Deguchi and A.Morita, J.Am.Ceram.Soc., **72**, 1465 (1989).

[46] A.K.Jonsson, G.A.Niklasson and M.Veszelei, Thin Solid Films, **402**, 242 (2002).

[47] R. Christoffersen and P.K. Davies, J.Am. Ceram. Soc., **75**, 5 (1992).

[48] C-L. Huang and C-H. Hsu, J. Appl. Phys., **96**, 1186 (2004).

[49] E-L.Mays, D.W.Hess and W.S. Rees Jr, J.Crys.Growth., **261**, 309 (2004).

Chapter-2

Preparation and Characterization Techniques Used for Bulk and Thin Films of Compositions in the System $(Zr,Sn)TiO_4$

This chapter describes the preparation and characterization techniques used for both bulk ZST and the thin films of compositions in the $(Zr,Sn)TiO_4$ system.

Section 2.1 and its subsequent sections describe the preparation of ZST ceramics by solid-state reaction method, sintering mechanisms, measurement techniques used for measuring microwave dielectric properties and impedance spectroscopy. Section 2.5 and its subsequent sections describe the preparation of (Zr,Sn) TiO4 films and its sub oxides by dc reactive magnetron sputtering. The characterization techniques used for measuring the optical, electrical and dielectric properties of these films are also described.

2.1 Preparation and characterization techniques for bulk $(Zr,Sn)TiO_4$:

This section deals with the preparation and characterization techniques used for the bulk ZST composition. Since this material has to be characterized for its DR properties in the microwave range, it has to be prepared in a regular geometry with highest possible densification. This being a ceramic oxide material, the available methods for its preparation are (a) Solid-state reaction method (or ceramic method) (b) Chemical methods and (c) Mechanical methods [1-3]. Of these, the method used for bulk ZST preparation in this study is the Solid-state reaction method.

2.1.1 Solid-state reaction method:

Ceramics are polycrystalline materials having fine crystalline grains and imperfections like grain boundaries, impurities segregated in the grains and grain boundaries, pores etc. Since they are in general brittle refractories, shaping them and densifying without cracks and deformation is a challenge. The solid-state reaction method is used for forming the ZST composition from the reagents. The shaping and densification are separate processes which are described in subsequent sections.

The conventional solid state reaction method involves the following steps: (a) Uniform mixing of the initial reagents (b) Phase formation of the required compound at

high temperature which is called the calcinations stage. The main disadvantages of this method are that it needs high processing temperatures in order to achieve best properties and this process increases the particle size. But cost effectiveness and simplicity are the major advantages of this process.

2.1.2 Stoichiometric weighing of reagents:

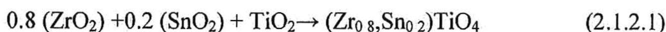

$$0.8\,(ZrO_2) + 0.2\,(SnO_2) + TiO_2 \rightarrow (Zr_{0.8},Sn_{0.2})TiO_4 \qquad (2.1.2.1)$$

The required ratios of the reagents as per the above chemical equation are weighed. The purity (>99.9%, Aldrich Chemicals) of the initial reagents is important to achieve control over impurities in the product and to maintain reproducible microwave dielectric properties. An electronic balance (A&D technologies, Model GR-120) is used to weigh the reagents, which has accuracy up to 0.001mgm.

2.1.3 Uniform mixing of reagents:

The individual reagents are to be mixed uniformly in order to increase the point of contacts between the reagents, which will act as product layer formation centres. Therefore the initial stoichiometric reagents mixture must be mixed uniformly with a suitable mixing medium. The powders were mixed (at 150 rotations per minute for 1 hour) using a planetary Ball mill (Retsch PM 100) in a zirconia jar with different diameters of zirconia balls. Deionized water was used as mixing medium.

2.1.4 Calcination stage:

The solid state, diffusion controlled chemical reaction between the initial reactants resulting in the desired phase formation is called calcination. It is the intermediate heat treatment at lower temperatures prior to sintering. Calcination could involve chemical decomposition reactions in which a solid reactant is heated to produce a new solid phase and to remove the gas which are commonly associated with the initial metal oxide compounds such as carbonates, hydroxides, nitrides, suphates, acetates and other metal salts. The parameters of calcination stage such as temperature, duration of heating and atmosphere are important factors influencing shrinkage during sintering. In the present case, the reagents being oxides, do not undergo any decomposition. With the

help of the X-ray diffraction pattern of the calcined products, the completion of reaction, desired phase formation and presence of impurity or secondary phases are identified.

2.1.5 Particle size reduction:

The particle size reduction (milling) of the complex oxides after the calcination stage is important to homogenize the formed phase. It is well known that the smaller initial particle size reduces the sintering temperature and enhances the density of the ceramics. The planetary ball mills are generally used for milling the powders to achieve particle size reduction. The planetary ball mill owes its name to the planet like movement of its vials. These are arranged on a rotating support disk and a special drive mechanism causing them to rotate around their own axes while revolving in a circle. The centrifugal force produced by the vials rotating around their own axes and that produced by the rotating support disk, both act on the vial contents, consisting of material to be ground and grinding balls added inside the vial.

There are several processing variables that determine the final size of the particles, after milling process, such as type of mill, vial, milling speed, milling time, type, shape, size, and size distribution of the milling medium, ball to powder ratio, extent of filling of vial, milling atmosphere, process control agent and temperature of milling [4]. In the present study, Retsch PM 100 planetary ball mill was employed to achieve the initial stoichiometric mixing before the calcination and to reduce the particle size of the calcined ceramic powders. Zirconia vials and different diameters of spherical (5, 10 & 20 mm) zirconia balls are used. All the processing parameters were optimized to achieve smaller particle sizes. In the milling process, the particle experiences mechanical stresses at their contact points due to compression, shear with the milling medium or with other particles. The mechanical stress leads to elastic and inelastic deformation. If the stress is exceeding the ultimate strength of the particle, it will fracture the particles. The mechanical energy supplied to the particle is used not only to create new surfaces but also to produce physical changes in the particle.

2.1.6 Uniaxial Pressing:

After reducing the particle size of the calcined powder, the fine powder is compacted in to cylindrical specimens (green pellets) by uniaxial pressing. The compaction of the powder should be done slowly to facilitate the escape of the entrapped air. To make the green pellets of the ceramic powder, a rigid die which is rust free is needed. To make the inner walls of the die smooth, stearic acid is used as an internal lubricant. The pressure gradient on the die as a function of the distance from the upper punch is given by the equation

$$P_X = P_a\, e^{-4\mu KL/D} \qquad (2.1.6.1)$$

where, μ is the coefficient of friction, P_a is the applied pressure, L is the length and D is the diameter of the die and K is a constant [5].

2.1.7a Solid-State Sintering:

In ceramics, porosity is an important parameter which governs may of its properties. For maximizing properties such as dielectric constant, quality factor, mechanical strength, translucency and thermal conductivity, it is desirable to eliminate as much of porosity as possible. The purpose of sintering is the reduction of porosity in the compact. The development of microstructure and densification during sintering is a direct consequence of mass transport through several possible paths and one of these paths is usually predominant at any given stage of sintering [5]. The sintering phenomena are of two types: solid state sintering and liquid phase sintering. In the former one, the densification is achieved through the change in particle shape, without particle rearrangement. In the liquid phase sintering, some liquid is present at sintering temperature that aids densification.

During sintering process, significant diffusion and viscous flow occurs when a liquid phase is present or produced by a chemical reaction. The driving force for sintering is the capillary pressure associated with surface curvature where the particles come in to contact. In order to reduce the surface area, atoms diffuse to the points of contact, permitting contact flattening. Contact flattening involves the removal of matter between particle centers by volume diffusion or diffusion through a liquid phase [6]. These mechanisms must be promoted for the pores to shrink and eventually to get eliminated.

Coarsening mechanisms such as surface diffusion or evaporation –condensation must be minimized as they only redistribute matter around surfaces. There are three major stages in sintering. In the initial stage, there is surface smoothening of the particles, neck growth and rounding of interconnected open pores. Diffusion of active, segregated dopants can occur and the porosity decreases by about12%. The initial density of the green ceramics is around 60% and after initial stage, the density will be around 70% of theoretical density (TD). However, in the initial stage the 10% densification reaches quickly in few minutes after reaching to higher sintering temperature, because of the large surface area and high driving force for sintering [6]. In the intermediate stage, there is a formation of neck growth as densification proceeds, particle centers approach one another, resulting in further shrinkage of the compact. The shrinkage in this stage can result in about 90% of TD.

In the final stage of sintering, isolated pores are eliminated by mass transport from the grain boundary at the pore and the uniform grain growth takes place. Pore on a grain boundary gets eliminated by grain boundary or lattice diffusion, but pores within the grains can be eliminated by lattice diffusion only, which can be a problem since volume diffusion often has higher activation energy. The complete elimination of porosity in the final stage of sintering can only happen when all pores are connected to fast and short diffusion paths along grain boundaries. In most ceramics, the lattice diffusivity of the slower rate-limiting constituent is often too slow for effective annihilation of pores that got trapped in grains. To achieve higher densities, the elimination of pores attached at the grain boundary is important.

In the initial stage, there are a number of competing paths for material to be transported to the neck area. Some of these paths will lead to densification, which is a shrinkage process that requires the centers of particles to approach each other. Other paths will lead to coarsening, which is the growth of neck between the particles leading to a reduction in specific surface area without shrinkage. These different paths of diffusion are competitive paths of transport. The mechanism that gives the fastest rate of neck growth will dominate and cause either densification or coarsening. Surface diffusion is the general transport mechanism that can produce surface smoothing, particle joining and pore rounding without volume shrinkage. In materials where vapor pressure is high,

sublimation and vapor transport to surfaces of lower vapor pressures also produce these effects. In contrast, grain boundary diffusion and lattice diffusion produce neck growth and volume shrinkage. At high temperatures, grain boundary diffusion and lattice diffusion tend to dominate and therefore promote densification. Firing at lower temperatures can cause coarsening without significant densification and can be useful in making mechanically strong but porous materials. Therefore the enhanced solid state sintering of DRs requires dopants that enhance volume and grain boundary diffusion at lower temperatures without affecting the microwave dielectric properties.

Solid state sintering of mixed cation oxides that are used in DRs is an ambipolar diffusion process in which anions and cations must be transported from the source to sink without kinetic de-mixing. The rate limiting mechanism will be slowest moving species along the fast path. Therefore, rate of sintering depends a great deal on the diffusivities and additives that influence diffusion. Additives often helps to decrease the rate of coarsening in the earlier stages of sintering, increase the rate of densification and decrease the rate of grain growth.

2.1.7b Recrystallization and grain growth

Primary recrystallization is the process by which nucleation and growth of a new generation of strain free grains occurs in a matrix which has been plastically deformed [6]. Grain growth is the process by which the average grain size of the strain free or nearly strain free material increases continuously during heat treatment without change in the grain size distribution. Secondary recrystallization, sometimes called abnormal or discontinuous grain growth, is the process by which a few large grains are nucleated and grow at the expanse of fine grained, but essentially strain free, matrix.

Primary recrystallization process has its driving force in the increased energy of a matrix which has been plastically deformed. If the isothermal change in grain size of strain free crystals in a deformed matrix is measured after an initial induction period, there is a constant rate of grain growth for the new strain free grains. If the grain size is d [6],

$$d = U\,(t - t_o) \qquad (2.1.7.1)$$

where, U is the growth rate (cm/sec), t is the time and t_o is the induction period.

The induction period corresponds to the time required for unstable embryos present to grow to the size of a stable nucleus. For a nucleus to be stable, its size must be larger than some critical diameter at which the lowered free energy of the new grain is equal to the increased surface free energy. If an unlimited number of sites are available, the rate of nucleation increases to some constant rate after an initial induction period. As the temperature increases, the rate of nucleation increases exponentially.

The growth rate remains constant until the grains begin to impinge on one another. The growth rate becoming constant results from the constant driving force (equal to the difference in energy between the strained matrix and strain free crystals). The final grain size is determined by the number of nuclei formed, i.e. the number of grains present when they finally impinge on one another.

Since both the nucleation and growth rate are strongly temperature dependent, the overall recrystallization changes rapidly with temperature. As the temperature is raised, the final grain size is larger, since the growth rate increases more rapidly than the rate of nucleation. However, at higher temperatures recrystallization is completed more rapidly so that the larger grain size observed can be due to the greater time available for grain growth following the recrystallization [6].

In general, it is observed that (1) some minimum deformation is required for recrystallization, (2) with the small degree of deformation a higher temperature is required for recrystallization to occur, (3) an increased annealing time lowers the temperature of recrystallization and (4) the final grain size depends on the degree of deformation, the initial grain size and the temperature of recrystallization. In addition, continued heat after the completion of recrystallization leads to the continuation of grain growth [6].

Grain growth: Whether or not primary recrystallization occurs, an aggregate of fine-grained crystals increases in average grain size when heated at elevated temperatures. As the grain size increases, it is obvious that some grains must shrink and disappear. An equivalent way of looking at grain growth is the rate of disappearance of grains. Then the driving force for the process is the difference in energy between the fine-grained material and the larger grain size product resulting from the decrease in grain boundary area and the total boundary energy [6].

2.1.8 Liquid phase sintering:

When a wetting liquid is present, bulk viscous flow can cause volume shrinkage [6]. When liquid coats at each grain, the material can often be sintered to a higher density at lower temperatures with less of a tendency for exaggerated grain growth. Less than 1vol% liquid phase is sufficient to coat the grains, if the liquid is distributed uniformly and grain size is about 1μm. The wetting liquid concentrates at the particle contacts and forms a meniscus, which exerts an effective compressive pressure on the compact. There is a rapid rearrangement of particles in to higher density configuration. After the initial rearrangements, further densification takes place as particle contacts flatten under the compressive stress applied to the point contacts by capillary pressure. The contact flattening occurs through dissolution at the particle contacts and transport of the materials towards stress free interfaces. This leads to appreciable grain growth compared to solid state sintering.

2.2 Characterization techniques used for the bulk compositions:

a. Powder X-Ray Diffraction
b. Scanning Electron Microscopy
c. Microwave Characterization Techniques

- Measurement of Dielectric Constant (ε_r)
- Measurement of Unloaded Quality Factor (Q_u)
- Measurement of Temperature Coefficient of Resonant Frequency (τ_f)

2.2a X-ray diffraction:

Powder X-Ray Diffraction is a powerful non-destructive method for determining a range of physical and chemical characteristics of materials. The applications include the type and quantities of phases present in the sample (phase analysis), the crystallographic unit cell and crystal structure, crystallographic texture, crystallite size, macro-stress and micro-strain and also electron radial distribution functions.

X-ray diffraction results from the interaction between X-rays and electrons of atoms. Depending on the atomic arrangement, interfaces between the scattered rays are

constructive when the path difference between two diffracted rays differ by an integral number of wavelengths which is described by the Bragg equation (Bragg's law)

$$2d \sin\theta = n\lambda \quad (2.2.1)$$

where, λ is the wavelength, d is the spacing between the planes and θ is the Bragg angle, which is the angle between incident and reflected beam [7].

In the present work, two types of X-ray diffractometeres were used to characterize the samples. One is with Co Kα (λ=1.7889Å) radiation in a wide angled powder X-ray diffractometer (INEL Model CPS120) equipped with a position sensitive detector and the other one is with Cu K_{α} (λ=1.54056 Å) radiation, using Philips PW 1830 diffractometer. Calibration using a Si standard was done to account for the instrumental line broadening and the value was approximately 0.15°.

2.2b Scanning electron microscopy:

In Scanning Electron Microscope (SEM), electrons are thermionically emitted from a tungsten cathode and are accelerated towards an anode. Alternatively, electrons can be emitted via field emission (FE). The electron beam, which typically has an energy ranging from a few hundred eV to 50 keV, is focused by one or two condenser lenses into a beam with a very fine focal spot size of 1 nm to 5 nm. The beam passes through pairs of scanning coils in the objective lens, which deflect the beam in a raster fashion over a rectangular area of the sample surface. Through these scattering events, the primary electron beam effectively spreads and fills a teardrop-shaped volume, known as the interaction volume, extending from less than 100 nm to around 5 μm into the surface. Interactions in this region lead to the subsequent emission of electrons which are then detected to produce an image. X-rays, which are also produced by the interaction of electrons with the sample, may also be detected in an SEM equipped for energy-dispersive X-ray spectroscopy or wavelength dispersive X-ray spectroscopy. The most common imaging mode monitors low energy (<50 eV) secondary electrons. Due to their low energy, these electrons originate within a few nanometers from the surface. The electrons are detected by a scintillator-photomultiplier device and the resulting signal is rendered into a two-dimensional intensity distribution that can be viewed and saved as a digital image. This process relies on a raster-scanned primary beam.

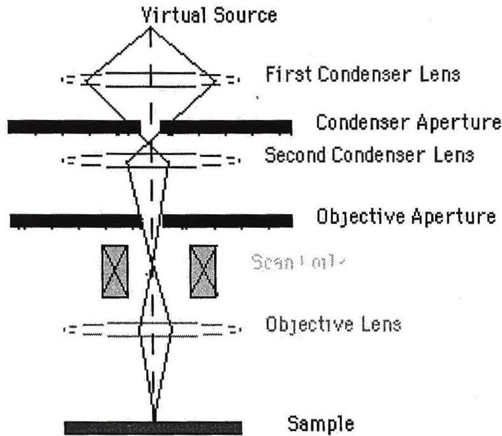

Figure 2.2b.1: Schematic diagram of SEM.

The brightness of the signal depends on the number of secondary electrons reaching the detector. If the beam enters the sample perpendicular to the surface, then the activated region is uniform about the axis of the beam and a certain number of electrons "escape" from within the sample. As the angle of incidence increases, the "escape" distance of one side of the beam will decrease, and more secondary electrons will be emitted. Thus steep surfaces and edges tend to be brighter than flat surfaces, which results in images with a well-defined, three-dimensional appearance. Using this technique, resolutions less than 1 nm are possible.

In addition to the secondary electrons, backscattered electrons can also be detected. Backscattered electrons may be used to detect contrast between areas with different chemical compositions.

2.3 Microwave measurements:

Miniaturization of microwave circuits is possible with the help of low loss, temperature stable dielectric resonators. These dielectric resonators are used to replace waveguide filters in such demanding applications as satellite communications where microstrip and stripline resonators cannot be used because of their inherently high losses [8]. The most accurate measurement methods for low loss dielectric materials at

microwave frequencies are resonance methods employing cavity, dielectric or open resonators [9]. The presence of air gaps is one of the most important factors limiting the measurement accuracy of high-permittivity solid materials, except when the electric field of the mode of interest does not have a component perpendicular to the surfaces of the sample. This is the situation for TE_{0np} modes of cylindrical cavities and dielectric resonators; Therefore methods employing these modes are considered to be among the most accurate [10]. The quasi-$TE_{01\delta}$ mode of operation (often called the TE_{011}-mode) is the mode most commonly used by manufacturers of dielectric materials for making dielectric loss tangent measurements. In this work, a resonant structure which can excite the TE_{011} mode in the reflection mode and having geometry as shown in figure 2.3.1 is used. It got a diameter which is 7 times that of the DR used.

The important characteristics of a DR are dielectric constant, loss tangent and temperature dependence of resonant frequency. The permeability of most of these materials is equal to that of free space, as they are non –magnetic materials. In this study a parallel-plate dielectric resonator structure known as Courtney set up [11] shown in figure 2.3.2 is used to measure the dielectric constant of the bulk dielectric material. The principle involved in the measurement is rather simple. The resonant frequency of a $TE_{01\delta}$ mode is measured for a dielectric resonator radius 'a' and height 'L'. Afterwards the dielectric constant is computed using the Courtney procedure [10]. Hakki and Coleman first introduced the procedure, the error analysis and investigation of temperature effects were later made by Courtney [11]. Another cylindrical cavity made of INVAR is used to measure the temperature coefficient of resonant frequency of the cylindrical DR. The negligible coefficient of thermal expansion of INVAR material helps to increase the accuracy of this measurement. The set up is shown in figure 2.3.3.

Theory

Consider now a circular cylindrical rod of relative dielectric constant ε_r, permeability μ_0, length 'L', and radius 'a' placed between two large perfectly conducting plates. If the dielectric material is isotropic then the characteristic equation for this resonant structure operating in the TE_{0nl} mode is

$$\alpha \frac{J_0(\alpha)}{J_1(\alpha)} = -\beta \frac{K_0(\beta)}{K_1(\beta)} \tag{2.3.1}$$

where, $J_0(\alpha)$ and $J_1(\alpha)$ are the Bessel functions of the first kind of orders zero and one, respectively, $K_0(\beta)$ and $K_1(\beta)$ are the modified Bessel functions of the second kind of orders zero and one, respectively. The parameters α and β depend on the geometry, the resonant wavelength, and dielectric properties. Thus

$$\alpha = \frac{2\pi a}{\lambda_0}\left[\varepsilon_r - \left[\frac{c}{v_p}\right]^2\right]^{1/2} \tag{2.3.2}$$

$$\beta = \frac{2\pi a}{\lambda_0}\left[\left(\frac{c}{v_p}\right)^2 - 1\right]^{1/2} \tag{2.3.3}$$

'c' being the velocity of light and v_p the phase velocity in the structure so that

$$\frac{c}{v_p} = \left(\frac{l\lambda_0}{2L}\right) \tag{2.3.4}$$

where, l is the number of longitudinal variations of the field along the axis, and λ_0 is the free space wavelength. It is seen that the characteristic equation is a transcendental equation and hence a graphical solution is necessary. The resulting mode charts are given by Hakki et al [10] where each value of β_l corresponds α_n.

2.3a Measurement of dielectric constant (ε')

The measurement can be done using transmission method introduced by Hakki and Coleman [11]. This setup is having two parallel plates with an adjustment for varying distance between the two plates. Two bent monopoles (rigid coaxial cables) are provided for coupling electromagnetic waves to the DR and are mounted in such a way that, they can be moved in any of the x, y and z directions. One can identify the modes of the DR by moving the bent monopoles in all three directions. The number of standing waves in z-directions indicates the third subscript of resonant mode. By rotating the rigid coaxial

cables around its own axis, one can find if the field is maximum in horizontal direction or vertical direction. Then the first subscript can be found by placing the coaxial cable at different angles in the plane of parallel plates. Once the resonant frequency of $TE_{01\delta}$ mode is measured using the procedure explained above, the relative dielectric constant for the dielectric resonator with known dimensions can be calculated using the equations (2.3.5) and (2.3.6).

$$\beta_l = \frac{2\pi a}{\lambda_0}\left[\left(\frac{l\lambda_0}{2L}\right)^2 - 1\right]^{\frac{1}{2}} \tag{2.3.5}$$

$$\varepsilon = \left(\frac{\alpha_n \lambda_0}{2\pi a}\right)^2 + \left(\frac{l\lambda_0}{2L}\right)^2 \tag{2.3.6}$$

Here β_l corresponds to α_n, which can be obtained from the mode chart given in [12] one of the characteristic equation.

2.3b Measurement of quality factor (Q)

Once the mode of operation and dielectric constant are determined, it is simple to derive the loss tangent of the dielectric material from a measured value of the unloaded Q_u value of the structure. The unloaded Q_u of the cavity is defined as 2π times the ratio of the maximum energy stored to the energy lost in one cycle. This measurement is done using reflection method with a cylindrical cavity having dimensions 7 times the DR. The rigid coaxial cable is provided at the center of the cavity as shown in figure 2.3.1 for electromagnetic field coupling and it can be moved in and out for adjusting between weak and strong coupling. The cavity is connected to the Vector Network Analyzer (VNA) through a rigid coaxial cable and is adjusted in such a way that weak coupling exists between the rigid coaxial cable and DR. The unloaded Q_u value is calculated using the coupling coefficient k, and loaded Q value, Q_ℓ, using the relation,

$$Q_u = Q_l(1+k) \tag{2.3.7}$$

Here k is the coupling coefficient, when the DR is under coupled.

2.3c Measurement of temperature coefficient of resonant frequency (τ_f)

The temperature dependent resonant frequency can be measured using the cavity made up of INVAR material. Invar material has least thermal expansion coefficient. The temperature is varied from room temperature to 80^0C to obtain the temperature coefficient of resonant frequency by using the equation (2.3.8)

$$\tau_f = \frac{1}{f_0}\frac{\Delta f}{\Delta T}\, ppm/^0 C \qquad (2.3.8)$$

where f_0 is the resonant frequency at room temperature and Δf is the change in resonant frequency for a variation in temperature of ΔT. The experimental setup used to measure τ_f is shown in figure 2.3.3.

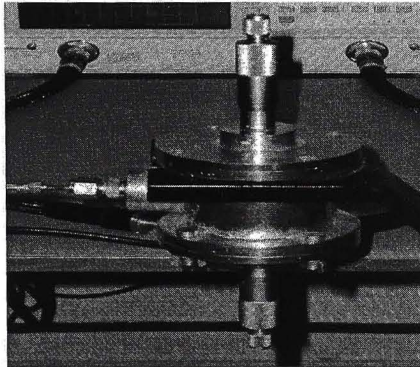

Figure 2.3.1: Cylindrical cavity resonator for measurement of quality factor.

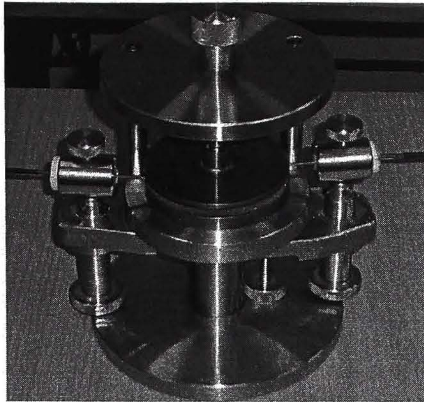

Figure 2.3.2: Sample holder used for the measurement of dielectric constant.

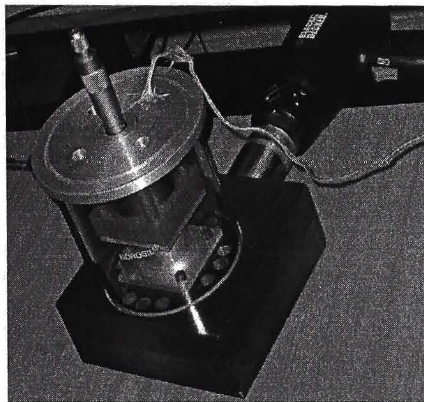

Figure 2.3.3: Cylindrical INVAR cavity resonator for measurement of τ_f

2.4 Electrical conductivity measurements:

DC measurement cannot yield the exact resistance of the samples due to the choice of electrode and polarization at the electrode-material interfaces. The equivalent circuit of a Metal-Insulator-Metal structure consists of circuit elements such as resistance (R), capacitance (C), inductance (L).The contribution of at least one component will be dependent on the frequency measurement [13,14]. Complex impedance analysis is a

technique in which the circuit elements are determined from the data obtained over a wide range of frequencies [15,16]. It involves the plotting of the real and imaginary parts of the complex electrical quantities such as

(a) Z^* - Complex Impedance

(b) Y^* - Complex Admittance

(c) ε^* - Complex Permitivity and

(d) Complex Modulus

These plots are characteristics of particular equivalent circuits and consist of a combination of semi circles and straight lines. The component values correspond to the intercepts with the real axis [17, 18]. The modulus of and permittivity plane plots are used for representing the response of the dielectric systems.

2.4.1 General theory

The applied voltage and the measurement current in an electrical network are given by

$$V(t)=Vo\ \exp(i\omega t) \qquad (2.4.1)$$

$$I(t)= Io\ \exp\ (i\omega t+\phi) \qquad (2.4.2)$$

where $\omega=2\pi f$, f is the frequency and ϕ is the phase angle.

$$Z^*(\omega)= |Z|\ \exp(-i\phi),$$

$$= |Z|\cos(\phi)-I\ |Z|\sin(\phi)$$

$$= Z'(\omega)-i\ Z''(\omega) \qquad (2.4.3)$$

where, $Z'(\omega)$ and $Z''(\omega)$ are the real and imaginary parts of the complex impedance. The relationships between various related quantities are:

$$|Z|=[Z'(\omega))^2+ Z''(\omega))^2]^{1/2} \qquad (2.4.4)$$

$$\text{Tan}\phi = Z'(\omega)/Z''(\omega) \quad (2.4.5)$$

$$\text{Admittance } Y''(\omega) = 1/Z^*(\omega) = G(\omega) + i\,B(\omega) \quad (2.4.6)$$

$$\text{Conductance } G(\omega) = Z'(\omega)/ Z'(\omega))^2 + Z''(\omega))^2] = 1/R \quad (2.4.7)$$

$$\text{Susceptance } B(\omega) = Z''(\omega) / [Z'(\omega))^2 + Z''(\omega))^2] = \omega C \quad (2.4.8)$$

The real and imaginary parts of the impedance/admittance of the samples are plotted and their frequency dispersion curves possess information about the electrode-material interface, bulk resistance etc. The idealized plots for certain lumped circuit elements are shown in figure 2.4.1.a. For parallel RC combination, we have

$$Z'(\omega) = R/(1 + (\omega RC)^2) \;\&\; Z''(\omega) = \omega R^2 C/(1 + (\omega RC)^2) \quad (2.4.9)$$

Elimination of ωRC leads to

$$(Z' - R/2)^2 + Z''^2 = (R/2)^2 \quad (2.4.10)$$

This is the equation of a semi circle, with radius =R/2 and center at (R/2, 0).

Consider a solid capacitor. Its equivalent circuit consists of a capacitance (C) in parallel with the sample resistance (R). The corresponding impedance and admittance plots are shown in figure 2.4.1a. The intercept of the dispersion curve on the real axis gives the bulk resistance/conductance. In addition to sample capacitance and resistance, for any real system there will be grain boundary and electrodes effects. Figures 2.4.2 (a-c) show the complex plane plots with electrode and grain boundary contributions.

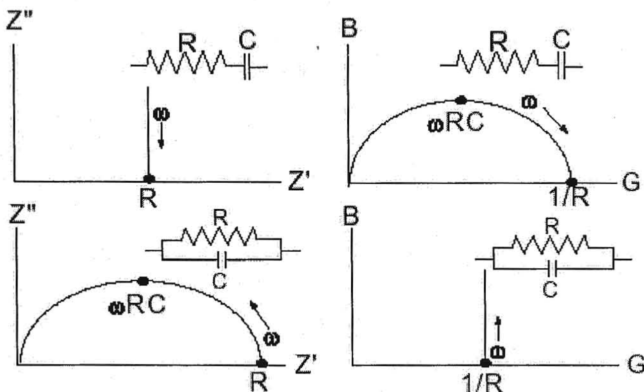

Figure 2.4.1a: Complex plane plots of impedance and admittance for R-C circuits.

For example, in figure 2.4.2a, in addition to a semi circle, a straight line at low frequencies is observed which a characteristic of the double layer capacitance is. In polycrystalline samples, there may be a contribution to the impedance from the presence of grain boundaries also. The grain boundary may act as a hindrance to ion transport or it may also provide a high conducting path (since the defect density may be larger in the interface region). Studying grain size effects on conductivity could help in identifying the conduction mechanism. Another common observation in the complex impedance is the depression of semi circle in the high frequency region, i.e. the center of the circle is situated below the real axis as shown in figure 2.4.2c. The depression in the semi circle is accounted by introducing a constant phase element (CPE) connected in parallel with the bulk resistance [16].

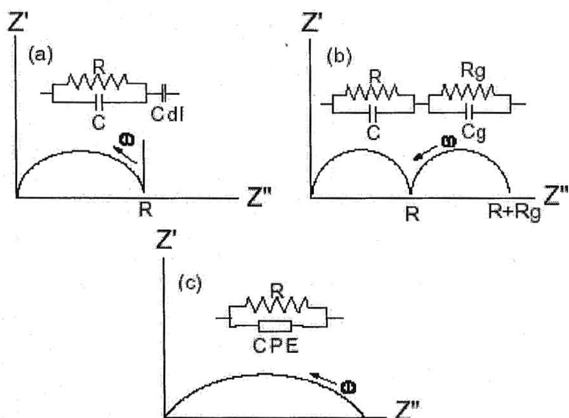

Figure 2.4.2(a-c): Different types of impedance behavior observed in solids.

Preparation and characterization techniques for thin films

2.5 Thin film preparation techniques:

Thin films are three dimensional solids, on which one dimension called the thickness is several orders of magnitude lower than the other two dimensions. Thin films range in thickness from a monolayer to several hundreds of nanometers. The properties of thin films are governed by the deposition method. In general, the preparation techniques of thin films are broadly classified in to two categories. (a) Chemical Vapor Deposition Techniques (CVD) and (b) Physical Vapor Deposition Techniques (PVD).

2.5.1 Chemical vapor deposition technique

When a volatile compound of the substance to be deposited is vaporized, and the vapor is thermally decomposed in to atoms or molecules and reacted with other gases, vapors or liquids on the substrate surface to yield non-volatile reaction products on the substrate this process is called as Chemical Vapor Deposition.

2.5.2 Physical vapor deposition

This is a general term used to describe any of a variety of methods to deposit thin films by the condensation of a vaporized form of the material onto various surfaces. The coating method involves purely physical processes such as high temperature vacuum evaporation or plasma sputter bombardment rather than involving a chemical reaction at the surface to be coated as in chemical vapor deposition.

2.5.2 Physical vapor deposition techniques

Physical Vapor Deposition (PVD) is divided in to two categories:

2.5.2a Thermal Evaporation and 2.5.2b Sputtering.

2.5.2a Thermal Evaporation

The solid materials vaporize when heated to sufficiently high temperatures. The condensation of vapor on to a substrate yields a thin solid film. Thermal evaporation of a material can be achieved by a variety of physical methods

(a) Pulsed laser deposition (PLD)
(b) Molecular beam epitaxy (MBE).
(c) Resistive heating
(d) RF heating
(e) Exploding wire technique
(f) Arc evaporation
(g) Flash evaporation
(h) Electron bombardment

2.5.2b Sputtering

Grove first discovered the sputtering phenomenon in 1852. The ejection of atoms from the surface of a material (target) when bombarded with energetic particles is called sputtering. If the ejection of atoms is due to positive ion bombardment it is referred to as a cathodic sputtering.

A simple source of ions for sputtering is provided by the glow discharge due to an applied electric field between two electrodes at low pressures. The gas breaks down to conduct electricity when a certain value of voltage is reached. The glow discharge maintains itself at a constant voltage and referred to as normal glow. The region where voltage and current increase together is called abnormal glow. A luminous layer, which covers the cathode partially in the normal glow and completely in the abnormal glow, is known as cathode glow. A fairly well defined region of relatively low luminosity known as Crookes or Cathode dark space is found adjacent to it. A bright negative glow region, Faraday dark space and then a positive column region follows this in sequence. The cathode dark space is the most important region. Most of the applied voltage is dropped (cathode fall) across it. Ions and electrons created at the breakdown are accelerated across this region. The different regions in the discharge are shown in figure 2.2.1

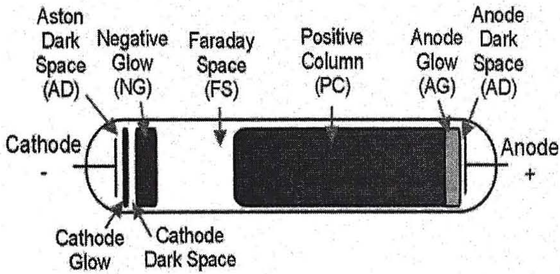

Figure 2.5.2b.1: Different regions in a typical glow discharge.

The energetic electrons produce more ions by collision with the gas atoms in the negative glow, and the energetic ions strike the cathode to produce sputtered flux and secondary electrons, which are essential to sustain the glow. The effective sputtering is possible only when both the number of ions and their energy are large and controllable.

Several sputtering techniques are proposed for thin film deposition including DC diode, RF diode and ion beam sputtering [19].

2.5.2b.1 DC sputtering

This technique is the simplest among the sputtering techniques. In this method the system consists of a pair of planar electrodes (cathode and anode). The front part of the cathode is covered with a target material, which is to be deposited, and the substrate is placed at anode. The sputtering chamber is filled with an inert gas (in general Argon gas) and the glow discharge is maintained under the application of dc voltage between the electrodes. The Ar^+ ions generated in the glow discharge are accelerated at the cathode fall and eject the atoms from the target resulting in the deposition of the thin film on to the substrate. In the DC sputtering technique, the target is composed of metal because the glow discharge is maintained between metallic electrodes.

In DC sputtering, sputtered particles collide with gas molecules and then eventually diffuse to the substrate since the gas pressure is high and the mean free path of the sputtered particles is less than the electrode spacing. The amount of sputtered material deposited on a unit substrate area, W is given by

$$W=k_1 W_o/pl \quad (2.5\ 1)$$

and the deposition rate (R) is given by

$$R=W/t \quad (2.5.2)$$

where, k_1 is a constant, W_o is the number of sputtered particles per unit cathode area, p is the discharge gas pressure, l is the electrode spacing and t is the sputtering time.

The number of sputtered particles from the unit cathode area, W_o is given by

$$W_o=(j_+/e)\ St\ (A/N) \quad (2.5.3)$$

where, j_+ is the ion current density at the cathode, e is the electron charge, S is the sputtering yield, A is the atomic weight of the sputtered materials and N is Avogadro's number [20].

Sputtering has attracted great attention because of low-temperature crystallization, thickness uniformity and control, high deposition rates, high adhesion and large throughput. However sputtering has some disadvantages too. In general the DC sputtering needs higher voltages (~2-3KV) in order for sputtering to take place and the

films cannot be deposited at lower pressures. Reduced deposition rates for oxide films and resputtering effects are other two difficulties. Reasonable sputtering rates at lower voltages and at lower pressures can be obtained by increasing the ionization of the sputtering gas by (i) increased ionizing efficiency of the available electrons and (ii) by increased supply of ionizing electrons. Using magnetic field, the ionizing efficiency can be increased conveniently by increasing the path length of the ionizing electrons.

2.5.2b.2 Magnetron Sputtering

In a magnetron-sputtering configuration, both an electric field E and a magnetic field B are used to confine the electrons to be near the cathode surface where electrons are emitted. An electron moving with a component of velocity perpendicular to the magnetic field will spiral around the magnetic field lines and will be confined by the magnetic field. Both the frequency and the radius of spiraling motion depend on the strength of the magnetic field. The interaction of an electron with the electric and magnetic fields depends on the magnitude and the orientation of the field as ExB. If the magnetic field is parallel to the cathode surface and the electric field is normal to the surface, an electron leaving the surface will be accelerated towards the anode and will spiral around the magnetic field lines. The magnetic field is oriented such that these drift paths for electrons form a closed loop. This electron trapping effect increases the collision rate between the electrons and the sputtering gas molecules. In addition, the increased ionization efficiency achieved in the magnetron sputtering allows the discharge to be maintained at lower pressures of operation and at lower operation voltages. In the present work, DC magnetron sputtering is used to deposit the thin films.

2.5.2b.3 Reactive magnetron sputtering

When a reactive gas species such as oxygen or nitrogen is introduced in to chamber, thin films of compounds such as oxides and nitrides are deposited by the sputtering of the appropriate metal targets and this process is known as Reactive Magnetron Sputtering. This process is used in practice for high rate of deposition of insulating metal oxide films.

2.5.2b.4 Mechanism of sputtering

Two models have been proposed for sputtering:

(i) Thermal vaporization theory: The surface of the target is heated enough to be vaporized due to bombardment of energetic ions.

(ii) Momentum transfer theory: Surface atoms of the target are emitted when kinetic momentum of incident particles is transferred to target surface atoms [21, 22].

A sputtering event is initiated by the first collision between incident ions and target surface atoms followed by the second and third collisions between the target surface atoms. The displacement of target surface atoms will be more isotropic due to successive collisions and atoms may finally escape from the surface. The sputtering collision on the target surface is shown in the figure 2.5.2.

2.5.2b.5 Sputtering yield

Sputtering yield (S) is defined as the mean number of atoms removed from the surface of a target per incident ion and can be measured by the following methods:

(a) Weight loss of a target (can be measured using a quartz crystal oscillator based microbalance).

(b) Reduction in target thickness

(c) Collection of the sputtered materials

(d) Detection of sputtered particles in flight

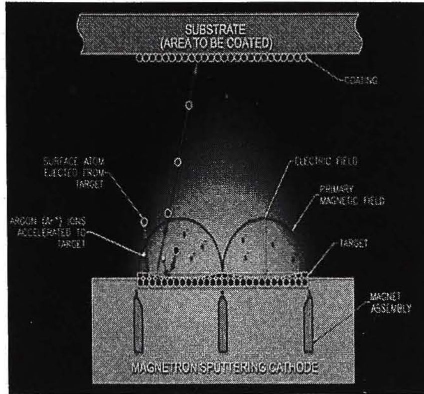

Figure 2.5.2: Sputtering process [23].

2.5.2b.6 Sputtering yield will be influenced by the following factors

(I) **Energy of incident particles:** A threshold energy exists for sputtering. The yield shows a maximum value in the high-energy region. The threshold energy is sensitive to the contamination of the target surface, incident angle of the ions, and the crystal orientation of the cathode material. At the energy region of the order of 100eV the number of displaced atoms is proportional to the incident energy. At higher energies 10-100keV the incident ions travel beneath the surface and the sputter yields are not governed by the scattering on the surface but by the scattering inside the target. Above 10keV, the sputter yields will decrease due to energy dissipation deep in the target.

(II) **Target materials:** Sputtering yield varies periodically with the element's atomic number. The yields increase consistently as the electronic d shells of target materials are filled with in Cu, Ag and Au having highest yields. Elements with the most open electronic structures result in the least sputtering yield.

(III) **Incident angle of particles:** Sputtering yield varies with the angle of incident ions. Metals with higher sputtering yield show very limited dependence on the angle but the materials with low sputtering yield show a very profound

dependence on the incident angle. The yield increases with the incident angle and reaches a maximum at angles between 60°-80°, while it decreases rapidly for larger angles. The influence of the angle is also governed by the surface structure of the target material.

(IV) **Crystal structure of the target surface:** The angular distribution may be either under cosine law or over cosine law when the target is composed of polycrystalline materials. Non-uniform angular distribution is often observed from the single crystal target.

To deposit the thin films in this study, a vacuum system (Cookes vacuum system, USA) is used. The vacuum system is equipped with conventional mechanical pump and oil diffusion pump (high vacuum pump). They are used to evacuate, to achieve a base pressure to 10^{-6} Torr.

In the present study we have chosen reactive DC magnetron sputtering to deposit films in the $(Zr,Sn)TiO_4$ system. There are very few reports on as grown nanocrystalline TiO_2 and ZrO_2 thin films, while there are no reports on $ZrTiO_4$ and $(Zr,Sn)TiO_4$ thin films by DC magnetron sputtering at ambient temperatures. Significantly $(Zr,Sn)TiO_4$ films were deposited using a single cathode from Zr, Sn and Ti metal targets. Interestingly, there were no reports on the deposition of these films in pure oxygen atmosphere.

Thin film characterization techniques

In the case of thin films also, XRD has been used to find out the crystalline phase of the films.

2.6 Optical properties:

The optical constants of the thin films were calculated using the envelope technique [24]. The spectral transmission characteristics in the wavelength range 190-1500nm were measured using a JASCO V570 UV-VIS-NIR spectrophotometer.

If light is incident on a film of refractive index n, coated on to a substrate of refractive index s, then at the air-film, film-substrate and substrate-air interfaces, part of the incident light is reflected and part of it is transmitted. Since the reflected and

transmitted beams originate from a single coherent source, the beams exhibit interference effects. The condition for constructive interference in such case is given by

$$2nd=m\lambda \tag{2.6.1}$$

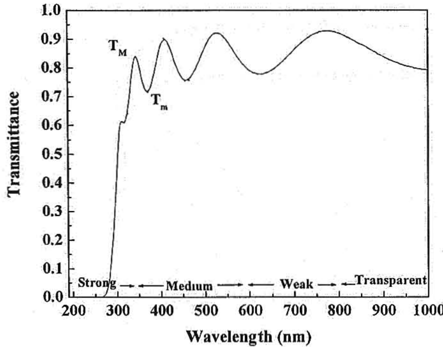

Figure 2.6.1.1: Typical transmittance spectrum of the film.

where, n is the refractive index of the film at a wavelength λ and m is the order of interference, d is the thickness of the film that can be calculated from the derived values of refractive indices.

In general the transmission T, is given by the expression

$$T = \frac{Ax}{B - Cx\cos\phi + Dx^2} \tag{2.6.2}$$

where $A=16n^2s$

$B=(n+1)^3(n+s)^2$

$C=2(n^2-1)(n^2-s^2)$

$D=(n-1)^3(n-s^2)$

$\phi=4\pi nd/\lambda$

$x=e^{-\alpha d}$

For such a system, at the points of constructive and destructive interference the transmittance T_M and T_m, respectively are given by

$$T_M = \frac{Ax}{B - Cx + Dx^2} \quad (2.6.3)$$

and $$T_m = \frac{Ax}{B + Cx + Dx^2} \quad (2.6.4)$$

For simplicity it can be assumed that the transmission is a continuously varying function of wavelength which can be approximated by drawing the envelope across the spectrum, connecting all the maximas and minimas as shown in the figure 2.6.1.1.

$$n = \left[N + \left(N^2 - n_s^{\ 2}\right)^{1/2}\right]^{1/2} \quad (2.6.5)$$

where, N is a constant, S is the refractive index of the substrate used and n_s is the refractive index of the film at that particular wavelength.

$$N = 2S\frac{T_M - T_m}{T_M T_m} + \frac{S^2 + 1}{2} \quad (2.6.6)$$

On adding the reciprocals of the equations 2.6. 3 and 2.6. 4 yields,

$$\frac{2T_M T_m}{T_M + T_m} = \frac{Ax}{B + Dx^2} \quad (2.6.7)$$

and solving for x we get,

$$x = \frac{F - F\left[F^2 - \left(n^2 - 1\right)\left(n^2 - s^4\right)\right]^{1/2}}{\left(n - 1\right)^3\left(n - s^2\right)} \quad (2.6.8)$$

where $$F = \frac{8n^2 s}{T_i} \quad (2.6.9)$$

and $$T_i = \frac{2T_M T_m}{T_M + T_m} \quad (2.6.10)$$

where, T_M is the maximum of the transmission on the envelope at a wavelength λ and T_m is the minimum in transmission on the envelope at the same wavelength. The T_M and T_m at each wavelength can therefore be read off from the envelope and the refractive index can be derived at each wavelength.

From the equation of constructive interference, it can be seen that for two successive maxima occurring at λ_1 and λ_2, the equation becomes

$$2n_1d=m_1 \lambda_1 \text{ and} \quad (2.6.11)$$

$$2n_2d=m_2 \lambda_2 \quad (2.6.12)$$

Also $|m_1-m_2|=1$.

Therefore, $$d=\frac{\lambda_1\lambda_2}{2(n_1\lambda_2-n_2\lambda_1)} \quad (2.6.13)$$

In the strong absorption region, from Beer-Lambert's law given by

$$I=I_o e^{-\alpha d} \quad (2.6.14)$$

where I_o is the incident intensity =1

I is the intensity at a given wavelength λ

d is the thickness of the film and

α is the absorption coefficient in cm^{-1}.

Since d is known from previous calculations and I is a measured quantity (i.e. transmission at a wavelength λ), the absorption coefficient α can be calculated. Knowing α from the expression for the so-called "Tauc gap", the fundamental absorption edge of the material can be determined. The expression for the Tauc gap is given by

$$\alpha h\nu= \text{constant x } (h\nu-E_g)^2 \quad (2.6.15)$$

X- Intercept of the extrapolation of the linear region in a plot of $(\alpha h\nu)^{1/2}$ vs. hv will give the value of bandgap E_g. The error associated with the measurement of k, n and d is ±0.005, ±0.02 and ±10nm respectively.

2.7 Measurement technique used to measure dielectric properties at microwave frequencies:

The microwave dielectric properties were measured using an extended cavity perturbation technique [25]. The experimental measurements were performed using a TE_{10n} rectangular cavity. The rectangular cavity of length 11.6cm, width 2.3 cm and height 1.07 cm is connected to a Vector Network Analyzer (VNA), (Model Agilent 8722ES) through a coaxial to wave-guide adapter after doing the one port calibration. The cavity was excited to three different modes, TE_{105}, TE_{107} and TE_{109} because only at these modes the sample placed centrally is at the maximum electric field position. The block diagram of the experimental set up is shown in figure 2.7.1.

A glass slide of thickness 1mm, length 25mm and width 4.8mm is taken and cleaned properly and placed inside the cavity through a slot drilled at the center of the cavity. The position of the slot is taken in such a way that the sample would be always in the maximum electric field position.

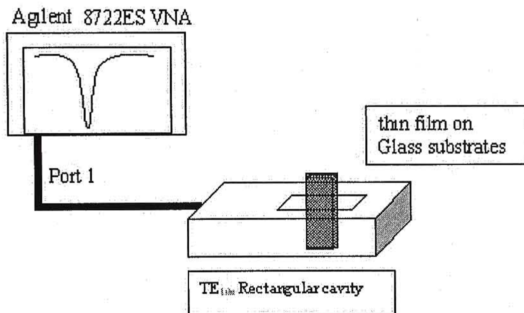

Figure 2.7.1: Block diagram of the experimental setup used for extended cavity perturbation technique.

The resonance frequency f_1 and half power width (Δf) were measured for the selected peaks and Q_1 of the cavity with substrate is calculated ($Q_1=f_1/\Delta f$). One side of the glass substrate is then coated with TiO_2, ZrO_2, $ZrTiO_4$ or ZST thin films. This coated sample is again inserted in to the cavity and the corresponding resonance frequency f_2 and quality factor Q_2 are determined for the TE_{105}, TE_{107}, and TE_{109} resonance modes. The resonance frequencies of these modes with the bare substrate inside the cavity were 8.98,

10.01 and 10.98 GHz and the corresponding quality factors were 6700, 6950 and 7150 respectively. The superimposed response of the empty cavity, cavity with bare substrate and cavity with film coated substrate are given in figure 2.7.2. The experimental values of ε'and ε" are obtained using the equations 2.7.1.1 and 2.7.1.2.

$$\varepsilon' = \left(\frac{f_1 - f_2}{f_2}\right)\frac{2V_c}{b\left[1+\frac{L}{n\pi}\sin\left(\frac{n\pi l}{L}\right)\right]\left[c+\frac{a}{\pi}\sin\left(\frac{\pi c}{a}\right)\right]}+1 \quad (2.7.\ 1.1)$$

$$\varepsilon'' = \left(\frac{1}{Q_2} - \frac{1}{Q_1}\right)\frac{V_c}{b\left[1+\frac{L}{n\pi}\sin\left(\frac{n\pi l}{L}\right)\right]\left[c+\frac{a}{\pi}\sin\left(\frac{\pi c}{a}\right)\right]} \quad (2.7.\ 1.2)$$

Here f_1 and f_2 are the resonance frequency of the cavity with the substrates and film-coated substrates respectively. Q_1 and Q_2 are the corresponding quality factors, c is the thickness of the film and l is the length of the sample in the axial direction of the cavity. L is the length of the cavity, a is the width and b is the height of the cavity used. V_c is the volume of the cavity, and V_s is the sample volume.

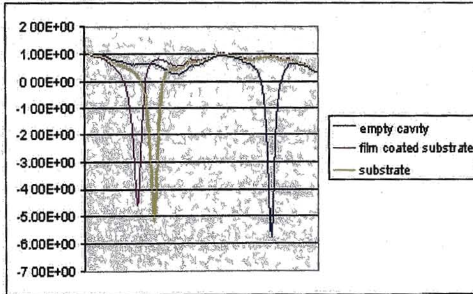

Figure 2.7.2: The response of the empty cavity, cavity with substrate and cavity with film coated substrate superimposed in the same scale.

2.8 Electrical measurements:

For the electrical characterizations metal insulator metal (MIM) type test structures were used. All the oxide thin films (TiO_2, ZrO_2, $ZrTiO_4$& ZST) were deposited

on Pt-coated Si-substrates. 200 nm thick Ag top electrodes were deposited on to the oxide layer through a shadow mask so as to define a capacitor structure (the diameter of top electrode is 40μm). The I-V and C-F characteristics of these test structures were measured using Radiant Precision Material Analyzer. The low frequency impedance and dielectric spectroscopy at zero dc bias from 100Hz to 10MHz were performed by using an Agilent 4294A Impedance Analyzer connected with a J Microtechnology make LMS 2709 DC Probe Station.

2.9 Atomic force microscope:

The microstructures of the deposited films were obtained using AFM. The AFM consists of a microscale cantilever with a sharp tip (probe) at its end that is used to scan the specimen surface. The cantilever is typically silicon or silicon nitride with a tip of radius of curvature of the order of nanometers. When the tip is brought into the proximity of a sample surface, forces between the tip and the sample lead to a deflection of the cantilever according to Hooke's law. Depending on the situation, forces that are measured in AFM include mechanical contact force, Van der Waals forces, capillary forces, chemical bonding, electrostatic forces, magnetic forces, Casimir forces, solvation forces etc. Typically, the deflection is measured using a laser spot reflected from the top of the cantilever into an array of photodiodes. The AFM can be operated in a number of modes, depending on the application. The primary modes of operation are static (contact) mode and dynamic mode [26].

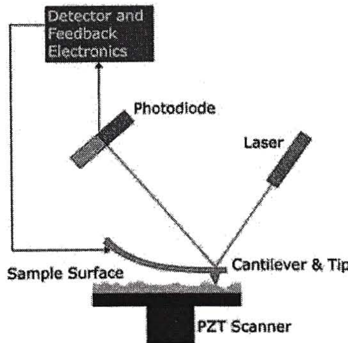

Figure 2.9.1: Schematic diagram of atomic force microscope.

In the static mode operation, the static tip deflection is used as a feedback signal. Because the measurement of a static signal is prone to noise and drift, low stiffness cantilevers are used to boost the deflection signal. However, close to the surface of the sample, attractive forces can be quite strong, causing the tip to 'snap-in' to the surface. Thus static mode AFM is almost always done in contact where the overall force is repulsive. Consequently, this technique is typically called 'contact mode'. In contact mode, the force between the tip and the surface is kept constant during scanning by maintaining a constant deflection through feedback circuitry.

In the dynamic mode, the cantilever is externally oscillated at or close to its resonance frequency. The oscillation amplitude, phase and resonance frequency are modified by tip-sample interaction forces. These changes in oscillation with respect to the external reference oscillation provide information about the sample's characteristics. Schemes for dynamic mode operation include frequency modulation and the more common amplitude modulation. In frequency modulation, changes in the oscillation frequency provide information about tip-sample interactions. Frequency can be measured with very high sensitivity and thus the frequency modulation mode allows for the use of very stiff cantilevers.

References:

[1] M.N.Rahaman "Ceramic processing and sintering" (Marcel Dekker, Inc, New York) 2003.

[2] D.Seagal " Chemical synthesis of advanced ceramic materials" (Cambridge University Press, Cambridge) 1991.

[3] R.E.Carter, J.Chem.Phys., **34**, 2010 (1961).

[4] C.Suryanarayana, Progress in Mater. Sci., **46**, 1 (2001).

[5] S-J. Kang " Sintering, densification, grain growth and microstructure" (Elsevier, Amesterdam) 2002.

[6] W.D.Kingery, H.K.Bowen and D.R.Uhlmann "Introduction to ceramics" (John Wiley & Sons, New York) 1975.

[7] D. Cullity, "X-ray Diffraction" (Addison-Wesley, Reading, MA) 1956.

[8] Dielectric resonators, D. Kajfez and P. Guillon (eds.), (Norwood, MA, Artech House) 1986.

[9] J. J. Krupka, K.Derzakowskiz, B. Riddlex and J.B.Jarvisx, Meas. Sci. Technol., **9**, 1751 (1998).

[10] B.W.Hakki, P.D. Coleman, IEEE Trans Microwave Theory Technol., **8**, 402 (1960).

[11] W.E Courtney, IEEE Trans Microwave Theory Technol., **18**, 476 (1970).

[12] Y.Kobayashi, M.Katoh, IEEE Trans Microwave Theory Technol., **33**, 586 (1985).

[13] B.A. Boukamp, Solid State Ionics, **143**, 47 (2001).

[14] D.C. Sinclair, A.R. West, J. Appl. Phys., **66**, 3850 (1989).

[15] A.R. West, E.J. Abram, and D.C. Sinclair, in Solid State Ionics, "Trends in the New Millennium", B.V.R. Chowdari, S.R.S. Prabaharan, M. Yahaya, I.A. Talib (Eds.), World Scientific, Singapore (2002) pp. 487.

[16] J.R. Macdonald (Ed.) "Impedance Spectroscopy Emphasising Solid Materials and Systems" (John Wiley & Sons, New York) 1987.

[17] J.E. Randles, Discussion of Faraday Soc., **1**, 11, (1947).

[18] J.E. Bauerle, J. Phys. Chem. Solids, **30**, 2657 (1969).

[19] D.Mc Clanahan, N.Laegreid "Production of thin films by controlled deposition of sputtered material, in: Sputtering by particle bombardment III, Topics in Applied Physics, (Springer Verlag, Berlin) 1991.

[20] K. Wasa, M.kitabatake and H.Adachi "Thin film materials technology: Sputtering of compound materials" (Springer, Verlag, Berlin) 2004.

[21] G.K.Wehner, Phys.Rev., **102**, 690 (1956).

[22] K.L. Chopra "Thin film phenomenon" (McGraw-Hill, New York) 1969.

[23] www.angstromsciences.com

[24] R.Swanpoel J.Phys.E: Sci.Instrum., **16**, 1214 (1983).

[25] H. M. Altschuler. "Handbook of Microwave Measurements" (Brooklyn Polytechnic Press, New York) 1963.

[26] www.siint.com

Chapter-3

Preparation and Characterization of Bulk $(Zr_{0.8},Sn_{0.2})TiO_4$ Ceramics

Synthesis of $(Zr_{0.8},Sn_{0.2})TiO_4$ (ZST) ceramics by solid-state method:

3.1 Preparation of pure ZST:

The weight ratios of initial reagents are calculated according to the stoichiometry of ZST. The reagents used are ZrO_2, SnO_2 and TiO_2 powders of purity (99.9%) of Sigma Aldrich, USA.

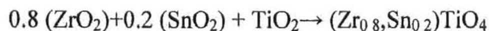

$$0.8\,(ZrO_2)+0.2\,(SnO_2) + TiO_2 \rightarrow (Zr_{0.8},Sn_{0.2})TiO_4$$

Steps involved in the processing of ZST ceramics

Weighing

↓

Mixing using ball mill

↓

Drying

↓

Calcination at 1300°C

↓

Phase analysis (XRD)

↓

Particle size reduction using ball mill

↓

Pelletization at (110 MPa)

↓

Sintering

↓

characterization (Density, SEM and microwave measurements)

↓

Optimization of the previous steps in case the shrinkage is poor.

↓

Addition of sintering aids to increase density and microwave dielectric properties.

↓

Check for reproducibility.

The stoichiometric amounts of these oxides are weighed using an electronic balance (accuracy0.001m.gm) and mixed in a zirconia jar with zirconia balls. Distilled water is used as mixing medium. To mix these powders a planetary ball mill (Retsch PM 100, Germany) is used and is shown in figure 3.1.1. For mixing of reagents the stoichiometric powders are mixed at the speed of 150 rpm (rotations per minute) for one hour. The mixed powders were dried in the hot air oven at 100°C for 1 hour. The calcination temperature of the ZST ceramics is optimized and the phase purity is ascertained in each case from the XRD (X-ray Diffraction) patterns. The optimum calcination treatment is found to be 1300°C for 1 minute.

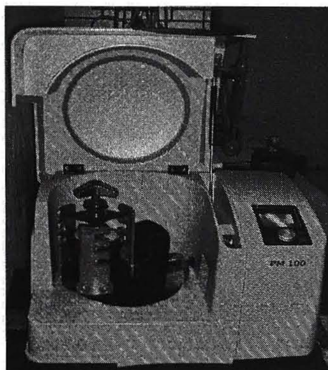

Figure 3.1.1: Photograph of the ball mill used in this study.

These powders were calcined in a high purity alumina crucible. The calcined powders were milled in the ball mill at 300 rpm for 10 hours with distilled water as a mixing medium. After every two hours of milling some amount of powder was taken out and pellets of 8 mm in diameter were made out of it and these pellets were sintered at 1650°C for 3 hours. The pellets were sintered in a high temperature furnace (MHI, USA). For sintering, the pellets were kept on a platinum mesh covering an alumina plate, to avoid reaction between the samples and the alumina plate.

The densities of the sintered ZST ceramics were measured using the formula ρ=M/V, where M is the mass of the pellet and V is its volume. The diameter and height of the pellets were measured using a micrometer (Mitutoyo). This method is followed because the sintered pellets are of uniform geometry. However the measured density values were verified by water displacement method (Archimedes principle) in a few cases and the results are given in table 3.1.1.I.

Milling time (hours)	ρ=Mass/Volume	Density by Archimedes principle
1	85±0.3	85.21
3	89.1±0.3	89.32
5	89.6±0.3	89.71
7	91.28±0.3	91.42
10	94.6±0.3	94.81

Table 3.1.1.I: Comparison of density of the ZST samples mesured by 2 methods. The samples are made of ZST powder milled for different durations.

It can be noted that there is no appreciable difference between two mwthods owing to the regular geometry of the samples measured.

The XRD patterns of the ZST ceramics sintered at 1650°C for 3 hours and milled for different times (2, 6 & 10 hours) are shown in figure 3.1.2. Samples showed a homogeneous ZST phase with α–PbO orthorhombic structure and the space group of the structure is D^{14}_{2h}=pbcn [1]. It is observed that the increase in the intensities and broadening of the peaks increased with increase in milling time. The crystallite size of the sintered ZST ceramics was calculated from the Williamson-Hall plot (βCosθ vs. Sinθ). The crystallite size of the ZST ceramics ranged between (40.5-62nm). From the XRD patterns it is observed that as the milling time increases, the crystallite size of the ZST ceramics is reduced.

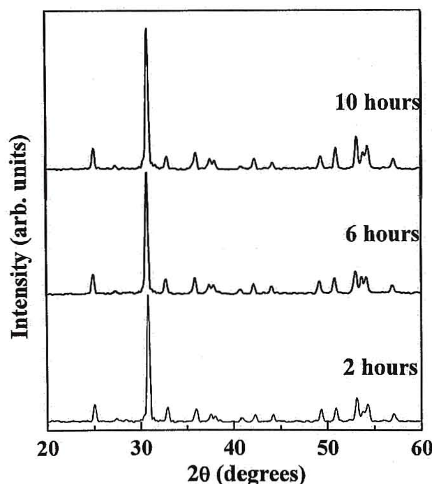

Figure 3.1.2: XRD patterns of the pure ZST ceramics milled for different time and sintered at 1650°C for 3 hours.

The variation in density as a function of milling time is shown in figure 3.1.3.

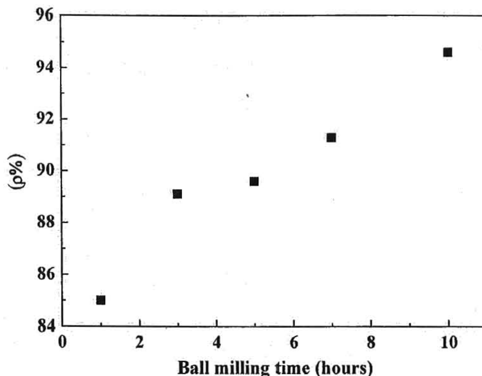

Figure 3.1.3: Density as a function of milling time for sintered pure ZST ceramics.

It is observed that as the milling time increases the density of the pure ZST ceramics is increasing. The maximum density is observed for the sample milled for 10 hours and its value is 94.6% of the theoretical density.

The microwave dielectric constant of the sintered ZST ceramics plotted as a function of density is shown in figure 3.1.4. It is observed that as the density increases the dielectric constant is also increasing and the maximum dielectric constant observed for the sample milled for 10 hours is found to be 36.1 when measured at 10.5GHz (by the dielectric resonator method, using $TE_{01\delta}$ mode).

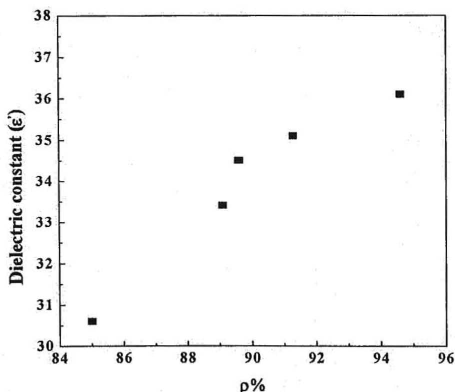

Figure 3.1.4: Microwave dielectric constant as a function of density of the pure ZST ceramics.

The quality factor (Qxf_o) of the ZST ceramics measured for $TE_{01\delta}$ mode ranged between 20,000-39,000 at 10.5 GHz and these lower values may be attributed to the lower densities of the pure ZST. The temperature coefficient of resonant frequency (τ_f) of the measured samples ranged between 1-3 ppm/°C when measured with $TE_{01\delta}$ mode. From this study it is observed that the density is playing an important role on the microwave dielectric properties of the ZST ceramics. The sintering temperature of the ZST ceramics is also as high as 1650°C. It is very difficult to densify the ZST ceramics below 1600°C without a sintering aid. So there is a necessity to reduce the sintering temperature without adversely affecting its microwave dielectric properties.

3.2 Effect of milling and addition of ZnO on ZST ceramics:

The practical use of ZST ceramics requires sintering additives that improve sinterability without degrading its microwave dielectric properties because achieving full densification without their presence is difficult [1]. ZnO is well known to fulfill these requirements because the added ZnO reacts with TiO_2 the main constituent, to form a liquid phase in the grain boundary and the ZnO do not diffuse in to the grains [2].

It has been reported that the ZST ceramics added with 1wt% ZnO as a sintering aid, can be densified at 1400°C without affecting its microwave dielectric properties and is reported to have an ε_r=37.8 and Qxf_o=45000 [3]. Many researchers have reported the microwave dielectric properties of ZST ceramics with the addition of small amount of additives such as Fe, Ni, La, Co and Zn [4-7]. It is thought that the addition of ZnO form a liquid phase between 1000-1400°C at the grain boundaries during sintering and so aids densification by rapid transportation of matter through the liquid phase.

In the present study we want to see the effect of initial particle size and the concentration of ZnO (1.0, 1.5, 2.0 & 2.5wt%) on the densification, microstructure and the microwave dielectric properties of ZST ceramics. A systematic study of the effect of milling time on ZST ceramics, added with different amounts of ZnO has not been reported. It is well known that the smaller initial particle size reduces the sintering temperature and thus enhances the densification. Initially the calcined powders were milled for 15 hours with the addition of 1wt% ZnO, and after every two hours of milling, the powders were collected. The pellets were made out of these

powders and sintered at 1400°C for 3 hours. Similarly the powders were milled for 15 hours with different concentration of ZnO (1.5, 2.0 & 2.5 wt%) and these pellets were sintered between 1300-1400°C for different sintering durations. The particle size of the milled powder was obtained by using particle size analyzer (Zeta Sizer 3000 HSA). The variation in particle size as a function of milling time is plotted in figure 3.2.1.

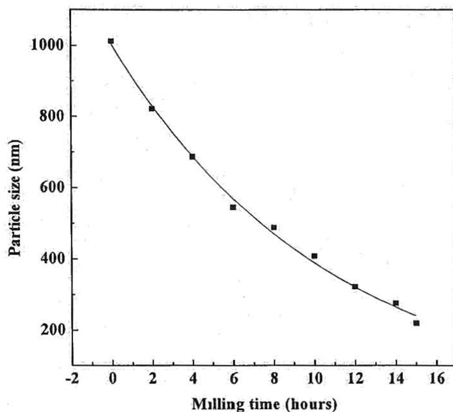

Figure 3.2.1: Particle size of the ZST ceramics powder as a function of milling time.

It is observed that as the milling time increases the initial particle size decreases exponentially and the particle size is ranged between 220-1012nm. The particle size of the calcined powder is 1012nm.

The X-ray diffraction patterns of the ZST ceramics with 1wt% ZnO, milled for 2, 10 and 15 hours and sintered at 1400°C for 3 hours is shown in figure 3.2.2 and that with different amounts of ZnO (1-2.5 wt %) sintered at 1350°C for 3 hours are shown in figure 3.2.3.

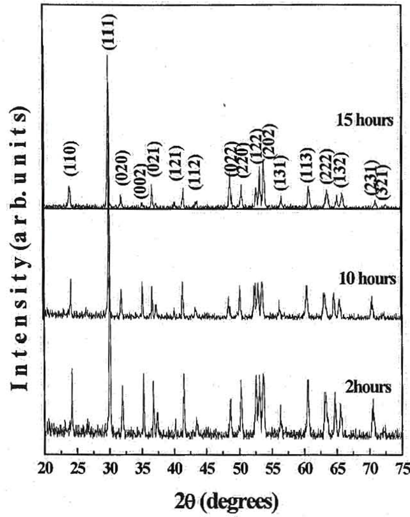

Figure 3.2.2: XRD patterns of the ZST ceramics milled for different times with 1wt% ZnO and sintered at 1400°C for 3 hours.

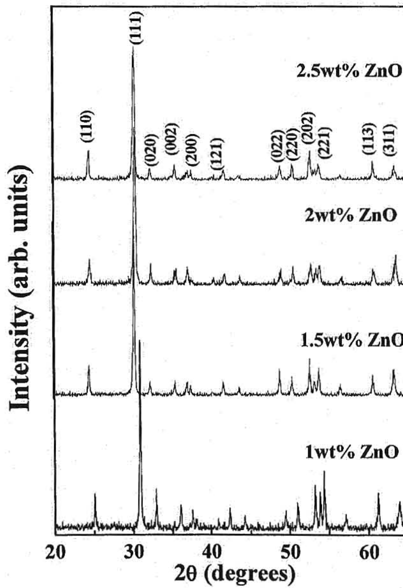

Figure 3.2.3: XRD patterns of the ZST ceramics milled for 15 hours, and added with different wt% of ZnO and sintered at 1350°C for 3 hours.

All the samples showed a homogeneous ZST phase with α–PbO orthorhombic structure. It is observed that the increase in the intensities and broadening of the peaks increased with increase in milling time. The crystallite size of the sintered ZST ceramics is calculated from the Williamson-Hall plot (βCosθ vs. Sinθ). The crystallite size ranged between 30-92.5 nm. As the milling time increases the crystallite size and particle size of the ZST ceramics have decreased. Although ZnO is well known to form boundary phases such as Zn_2TiO_4, it is not present in the XRD patterns of the samples. Secondary phases were not observed below the 2.5-wt% level of ZnO addition due to the fact that the detection of minor secondary phases by X-Ray Diffraction is extremely difficult. It is well known that ZnO forms a liquid phase at the grain boundaries during sintering, and hence aid densification through rapid transport of matter through the liquid phase. Even though no secondary phase is observed, there is a variation in peak intensities and splitting of the peaks. The components of the peaks which got split however belong to ZST itself.

Figure 3.2.4 shows the variation of density as a function of milling time for 1wt% ZnO added ZST. It is found that the density is increasing with increase in milling time and the ceramics sintered at 1400°C itself showed better densification. It is found that lower the particle size, higher the densification and uniform is the grain growth. The variation in density as a function of wt% of ZnO, for samples sintered at 1300, 1350, 1400 and 1450°C for 3 hours is shown in figure 3.2.5. As the sintering temperature increases, the density of the ZnO added ZST ceramics increased up to 1350°C, and above that it started decreasing. It is found that as the wt% of ZnO increases, density of the ZST ceramics is decreasing up to 2wt% of ZnO and at 2.5 wt% of ZnO, it started increasing. The decrease in density at higher sintering temperatures can be attributed to the evaporation of ZnO and the formation of secondary phases, which are difficult to identify with XRD and also to the onset of non-uniform grain growth. It may be noted that samples sintered at 1300°C did show still lower densities. However that could be attributed to insufficient sintering temperature. Figure 3.2.6 shows the variation in density as a function of wt% of ZnO sintered at 1350°C for different sintering durations. In this case it is observed that as the sintering duration increases the density of the ZST ceramics is increasing. It is found that ZST ceramics milled for 15 hours with 1wt% of ZnO addition can be densified at 1350°C itself.

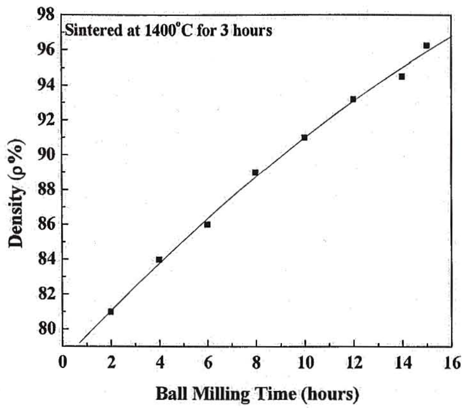

Figure 3.2.4: Density of 1wt% ZnO added ZST, as a function of milling time.

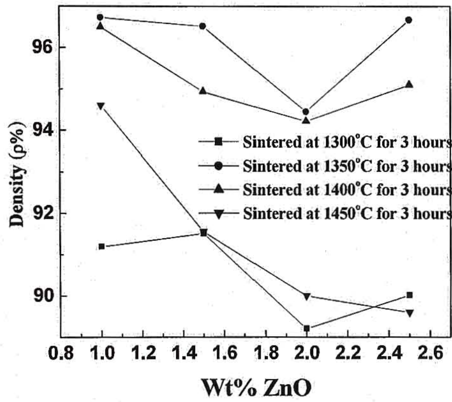

Figure 3.2.5: Density of ZST as a function of wt% of ZnO and sintered at different sintering temperatures. Sintering time: 3 hours.

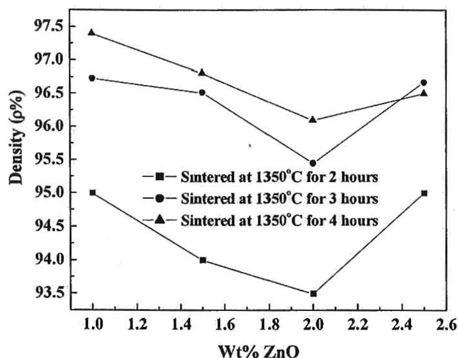

Figure 3.2.6: Density of ZST as a function of wt% of ZnO. Sintered at 1350°C for different sintering durations.

Figure 3.2.7a-d shows the SEM micrographs of 1wt% ZnO added ZST ceramics sintered at 1400°C for 3 hours with various milling times of 2, 6, 10 and 15 hours respectively. It is found that as the milling time increase, the grain size increased with uniform grain growth. The variation in crystallite size and average grain size as a function of milling time are tabulated in Table 3.2.I. Figure 3.2.8a-d shows the SEM micrographs of the ZST ceramics sintered at 1350°C for 3 hours with different amounts of ZnO. These micrographs shows that as the wt% of ZnO increase the grain size started decreasing and the grain growth is becoming non-uniform. The average grain size as a function of wt% of ZnO for samples milled for 15 hours and sintered at 1350°C for 3 hours is tabulated in Table 3.2.II. It is interesting to note from Table 3.2.I that as the initial particle size decreases by increasing milling time, the grain size of the sintered ZST ceramics increases. The increase in grain size at higher milling time can be attributed to the higher reactivity of the finer particles. When an aggregate of fine grained crystals are heated at high temperatures, recrystallization takes place and the average grain size increases. As the initial particle size decreases the driving force for the process increases because of the increased surface area, resulting in increased density and grain size, reducing the grain boundary area. The average grain size of the ZST ceramics ranged between 6 to 18μm. ZST ceramics sintered at 1350°C showed higher grain sizes than the samples sintered at 1400°C. The sample sintered at 1300°C for 3 hours is shown in figure 3.2.8e. It is observed that the grain size of this sample is smaller and the densification process appears to be

incomplete due to the insufficient sintering temperature. Further the ZST ceramics sintered at 1450°C for 3 hours is shown in figure 3.2.8f. It is found that the average grain size of this sample is lower compared to the other samples sintered at 1350°C for 3 hours with the same amount of ZnO addition. But the grain growth is non-uniform as could be seen from the SEM micrograph. The decrease in grain size at higher temperatures may be due to the evaporation of ZnO and the consequent reduction in driving force, which could cause the decrease in grain size. From the SEM pictures it is clear that initial particle size plays an important role on the densification, uniform grain growth and increase in average grain size leading to the differences in the microwave dielectric properties.

Figure 3.2.7: SEM pictures of ZST samples made with powder milled for different durations.

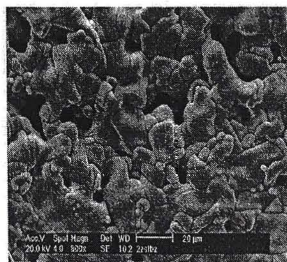

Figure 3.2.7a
Sample: ZST+ 1wt% ZnO
Milling time: 2 hours
Sintering conditions: 1400°C, 3 hours.

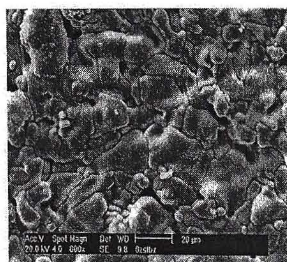

Figure 3.2.7b
Sample: ZST+ 1wt% ZnO
Milling time: 6 hours
Sintering conditions: 1400°C, 3 hours.

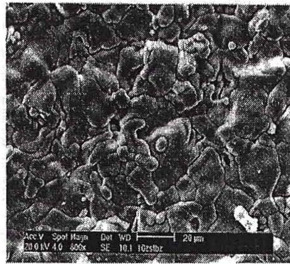

Figure 3.2.7c
Sample: ZST+ 1wt% ZnO
Milling time: 10 hours
Sintering conditions: 1400°C, 3 hours.

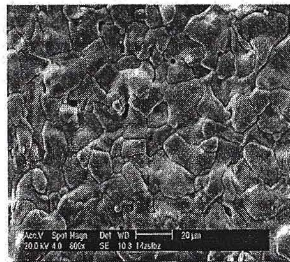

Figure 3.2.7d
Sample: ZST+ 1wt% ZnO
Milling time: 15 hours
Sintering conditions: 1400°C, 3 hours.

Figure 3.2.8: SEM pictures of the samples milled for 15 hours, added with different amounts of ZnO.

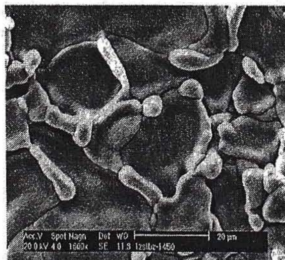

Figure 3.2.8a
Sample: ZST+ 1.0wt% ZnO
Sintering conditions: 1350°C, 3 hours.

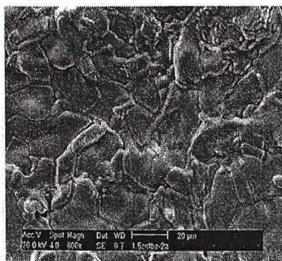

Figure 3.2.8b
Sample: ZST+ 1.5wt% ZnO
Sintering conditions: 1350°C, 3 hours.

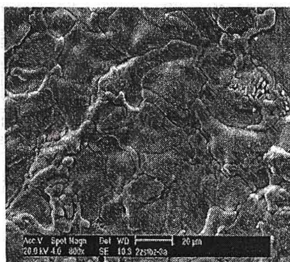

Figure 3.2.8c
Sample: ZST+ 2.0wt% ZnO
Sintering conditions: 1350°C, 3 hours.

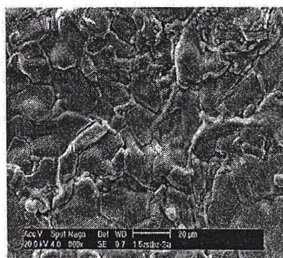

Figure 3.2.8d
Sample: ZST+ 2.5 wt% ZnO
Sintering conditions: 1350°C, 3 hours.

4879

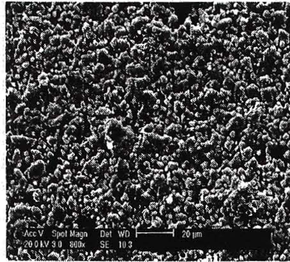

Figure 3.2.8e
Sample: ZST+ 1.0 wt% ZnO
Sintering conditions: 1300°C, 3 hours.

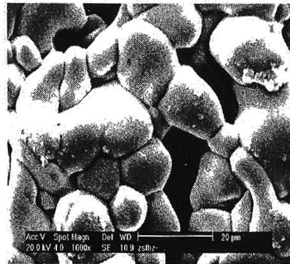

Figure 3.2.8f
Sample: ZST+ 1.0 wt% ZnO
Sintering conditions: 1450°C, 3 hours.

Ball milling (hours)	**Crystallite size (nm)**	**Grain size (μm)**
2	92.5	6
6	67.2	8
10	42	10
15	35	12

Table 3.2.I: Crystallite size and average grain size of ZST ceramics milled for different milling durations and sintered at 1400°C for 3 hours.

Wt% ZnO	Average grain size (μm)
1.0	18
1.5	16
2.0	15
2.5	14

Table 3.2. II: Average grain size of ZST ceramics with different concentrations of ZnO and sintered at 1350°C for 3 hours.

Figure 3.2.9a shows the variation of dielectric constant as a function of density for 1wt% ZnO added ZST ceramics. The microwave dielectric constants of the samples are measured at 10.5 GHz frequency. As the density increases the dielectric constant also increases as expected. The ε_r values of ZST samples sintered with 1wt% ZnO ranged from 26 to 38.5. Figure 3.2.9b & c shows the variation in dielectric constant as a function of wt% of ZnO for the samples sintered at different temperatures for 3 hours and for the samples sintered at 1350°C for different durations respectively. The dielectric constant values ranged from 33.3-39.3 for the samples sintered at different temperatures for 3 hours and 35.8-38.9 for the samples sintered at 1350°C for different durations. It may be noted that under the measurement procedures followed for the measurement of Q values, 1/Q gives the loss tangent of the material (Tanδ) which is related to the dielectric loss ε" of the material through the relation Tanδ = ε"/ε'.

Figure 3.2.10a shows the variation of Q x f_0 as a function of density of ZST ceramics. To achieve different density values the samples with 1wt% ZnO were milled for different durations. It can be clearly seen that the Q x f_0 value increases steadily with the density. Figure 3.2.10b & c shows the variation in Q x f_0 as a function of wt% of ZnO and sintered at different temperatures for 3 hours, and for the samples sintered at 1350°C for different sintering durations. It is found that in all the cases, as the density increases the Q x f_0 value also increases. The maximum Q x f_0 value is 48,000 for the sample milled for 15 hours and sintered at 1400°C for 3 hours and 49,600 for the sample sintered at 1350°C for 4 hours, each with 1wt% of ZnO addition. Apart from density, the increase in Q x f_0 value could also be attributed to the increase in grain size, as could also be seen by comparing Table 3.2.I with figure 3.2.10 a and Table 3.2.II with figure 3.2.10 c. The specimen with large grain size is

expected to have a high Q x f_0 value because the grain growth decreases the grain boundary area [3].

The temperature coefficient of resonant frequency (τ_f) is known to be related to the composition and secondary phases in the material. Since ZST ceramics are temperature stable and the addition of ZnO did not cause any noticeable secondary phase, the τ_f values did not change much. The τ_f value of all the samples was in the range of +3 to +4 ppm°C^{-1}.

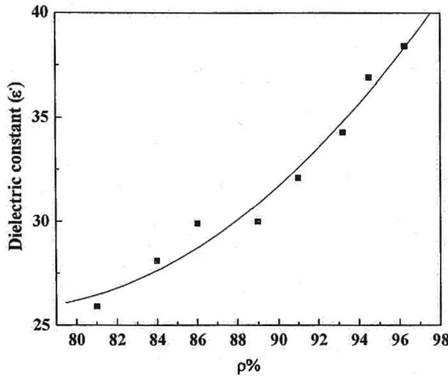

Figure 3.2.9a: Dielectric constant of ZST ceramics measured at 10.5 GHz and plotted as a function of density. The samples are milled for different durations and sintered at 1400°C for 3hours to achieve different densities.

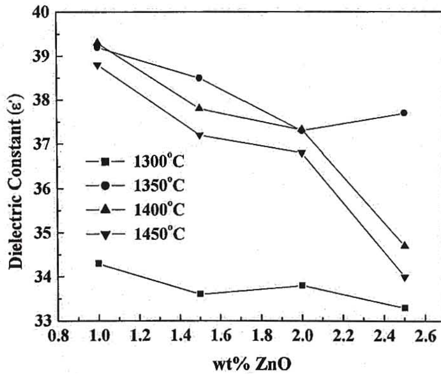

Figure 3.2.9b: Dielectric constant at10.5 GHz as a function of wt% of ZnO for the samples milled for 15 hours and sintered at different temperatures for 3hours.

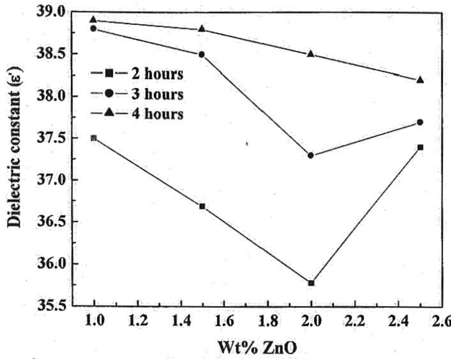

Figure 3.2.9c: Dielectric constant at 10.5 GHz as a function of wt% of ZnO and sintered at 1350°C for different sintering durations.

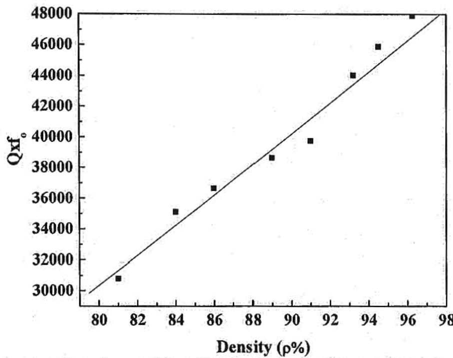

Figure 3.2.10a: Qxf$_o$ as a function of density for the samples milled for different durations and sintered at 1400°C for 3hours.

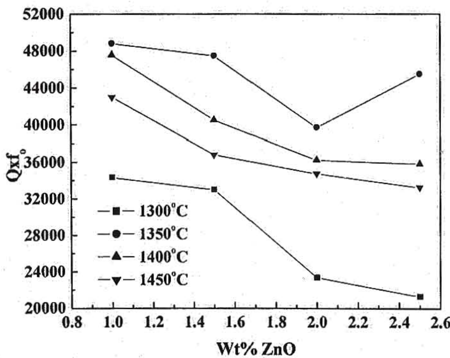

Figure 3.2.10b: Qxf$_o$ as a function of wt% of ZnO for the samples milled for 15 hours and sintered at different sintering temepratures for 3hours.

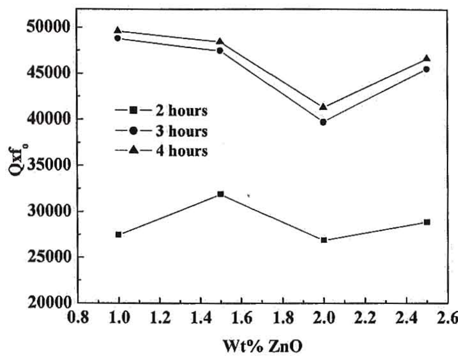

Figure 3.2.10c: Qxf_o as a function of wt% of ZnO and sintered at 1350°C for different sintering durations.

From this study it is observed that the effect of milling along with addition of ZnO significantly reduced the sintering temperature (1650°C to 1350°C) without deteriorating the microwave dielectric properties of ZST ceramics. ZST ceramics added with 1wt% ZnO, milled for 15 hours effectively reduced the sintering temperature with improvement in microstructure and microwave dielectric properties.

3.3 Effect of milling and addition of ZnO and CuO on ZST ceramics:

For the industrial applications of ZST ceramics, minimization of the cost and processing parameters such as sintering temperature, sintering duration, milling time etc are very important. To reduce the sintering temperature further, CuO is added along with 1wt% ZnO. Huang et al [6] investigated the liquid phase effects of CuO addition on the microwave dielectric properties of ZST ceramics. The liquid phase effect was believed to be caused by the eutectic of CuO-Cu_2O-TiO_2 at 1070°C.

In the present study, the effect of different concentrations of CuO (0.5, 1.0 & 1.5wt%) as a function of ball milling (1, 5 & 7 hours) on the ZST ceramics has been studied systematically as there is no such systematic study available in the literature. The pellets were sintered at different temperatures for a constant sintering duration to identify the sintering temperature, and after identifying the sintering temperature sintering duration is varied to achieve the maximum density. In the ball milling stage, 1wt% ZnO is added in every case and hence it will not be mentioned explicitly every time.

XRD patterns of the ZST ceramics added with different concentrations of CuO milled for different milling times (1, 5 & 7 hours) and sintered at 1300°C for 3.5 hours

are shown in figure 3.3.1a-c. It is observed that all the samples exhibited orthorhombic, α-PbO structure. No secondary phases were observed in the 0.5-1.5wt% range of additions of CuO, due to the fact the detection of a minor phase by XRD is very difficult. Because the ionic radius of Cu^{2+} (0.73nm) is comparable to that of Zr^{4+} (0.72nm), Sn^{4+} (0.69nm), and Ti^{4+} (0.605nm), Cu^{2+} ion could completely substitute for the tetravalent elements of ZST ceramics. Furthermore, the total charges of two Cu^{2+} ions are equal to a tetra valent ion. Hence it is believed that CuO dissolves in ZST ceramics [8].

The variation in densities as a function of wt% of CuO sintered at different sintering temperatures (1300-1400°C) for a constant sintering duration (3.5 hours) milled for 1 and 5 hours are shown in figure 3.3.2a & b respectively. In both the cases it is observed that as the temperature increases the density of the ZST ceramics decreases.

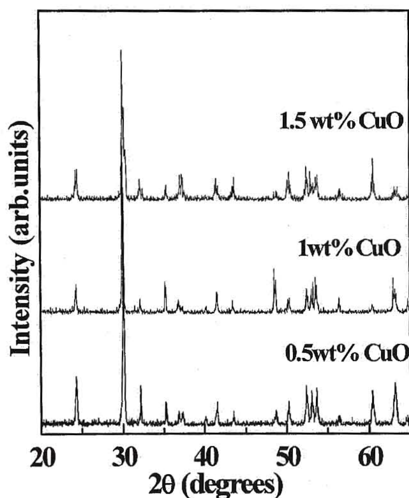

Sample: ZST+ 1.0 wt% ZnO+ CuO (0.5 wt% to 1.5 wt%)
Milling time: 1 hour
Sintering conditions: 1300°C, 3.5 hours.

Figure 3.3.1a: XRD patterns of the ZST ceramics with 1 hour milling time.

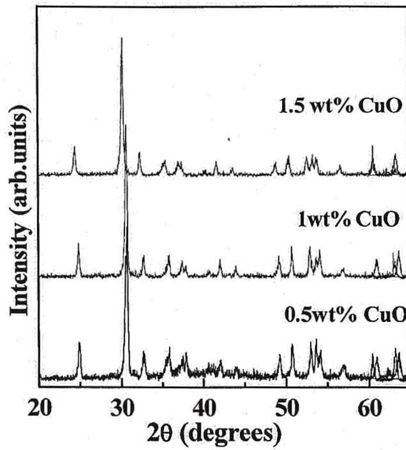

Sample: ZST+ 1.0 wt% ZnO+ CuO (0.5 wt% to 1.5 wt%)
Milling time: 5 hours
Sintering conditions: 1300°C, 3.5 hours.

Figure 3.3.1b: XRD patterns of the ZST with 5 hours milling time.

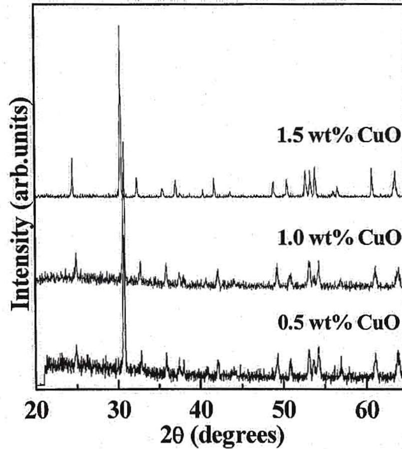

Sample: ZST+ 1.0 wt% ZnO+ CuO (0.5 wt% to 1.5 wt%)
Milling time: 7 hours
Sintering conditions: 1300°C, 3.5 hours.

Figure 3.3.1c: XRD patterns of the ZST ceramics with 7 hours milling time.

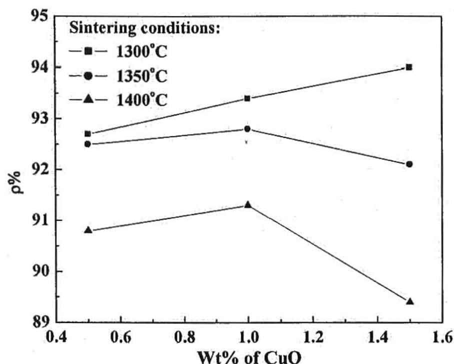

Sample: ZST+ 1.0 wt% ZnO+ CuO (0.5 wt% to 1.5 wt%)
Milling time: 1 hour
Sintering duration: 3.5 hours
Sintering temperature: 1300-1400°C.

Figure 3.3.2a: Density of ZST milled for 1hour.

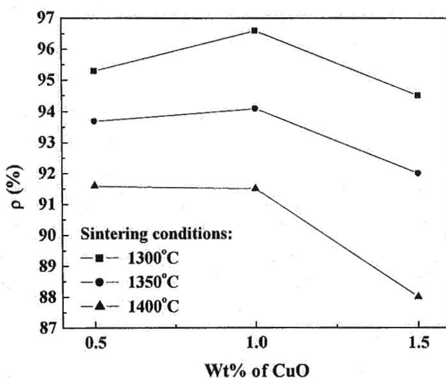

Sample: ZST+ 1.0 wt% ZnO+ CuO (0.5 wt% to 1.5 wt%)
Milling time: 5 hours
Sintering duration: 3.5 hours
Sintering temperature: 1300-1400°C.

Figure 3.3.2b: Density of ZST milled for 5hours.

At 1300°C they gave maximum density. Also the density of the samples increased with increase in wt% of CuO in the case of samples milled for 1 hour. But for the samples milled for 5 hours, the density of the samples increased up to 1wt% addition of CuO, and above that it started decreasing. The variation in density as a

function of wt% of CuO for samples sintered at 1300°C for different sintering durations and milled for 1,5& 7 hours are shown in figures 3.3.3a -c respectively.

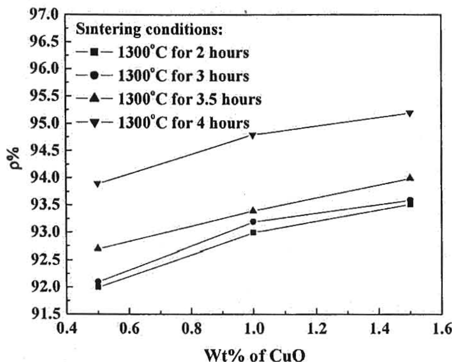

Figure 3.3.3a: Density of ZST ceramics, milled for 1 hour as a function of wt% of CuO.

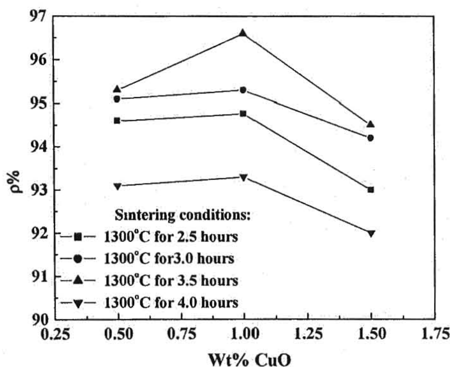

Figure 3.3.3b: Density of ZST ceramics, milled for 5 hours as a function of wt% of CuO.

It is observed that the sintering duration is decreasing with increasing milling time. It is interesting to know that as the milling time increases, the ZST ceramics showed higher densities with decreasing concentrations of CuO; i.e. samples milled for 1 hour showed higher density with 1.5wt% addition of CuO, samples milled for 5 hours showed better density with1wt% addition of CuO and the samples milled for 7 hours showed maximum densities with 0.5wt% addition of CuO.

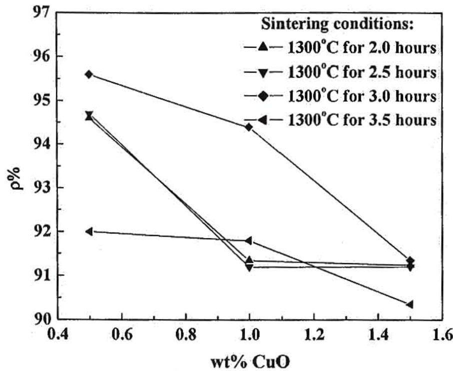

Figure 3.3.3c: Density of ZST ceramics, milled for 7 hours as a function of wt% of CuO.

In the case of samples milled for 1 hour, the densities of the samples increased with increase in sintering duration and the wt% of CuO. But in the case of 5 and 7 hours milled samples, the densities increased with increase in sintering duration up to 3.5 and 3 hours respectively. The densities were also decreased with increase in wt% of CuO. The maximum densities observed were 95.2, 96.6 and 95.6 of theoritical density for the samples milled for 1, 5 & 7 hours, and sintered at 1300°C for 4, 3.5 and 3 hours respectively. The increase in density with increasing milling time can also be attributed to the smaller initial particle size. It is well known that the smaller initial particle size reduces the sintering temperature due to the higher reactivity of the finer particles. In all the cases the decrease in density at higher temperatures and longer sintering durations may be attributed to the evaporation of CuO, formation of a liquid phase, non-uniform grain growth and secondary phases. The increase in density is attributed to the uniform grain growth and the reduction in porosity. It is observed that the addition of CuO reduced the sintering temperature of the ZST ceramics without enhancing the grain growth. The reduction in sintering temperature is primarily attributed to a liquid phase formation of the CuO with TiO_2 [3]. The wetting liquid concentrates at the particle contacts and forms a meniscus, which exerts an effective compressive pressure on the compact. There is a rapid rearrangement of particles in to a higher density configuration. After the initial rearrangements, further densification takes place as particle contact surfaces flatten under the compressive stress applied to the point contacts by capillary pressure [8].

The microstructures of the ZST ceramics milled for 1, 5 & 7 hours and sintered at 1300°C with different concentrations of CuO (0.5, 1.0 & 1.5wt%) are shown in figures 3.3.4a-c, 3.3.5a-c and 3.3.6a-c respectively. It is observed that the uniform grain growth is observed in all the cases as well as increases in grain size with increase in ball milling time. As the milling time increases the grain size becomes finer and the grain growth is uniform. The average grain size of the ZST ceramics with the addition of CuO for different milling times are tabulated in table 3.3.I. For samples milled for 1 hour it is observed that as the concentration of CuO increases the grain size increases, where as for the samples milled for 5 hours the grain size is increased only up to 1wt% addition of CuO. For the samples milled for 7 hours, again the grain size increased with increase in wt% of CuO. The presence of liquid phase effect can be seen from the SEM micrographs for the samples milled for 5 hours with 1.5wt% of CuO (figure 3.35c) and for the samples milled for 7 hours and added with 1.0 and 1.5wt% CuO (figure 3.3.6b & c). The maximum average grain size of the well sintered ZST ceramics are found to be 10, 13 & 12 μm observed for the samples doped with 1.5, 1& 0.5wt% CuO and milled for 1, 5 & 7 hours respectively.

From this study it is clear that the optimization of processing parameters such as milling time, sintering temperature, sintering duration and type and amount of the additive plays an important role in achieving better densification and microstructure, which influences the microwave dielectric properties of the ZST ceramics.

Figure 3.3.4: SEM micrographs of the samples with CuO and milled for 1hour.Sintered at 1300°C for 3.5 hours in all cases.

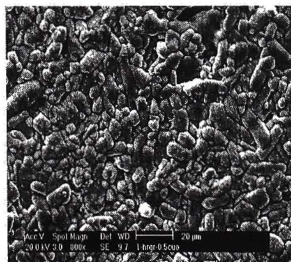

Figure 3.3.4a: Amount of CuO: 0.5 wt%.

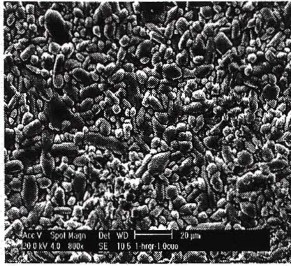

Figure 3.3.4b: Amount of CuO: 1.0 wt%.

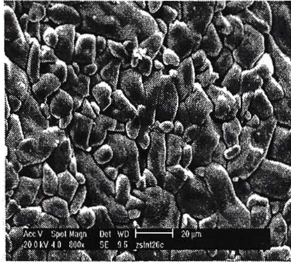

Figure 3.3.4c: Amount of CuO: 1.5 wt%.

Figure 3.3.5: SEM micrographs of the samples with CuO and milled for 5hours.Sintered at 1300°C for 3.5 hours in all cases.

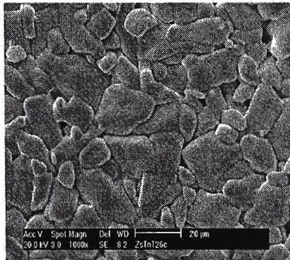

Figure 3.3.5a: Amount of CuO: 0.5 wt%

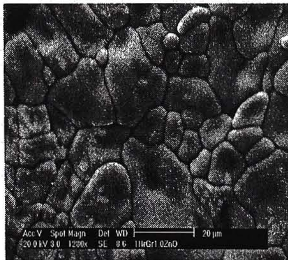

Figure 3.3.5b: Amount of CuO: 1.0 wt%

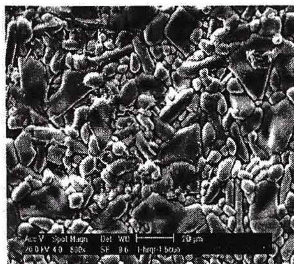

Figure 3.3.5c: Amount of CuO: 1.5 wt%

Figure 3.3.6: SEM micrographs of the samples with CuO and milled for 7hours.Sintered at 1300°C for 3.5 hours in all cases.

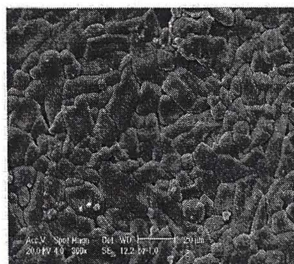

Figure 3.3.6a: Amount of CuO: 0.5 wt%

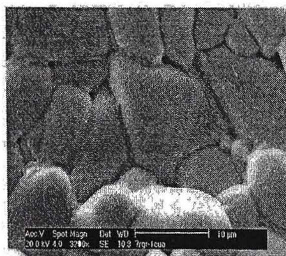

Figure 3.3.6b: Amount of CuO: 1.0 wt%

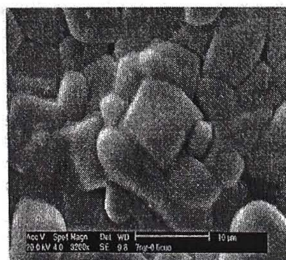

Figure 3.3.6c: Amount of CuO: 1.5 wt%

Wt% of CuO	Grain size (μm) for a ball milling time of		
	1 hour	5 hours	7 hours
0.5	5	8	10
1.0	6	13	11
1.5	10	9	12

Table 3.3.I: The average grain size of the samples added with different concentrations of CuO and subjected to different ball milling time.
Sintering condition: 1300°C for 3.5 hours.

Figure 3.3.7a -c shows the variation in dielectric constant as a function of wt% of CuO when sintered at 1300°C for different sintering durations and ball milled for 1, 5 and 7 hours respectively. In all the three cases, dielectric constant Vs wt% of CuO followed the similar trend as the density Vs wt% of CuO. The dielectric constant values measured at 10.5 GHz ranged from 33.8-37.5, 35-38.4 and 31.8-37.3 for the samples, ball milled for 1, 5 and 7 hours respectively. The dielectric constant values of the well sintered ZST ceramics ranged from 36-38.4. The increase in dielectric constant is attributed to the higher densities because higher density means lower porosity.

Figure 3.3.7: Dielectric constant as a function of wt% of CuO for the samples milled for different durations and sintered at 1300°C for different sintering durations.

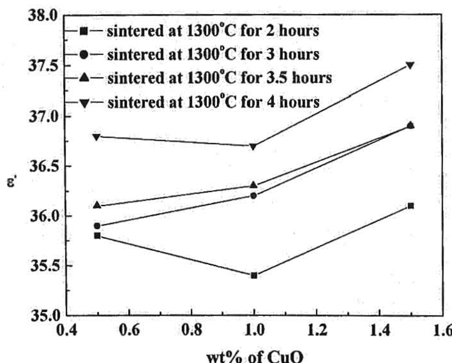

Figure 3.3.7a: Milling time: 1hour.

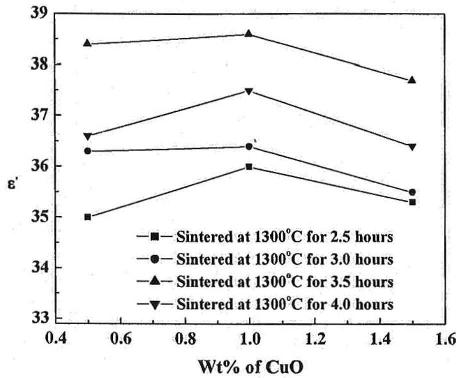

Figure 3.3.7b: Milling time: 5hours.

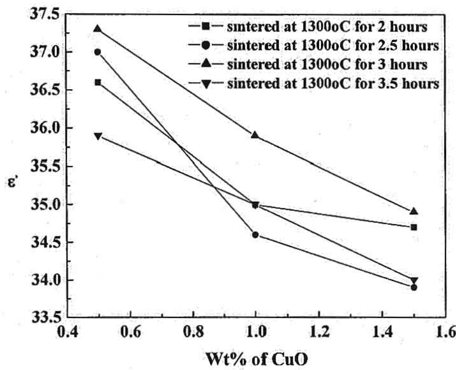

Figure 3.3.7c: Milling time: 7hours.

The variation in Qxf_o as a function of wt% of CuO sintered at 1300°C for different sintering durations and ball milled for 1, 5 and 7 hours respectively are shown in figures 3.3.8a-c. In all the three cases Qxf_o Vs wt% of CuO followed the similar trend as the density Vs wt% of CuO, which clearly shows the role of density on ZST ceramics. The maximum Qxf_o values are 48900 for the sample ball milled for 1 hour with 1.5wt% of CuO, 66300 for the sample ball milled for 5 hours with 1.0wt% of CuO and 51200 for the sample ball milled for 7 hours with 0.5 wt% of CuO. It is found that as the milling time increases, the ZST ceramics showed better

properties with lower amounts of CuO. The lower values of Qxf_0 are attributed to the lower densities and the liquid phase, which is observed from the SEM pictures. The relative density plays an important role in controlling the loss and is observed in this study also. The improvement in Qxf_0 value is primarily attributed to the uniform grain growth, increase in grain size and also to enhanced density. The specimen with large grain is expected to have a high Q value because the grain growth decreases the grain boundary area [7]. In this case the grain morphology is suggested to dominate Qxf_0 values of ZST ceramics with the addition of CuO and the optimization of milling time. From this study it can be concluded that the initial particle size and the concentration of CuO plays a major role in the densification and the microstructure, which influences the microwave dielectric properties of the ZST ceramics. The sintering temperature came down to 1300°C from 1650°C, with ball milling and CuO addition along with 1wt% ZnO.

Figure 3.3.8: Qxf_0 as a function of wt% of CuO for the samples milled for different durations and sintered at 1300°C for different sintering durations.

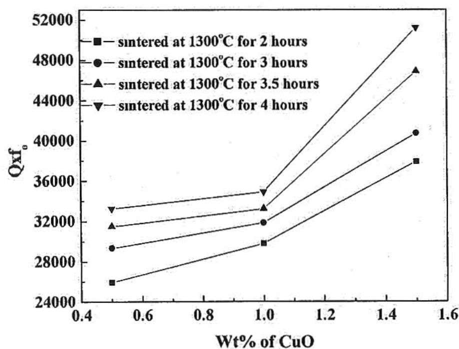

Figure 3.3.8a: Milling time: 1hour.

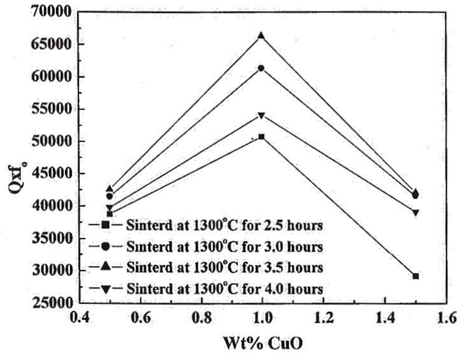

Figure 3.3.8b: Milling time: 5hours.

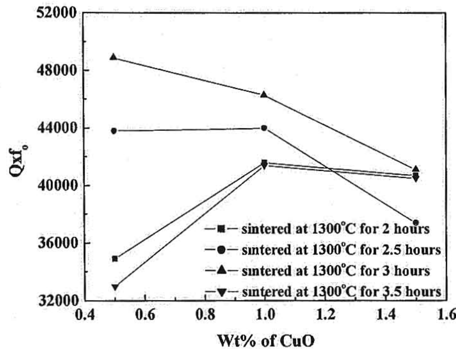

Figure 3.3.8c: milling time: 7hours.

Since the ZST ceramics are temperature stable and the addition of CuO did not cause any noticeable secondary phase, the τ_f values did not change much. The τ_f values of all the samples are in the range of 2-3 ppm/°C.

The microwave dielectric loss is caused not only by the anharmonic lattice vibrational modes, but also by extrinsic factors like pores, secondary phases, grain boundary and oxygen vacancies [9,10] which are heavily dependent on processing conditions. The densities and the microstructures of the ZST ceramics were improved at lower processing temperatures with improvement in the microwave dielectric properties especially the quality factor.

3.4 Microwave dielectric properties at cryogenic temperatures:

Cryogenic electronics is a growing branch of modern electronics, especially since the discovery of high temperature superconductors that allowed for significant reduction of losses and noise in microwave filters and oscillators. The microwave dielectric properties of ZST ceramics were investigated as a function of temperature to understand the feasibility of using this material in cryogenic and low temperature devices. Successful design and manufacturing of low loss devices at cryogenic temperatures require careful choice of dielectric materials for their construction. Low loss dielectric materials can be used in conjunction with the high Q-factor super conducting system to reduce the over all loss of the device.

The previous section showed that the addition of trace amounts of CuO along with 1wt% addition of ZnO exhibited good microwave dielectric properties, with lower sintering temperatures. To understand the loss mechanisms of ZST ceramics added with 1wt% ZnO alone, and with different concentrations of CuO (0.5, 1.0 & 1.5wt%) added additionally at cryogenic temperatures and to see the feasibility of using this material in cryogenic and low temperature devices, this study is performed. The experimental and characterization techniques of this study are discussed elsewhere [11-14]. However, the microwave dielectric properties of ZST ceramics at cryogenic temperatures were not reported earlier. The processing conditions of the samples are reported in sections 3.2 & 3.3.

The variation in the resonant frequency of the ZST ceramics doped with different concentrations of CuO and without CuO, measured as a function of temperature is shown in figure 3.4.1a. It is observed that there is difference in the resonant frequencies of the ZST ceramics prepared as dielectric resonators with and without the addition of CuO, the dimensions being kept constant. The difference in the resonant frequency is due to the difference in the real part of the permitivity of the sample and slight difference in the sample dimensions. In order to obtain the highest accuracy in the permitivity, the exact dimension of each sample is accounted separately.

The variation in dielectric constant as a function of temperature of the ZST ceramics is plotted in figure 3.4.1b. It is observed that the decrease in dielectric constant with increase in temperature over the wide range of temperature is quite small. Sample without CuO showed higher dielectric constant of 37.88 at 15K and 37.62 at room temperature. ZST ceramics doped with CuO showed lower values

compared to the undoped sample. There is not much variation in dielectric constant with the variation in wt% of CuO at cryogenic temperatures. For samples with CuO added in the range of 0.5 – 1.5 wt%, the variation in dielectric constant is in between 34.89 and 35.15 at 15K and 34.63 and 34.94 at 290K. The set-up used for cryogenic measurements and for measurement at ambient are different.

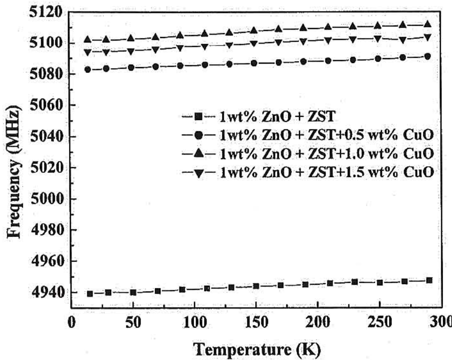

Figure 3.4.1a: Resonant frequency of the ZST ceramics added with different concentrations of CuO and without CuO.

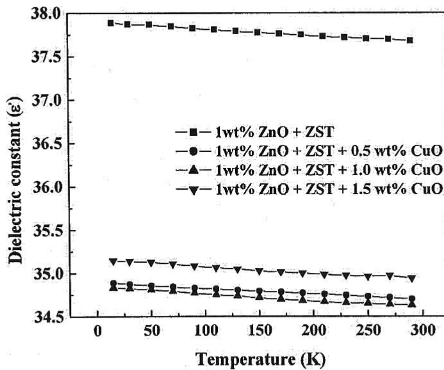

Figure 3.4.1b: Dielectric constant as a function of temperature of the ZST ceramics added with different concentrations of CuO and without CuO.

The unloaded Q-factor of the ZST ceramics measured as a function of temperature is shown in figure 3.4.1c. It is found that the unloaded Q-factor decreased with increase in temperature. In the case of ZST without CuO, the unloaded Q-factor

is higher compared to CuO added samples at cryogenic temperatures but decreased drastically with increase in temperature compared to other samples. The maximum unloaded Q-factor (Q_u) of CuO free ZST is 15000 at 15K and 3180 at 290K. In the case of CuO added samples even though the unloaded Q_u -factors are lower compared to the CuO free sample at 15K, the reduction in the unloaded Q_u -factor with increase in temperature is lower resulting in the modified sample giving higher Q_u value towards room temperature.

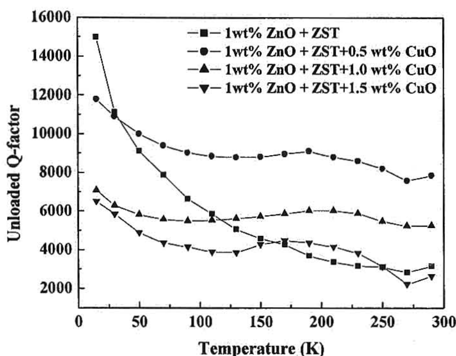

Figure 3.4.1c: The unloaded Q-factor of the ZST ceramics measured as a function of temperature.

The sample doped with 0.5wt% of CuO showed higher value of Q_u compared to 1.0 and 1.5wt% of concentrations. Q_u for this sample ranged between 11800 at 15K and 7886 at 290K. The maximum values of Q_u among the CuO added resonators are ranged between 11800-6510 at 15K and 7886-2660 at 290K. The unloaded quality factor (Q_u) of the ZST ceramics measured at ambient conditions increased with increase in concentration of CuO up to 1wt% and decreased with further increase in wt% of CuO. The difference between ambient measurement and measurement in the controlled environment of a cryogenic system is attributed to humidity and hence for further discussion, only the data obtained with the cryogenic set-up will be used. The maximum contrast in Q_u value is exhibited between the sample without CuO and the sample with 0.5 wt% of CuO. The addition of CuO modified the microstructure and microwave dielectric properties along with the reduction in sintering temperature. The modification in microstructure and sintering temperature shows that CuO is influencing the recrystllisation process and thereby the extrinsic loss mechanisms commonly found in ceramics. However, the drastic variation between sample without

CuO and the sample with 0.5 wt% of CuO shows that the CuO in limited quantities must be influencing the very intrinsic loss mechanism in ZST, that is, it must be getting in to the lattice of ZST and modifying its lattice dynamics. The fact that ε' is decreasing while Q_u value increases shows that the polarizable lattice modes are getting confined to their harmonic limits. Under such conditions, the unharmonicity associated with those modes will be less, resulting in lower values of dielectric loss and thereby higher Q_u values. At the same time, within the harmonic limits, the polarizability of polar lattice modes will be less and hence the resulting dielectric constant also will be less.

The product of the Quality factor and resonant frequency is considered as a tool for evaluating the quality of dielectric materials. Figure 3.4.1d shows the Q_0xf_0 of the resonator loaded with ZST sample under test. The results substantiates that the dielectric properties improved as a result of the 0.5wt%% and 1.0wt% of CuO doping.

The variation in loss tangent as a function of temperature is plotted in figure 3.4.1e. It is observed that as the temperature increases the loss tangent of the samples increases.

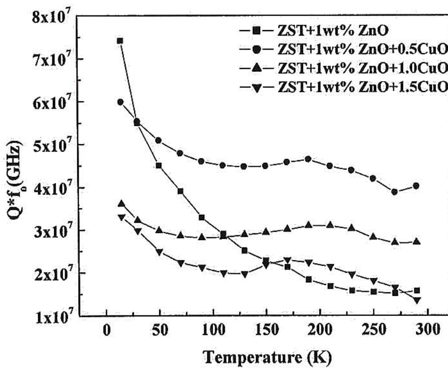

Figure 3.4.1d: Qxf_o of the ZST ceramics as a function of temperature.

For the sample without CuO, the loss is higher compared to CuO added samples at higher temperatures. The loss tangent of the ZST ceramics increased with increase in the concentration of CuO. This shows that with additional CuO, the extrinsic losses must be increasing.

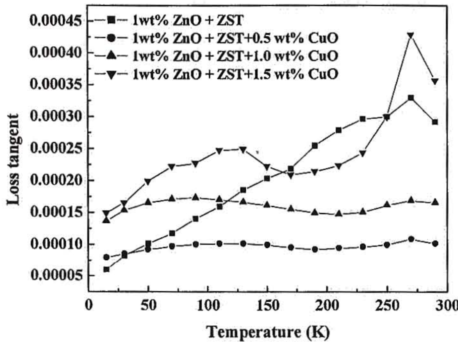

Figure 3.4.1e: Loss tangent of the ZST ceramics as a function of temperature.

In other words, the intrinsic losses could be influenced only to a limited extent. Attempt to influence it further by adding more CuO unleashes more extrinsic factors associated with the recrystallisation process giving rise to increase in total loss. Sample doped with 0.5wt% of CuO showed low loss tangent and is almost stable with increase in temperature. The increase in tanδ in the case of the sample added with 1.5wt% of CuO with increase in temperature can be attributed primarily to the extrinsic losses. From the SEM micrographs it is clear that for this sample, there is the remnance of liquid phase sintering and it exhibits smaller grain sizes and gave lower density. It is well known that smaller grain sizes increase the grain boundary areas, which are sources of many extrinsic loss inducing centers. For most of the temperatures where measurement is made, loss exhibited by this sample is higher than the loss of the CuO free sample and the slope of its temperature dependence is different. Infact, not only the magnitude but also the slope of the temperature dependence of loss of sample with 1.5wt% of CuO is different from the other two CuO added samples. This indicates that the origin of the loss in this sample differs from other cases. The difference in the microstructure for this case is quite drastic and the increased loss could therefore be attributed to it.

The difference in slope of the Q_u Vs. temperature response of the CuO free sample in comparison with the CuO added samples shows that CuO doping brings in a fundamental difference in the loss mechanism of the ZST system. Again it could be attributed to a moderation in the anharmonicity of lattice modes because that will result in both a reduction in loss as well as a reduction in temperature dependence, which is indeed observed.

In general, the microwave dielectric loss can be attributed to both the intrinsic and extrinsic losses.

The intrinsic losses are due to the anharmonic forces that mediate the interaction between crystal lattice modes and phonons, which leads to damping of the optical phonons. On the other hand the extrinsic losses are caused by the extended dislocations, grain boundaries, porosity, oxygen vacancies and secondary phases. These losses are caused mainly by the dipole relaxation of the defect-oriented polarizations concentrated at the interfaces [15]. The unharmonicity terms in the potential energy when a pair of atoms is at mean separation decrease with decrease in temperature, which is in agreement with the second law of thermodynamics. The frequency dependence of dielectric loss tangent is given by [16]

$$\tan \delta = \omega\gamma/\omega^2{}_T \qquad (3.4.1.1)$$

where, ω_T is the resonant frequency of the transverse optical mode lattice vibration and γ is its damping constant. The damping constant γ is proportional to temperature and hence the intrinsic losses increase with temperature. The specimen with large grain size is expected to have a high Q value because the grain growth decreases the grain boundary area [5]. Yet in this case it could be seen that CuO free sample got the highest grain size but the highest loss and temperature dependence also. This again strengthens the assumption that the difference between CuO free sample and the rest of them are primarily intrinsic in origin. The observation that the slope of Q_u Vs. temperature behaviour of CuO free sample is drastically moderated with CuO addition leads to the assumption that γ got reduced with CuO addition. A lower γ value leads to higher Q_u value and lower temperature dependence. The addition of CuO tailored the microwave dielectric properties of ZST ceramics at room temperature to make it suitable for dielectric resonator applications.

From the measured resonant frequency of the ZST dielectric resonator, the temperature coefficient of resonant frequency (τ_f) value is calculated using the equation:

$$\tau_f = \frac{f_0 - f_{0T}}{f_0} \frac{10^6}{\Delta T} \qquad (3.4.1.2)$$

where, f_0 and f_{0T} are the resonant frequency at room temperature and at temperature T respectively. The calculated τ_f as a function of temperature is shown in Figure 3.4.2a. It is observed that the temperature coefficient of frequency is good for 1wt% CuO

doping. The temperature coefficient of permittivity (τ_ε) as a function of temperature is also calculated and shown in Figure 3.4.2b. It is found that there is no significant difference in the τ_ε of the four materials studied.

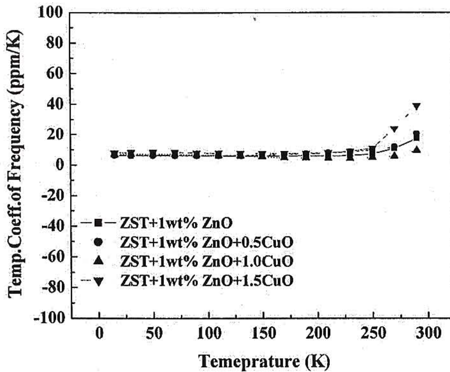

Figure 3.4.2a: Temperature coefficient of resonant frequency of the ZST ceramics as a function of temperature.

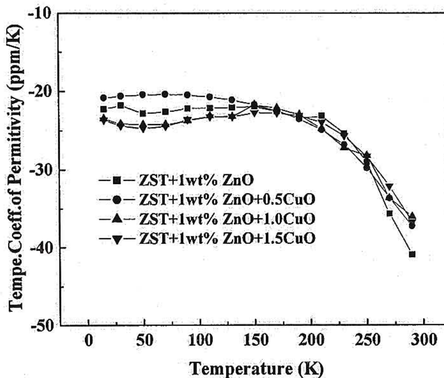

Figure 3.4.2b: Temperature coefficient of permittivity of the ZST ceramics as a function of temperature.

3.5 Impedance spectroscopy of ZST ceramics:

Recent studies have indicated that interesting electrical properties in ceramic oxides of wide variety of crystal structures arise from ionic and electronic defect structures [17]. This results in the electrical behavior exhibited by these systems varying from insulating to ionic or electronic conductor, or a combination of both.

Apart from this, local topography and microstructure will also play a role in governing the mechanism of electrical transport. A good picture of the correlation of sample microstructure with their electrical properties can be obtained by doing a complex impedance spectroscopy (CIS) on them. In the present work we have studied the impedance characteristics of this ceramic system. CIS has been recognized as a powerful technique to distinguish the grain and grain boundary contribution of oxide ceramic materials [18, 19]. Data from the CIS can be analyzed using the different complex formalisms namely impedance (Z^*), admittance (Y^*), permittivity (ε^*) and electric modulus (M^*), each consists of real and imaginary components. For example, $Z^* = Z' - jZ''$, where Z' and Z" are the real and imaginary components of the impedance, respectively. These four complex quantities are interrelated. i.e. $M^* = 1/\varepsilon^* = j\omega C_0 Z^* = j\,\omega C_0(1/Y^*)$, where ω is the angular frequency and C_0 is the empty cell capacitance. Data can be presented in complex plane plot. All the formalisms are valuable because of their different dependence on frequency. An analysis of the impedance data provides unique relaxation frequency describing the relaxation process occurring within a polycrystalline sample. The relaxation frequency (ω_{max}) of the material at a given temperature is a unique intrinsic property of the material independent of the sample's size and shape. Consequently the analysis of electrical properties carried out using the relaxation frequency (ω_{max}) values will give more exact results than those taken at some arbitrary frequencies. The relaxation frequency ω_{max} of the material obeys the condition,

$$\omega_{max}\tau = \omega_{max}RC = 1 \qquad (3.5.1.1)$$

where, τ is the relaxation frequency of the sample, R and C are the corresponding equivalent circuit parameters at the resonance.

The impedance measurements were carried out over a range of 100Hz to 4MHz using Agilent 4294A impedance analyzer interfaced with PC in the temperature range of 300K-600K.

In the previous study, it was found that the addition of CuO along with 1wt% of ZnO influenced the microwave dielectric properties of the ZST ceramics. CIS is used to distinguish the grain and grain boundary contribution to the electrical conductivity of ZST ceramics. In the previous sections the effect CuO and milling time on the structural, microstructural and the microwave dielectric properties of ZST ceramics are discussed both at cryogenic and room temperatures. The present section

discuss the effect of CuO on the electrical properties of ZST ceramics compared to the CuO free samples. To study the CIS, the samples added with 1wt% of ZnO alone and the samples added with 0.5 and 1.0wt% of CuO along with 1wt% ZnO were chosen. The Cole-Cole (Z^{ll} Vs. Z^{l}) plots of these samples at various temperatures are shown in figures 3.5.1a-c respectively. The Cole-Cole plots of these samples measured at 550K alone is shown in figure 3.5.1d, and in the inset of this figure data of the samples added with 0.5 and 1.0wt% of CuO along with 1wt% ZnO are shown.

From the complex impedance plots of the samples, it can be observed that the resistance of the samples are decreasing with increase in wt% of CuO. It is interesting to know that the sample without CuO exhibited a bulk resistance of more than 10^9 Ω. With the addition of CuO, it was found that the bulk resistance of the material is decreasing by an order of magnitude. The addition of CuO might be causing a slight increase in the charge carrier concentration.

Figure 3.5.1: Cole-Cole plots of ZST ceramics at various temperatures.

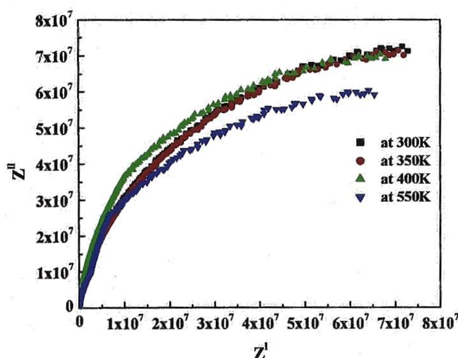

Figure 3.5.1a
Sample: ZST with 1wt% ZnO

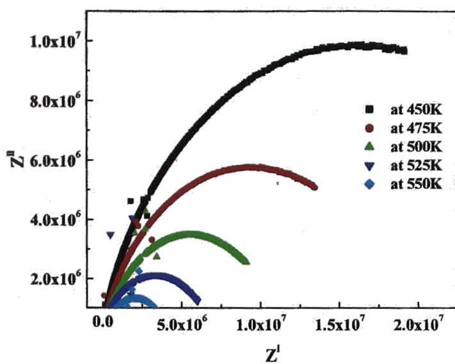

Figure 3.5.1b
Sample: ZST with 1wt% ZnO+0.5 wt% CuO

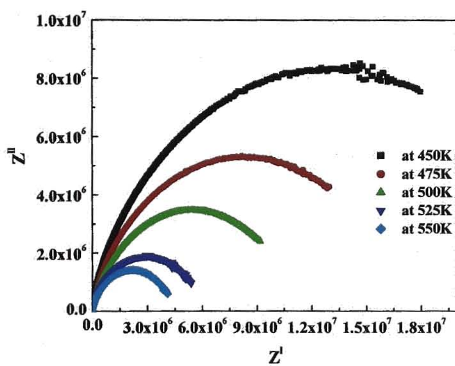

Figure 3.5.1c
Sample: ZST with 1wt% ZnO+1.0 wt% CuO.

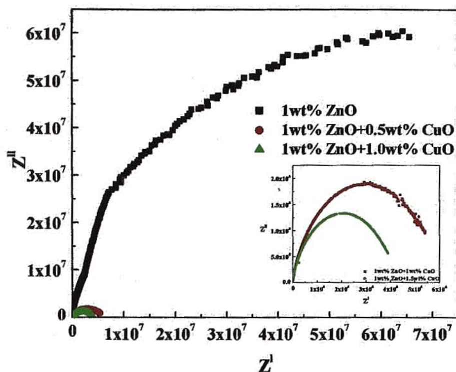

Figure 3.5.1d: Cole-Cole plots of CuO free and CuO added ZST ceramics measured at 550K.

The complex impedance plot typically comprises of a single semicircular arc that becomes gradually resolved with rise in temperature. The presence of a single arc in the impedance spectrum indicates that the electrical processes in the material arise only due to the contribution of bulk material [20]. The bulk resistance (d. c. resistance) decreases with rise in temperature as indicated by the corresponding reduction in the diameter of the semicircles with increase in temperature. This type of d. c. resistance variation with rise in temperature indicates an increase in bulk conductivity of the material with increase in temperature. In general, a negative temperature coefficient of resistance (NTCR) property is normally exhibited by insulators and semiconductors.

The real part of complex impedance of the ZST ceramics added with CuO (0.5 & 1.0 wt%) and without CuO was shown in figure 3.5.2a-c. It is observed that at lower frequencies there is no systematic variation in the real part of the complex impedance. At lower frequencies the real part of the complex impedance for the CuO free samples showed $7x10^7$ Ω where as for the samples added with 0.5 wt% CuO this value decreased to $5x10^7$ Ω. With further increase in the concentration of CuO the real part of complex impedance increased to $1x10^8$ Ω. It is clear from figures 3.5.2a-c that Z' has higher values at lower frequencies and decreases monotonically with rise in frequency and attain a constant value at higher frequencies for almost all temperatures. The frequency where the change of slope appears is shifting gradually towards higher frequency side with the rise in temperature.

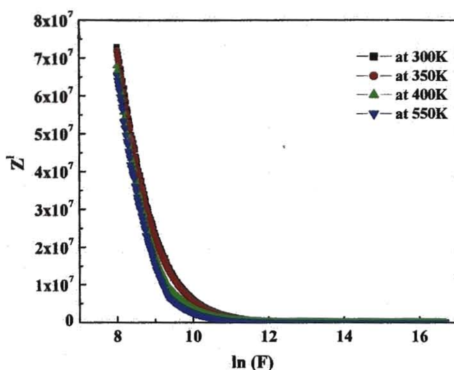

Figure 3.5.2a: Real part of impedance (Z') as a function of frequency of the sample added with 1wt% ZnO alone, at different temperatures.

The magnitude of Z' decreases with increase in temperatures and merge in higher frequency domain for all temperatures. The decrease in the real part of impedance (Z') with increase in temperature and frequency indicates a possibility of increase in ac conductivity with increase in temperature and frequency. It could be the result of release of space charges following a lowering of barrier potentials in the material [21].

Figure 3.5.2b & c: Real part of impedance (Z') as a function of frequency for the samples added with 0.5 and 1.0 wt% of CuO measured at different temperatures.

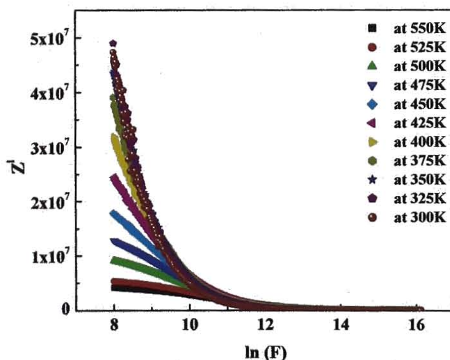

Figure 3.5.2b

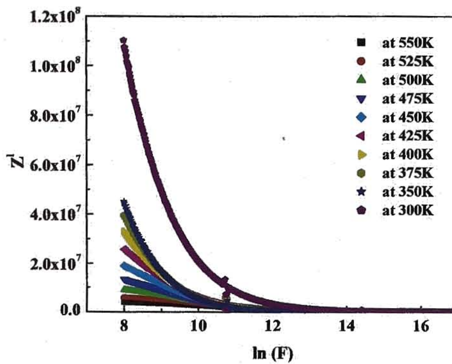

Figure 3.5.2c

Figure 3.5.3a-c shows the variation of the imaginary part of impedance (Z'') of the ZST ceramics with and without the addition of CuO measured as a function of frequency at different temperatures. The typical variation indicates that Z'' attains a maximum value at a particular frequency which is different at different temperatures. The variation shows a considerable decrease in the magnitude of Z" with the decrease in temperature and a clear shift in the frequency peak towards the higher frequency side with rise in temperature. The trend of variation of Z"with frequency is typical of the presence of electrical relaxation phenomena in the material and the relaxation is temperature dependent. At lower temperatures, the relaxation process may be attributed to orientation effects of the immobile species as indicated by monotonous fall of Z" with frequency. The decrease in the magnitude of Z" with a shift in peak towards the higher frequency side, with rise in temperature arises from the possible presence of space charge in the material and is in agreement with the observation of complex impedance data. This trend can be attributed to the generation of charge carriers with increase in temperature, a typical insulating material behavior. This study shows that this material does not have any other loss generating mechanism at lower frequencies except the temperature dependent generation of charge carriers. This explains its excellent dielectric properties at microwave frequencies.

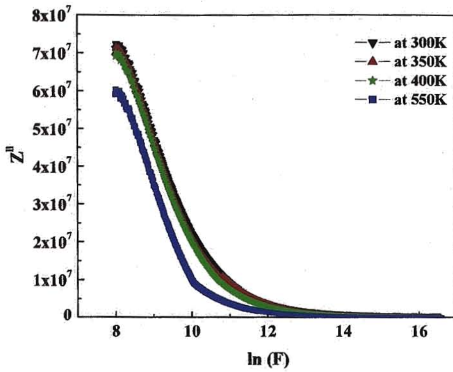

Figure 3.5.3a: Imaginary part of impedance (Z") vs. frequency for the sample added with ZnO alone and its temperature dependence.

Figure 3.5.3b & c: Z" as a function of frequency for the samples added with 0.5 and 1.0 wt% of CuO and its temperature dependence.

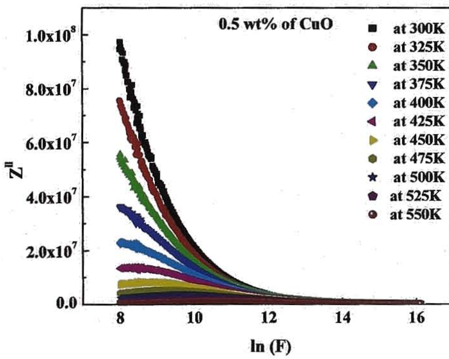

Figure 3.5.3b

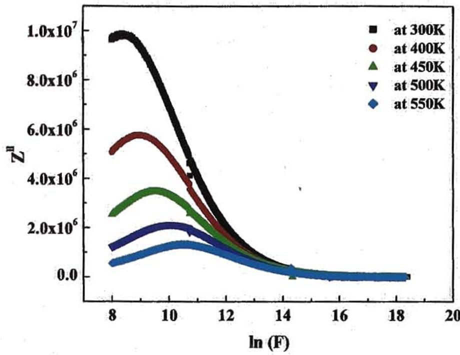

Figure 3.5.3c

Figure 3.5.4a & b shows the frequency variation of the electrical conductivity σ_{ac} of the materials as a function of frequency at different temperatures. The following features are observed from the ac conductivity spectra. The ac conductivity is almost independent of frequency at lower frequencies, and it approaches the dc conductivity σ_{dc} as the frequency is decreased.

The ac conductivity and dc conductivity can be related using the Jonschers power law equation.

$$\sigma_{(\omega)} = \sigma_{dc}\left[1 + \left(\frac{\omega}{\omega p}\right)^{n}\right] \qquad (3.5.4.1)$$

σ_{dc} is the dc conductivity and ω_p is the hopping frequency.

The translational motion of the mobile charges present in the material causes the dc conductivity. For frequencies higher than the hopping frequencies, the σ_{ac} is found to be following an exponential power law and this characterize a typical non-Debye behavior. This sort of frequency dependent conductivity obeys Jonschers power law equations [22].

Figure 3.5.4a & b: Variation in σ_{ac} as a function of frequency for the samples added with 0.5 &1.0 wt% of CuO respectively.

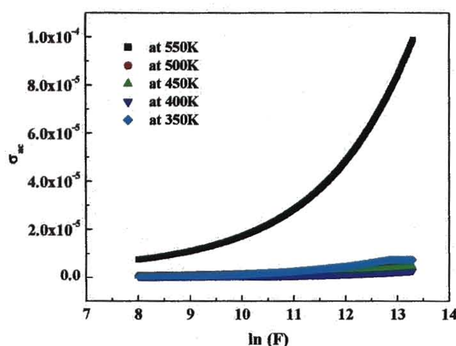

Figure 3.5.4a

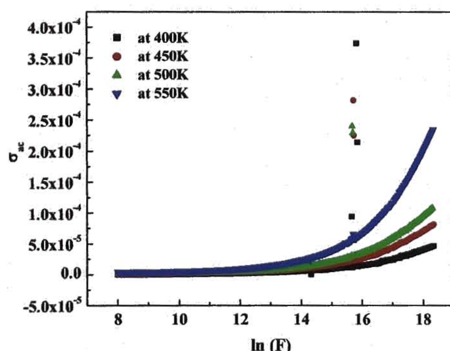

Figure 3.5.4b

The variation in relaxation time (τ) for the samples added with 0.5 & 1.0 wt% of CuO are shown in figure 3.5.5a & b respectively. These plots were obtained from the impedance data as a function of temperature. The relaxation time has been computed from the peek position of Z" Vs frequency plot in accordance with the relation $\omega\tau=1$. The τ Vs $10^3/T$ plots show that the relaxation time vary linearly with the inverse of the temperature and can be approximated to the Arrhenious type relation

$$\tau = \tau_0 e^{-E/KT} \qquad (3.5.5.\ 1)$$

where, E is the activation energy and K is the Boltzmann constant.

Figure 3.5.5a & b: The variation in relaxation time τ with temperature for the samples added with 0.5 & 1.0 wt% of CuO respectively.

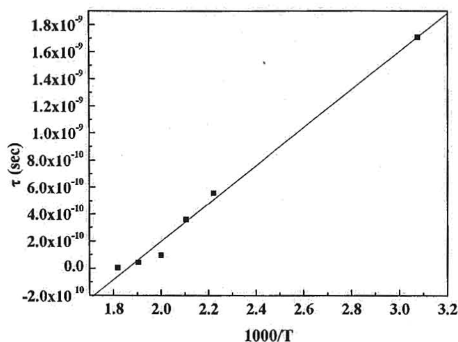

Figure 3.5.5a

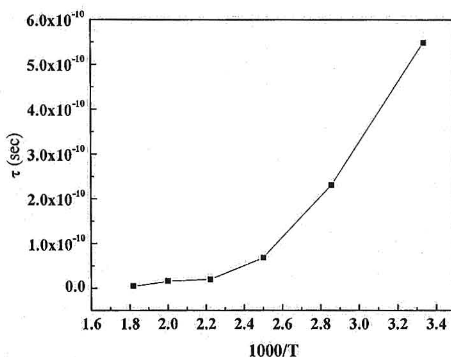

Figure 3.5.5b

The results shows a variation in relaxation time from $1x10^{-10}$ to $6x10^{-10}$ seconds which is an indication that the electrical processes taking place in the material got a spread in relaxation time. The estimated value of activation energy for this process is 0.61eV.

It is well known that the ionization of the oxygen vacancies will create conducting electrons in the oxides of perovskite structure containing titania which can be written as

$$V_O \Leftrightarrow V_O^{\bullet} + e^{'} \quad (3.5.5.2)$$

$$V_O^{\bullet} \Leftrightarrow V_O^{\bullet\bullet} + e' \qquad (3.5.5.3)$$

Generally the ionization energy will be less than 1 eV for the V_O activation and will be greater than 1eV for $V_O^{\bullet\bullet}$ activation. The electrons produced are also thermally active and will be the conducting electrons generated at higher temperatures. This could be the reason for the increased conductivity of this system at higher temperatures. More over the average activation energy for this process is found to be around 0.6 eV and hence the first reaction may be taking place. Also since there is a spread in relaxation time, at this point of time it is not clear whether the relaxing species is the oxygen vacancy itself or the electrons released from the oxygen vacancies. The electrons released from the oxygen vacancies could be the main cause of the space charge polarization, which is getting relaxed at a certain temperature.

Conclusions:

- ZST ceramics were prepared using solid-state reaction technique. The efforts were made to improve the densification by reducing the initial particle size and with the addition of 1wt% ZnO.
- Significantly, the addition of 1wt% ZnO and with the reduction of initial particle size to about 220nm, the sintering temperature is reduced from 1650 °C to 1350°C with improved microwave dielectric properties, compared to pure ZST ceramics. The microwave dielectric properties of the ZST ceramics were also studied with the variation in wt% of ZnO.
- The dielectric properties of ZST at microwave frequencies where investigated in detail both at cryogenic and room temperatures. It is found that as temperature increases the dielectric constant of ZST ceramics is not affected much, where as the Q_u-factor of pure ZST ceramics decreased compared to the CuO added samples. The addition of CuO changes the real part of complex permittivity significantly.
- The addition of CuO tailored the microwave dielectric properties of ZST ceramics particularly near room temperature. The improvement in Q_u-factor at cryogenic temperatures is attributed primarily to reduction in intrinsic losses.
- The moderation in the loss and temperature dependence of loss factor with CuO addition in ZST is also attributed to the CuO influencing the intrinsic loss

mechanism of ZST. The difference with variation in CuO doping concentration is attributed to extrinsic factors.

- The impedance spectroscopy of the samples with CuO and without CuO was carried out and it was found that this material does not have any other loss generating mechanism at lower frequencies except the temperature dependant generation of charge carriers.
- The ZST ceramic doped with ZnO and CuO resulted in a high permittivity dielectric with reasonably stable performance with temperature, which promises it as a potential entrant in the field of devices for microwave communication.

References:

[1] S.Hirano, T.Hayashi and A.Hattori, J.Am.Ceram.Soc., **74**, 1320 (1991).

[2] K.Wakino, K.Minai and H.Tamura, J.Am.Ceram.Soc., **67**, 278 (1984).

[3] C. L. Huang, M. H. Weng and H. L. Chen: Mater. Chem. Phys., **71**, 17 (2001).

[4] R. Christoffersen, P. K. Davies and X. Wei, J.Am.Ceram.Soc., **77**, 1441 (1994).

[5] R.Kudesia, A.E.McHale and R.L.Synder, J.Am.Ceram.Soc., **77**, 3215 (1994).

[6] C.L. Huang, C.C.You and B.C.Shen, J.Wave.Mater.Int., **10**, 25 (1995).

[7] N.Michimura, T.takekawa, Y.Higuchi and H.Tamura, J.Am.Ceram.Soc., **78**, 1793 (1995).

[8] C.L.Huang and M.H.Weng, Mater.Res.Bull., **35**, 1881 (2000).

[9] W. S. Kim, T. H. Hong, E. S. Kim and K. H.Yoon, Jpn. J. Appl. Phys., **37**, 5367 (1998).

[10] K. H. Yoon, Y. S. Kim, and E. S. Kim: J. Mater. Res., **10**, 2085 (1995).

[11] C. Zuccaro, M. Winter, N. Klein and K. Urban, J.Appl. Phys., **82**, 5695 (1997).

[12] M. V. Jacob, Science and Technology of Advanced Materials, **6**, 944 (2005).

[13] E. L. Ginzton, "Microwave Measurements" (McGraw Hill Book Co) 1995.

[14] M. V. Jacob, J. Mazierska, K. Leong and J. Krupka, IEEE Trans of Microwave Theory and Techniques, **49**, 2401 ((2001).

[15] W.Wersing, "In Electronic ceramics" (Elsevier Applied Science) 1991.

[16] K.Wakino, M.Murata and H.Tamura, J.Am.Ceram.Soc., **69**, 34 (1986).

[17] K. Saski and J.Maier, J. Appl. Phys., **86**, 5422 (1999).

[18] J.R. Jurado, M.T Colomer and J.R Frade, J. Am. Ceram. Soc., **83**, 2715 (2000).

[19] S. Rodewald, J. Fleig and J.Maier, J. Am. Ceram. Soc., **84**, 521 (2001).

[20] H.J. Cho, H.Youn, J.Lee and K.S.Hong, J Am.Ceram.Soc., **84**, 753 (2001).

[21] J.Maier, J. Euro. Ceram. Soc., **24**, 1343 (2004).

[22] S. S. Sekara Pandyan and M.Vijayakumar, Mater. Chem. Phys., **80**, 29 (2003).

Chapter- 4

Effect of Additives on ZST Ceramics

4.1 Brief literature review of ZST processing:

ZST is one of the best materials being used as dielectric resonators in microwave devices. ZST ceramics prepared by solid-state route requires sintering additives to improve sinterability but they should not degrade the microwave dielectric properties [1]. Achieving full densification without additives is not reported for ZST prepared by solid-state route. To reduce the sintering temperature of ZST, three methods are known, viz. wet chemical processing, addition of glassy phases and use of liquid phase sintering aids.

4.1a Low temperature sintering of ZST ceramics by wet chemical processing:

In order to improve the microwave dielectric properties of ZST ceramics, expensive and energy consuming physical treatments are generally needed. Therefore wet chemical methods such as sol-gel, co-precipitation and hydrothermal synthesis were developed to obtain ultra fine and homogeneous powders which sinter at lower temperatures.

Sol-gel method:- Hirano et al [1] investigated the processing and microwave characteristics of ZST ceramics without any additives by sol gel process using metal alkoxides. Monosized spherical particles of ZST with chemical homogeneity could be synthesized by the controlled hydrolysis of metal alkoxides. The pellets were sintered at1600°C for 3 hours. The dense pellets showed good microwave properties like ε_r=40, Qxf_o=5000 and τ_f =3ppm/°C at 10 GHz. They concluded that the dielectric constant remarkably dependent on the relative densities of the sintered pellets and the change of the lattice parameters with change in sintering temperatures, while the Q value was affected mainly by the oxygen deficiency.

Hydrothermal synthesis:- Chen et al [2] studied the synthesis and characterization of ZST ceramics through this method. This method has two advantages. (a) Reaction takes place at low temperatures. (b) The obtained particle size distribution is narrow. The samples prepared by this method were sintered at 1200°C for 24 hours in the presence of oxygen. However, the pellets showed low Q value. ε_r=44.1, Q=24166 at 8.6 GHz. Z.X.Xiong et al [3] prepared nano ZST ceramics from $ZrOCl_2$, $ZrO(NO_3)_2$,

$SnCl_2$, TiO_2 and de-ionized water. The particle size was ranged from 10-120nm. The pellets were sintered at 1200-1300°C without any additives. The dielectric properties of the samples reported are ε_r=30-45, Q=1,000-2,500 at 10GHz which is rather low.

Co-precipitation method:- Kudesia et al [4] prepared ZST ceramics with 0.05wt% La_2O_3 and 1.0wt% ZnO using this technique. The samples were sintered at 1325°C for 16 hours. The ceramics exhibited values of ε_r =37.6, Qxf_o =53,760 (at 4.2 GHz) and τ_f =-4.5ppm/°C. On the other hand without additives by this method ZST gave the following values: ε_r =29.8, Qxf_o = 36960 (at 4.2 GHz) and τ_f =-4.5ppm/°C. Han et al [5] reported a method for preparing sub micrometer ZST powder by this method from an aqueous Zr^{+4}-Ti^{+4} solution with NH_4OH in the presence of SnO_2 particles and followed by a calcination at 900°C for 2hours. The density of pellets is 95% when sintered at 1400°C for 2hours and the reported values of ε_r=37.3 and Qxf_o=46,000. To reduce the sintering temperature Jang et al [6] prepared the ZST ceramics by adding 3mol% Zn $(NO_3)_2$ to the ZST powder derived from the co-precipitation of a Zr^{+4}-Ti^{+4} solution with ammonia in the presence of SnO_2 particles. The pellets were sintered at 1200°C for 2hours. The densities of the pellets are 98.6% of theoretical density which showed the microwave properties of ε_r =38.4, Qxf_o=42,000 and τ_f =-1ppm/°C. The pellets sintered at 1250°C showed better properties with density 99% and ε_r =40.9, Qxf_o =49,000 and τ_f=-2ppm/°C.

4.1b Low temperature sintering with liquid-phase sintering aids

In the quest for improving sinterabilty of ZST without degrading the dielectric properties many sintering aids were identified. It has been found that ZST powders don't sinter by solid-state diffusion alone. Therefore sintering aids such as ZnO have been invariably added to achieve good densification at temperatures between 1000-1400°C. It's thought that the added ZnO reacts with constituent TiO_2 to form a liquid phase at the boundary, ZnO do not diffuse in to the grains to produce the lattice defects. There are number of publications and patents [7-11] which reported on the efficacy of a variety of liquid phase sintering aids which were employed to densify and improve microwave dielectric properties of ZST ceramics. These includes $BaCuO_2$+CuO, CuO and V_2O_5. The system $BaCuO_2$-CuO forms a eutectic of $BaCuO_2$+CuO (BCC) at 926°C. Moreover it has good wetting with ZST. Jean et al [8] studied the effects of BCC on densification and microwave dielectric properties of

ZST ceramics. With small amount of BCC (2.0-2.5 wt%) added the ZST could be densified at a temperature of 1000°C, which is 300-400°C lower than that required for pure ZST. When the amount of BCC increased further however the densification became retarded. For the samples added with 2.0-2.5-wt% BCC, the ZST ceramics have dielectric constants and values of Q at 7GHz in the range of 35-38 and 2800-5000 respectively.

David Houviet et al [12] have studied the effect of NiO and La_2O_3 on the dielectric properties of ZST and the effect of annealing in ZST ceramics. The ZST ceramics were sintered at 1370°C for 20hours and the microwave properties reported are ε_r=37.1 and Qxf_o =41,500 at 4GHz. After annealing the dielectric constant remains constant. However the Qxf_o value is strongly affected by the annealing process. At 1300°C, annealing has no effect on the quality factor. Annealing at temperatures of 1225°C and 1200°C induce approximately 50% reduction of Qxf_o values. Intermediate annealing temperatures of 1275°C and 1250°C induce an approximately 25% improvement of Qxf_o values. A.Ioachim et al [13] also studied the effect of NiO on ZST properties. The sintering temperature does not affect the dielectric constant but results in a decrease in dielectric loss. The material has a dielectric constant ε_r =36, Qxf_o=50,000 and τ_f=1.14ppm/°C.

Sreemoolanadhan et al [14] have studied the Hafnium –substituted ZST ceramics with the general formula $(Zr_{0.8}, Sn_{0.2}) (Ti_{1-x}, Hf_x) O_4$ with x=0, 0.05, 0.2, 0.4, 0.6, 0.8 and 1.0. They observed that the sintering temperature increased with increasing Hf content because Hf ions have larger ionic radius than the Ti ions. The density of the sample increases as the content of the heavier Hf increases. It was observed that the replacement of Ti ions with Hf ions led to a deterioration of the dielectric properties i.e. ε_r and Q values decreases and τ_f increases. One interesting aspect of the Hf substitution is that the material undergoes structural change for values of x>0.6.

4.1c Sintering of ZST ceramics using glassy phases

Microwave ceramics are increasingly used for resonators, filters, duplexers and antenna systems for wireless communications. Especially, multilayer microwave devices are being investigated to let those devices increase volume efficiency. Multilayer chip inductors (MLCI) are one of the key surface mounted devices and

have been extensively developed in recent years. These components are fabricated by lamination of ferrite and Ag electrode paste alternately and then co- fired to form a monolithic structure [15]. To keep up with the trend in miniaturization of electronic equipments and related components, particularly with the rapid development of integrated circuits and surface mounting technology, the demand for multilayer ceramic capacitors is increasing drastically [16]. Accordingly, low temperature co fired ceramics (LTCC) technology becomes more important for cost effectiveness. Often LTCC is used as substitute for multi chip modules (MCM). Integration proceeds by combining thick film and LTTC materials [17]. The sintering temperatures of microwave dielectrics such as ZST are too high to use low melting point electrodes. It was imperative to lower the sintering temperature of these microwave ceramics in order to use silver or copper electrodes. i.e. the sintering temperature of co firing with high conductivity metals should be lower than the melting temperature of Ag (961°C) or Cu (1064°C) [18-20].

Lowering the firing temperature with glass additions is generally the most effective and least expensive technique [21]. Takada et al [20] tried to sinter ZST ceramics with glass flux below 1200°C. The samples were prepared through conventional mixed oxide methods. Mixtures of ZST were sintered in the temperature range 900-1200°C using ZnO-B_2O_3-SiO_2 showing 20% higher density than that of pure ZST sintered at the same temperature. 5wt% addition of SiO_2 to ZST ceramics, when sintered at 1200°C showed the best results in density.

4.2 Introduction to the additives that are used with ZST in this study:

It is well known that the additives play an important role on the densification, microstructure and on the microwave dielectric properties especially on the quality factor of the ZST ceramics. In the present study alkaline earth metal oxides (divalent), rare earth oxides (trivalent) pentavalent oxides (pentavalent), and glass additives were added to ZST ceramics to see their effect on the sinterability, microstructure and on the microwave dielectric properties of ZST ceramics.

4.2a ZST sintering with alkaline earth metal oxides

The property of ZnO in giving liquid phase sintering [21] for ZST mentioned in section 4.1b. Similar to ZnO, some alkaline earth metal oxides have the ability to form eutectic liquids with TiO_2 at temperatures at or around 1400°C [22]. It is

reported that all of the alkaline earth metal oxides are effective for densification and the order of effectiveness is found as $Mg<Ca<Sr<Ba$. The alkaline earth metal oxides are added to ZST ceramics in this study to their effect on densification, microstructure and on microwave dielectric properties.

4.2b Pentavalent oxides

It is well known that pentavalent oxides (oxide compensators) improve the Q factor of the ZST ceramics sintered at lower temperatures. Many reports have focused on oxide compensators to improve the Q factor in the ZST ceramics. Iddles et al. [23] reported that acceptor ions such as La^{3+} produces holes and increased the dielectric loss, where as donor ions such as Nb^{5+} reduced the number of oxygen vacancies and reduced the dielectric loss. Yoon et al [24, 25] observed that the reduction in dielectric loss with increase in the concentration of Ta_2O_5, Nb_2O_5 and Sb_2O_5 up to 1wt% is arising from the reduction in oxygen vacancies in the ZST lattice. Among these oxides V_2O_5 is one of the liquid phase flux formers due to its lower melting point (650°C). Huang et al [26] studied the effect of V_2O_5 on ZST. It was observed that up to 2wt% addition of V_2O_5 along with 1wt% ZnO, ZST ceramics got densified at 1300°C it self and the samples gave good microwave dielectric properties. Pentavalent oxides are added to ZST ceramics to see their effect on densification (especially in the case of V_2O_5), microstructure, on the Q factor of the ZST ceramics and to verify whether these additives are able to compensate the oxygen vacancies in the ZST ceramics.

4.2c Rare earth oxides

It is interesting to know the effect of rare earth oxides on the densification, microstructure and on the microwave dielectric properties of ZST. However a systematic study with the addition of rare earth oxides to the ZST ceramics has not been reported so far. Hence such a study was carried out and the results are presented in the section 4.4 onwards.

4.3 Properties of ZST ceramics prepared with various additives:

Hence from a brief literature survey, it is clear that even though the ZST ceramic possess a high dielectric constant, low loss and temperature stability, a comprehensive effort is needed to correlate the complex relationship between the

processing and the factors that influences the quality factor of the ZST ceramics. This is a challenging problem in the science of dielectric materials. A number of parameters starting from the synthesizing stage up to the final high temperature densification have to be controlled to achieve best microwave dielectric properties for the ZST ceramics, especially the quality factor. The origin and purity of the initial raw materials also have a considerable influence on the sinterability, phase and microstructure, which influences the microwave dielectric properties. Moreover the particle size of the starting materials, sintering temperature, sintering duration and annealing etc make substantial influence on the quality factor of the ZST ceramics when it is prepared through solid state reaction method. Though only few research groups have studied the effect of various additives on the microwave dielectric properties and sinterabilty of ZST, the reported doping were performed under different conditions like different calcination and sintering temperatures, and sintering durations. Due to the variations in all the processing parameters by different groups there is a wide variation in the microwave dielectric properties and especially the quality factor. To overcome this difficulty, we carried out a comprehensive investigation in which different additives are added to calcined ZST under similar conditions in a systematic way. The objective of this study is to investigate the effect of various additives of different ionic radii and valency on the densification, sinterability and the microwave dielectric properties of ZST ceramics. The optimization of the synthesizing conditions was done prior to the doping of these additives.

The ZST powder was calcined at 1300°C for 1 minute and the calcined powders were ball milled at 300 rotations per minute (rpm) for 15 hours. Then the powders were mixed with different concentrations (0.5, 1.0 & 1.5 wt%) of the additives for 1 hour. In the case of ZST ceramics added with glass additives, the dopant concentration were 0.2, 0.5 and1.0wt%. The sintering temperature and sintering duration of the ZST ceramics added with different additives and concentrations were optimized in all the cases because of the differences in the melting temperature of the additives. In all the cases along with the additives, 1.0wt% of ZnO was also added as a sintering aid. The phase purity and the structure were determined by X-ray diffraction with Cu K_α (λ=1.54056 Å) radiation using powder X-ray diffractometer (Philips PW 1830). Calibration using a Si standard was done to

account for the instrumental broadening. The microstructure of the sintered ZST ceramics was observed by Scanning Electron Microscopy (Philips XL 30 ESEM). A vector network Analyzer (Agilent 8722ES) was used to measure the microwave dielectric properties. Dielectric constant (ε_r) and the quality factor values (Q) at microwave frequencies were measured using the Hakki-Coleman dielectric resonator method as modified and improved by Courtney. The temperature coefficient of resonance frequency (τ_f) at microwave frequency was measured in the temperature range 25-80°C. The description of the techniques used for measuring dielectric properties is described in Chapter 2, section 2.3.

BaO, SrO and MgO are the alkaline earth metal oxides added to the ZST ceramics in this study. To remove the carbonates from $BaCO_3$ and $SrCO_3$, the powders were calcined at 1200°C for 6 hours and the phase purity of BaO and SrO are confirmed from XRD patterns. To see the effect of pentavalent oxides on the ZST ceramics Ta_2O_5, Nb_2O_5 and V_2O_5 were used and to study the effect of trivalent oxides, the rare earth oxides such as CeO_2, Nd_2O_3 and Sm_2O_3 were added to the ZST ceramics. In the case of the glass additives, they are weighed stoichiometrically and mixed for two hours in an agate mortar using deionized water as a medium. The constituents were then melted above their deformation temperature and powdered (450°C for B_2O_3, 610°C for ZnO-B_2O_3 and 570°C for $5ZnO$-$2B_2O_3$). The formation of the glass phase was conformed using XRD.

4.4 Effect of dopants on the structure of ZST ceramics:

The XRD patterns of the ZST ceramics added with BaO, SrO and MgO with different concentrations (0.5, 1.0 &1.5 wt%) and sintered at 1300°C, 1350°C & 1400°C for 3 hours are shown in figures 4.4.1a-c respectively. Although BaO is well known to form boundary phases such as (Ba_2TiO_4), it is not present in the XRD patterns of the samples. Secondary phases are not observed at the 1.5 wt% level of BaO addition. In the case of SrO and MgO added samples also, no secondary phases are observed up to 1.5wt%. Figure 4.4.2a-c shows the XRD patterns of the ZST ceramics with different amounts of the pentavalent additives (0.5-1.5wt%) of Ta_2O_5, Nb_2O_5 and V_2O_5, sintered at 1400, 1350 and 1300°C for 4 hours respectively. The XRD patterns of ZST ceramics added with CeO_2, Nd_2O_3 and Sm_2O_3 sintered at 1400°C for 3hours are shown in figure 4.4.3a-c respectively. The XRD patterns of the ZST ceramics doped with B_2O_3, ZnO-B_2O_3 and $5ZnO$-$2B_2O_3$ at different

concentrations and sintered at 1150, 1200 and 1250°C respectively for a constant sintering duration of 3 hours are shown in figure 4.4.4a-c respectively.

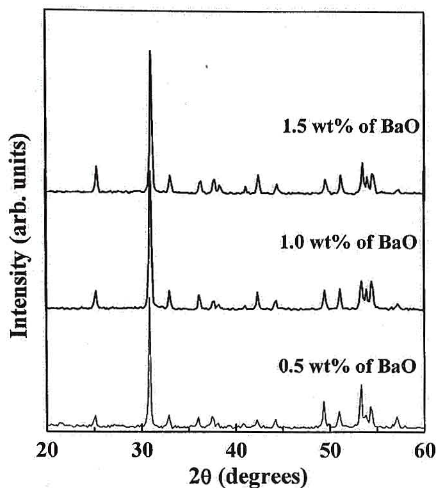

Figure 4.4.1a: XRD patterns of the ZST ceramics added with different concentrations of BaO and sintered at 1300°C for 3 hours.

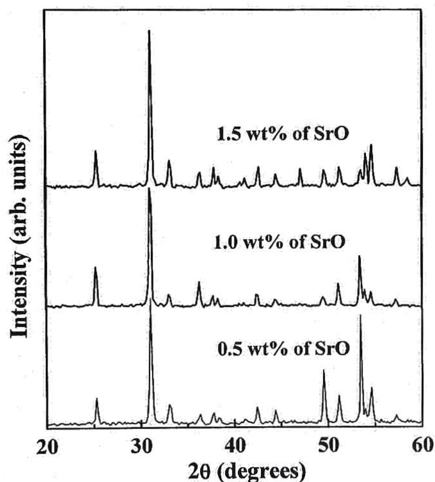

Figure 4.4. 1b: XRD patterns of the ZST ceramics added with different concentrations of SrO and sintered at 1350°C for 3 hours.

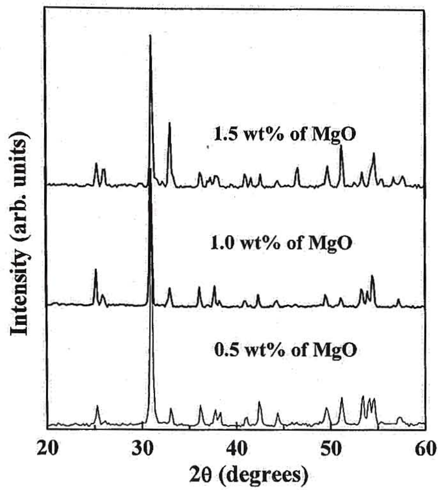

Figure 4.4.1c: XRD patterns of the ZST ceramics added with different concentrations of MgO and sintered at 1400°C for 3 hours.

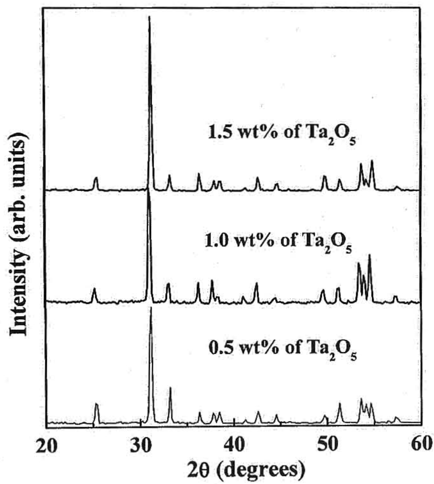

Figure 4.4.2a: XRD patterns of the ZST ceramics added with different concentrations of Ta_2O_5 and sintered at 1400°C for 4 hours.

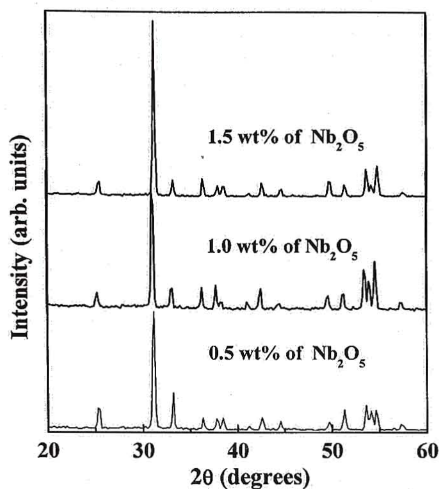

Figure 4.4.2b: XRD patterns of the ZST ceramics added with different concentrations of Nb_2O_5 and sintered at 1350°C for 4 hours.

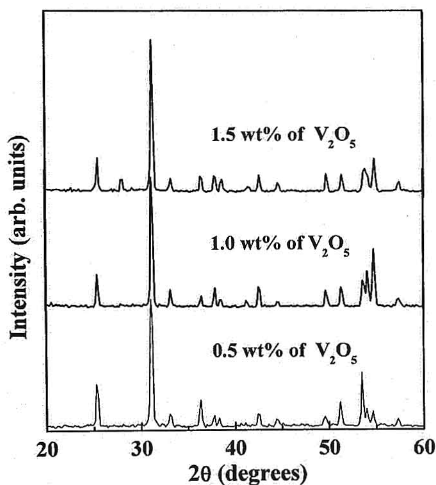

Figure 4.4.2c: XRD patterns of the ZST ceramics added with different concentrations of V_2O_5 and sintered at 1300°C for 4 hours.

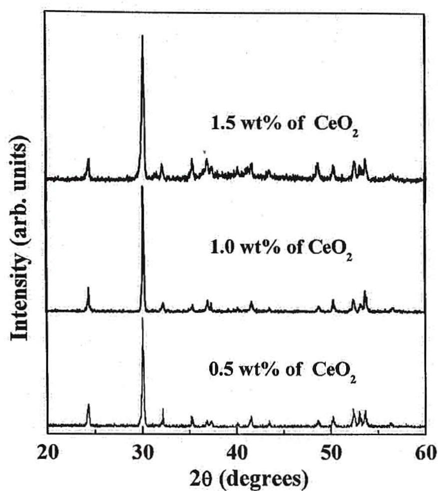

Figure 4.4.3a: XRD patterns of the ZST ceramics added with different concentrations of CeO_2 and sintered at 1400°C for 3 hours.

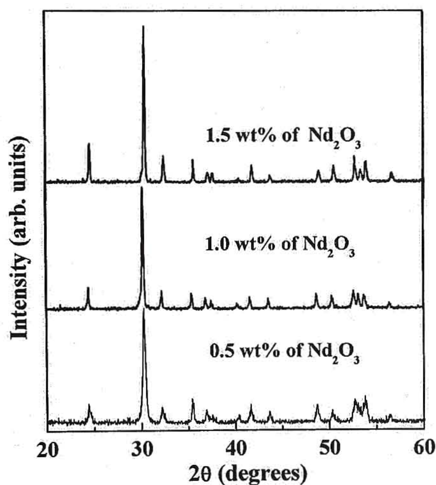

Figure 4.4.3b: XRD patterns of the ZST ceramics added with different concentrations of Nd_2O_3 and sintered at 1400°C for 3 hours.

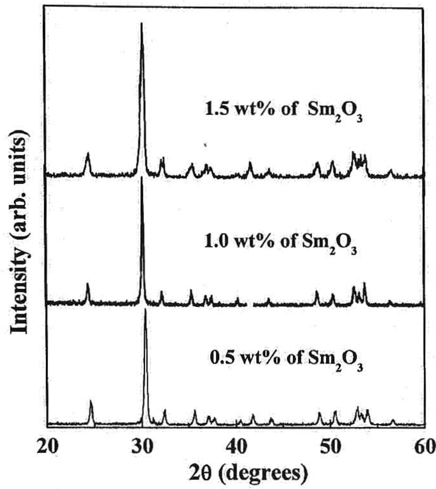

Figure 4.4.3c: XRD patterns of the ZST ceramics added with different concentrations of Sm_2O_3 and sintered at 1400°C for 3 hours.

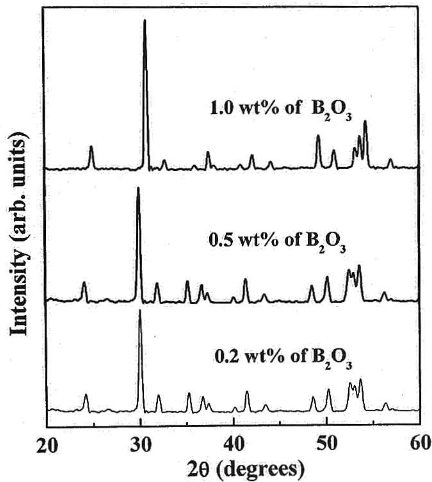

Figure 4.4.4a: XRD patterns of the ZST ceramics added with different concentrations of B_2O_3 and sintered at 1150°C for 3 hours.

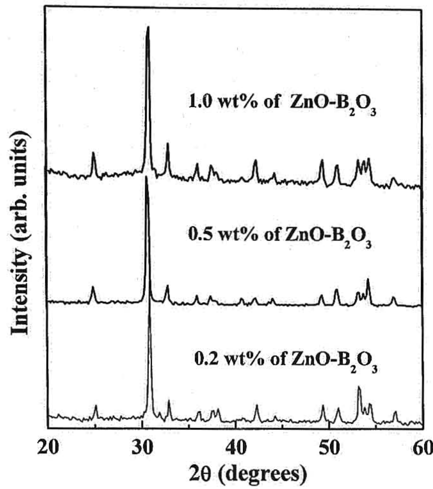

Figure 4.4.4b: XRD patterns of the ZST ceramics added with different concentrations of B_2O_3-ZnO and sintered at 1200°C for 3 hours.

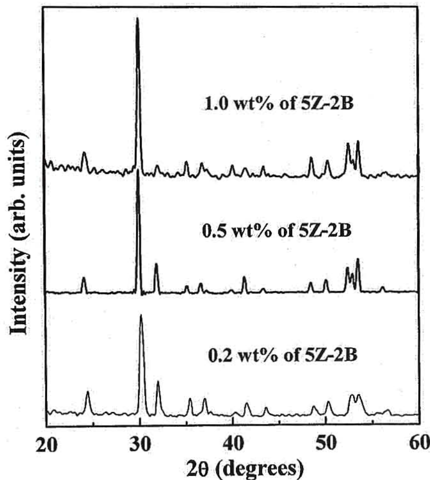

Figure 4.4.4c: XRD patterns of the ZST ceramics added with different concentrations of $5ZnO-2B_2O_3$ and sintered at 1250°C for 3 hours.

All the samples showed a homogeneous ZST phase with α–PbO orthorhombic structure and the space group of the structure is D^{14}_{2h}=pbcn. The crystallite size of the

sintered ZST ceramics was calculated from the Williamson-Hall plot (βCosθ vs. Sinθ). The crystallite size of the calcined powder is about 40nm and the crystallite sizes of the sintered pellets ranged between 40-65.5nm. These changes may be attributed to the differences of ionic sizes. The ionic radii of the elements used as given by Shannon et al [28] are Ba^{2+} (1.35 Å), Sr^{2+} (1.37 Å), Mg^{2+}(0.72Å), Ce^{4+} (0.87 Å), Nd^{3+} (0.983 Å) and Sm^{3+} (0.958 Å). They are much larger than the ions of ZST, $Zr4^{+}$ (0.72 Å), Sn^{4+} (0.69 Å) and Ti^{4+} (0.605 Å) [28]. Ta^{5+} (0.64 Å), V^{5+} (0.54 Å) and Nb^{5+} (which has an identical ionic radius as that of Ta^{5+}) are smaller to that, of the elements of the ZST ceramics. i.e. alkaline earth metal oxides and rare earth oxides have the larger ionic radii where as the pentavalent oxides got the smaller ionic radii when compared with the ionic radii of the elements in the ZST ceramics. In all these cases the additives did not form any secondary phases due to the fact that the detection of minor secondary phases by X-ray diffraction is extremely difficult. Even though no secondary phase is observed, there is a variation in peak intensities and splitting of the peaks.

4.5 Effect of additives on the densification of ZST ceramics:

4.5a Densification with divalent oxides

Figure 4.5.1a shows the variation of density as a function of wt% of BaO sintered at different temperatures for 3 hours. It is observed that as the temperature increases the density of ZST ceramics decreased. The density is high for the sample with 0.5wt% of BaO at 1350°C and for higher addition of BaO, the density started decreasing. Figure 4.5.1b shows the variation of density as a function of wt% of BaO sintered at 1300°C for different sintering durations. It is observed that the density is higher for the samples sintered for 4 hours. However with 1wt% BaO, the duration for higher density decreases to 3 hours.

The variation of density as a function of wt% of SrO sintered at different temperatures for 3 hours is shown in figure 4.5.2a. It is observed that as the temperature increases the density is increased up to 1350°C, and above that temperature. The density started decreasing. Also, as the wt% of SrO increases the density of ZST ceramics decreased in all the cases. The density is high for the sample with 0.5wt% of SrO at 1400°C and for higher addition of SrO the density started

decreasing. Figure 4.5.2b shows the variation of density as a function of wt% of SrO sintered at 1350°C for different sintering durations. It is observed that the density is higher for the samples sintered for 3 hours with 0.5wt% SrO and also for the sample with 1.5wt% of SrO but sintered for 2 hours.

Figure 4.5.3a shows the variation in density as a function of wt% of MgO additive sintered at different temperatures for 3 hours. It is observed that as the temperature increases, the density increased up to 1400°C and above that it started decreasing as well as with increasing wt% of MgO. Figure 4.5.3b shows the variation in density as a function of wt% of MgO sintered at 1400°C for different sintering durations.

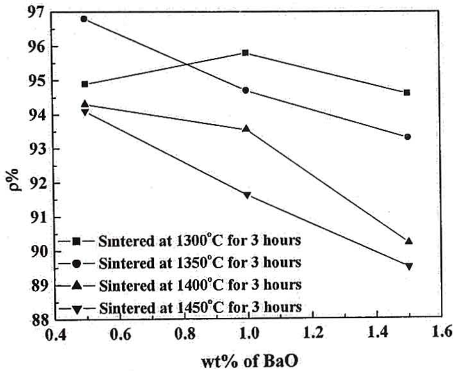

Figure 4.5.1a: Density as a function of wt% of BaO additive.

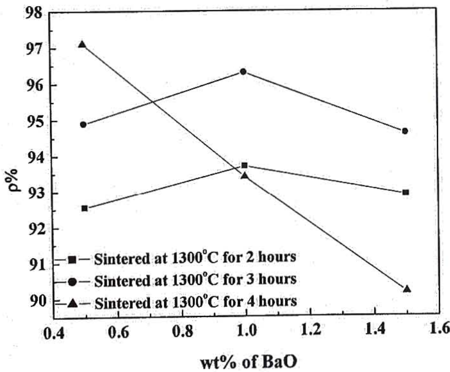

Figure 4.5. 1b: Density as a function of wt% of BaO additive.

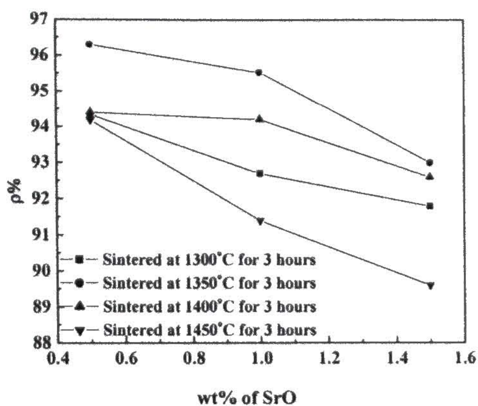

Figure 4.5.2a: Density as a function of wt% of SrO additive

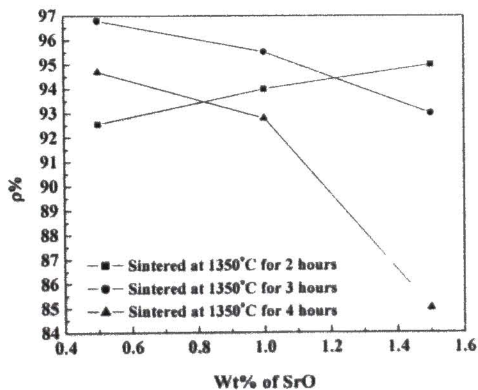

Figure 4.5.2b: Density as a function of wt% of SrO additive.

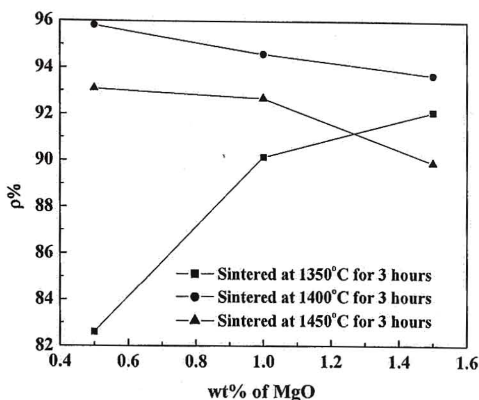

Figure 4.5.3a: Density as a function of wt% of MgO additive.

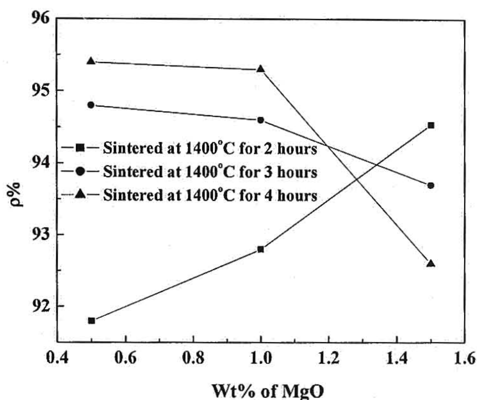

Figure 4.5. 3b: Density as a function of wt% of MgO additive.

The reduction in density with higher amounts of SrO and MgO may be due to the secondary phases which are difficult to observe from XRD patterns or due to the evaporation of ZnO at higher temperatures and longer durations of sintering. Non-uniform grain growth also could be a reason as will be shown in section 4.6. In the case of MgO added samples the reduction in density with increase in concentration can be attributed to the non-uniform grain growth and to the formation of secondary phases, which are clearly observed from SEM pictures [figure 4.6.3 b & c]. The lowest eutectic points that have been observed in the phase diagrams for BaO, SrO

and MgO additives with TiO_2 are 1312°C, 1420°C and 1620°C respectively [16]. The enhancement in densification with the addition of BaO is attributed to the formation of a eutectic liquid. The sintering temperatures in this study are lower than those reported in the literature. Kim et al. [16] reported that sintering temperatures of the BaO, SrO and MgO are 1375°C, 1400°C and 1450°C respectively and S.H.Zhang et al [29] reported 1350°C for BaO added samples. The decrease in sintering temperature in this study can be attributed to the smaller initial particle sizes. However, it may be noted that S.H.Zhang et al did not reported the particle size. It is found that as the initial particle size decreases, the sintering temperature is reduced and the grain size is increases. The initial particle size of the milled powder is 220 nm. It is generally agreed that a smaller particle size in the starting powder leads to a faster densification rate.

4.5b Densification with pentavalent oxides

The densities of ZST ceramics doped with Ta_2O_5 and sintered at different temperatures for a constant sintering duration are shown in figure 4.5.4a. While that for the samples sintered at 1400°C for different sintering durations is shown in figure 4.5.4b. 1400°C was chosen because at that temperature maximum densification is obtained. It is observed that as the sintering duration increases and with increase in amount of additive the density is decreased. The decrease in density at higher temperatures and longer sintering durations could be due to the evaporation of ZnO, non-uniform grain growth and presence of secondary phases. The last two reasons are confirmed from SEM micrographs [figure 4.6.4a-c]. In the case of Nb_2O_5 additive (figure 4.5.5 a and b. The results are slightly different in that at 1350°C higher densification is is obtained and with increasing temperature, the density goes through a minimum while longer sintering duration gives better densification. As in the previous case increasing quantities of the additive gave decreasing densities.

The dependence of densification of ZST with different amounts of V_2O_5 additive on sintering temperature is given in figure 4.5.6a and that on sintering duration is given in figure 4.5.6b. In this case as the temperature and the wt% of V_2O_5 is increased the density decreased except at the lowest sintering temperature. For sintering durations of 2 and 3 hours, the density of the samples increased with increase in wt% of V_2O_5 while at 4hour duration the density decreased with increase in additive concentration.

The lower densities some of the V_2O_5 added samples are associated with abnormal grain growth and secondary phases as observed from SEM micrographs [figures 4.6.6a-c] as well as evaporation of V_2O_5. The lower sintering temperature in this case can be the result of low melting point of V_2O_5 (650°C) and also because it forms a flux at1300°C. In the case of Nb_2O_5 and Ta_2O_5 added samples the sintering temperatures are higher due to their higher melting points 1520 and 1850°C respectively. The increase in density in all cases is associated with reduction in porosity and uniform grain growth.

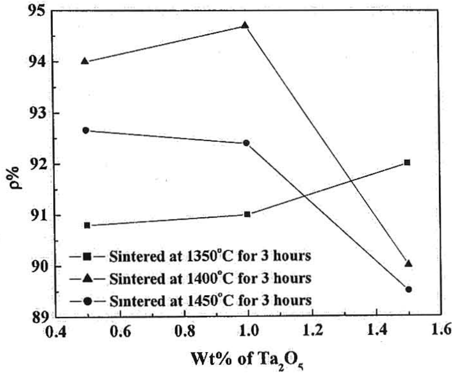

Figure 4.5.4a: Density as a function of wt% of Ta_2O_5 additive.

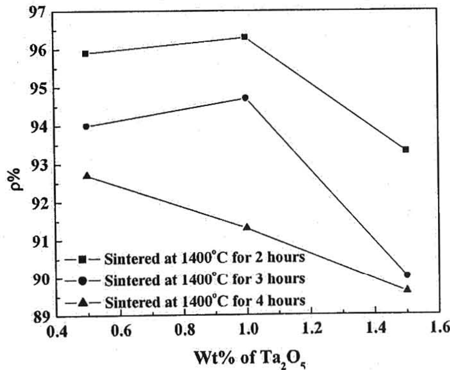

Figure 4.5.4b: Density as a function of wt% of Ta_2O_5 additive.

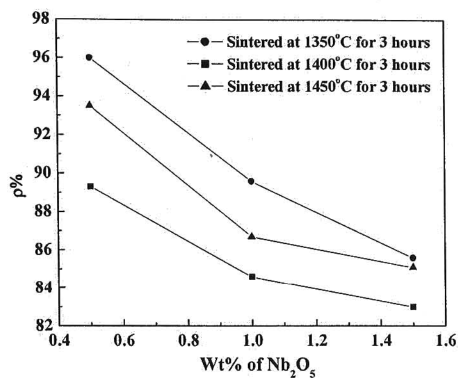

Figure 4.5.5a: Density as a function of wt% of Nb_2O_5 additive.

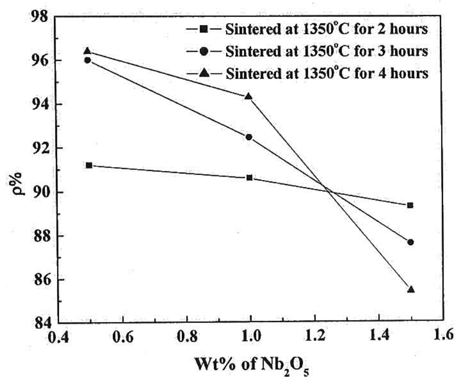

Figure 4.5.5b: Density as a function of wt% of Nb_2O_5 additive.

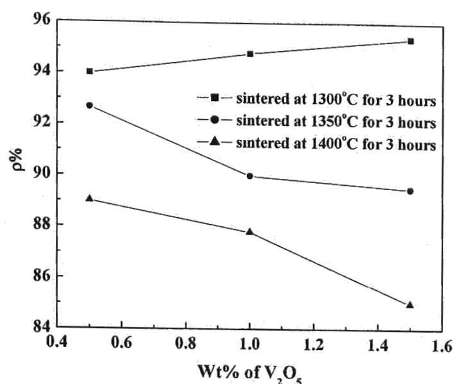

Figure 4.5.6a: Density as a function of wt% of V_2O_5 additive.

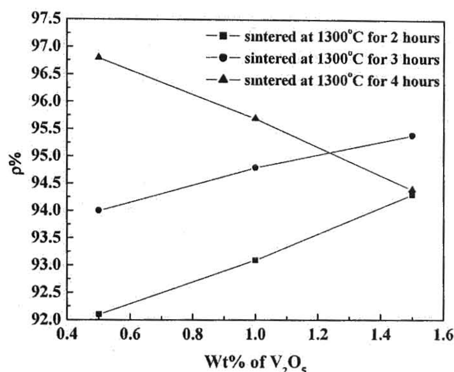

Figure 4.5.6b: Density as a function of wt% of V_2O_5 additive.

4.5c Densification with trivalent rare earth oxides

The variation in density for the ZST samples added with CeO_2, Nd_2O_3 or Sm_2O_3 as a function of wt% of the additive and sintered at different sintering temperatures for a constant duration are given in figures 4.5.7a, 4.5.8a and 4.5.9a respectively. Their corresponding densities when the sintering duration is varied at constant temperature for different amounts of additives are shown in 4.5.7b, 4.5.8b and 4.5.9b respectively. All these additives gave maximum density at 1400°C. In the case of CeO_2 and Nd_2O_3 the densities of the samples increased with increase in sintering temperature up to 1400°C irrespective of the additive concentration.

However for Sm_2O_3, higher amount of additive and lower sintering temperatures (in the temperature range studied) gave better densification.

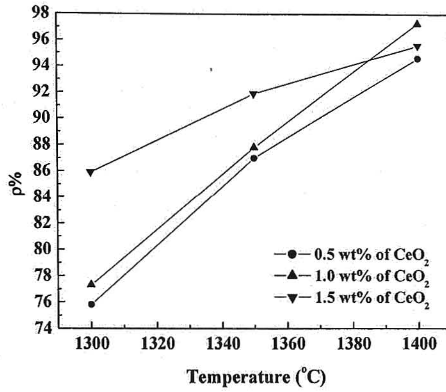

Figure 4.5.7a: Density as a function of temperatures and sintered at for a constant duration for the samples added with different wt% of CeO_2 additive.

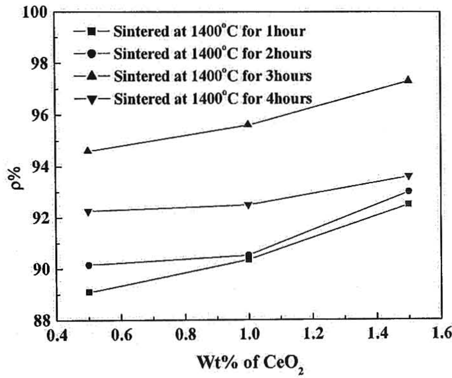

Figure 4.5.7b: Density as a function of wt% of CeO_2 additive.

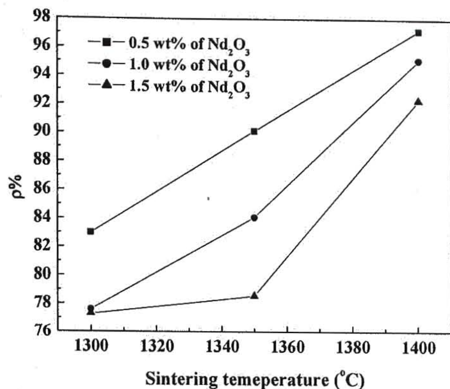

Figure 4.5.8a: Density as a function of temperatures and sintered at for a constant duration for the samples added with different wt% of Nd_2O_3 additive.

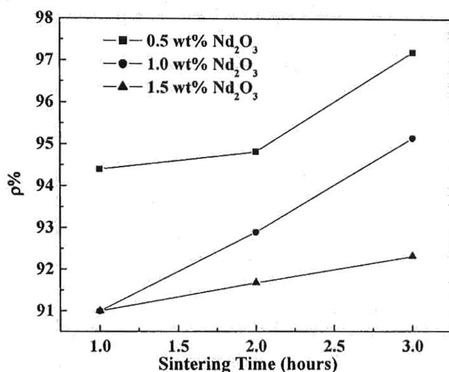

Figure 4.5.8b: Density as a function of sintering duration for the samples added with different wt% of Nd_2O_3 additive.

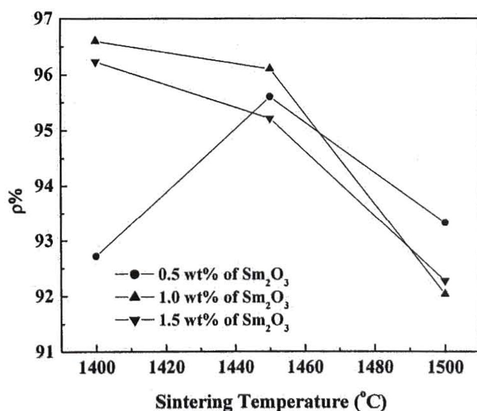

Figure 4.5.9a: Density as a function of temperatures and sintered at for a constant duration for the samples added with different wt% of Sm_2O_3 additive.

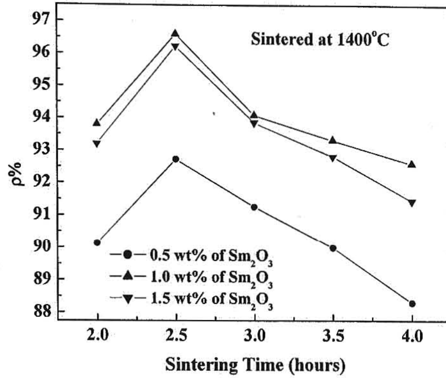

Figure 4.5.9b: Density as a function of sintering duration for the samples added with different wt% of Sm_2O_3 additive.

The maximum densities of 97.3, 97.2 and 96.6 are observed with 0.5, 1.0 and 1.5 wt% of Nd_2O_3, Sm_2O_3 and CeO_2 respectively. It was observed that the trivalent rare earth oxides did not reduce the sintering temperature, and this could be due to their higher melting points (>2300°C). Compared to the other additives the rare earth additives did not result in reduction in sintering temperature. However La_2O_3 is reported to give good sintering at 1325°C [4]. The microstructures of these samples [figures 4.6.7a-c, 4.6.8a-c and 4.6.9a-c] show that their microstructure is sensitive to the amount of additive.

4.5d Densification with glass additives

The maximum possible density of the mixtures of ZST ceramics with the addition of glassy phases is calculated using the equation (4.5.1.1) [30].

$$D = \frac{(W_1 + W_2)}{\left(\frac{W_1}{D_1} + \frac{W_2}{D_2}\right)} \qquad (4.5.1.1)$$

where, w_1 is the weight percent of ZST and w_2 is the weight percent of glass phase in the mixture. D_1 is the best density achieved for ZST without glass additive and D_2 is the density of the glass. To calculate the density of ZST added with glassy phase as a

percent the theoretical density, the values calculated from equation 4.5.1.1 were taken as the maximum possible density.

The variation in density as a function of wt% of different glassy additives (B_2O_3, $ZnO-B_2O_3$ (BZ) and $5ZnO-2B_2O_3$ (5Z-2B)) up to 1wt% is plotted in figure 4.5.10a-c respectively. All the samples were sintered in the 1100-1250°C ranges for 3 hours. In all cases it is found that as the wt% of the glass additives is increased the density of the ZST ceramics decreased. The samples showed maximum densities of 98.6, 98.2 and 98.7 at 1150, 1200 and 1250°C for the samples added with B_2O_3, ZnO-B_2O_3 and $5ZnO-2B_2O_3$ respectively for 3 hours of sintering. The difference in the sintering temperatures is could be the consequence of the difference in the melting points of the glass additives used. The decrease in density at higher temperatures may be due to the evaporation of additives non-uniform grain growth and secondary phases. The latter reasons are obvious from their microstructures [figures 4.6.10a-c, 4.6.11a-c and 4.6.12a-c]. The decrease in sintering temperature is attributed to the flux formation of the glass additives and also due to the small initial particle sizes. Thus it is found that among all the additives considered, highest densification and that too at lowest temperatures are obtained with these glass additives, a result significant for LTCC applications.

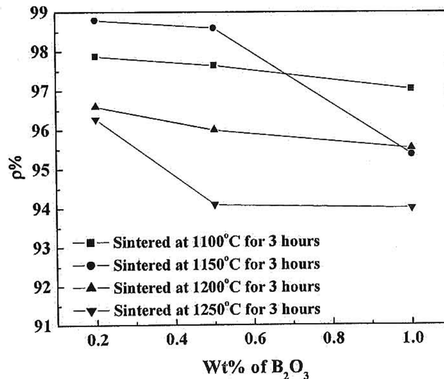

Figure 4.5.10a: Density as a function of wt% of B_2O_3 additive.

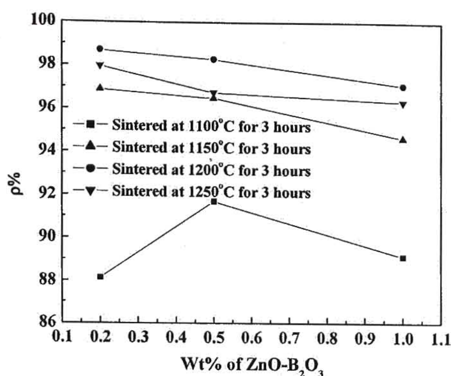

Figure 4.5.10b: Density as a function of wt% of $ZnO-B_2O_3$ additive.

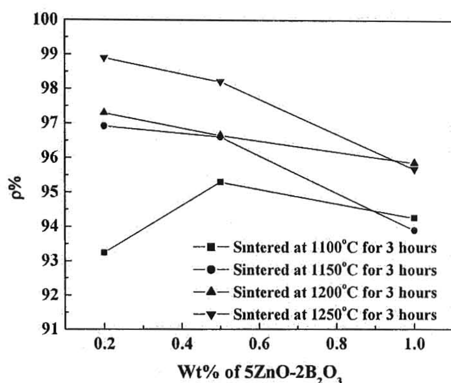

Figure 4.5.10c: Density as a function of wt% of $5ZnO-2B_2O_3$ additive.

4.6 The effect of the additives on the microstructure:

The SEM micrographs of ZST samples sintered with additives are presented in this section. In all the cases SEM pictures are taken for samples sintered at the optimized sintering temperature and time with different amount of the additives.

4.6a Microstructure with divalent oxides

Figure 4.6.1a-c shows the SEM pictures of the BaO (0.5-1.5 wt %) added samples sintered at 1300°C for 3 hours. It is found that the grain growth is uniform at 0.5wt% and shows abnormal grain growth afterwards. The average grain size is

ranged between 10-19μm. The grain size is higher with the 1.0 and 1.5wt% of BaO and the size distribution is non uniform. Figure 4.6.2a-c shows the SEM pictures of the SrO (0.5-1.5 wt %) added samples sintered at 1350°C for 3 hours. These micrographs show that SrO gives similar microstructure development as that of BaO. The grain sizes are in the range of 4-17μm. Figure 4.6.3a-c shows the SEM pictures of the MgO (0.5-1.5 wt %) added samples sintered at 1400°C for 4 hours. As the wt% of the MgO increases the shape of the grains changed from square to rod like growth. Grain size is uniform with 0.5wt% MgO added sample and the average grain size is 9μm. In all the cases with alkaline earth oxide addition the decrease in density with increase in concentration of additives can be attributed to non-uniform grain growth. From all these observations it can be concluded that the additive and its concentration on ZST ceramics plays an important role on the densification, grain growth and on grain size.

Figure 4.6.1 (a-c): SEM pictures of the ZST ceramics added with 0.5, 1.0 &1.5wt% of BaO and sintered at 1300°C for 3 hours

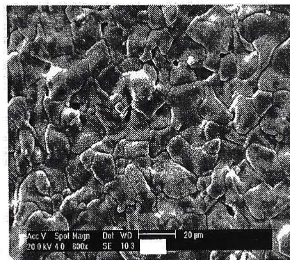

Figure 4.6.1a

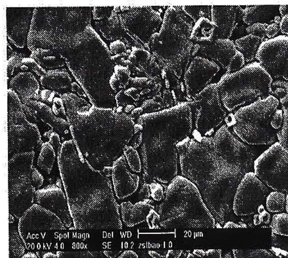

Figure 4.6.1b

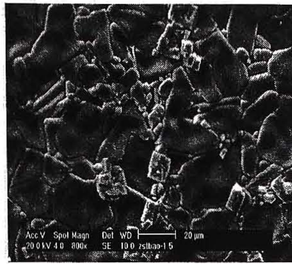

Figure 4.6.1c

Figure 4.6.2 (a-c): SEM pictures of the ZST ceramics added with 0.5, 1.0 &1.5wt% of SrO and sintered at 1350°C for 3 hours.

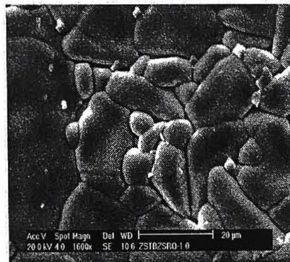

Figure 4.6.2a

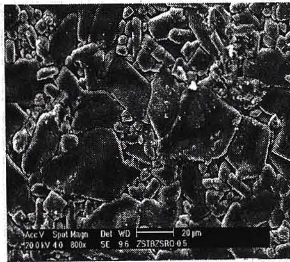

Figure 4.6.2b

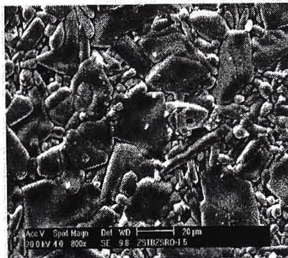

Figure 4.6.2c

Figure 4.6.3 (a-c): SEM pictures of the ZST ceramics added with 0.5, 1.0 &1.5wt% of MgO and sintered at 1400°C for 4 hours.

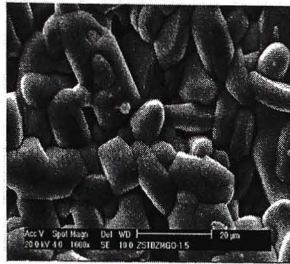

Figure 4.6.3a

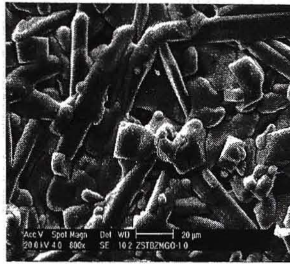

Figure 4.6.3b

Figure 4.6.3c

4.6b Microstructure with pentavalent oxides

The microstructure of the ZST ceramics added with 0.5, 1.0 and 1.5wt% of Ta_2O_5 and sintered at 1400°C for 2 hours are shown in figure 4.6.4a-c. The close packing corresponding to the highest dense sample with 1wt% of Ta_2O_5 is evident from the micrographs. The average grain size 14µm. The SEM pictures of the ZST ceramics doped with Nb_2O_5 sintered at 1350°C for 4 hours shown in figure 4.6.5a-c and that for V_2O_5 sintered at 1300°C for 4 hours (shown in figure 4.6.6a-c) gave similar results that the samples with the least additive gave best density and close

Figure 4.6.5 (a-c): SEM pictures of the ZST ceramics added with 0.5, 1.0 &1.5wt% of Nb_2O_5 and sintered at 1350°C for 4 hours.

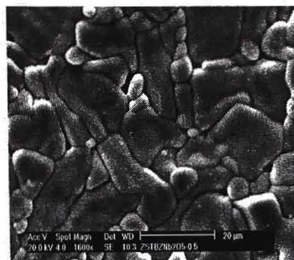

Figure 4.6.5a

Figure 4.6.5b

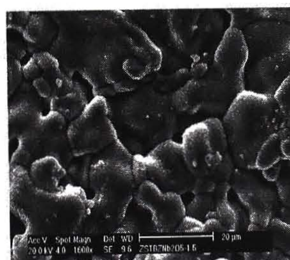

Figure 4.6.5c

Figure 4.6.6 (a-c): SEM pictures of the ZST ceramics added with 0.5, 1.0 &1.5wt% of V_2O_5 and sintered at 1300°C for 4 hours.

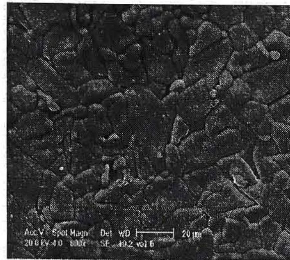

Figure 4.6.6a

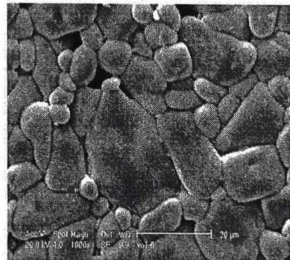

Figure 4.6.6b

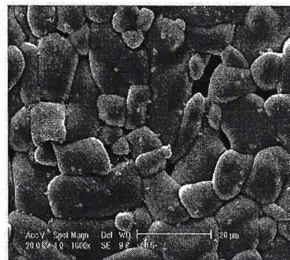

Figure 4.6.6c

4.6c Microstructure with rare earth trivalent oxides

Figure 4.6.8 to 4.6.10 gives the SEM micrographs of ZST samples sintered at 1400°C for optimum durations with CeO_2, Sm_2O_3 and Nd_2O_3 respectively. In each case figures a, b and c represents samples with 0.5, 1.0 and 1.5wt% of the respective additives. Figures 4.6.7c, 4.6.8b and 4.6.9a are the microstructures of the densified

samples in each case. The same microstructure gave higher grain size and relatively uniform grain distribution among the respective additives.

Figure 4.6.7 (a-c): SEM pictures of the ZST ceramics added with 0.5, 1.0 &1.5wt% of CeO_2 and sintered at 1400°C for 3 hours.

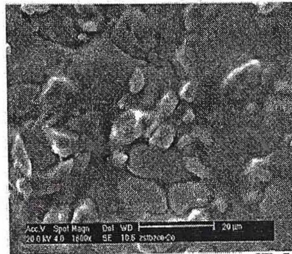

Figure 4.6.7a

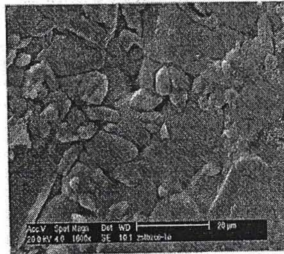

Figure 4.6.7b

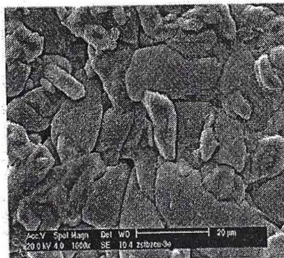

Figure 4.6.7c

Figure 4.6.8 (a-c): SEM pictures of the ZST ceramics added with 0.5, 1.0 &1.5wt% of Sm_2O_3 and sintered at 1400°C for 2.5 hours.

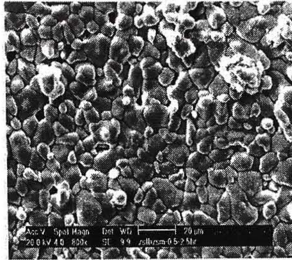

Figure 4.6.8a

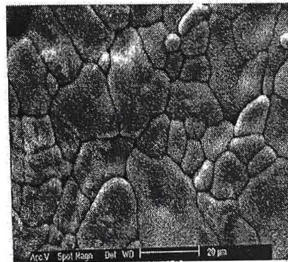

Figure 4.6.8b

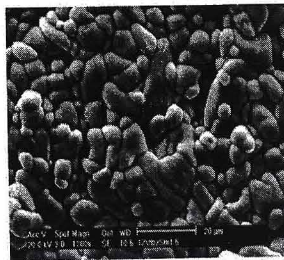

Figure 4.6.8c

Figure 4.6.9 (a-c): SEM pictures of the ZST ceramics added with 0.5, 1.0 &1.5wt% of Nd_2O_3 and sintered at 1400°C for 3 hours.

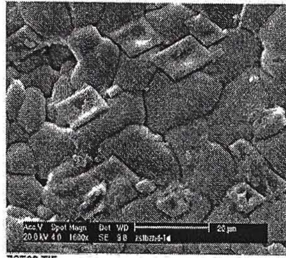

Figure 4.6.9a

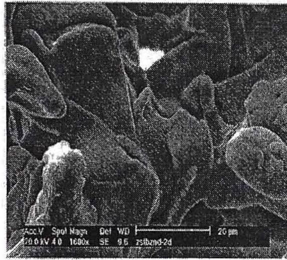

Figure 4.6.9b

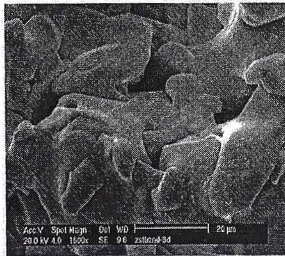

Figure 4.6.9c

A comparison of the average grain size of ZST with various additives, their ionic radii and density are tabulated in table 4.6.I. The sintering temperature for all the samples is 1400°C.

It was observed that with the addition of trivalent rare earth oxides to ZST ceramics, as the ionic radii of the additive increases the theoretical density and the

average grain size of the ZST ceramics increases. It can also be noticed that with higher ionic radius of the additive, the maximum density was achieved with lower additive concentration. The grain size increases apparently because of the incorporation of Ce^{+3}, Nd^{+3} and Sm^{+3} ions in to the grains. The addition of these additives enhances the mass transport rate through a compensatory increase in oxygen vacancies. Wakino et al observed a similar effect on the addition of Fe_2O_3 in ZST [15]. Since Ce, Sm and nd are bigger in ionic radii compared to that of Zr, Sn and Ti (0.72, 0.69 and 0.605 Å respectively), the mass transport must be happening primarily based on their ability to form oxygen vacancies.

Additive apart from 1wt% ZnO	Amount of additive for maximum densification	Sintering duration for maximum densification (Hours)	Ionic radius of the RE ion (Å)	Density (%)	Average grain size (μm)
Nil		3		96.25	12
CeO_2	1.5	3	0.87	96.6	14
Sm_2O_3	1.0	2.5	0.958	97.2	16
Nd_2O_3	0.5	3	0.983	97.3	18

Table 4.6.I: Comparison of the average grain size of ZST with various additives, their ionic radii and density.

4.6d Microstructure with glass additives

The microstructures of the ZST ceramics added with different glass additives B_2O_3, $ZnO-B_2O_3$ and $5ZnO-2B_2O_3$ are shown in figure 4.6.10a-c, 4.6.11a-c & 4.6.12a-c respectively where a, b and c corresponds to 0.2,0.2 and 1.0 wt% of the additive concentration. The sintering temperatures of ZST ceramics added with B_2O_3, $ZnO-B_2O_3$ and $5ZnO-2B_2O_3$ were 1150, 1200 and 1250°C respectively and the sintering duration is 3 hours in all cases. As mentioned in section 4.5d, sample shown in figure 4.6.10a gave the highest density among B_2O_3 added samples with an average grain size of 12μm with 0.2 wt% B_2O_3 (figure 4.6.10b) the average grain size is higher (18μm) but the density remained almost the same. Microstructure with 1wt% B_2O_3 is quiet different and the density also low. In the cases of other two glass additives also, lower concentration of the additive gave the highest density with uniform microstructure and the largest average grain size. With higher concentration of the additive either the grain growth became non-uniform or grows in to smaller grains. It

can be seen that the lower sintering temperatures are favoring densification with glassy additives compared to similar literature [20] the microstructure obtained in this study is better and that is attributed primarily to the fact that reduced particle size (220nm) powders are used in this study. As the initial particle size decreases the driving force for the densification process increases because of the increased surface area resulting in increase in density. It is interesting to note that higher density cases gives uniform grain growth with higher average grain size which is ideal for good microwave dielectric resonator characteristics.

Figure 4.6.10 (a-c): SEM pictures of the ZST ceramics added with 0.2, 0.5 &1.0wt% of B_2O_3 and sintered at 1150°C for 3 hours.

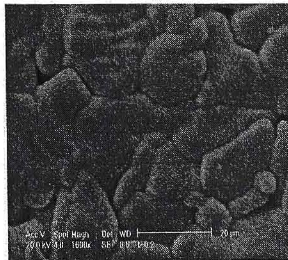

Figure 4.6.10a

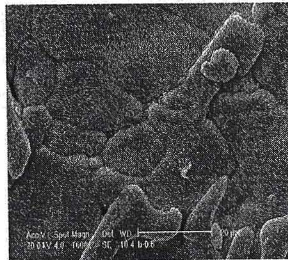

Figure 4.6.10b

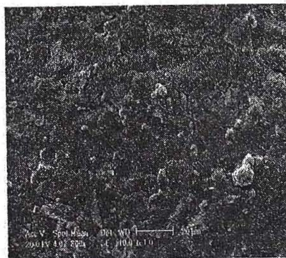

Figure 4.6.10c

Figure 4.6.11 (a-c): SEM pictures of the ZST ceramics added with 0.2, 0.5 &1.0wt% of ZnO-B_2O_3 and sintered at 1200°C for 3 hours.

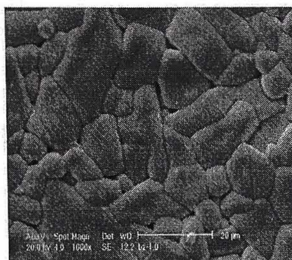

Figure 4.6.11a

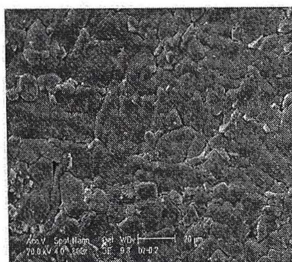

Figure 4.6.11b

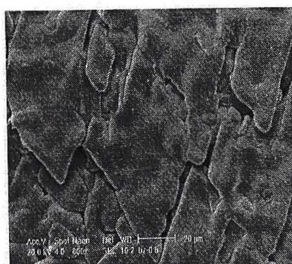

Figure 4.6.11c

Figure 4.6.12 (a-c): SEM pictures of the ZST ceramics added with 0.2, 0.5 &1.0wt% of $5ZnO\text{-}2B_2O_3$ and sintered at 1250°C for 3 hours.

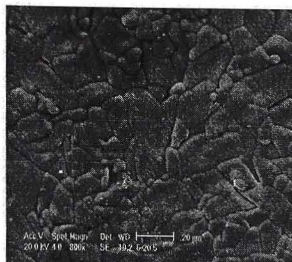

Figure 4.6.12a

Figure 4.6.12b

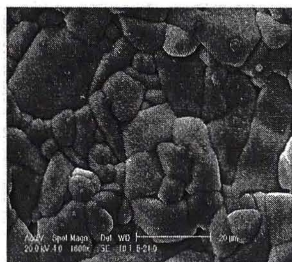

Figure 4.6.12c

4.7 Microwave dielectric properties:

4.7.1 Effect of the additives on microwave dielectric constant:

4.7.1.1 Divalent oxide additives

Microwave dielectric constants of the ZST ceramics with different additives of BaO, SrO and MgO are shown in figure 4.7.1.1a-c respectively. In all the cases dielectric constant Vs wt% of the additives followed a similar trend as that of density Vs wt% (figures 4.5.1b, 2b and 2c). It is observed that as the wt% of the additives increases dielectric constant is decreased. In the case of BaO added samples dielectric constant increased up to 1wt% and above that it started decreasing, where as in SrO and MgO added samples, dielectric constant started decreasing above 0.5 wt%. The dielectric constants of the ZST ceramics doped with BaO, SrO and MgO ranged between 34.4-38.2, 34.6-37 and 33.7-36.9 respectively.

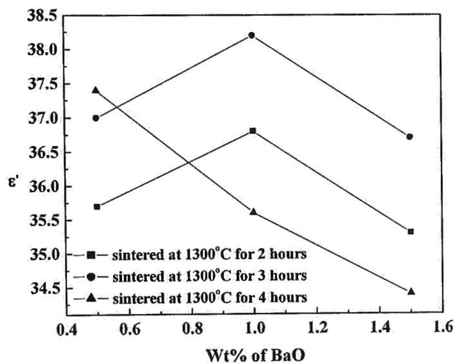

Figure 4.7.1.1a: Dielectric constant as a function of wt% of BaO additive.

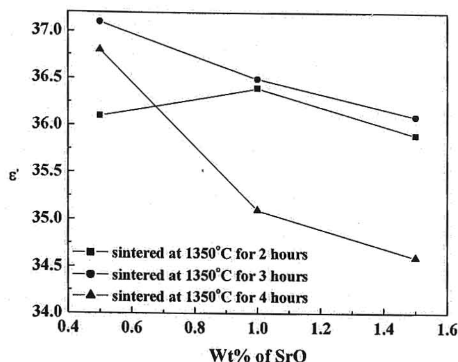

Figure 4.7.1.1b: Dielectric constant as a function of wt% of SrO additive.

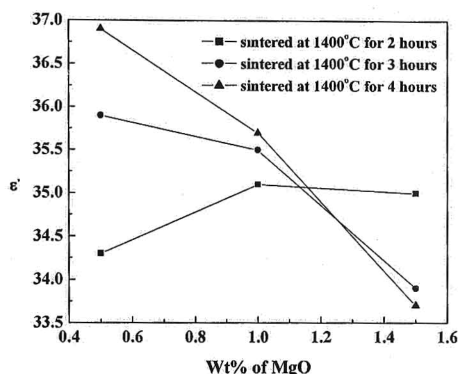

Figure 4.7.1.1c: Dielectric constant as a function of wt% of MgO additive.

4.7.1.2 Pentavalent oxide additives

The variation in dielectric constant as a function of wt% of these additives are plotted in figure 4.7.1.2a-c for Ta_2O_5, Nb_2O_5 and V_2O_5 sintered at 1400, 1350 and 1300°C respectively. In this case also a comparison with figures 4.5.4b, 5b and 6b shows that the microwave dielectric constant follows the same trend as density with variation in amount of additive. Therefore it is observed that the differences in sintering temperature, duration, type of additive and the amount of additive resulted in variations in density and that is getting reflected in their respective dielectric constant values. In other words, these factors are influencing only the densification process without influencing the intrinsic dielectric constant of the material. In the case of

Ta_2O_5 added samples the dielectric constant decreased with increase in sintering duration and the concentration of the additive. The dielectric constant values ranged between 33.3-38. In the case of Nb_2O_5 added samples the dielectric constant increased with increase in wt% of Nb_2O_5 for shorter sintering duration. With further increase in sintering duration, the dielectric constant decreased for higher concentration and the ε_r values ranged from 38.7-32.9. The dielectric constant increased with increase in wt% of V_2O_5 for shorter sintering durations but decreased with increasing wt% of the additive for longer sintering duration and the values ranged from 29.2-37.7. In all the cases the increase in dielectric constant is attributed to the increase in density and the uniform grain growth, which causes a reduction in porosity.

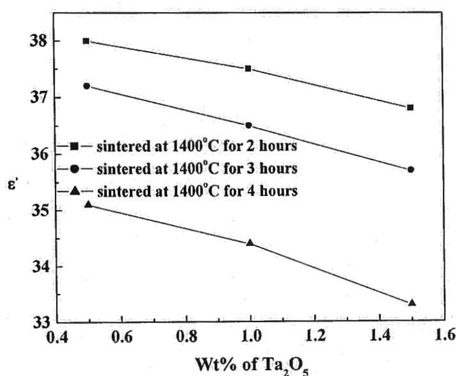

Figure 4.7.1.2a: Dielectric constant as a function of wt% of Ta_2O_5 additive.

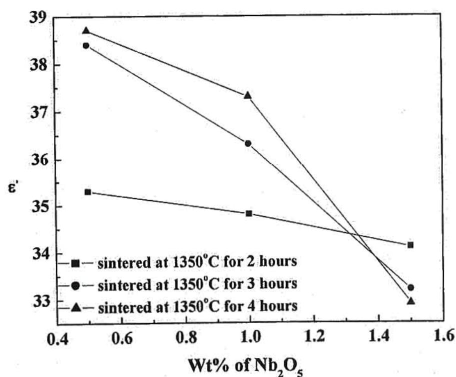

Figure 4.7.1.2b: Dielectric constant as a function of wt% of Nb_2O_5 additive.

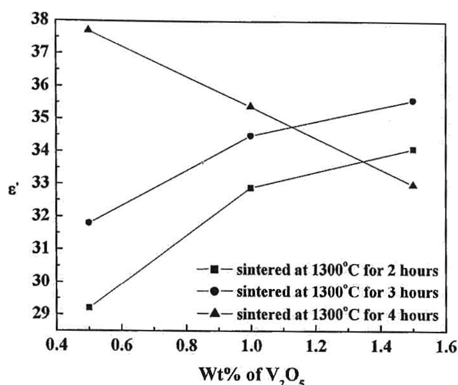

Figure 4.7.1.2c: Dielectric constant as a function of wt% of V_2O_5 additive.

4.7.1.3 Rare earth oxide additives

Similar results are obtained for the dielectric constants of ZST ceramics sintered at 1400°C with different wt% of CeO_2 and Nd_2O_3 and Sm_2O_3 added samples were sintered at different sintering temperatures for a constant sintering duration are shown in figure 4.7.1.3a-c. It is observed that in this case also the dielectric constant as a function of additives is following the trend as that of density vs. wt% of the additives. The dielectric constant values (ε_r) ranged from 34.75-38.3, 36-40 and 34.9-39.3 for the samples modified with CeO_2, Nd_2O_3 and Sm_2O_3 respectively. The samples with 1.5 wt% of CeO_2 and 0.5 wt% of Nd_2O_3 showed higher ε_r values, but decreased for the samples with higher amounts of Nd_2O_3. ZST ceramics added with Sm_2O_3 and sintered at 1400°C (Fig.4.7.1.3c) showed increase in dielectric constant with increase in wt% up to 1wt% but for the samples sintered above 1400°C the dielectric constant decreased with increase in additive concentration.

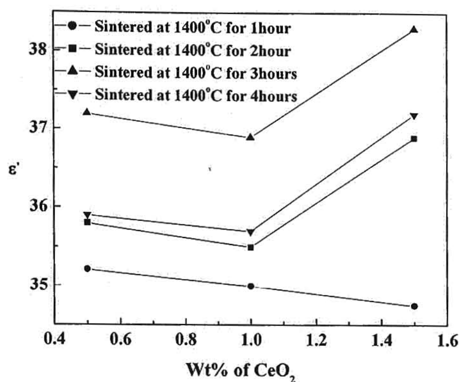

Figure 4.7.1.3a: Dielectric constant as a function of wt% of CeO_2 additive.

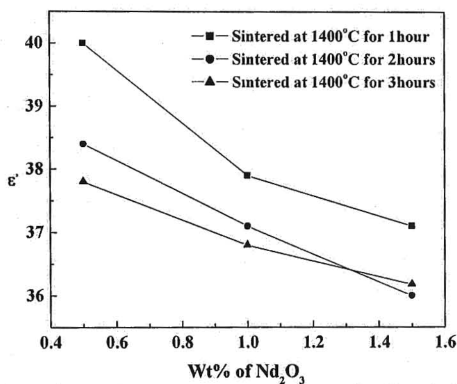

Figure 4.7.1.3b: Dielectric constant as a function of wt% of Nd_2O_3 additive.

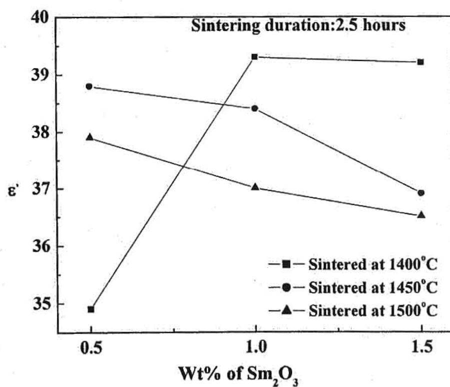

Figure 4.7.1.3c: Dielectric constant as a function of wt% of Sm_2O_3 additive.

4.7.1.4 Glass additives

The microwave dielectric constants of the ZST ceramics doped with different glass additives are plotted in figures 4.7.1.4a-c for B_2O_3, $ZnO-B_2O_3$ and $5ZnO-2B_2O_3$ respectively. In all the cases it is observed that the dielectric constant vs. wt% of the additive concentration followed a similar trend as the density vs. wt% of the additive concentration. The dielectric constants of the ZST ceramics doped with B_2O_3 are ranged from 38.7 to 32.3 and for the samples doped with $ZnO-B_2O_3$ & $5ZnO-2B_2O_3$ they are ranged between 29 to 38.2 and 31.5 to 39.1 respectively.

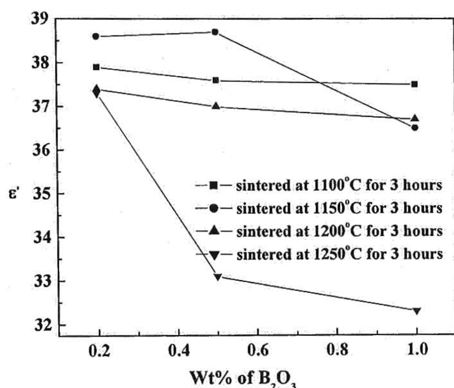

Figure 4.7.1.4a: Dielectric constant as a function of wt% of B_2O_3 additive.

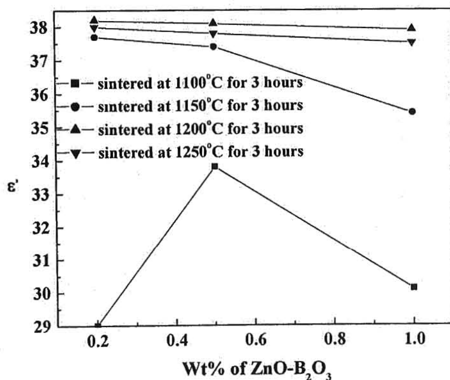

Figure 4.7.1.4b: Dielectric constant as a function of wt% of $ZnO-B_2O_3$ additive.

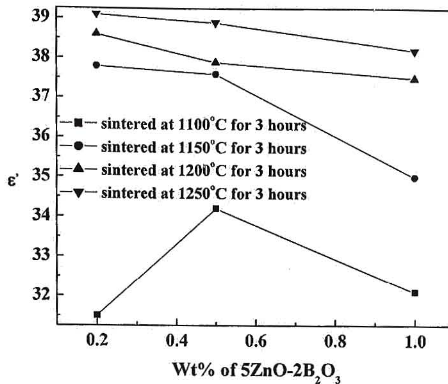

Figure 4.7.1.4c: Dielectric constant as a function of wt% of $5ZnO\text{-}2B_2O_3$ additive.

From the above observations it can be noted that the increase in dielectric constant follows the increase in density and uniform grain growth because higher density means lower porosity.

4.7.2 Effect of the additives on quality factor (Qxf_o):

The product of the Quality factor and resonant frequency (Qxf_o) is considered as a tool for evaluating the quality of dielectric materials.

4.7.2.1 Divalent oxide additives

The Qxf_o of ZST ceramics as a function of wt% of BaO, SrO and MgO is plotted in figure 4.7.2.1a-c respectively. It is observed that in all the cases, Qxf_o Vs wt% of the additives followed a similar trend as density Vs wt%. The maximum values of Qxf_o of the ZST ceramics measured at 9 GHz, when doped with BaO, SrO and MgO are found to be 60300, 54250 and 38850 respectively. In the case of MgO added ZST ceramics the grain growth is non-uniform with higher concentration of MgO and Qxf_o value got drastically reduced. D.J.Kim et al [16] attribute it to the diffusion of Mg^{2+} in to the Zr^{4+}, Sn^{4+} and Ti^{4+} sites, thus generating oxygen vacancies. Also they noticed that during the sintering, a eutectic liquid phase is formed at the grain boundaries aiding sintering and the rod like growth is one of the indications of the secondary phase. It is well known that the microwave dielectric loss of an ionic crystal drastically increases when the defects accompany a disordered charge

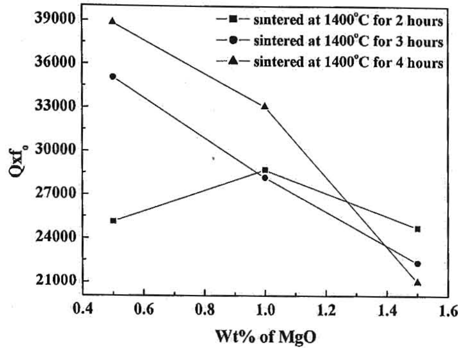

Figure 4.7.2.1c: Qxf_o as a function of wt% of MgO additive.

4.7.2.2 Pentavalent oxide additives

The variation in Qxf_o of the ZST ceramics as a function of wt% of the additives is plotted in figure 4.7.2.2a-c for Ta_2O_5, Nb_2O_5 and V_2O_5 sintered at 1400, 1350 and 1300°C respectively. The highest Qxf_o value obtained in each series is 63170, 56740 and 54790 respectively for the samples doped with 1wt% of Ta_2O_5, 0.5wt% of Nb_2O_5 and 0.5wt% of V_2O_5 Even though for lower concentrations these additives are improving the Qxf_o values, it could be noted that at higher concentrations it decreases for all the 3 pentavalent additives. In each series when Qxf_o value is highest, the corresponding density and grain size is also highest. The specimen with large grain size is expected to have a high Q x f_0 value because the grain growth decreases the grain boundary area [11], which are potential loss centers. Apart from density and increase in uniform grain size the increase in Qxf_o values can also be attributed to the reduction in oxygen vacancies which decreases the anharmonic interaction in the ZST ceramics that influence the intrinsic dielectric loss of the material. The existence of oxygen vacancies in ZST ceramics can arise in the following manner. Since Ta^{+5}, Nb^{+5} and V^{+5} act as donors the reaction can be expressed as

$$A_2O_5 + V_o^{''} \rightarrow 2A_{Ti}^{'} + 5O_0 \qquad (4.7.2.2.1)$$

where, $A_2 = Ta_2$, Nb_2 or V_2.

Then after neutralizing the oxygen vacancies, further increase in the additive concentration, the excess additive results in the generation of charge carriers with

resulting lower Q value. Indeed that is what is observed with all three pentavalent additives used.

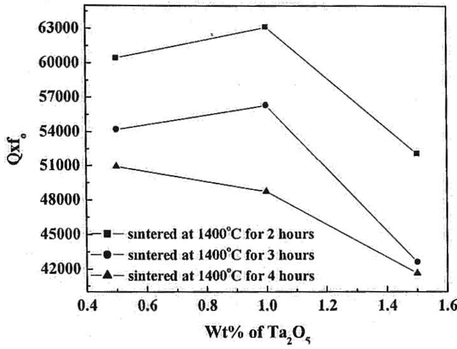

Figure 4.7.2.2a: Qxf_o as a function of wt% of Ta_2O_5 additive.

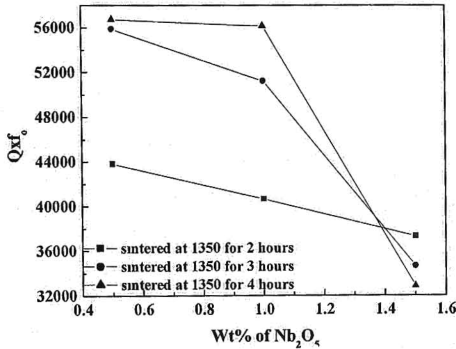

Figure 4.7.2.2b: Qxf_o as a function of wt% of Nb_2O_5 additive.

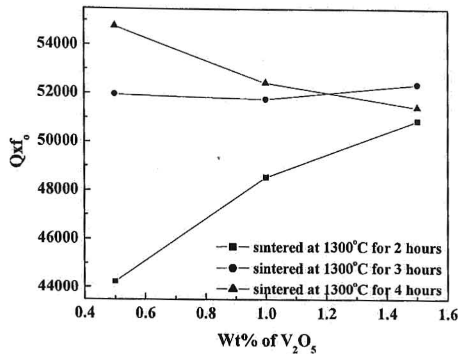

Figure 4.7.2.2c: Qxf_o as a function of wt% of V_2O_5 additive.

4.7.2.3 Rare earth oxide additives

The Qxf_o of ZST ceramics as a function of different concentrations of CeO_2, Nd_2O_3 and Sm_2O_3 are plotted in figure 4.7.2.3a-c respectively. In this case also Qxf_o values are following a similar trend as density vs. wt% of respective additives. The Qxf_o value of the ZST ceramics increased with increase in wt% of CeO_2 while with increasing amount of Nd_2O_3 the Qxf_o value has decreased. For the samples added with Sm_2O_3, the Qxfo values reached a peak with 1wt% of additive concentration. The maximum Qxf_o values were obtained for the samples with 1.5 wt% of CeO_2, 1.0 wt% of Sm_2O_3 and 0.5 wt of Nd_2O_3, and the values are 57,500, 63,850 and 59,300 (measured at 12.04GHz) respectively.

The grain sizes are suggested to affect the Qxf_o values of the dielectric resonators [32]. It is observed that the grain morphology for 1.5 wt% CeO_2, 1wt% of Sm_2O_3 and 0.5 wt% of Nd_2O_3 addition is more uniform compared to other concentrations of additives, and they gave higher grain sizes also. A higher grain size indicates a better recrystallization process with reduced lattice imperfections [33]. Since Nd^{3+} and Sm^{3+} ions act as acceptors, the reaction could be expressed as [32, 34]

$$A_2O_3 \rightarrow 2A'_{Ti} + 3O_o + V_o^{\bullet\bullet} \qquad (4.7.2.3.1)$$

where, A is Sm or Nd

In the case of Cerium oxide which bears multiple oxidation states of +3 and +4, it is known that the oxidation and reduction of CeO_2 plays a great role in controlling the microwave dielectric loss aspects of dielectric ceramics [35]. CeO_2

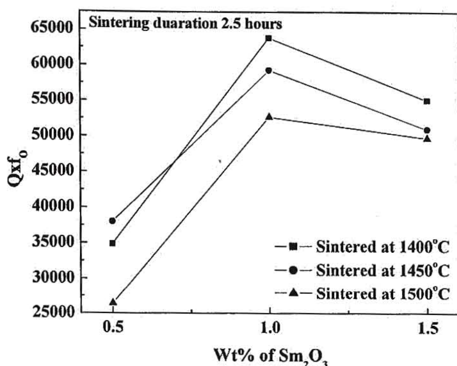

Figure 4.7.2.3c: Qxf$_o$ as a function of wt% of Sm_2O_3 additive.

4.7.2.4 Glass additives

The Qxf$_o$ values of the ZST ceramics doped with different wt% of B_2O_3, ZnO-B_2O_3 and 5ZnO-2B_2O_3 are shown in figure 4.7.2.4a-c respectively. It is observed that the Qxf$_o$ vs. wt% of the dopant concentration followed a similar trend as that of the density vs. wt% of the dopant concentration. The maximum Qxf$_o$ values of the ZST ceramics added with different glass additives are found to be 61550, 48500 and 51950 for the samples doped with B_2O_3, ZnO-B_2O_3 and 5ZnO-2B_2O_3 respectively showing that B_2O_3 gave the best results in this series. The lower Qxf$_o$ values with increase in the concentration of 1wt% ZnO-B_2O_3 is due to the secondary phases segregated at the grain boundary and the non-uniform grain growth as clearly observed from the SEM picture (figure 4.6.11c).

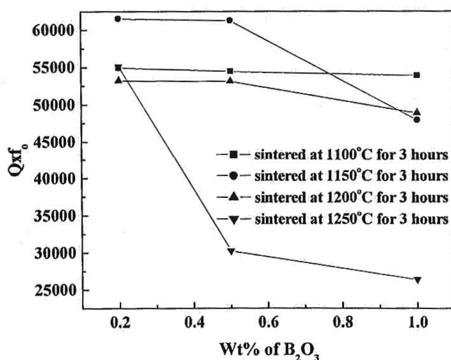

Figure 4.7.2.4a: Qxf$_o$ as a function of wt% of B_2O_3 additive.

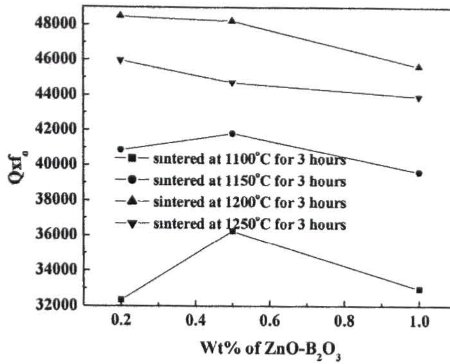

Figure 4.7.2.4b: Qxf$_o$ as a function of wt% of $ZnO-B_2O_3$ additive.

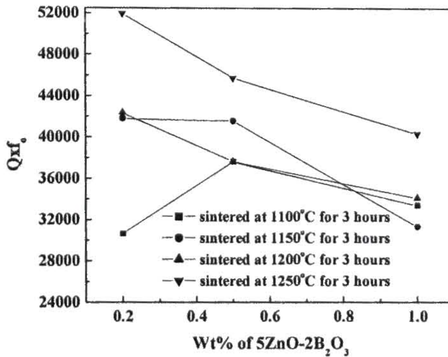

b

Figure 4.7.2.4c: Qxf$_o$ as a function of wt% of $5ZnO-2B_2O_3$ additive.

Even though glass additives gave good densification that is not getting reflected in their Qxf$_o$ values. In that way they differ from other additives. However it is worth noting that only with 1wt% $ZnO-B_2O_3$ the abnormal grain growth was observed which is an indication of secondary phase in the SEM picture, giving rise to increase the losses.

In general, the microwave dielectric losses have the intrinsic and extrinsic origins. The intrinsic losses are due to the anharmonic forces that mediate the interaction between crystal lattice modes and electromagnetic radiation, which leads to damping of the optical phonons. On the other hand the extrinsic losses are caused

by the extended dislocations, grain boundaries, porosity, oxygen vacancies and secondary phases [32,34], which are heavily dependent on processing conditions. These losses are caused mainly by the dipolar relaxation of the defect-oriented polarizations concentrated at the interfaces [11].

In the present study the increase in Qxf_o values is goes with the increase in density and the uniform grain size. Significantly, with smaller initial particle size and with small amounts of glass additives the microstructure and the microwave dielectric properties of the ZST ceramics improved even at lower sintering temperatures. There is not much variation in dielectric constant among the samples where maximum densification is achieved, but the Qxf_o values are affected with these additives.

4.7.3 Effect of the additives on the temperature coefficient of the resonant frequency (τ_f):

It is well known that the temperature coefficient of resonant frequency is intimately related to the coefficient of linear expansion (α) and the temperature coefficient of the dielectric constant (τ_ε).

$$\tau_f = 1/2\ \tau_\varepsilon - \alpha_L \qquad (4.7.3.1)$$

Since ZST ceramics are temperature stable and the addition of all these additives did not cause any formation of secondary phase, the (τ_f) values did not change much. The measured τ_f values with each of the additives used are tabulated in table 4.7.3.I

	Name of the additive	**τ_f ppm/°C**
Divalent oxides	BaO	0.8 to 3
	SrO	1.5 to 2.9
	MgO	2 to 6.2
Trivalent oxides	CeO_2	1 to 4
	Nd_2O_3	-2 to –3.2
	Sm_2O_3	-1 to 4
Pentavalent oxides	Ta_2O_5	-1.5 to -2.8
	Nb_2O_5	-1 to –4.2
	V_2O_5	-3 to -5
Glass additives	B_2O_3	-1 to -4
	$ZnO-B_2O_3$	2 to –5.4
	$5ZnO-2B_2O_3$	1 to 3

Table 4.7.3.I: τ_f values of ZST ceramics sintered with various additives.

	Name of the additive	Wt% of the additive	Sintering temperature (°C)	Sintering duration (hours)	Density (%)	Average grain size (μm)	ε_r	Qxf$_o$
Divalent oxides	BaO	0.5	1300	4	97.1±0.3	19	38.2±0.1	60300±1000
	SrO	0.5	1350	3	96.8±0.3	20	37±0.1	54250±1000
	MgO	0.5	1400	4	95.4±0.3	9	36.9±0.1	38850±1000
Trivalent oxides	CeO_2	1.5	1400	3	97.3±0.3	14	38.3±0.1	57500±1000
	Nd_2O_3	0.5	1400	3	97.2±0.3	18	40±0.1	59300±1000
	Sm_2O_3	1.0	1400	2.5	96.6±0.3	16	39.3±0.1	63850±1000
Pentavalent oxides	Ta_2O_5	1.0	1400	2	96.3±0.3	14	38±0.1	63170±1000
	Nb_2O_5	0.5	1350	4	96.4±0.3	10	38.7±0.1	56740±1000
	V_2O_5	0.5	1300	4	96.8±0.3	8.5	37.7±0.1	54790±1000
Glass additives	B_2O_3	0.2	1150	3	98.8±0.3	12	38.7±0.1	61550±1000
	$ZnO-B_2O_3$	0.2	1200	3	98.7±0.3	9.5	38.2±0.1	48500±1000
	$5ZnO-2B_2O_3$	0.2	1250	3	98.9±0.3	11	39.1±0.1	51955±1000

Table 4.7. I: Optimized conditions for each of the additives which gave best microwave dielectric properties.

The results of the most densified case with each additive are tabulated in table 4.7.I. Their sintering conditions, densities, dielectric constant Qxf_o value and average grain size are also listed.

Conclusions:

- The systematic study of ZST ceramics with different type and amount of additives has been studied and in each case their densification dependence on sintering conditions studied
- All the crystalline additives did not cause any secondary phases up to 1.5wt% of the additive concentration. In the case of glass additives, it is the case up to 1wt%. In most of the cases samples added with smaller concentration of the additives gave better density, uniform grain size and good microwave dielectric properties.
- The microstructures of the ZST ceramics are getting modified with the addition of these additives. It is observed that the nature of the additive and its concentration played an important role on the sintering temperature and duration to get maximum density.
- With the addition of all these additives it was found that there is not much change in the dielectric constant and temperature coefficient of the resonant frequency, where as the quality factor is significantly affected.
- The dielectric constant and Qxf_o values as a function of wt% of the additives followed a similar trend as that of density Vs additive concentration, for each of the additives.
- The increase in quality factor is primarily attributed to the increase in uniform grain size, reduction in porosity (improvement in density) and the reduction in oxygen vacancies.
- It is also observed that irrespective of the additive and its processing conditions the samples with higher densities exhibited higher uniform grain sizes, which play an important role in achieving best microwave dielectric properties in ZST ceramics.

References:

[1] S.Hirano, T.Hayashi and A.Hattori, J.Am.Ceram.Soc., **74**, 1320 (1991).

[2] D.Chen, X.Jiao and M.Zhang, Mater.Res.Bull., **35**, 2101 (2000).

[3] Z.X.Xiong, J.R.Huang, C.Fang and Z.Y.Pan, J.Euro.Ceram.Soc., **23**, 2515 (2003).

[4] R.Kudesia, A.E.McHale and R.L Snyder, J.Am.Ceram.Soc., 77, 3215 (1994).

[5] K.R.Han and J.W.Jang, J.Korea.Ceram.Soc., **81**, 1293 (1994).

[6] K.R.Han, J.W.Jang and S.Y.Cho, J.Am.Ceram.Soc., **81**, 1209 (1998).

[7] J.H. Jean, S.C.Lin, Low fire dielectric composition and its use in laminated microwave dielectric ceramic elements, US Pat. No 5872071 (1999).

[8] J.H. Jean and S.C.Lin, J.Am.Ceram.Soc., **83**, 1417 (2000).

[9] C.L Huang and M.H.Weng, Mater.Res.Bull., **35**, 1881 (2000).

[10] C.L Huang, M.H.Weng, C.C.Wu and C.C.Wei, Jpn.J.Appl.Phys., **40**, 698 (2001).

[11] C.L Huang, M.H.Weng and H.L.Chen, Mater.Chem.Phys., **71**, 17 (2001).

[12] D.Houviet, Jaafar El Fallah, B.Lamagnere and J.M.Haussonne, J.Euro.Ceram.Soc., **21**, 1727 (2001).

[13] A.Ioachim and M.I.Toacsan, J.Opto.Ele.and advanced materials, **5**,1395 (2003).

[14] H.Sreemoolanadhan, R.Ratheesh, M.T.Sebstian N.Rodrigues and J.Phillip, J.Phys D: Appl.Phys., **30**, 1809 (1997).

[15] R.Zou, L.Li and Z.Gui, Ceramics International, **26**, 673 (2000).

[16] N.Setter, and R.Waser, Acta Material, **48**, 151 (2000).

[17] W.C.Tzou, C.F.yang, Y.C.Chen and P.S.Cheng, J.Euro.Ceram.Soc., **20**, 991 (2000).

[18] C.L.Huang, and M.H.Weng, Mater.Lett., **43**, 32 (2000).

[19] T.Takada, S.F.Wang, S.yoshikawa, S.J.Jang and R.E.Newnham, J.Am.Ceram.Soc., 77, 1909 (1994).

[20] T.Takada, S.F.Wang, S.Yoshikawa, S.J.Jang and R.E.Newnham, J.Am.Ceram.Soc., **77**, 2485 (1994).

[21] K.Wakino, K.Minai and H.Tamura, J.Am.Ceram.Soc., **67**, 278 (1984)

[22] D.J.Kim, J.W.Hahn, G.P.Han, S.S.Lee, T.G.Choy, J.Am.Ceram.Soc., **83**, 1010 (2000).

[23] M.D.Iddles, A. Bell, and A.J.Moulson, J.Mater.Sci., **27**, 6303 (1992).

[24] K.H Yoon, and E.S.Kim, Mater.Res.Bull., **30**, 813 (1995).

[25] K.H Yoon, Y.S.Kim and E.S.Kim, J.Mater.Res., **10**, 2085 (1995).

[26] C.L.Huang, and M.H.Weng, Mater.Res.Bull., **35**, 1881 (2000).

[27] Z.Yue, J.Zhou, H.Zhang, Z.Gui and L.Li, J.Mater.Sci.Lett., **19**, 213 (2000).

[28] R.D.Shannon and C.T.Prewitt, Acta Crystallogr., **B25**, 925 (1969).

[29] S.X.Zhang, J.B.Li, H.Z.Zhai and J.H.Dai, Ceramics International **28**, 407 (2002).

[30] "Powder glass, glass paste" in Asahi Glass company Catalog, Tokyo, Japan (1990).

[31] E.Schlomann, Phys.Rev A. **135**, 413 (1964).

[32] W.S.Kim, T.H.Hong, E.S.Kim and K.H.Yoon, Jpn.J.Appl.Phys., **37**, 5367 (1998).

[33] B.D.Silverman, Phys.Rev., **125**, 1921 (1962).

[34] K.H. Yoon, Y.S.Kim and E.S.Kim, J.Mater.Res., **10**, 2085 (1995).

[35] N.Santha, M.T.Sebastian, P.Mohanan, S.Kamba, J.Petzeelt, N.M.Alford, R.C.Pullar and V.Sharma, J.Am.Ceram.Soc., **87**, 1233 (2004).

Chapter-5

Preparation, Structure and Morphology of Films in the $(Zr,Sn)TiO_4$ System

5.1 Literature review and experimental details of the systems:

5.1.1 Literature review of thin film TiO_2

Several methods have been used to prepare TiO_2 films but in the present study the brief literature review is focused only on the deposition of TiO_2 films using sputtering.

Titanium Oxide has been one of the extensively studied oxides because of its remarkable properties. TiO_2 films have good durability and high refractive index. Hence they are suitable for applications such as antireflection coatings, interference coatings and optical wave-guides. TiO_2 films have also attracted attention for use in fabrication of capacitors in microelectronics due to their relatively high dielectric constants. Anatase TiO_2 has been found to exhibit interesting properties, which makes it a promising material for gas sensors and solar cells. TiO_2 exists in three crystalline phases: Rutile and Anatase in tetragonal structure and Brookite in orthorhombic structure.

Suhail et al [1] have reported the structural and optical properties of TiO_2 by DC magnetron sputtering. They found that the as deposited films were amorphous. The crystallinity of the films was found above 300°C during deposition or by post deposition annealing. The crystalline films were found to have both anatase and rutile phases coexisting up to 600°C, above which anatase phase was found to be dominated. They found that the refractive index (2.24-2.46) and extinction coefficient (2.6×10^{-3} to 10.4×10^{-3}) increase with increase in deposition temperature along with the packing density and homogeneity of the films. Marius et al [2] reported the structural and dielectric properties of TiO_2 films deposited by DC magnetron sputtering technique and found that the as deposited films were amorphous and the crystalline peaks of anatase phase were found when films were annealed above 500°C. The dielectric constant of the films increased with increase in thickness up to 300nm and thereafter started decreasing (i.e. at 300nm, ε_r=70 and at 600nm ε_r=50 at 100 KHz)

Takahashi et al [3] observed partially crystalline films by varying the distance between target and substrate and as well as by variation of working pressure. They found that the films deposited at smaller distance between the target to the substrate distance and lower working gas pressure showed better crystallinity. They also reported that the surface roughness of the as deposited films increased with an increase in plasma exposure and decrease in working pressure. DeLoach et al [4] studied the variation in crystallinity of the RF sputtered films with increase in annealing temperature and the films were annealed in the temepratture range of 700-1000°C. The variation in the bandgap values was attributed to the variation in crystalline phase. Ya-Qi et al [5] reported crystallinity in films annealed between 300-1100°C. They found that the films annealed between 500-700°C showed only anatase phase where as the films annealed between 900-1100°C exhibited only rutile phase. Mardare et al [6] observed that the-as deposited films were amorphous. The structure changes to a mixed one of 70% anatase and 30% rutile phases after annealing. The optical properties of TiO_2 films measured by them, using ellipsometric method, gave refractive index (2.26) and extinction coefficient (0.035) higher values after annealing due to increase in crystallinity and increase in the packing density. Zhang et al [7] reported the photocatalysis of TiO_2 films with the variation in argon flow rate by DC magnetron sputtering. The films were deposited for 5 hours and the substrate temperature was raised to 130°C during deposition. It was found that with increase in argon percentage in the sputtering environment the photocatalytic activity of the films enhanced due to the generation of electrons and holes [7]. Takamura et al [8] studied the structural properties of RF sputtered TiO_2 films with the variation in oxygen percentage in the sputtering environment and found that the films were amorphous irrespective of oxygen percentage in the sputtering environment. Barnes et al [9] reported the ambient temperature growth of TiO_2 films using DC magnetron sputtering with the variation in power (200-800W), the substrate to target distance and with the variation of working pressures. They found that the films showed better crystallinity for the films deposited at 30mm of substrate to target distance and at 0.27Pa pressure with 200W of power. Amor et al [10] reported the structural and optical properties of TiO_2 films using RF magnetron sputtering. They observed that the as-deposited films were amorphous and started crystallizing above 350°C of post deposition annealing. The packing density of the films increased with increase in RF power and at lower working pressures. The refractive index and the extinction

coefficient of the films increased with increase in annealing temperature whereas the bandgap of the films was decreased.

Tachibana et al [11] reported that it is possible to prepare films by reactive DC magnetron sputtering starting from partially oxidized and conducting TiO_{2-x} targets. They found that transparent TiO_2 films were obtained with about 8 times higher deposition rate efficiency, by using TiO_{2-x} sputter method, than that of the conventional reactive sputtering from Ti target. This high deposition-rate efficiency is due to the metallic surface state of the TiO_{2-x} target during sputtering. H.Tomaszewski et al [12] deposited the TiO_2 films from a ceramic target using DC magnetron sputtering in the presence of $Ar+O_2$ environment. They found that nearly stoichiometric films can be obtained with small amount of oxygen in the sputtering environment and the as deposited films were amorphous. Asanuma et al [13] reported the deposition of TiO_2 films in pure oxygen atmosphere using RF magnetron sputtering. They found that the films deposited at 200W with 4 Pa pressure showed strong rutile phase and above that only anatase phase was observed whereas below 4Pa the films were amorphous.

5.1.2 Literature review of thin film ZrO_2

Zirconia with its wide range of properties is a very important candidate material for a number of technological applications. It has been used in tribological applications, as thermal barrier coatings, as buffer layer for superconducting coatings and as a high-k gate oxide apart from its use in optical thin film devices. It exhibits polymorphism: it exists in the monoclinic phase at room temperature, transform to the tetragonal phase at 1200°C and finally to the cubic phase at 2200°C.

ZrO_2 films have been prepared through various methods but here we give a brief review of ZrO_2 films deposited by sputtering. Suhail et al [14] deposited ZrO_2 films using DC reactive magnetron sputtering technique and studied their structural and optical properties. They have observed that the as deposited films were amorphous and the films were crystallized at 400°C. Both the monoclinic and tetragonal phases were present and with increase in temperature above 700°C the tetragonal phase intensity started decreasing. The refractive index (1.71-1.93) and extinction coefficient ($2.5x10^{-3}$ to $0.5 x10^{-3}$) increased with increase in temperature.

Amor et al [15] deposited the ZrO_2 films using RF magnetron sputtering from ZrO_2 target. They found that the films deposited in the pure argon presence exhibited

cubic phase where as the films deposited in reactive plasma showed monoclinic phase. The crystallinity of the films increases with increase in RF power when O_2% and total pressure decreases. The FTIR spectra show excess of oxygen detected in the films exhibiting columnar structure results from the incorporation of water and hydroxyl groups. The refractive index has decreased with increase in thickness of the film, increase in total sputtering pressure, O_2% and decrease in RF power.

Gao et al [16] deposited ZrO_2 films using RF sputtering at different O_2 concentrations. It was observed that the monoclinic phase is the dominant phase in the films and there is a small fraction of tetragonal phase in the films deposited at lower working pressures. The roughness and extinction coefficient of the films increased with increase in O_2% where as the refractive index was decreased.

Jeong et al [17] reported the yttrium stabilized zirconia (YSZ) and ZrO_2 films deposited by RF sputtering in the argon atmosphere and studied their electrical and dielectric properties. They found that in both the cases the as deposited films were amorphous and did not show crystallization below 800°C of annealing. The leakage current decreased with decrease in substrate to target distance and increase in RF power (leakage current density=10^{-10} A/cm^2 *at* 1Volt) and the dielectric constant of amorphous YSZ films was 24 at 1MHz.

Goedicke et al [18] reported the ambient temperature growth of ZrO_2 films deposited by pulsed magnetron sputtering. They found that the films deposited at lower (0.3Pa) working pressures exhibited monoclinic phase where as the films deposited at higher working pressures (3.5Pa) showed cubic phase. The roughness of the films increased with increase in sputtering pressure where as the refractive index of the films decreased (2.2-2.1). Collared at al [19] reported the stabilization of cubic phase at ambient temperatures with nitrogen and oxygen as reactive gases using DC magnetron sputtering. Venkataraj et al [20] reported the ambient temperature growth of ZrO_2 films deposited by DC reactive magnetron sputtering. They observed that as deposited films were in monoclinic phase and even after annealing at 900°C monoclinic phase still presented and no mixed phases were present. It was reported that the refractive index of the films decreased with increasing annealing temperature where as the bandgap increased and was attributed to the intermixing of Si with ZrO_2 and increase in the surface roughness of the films. Wong et al [21] deposited ZrO_x films in the presence of Ar and with different O_2% gas mixtures using pulsed DC magnetron sputtering. They observed that the films deposited with the oxygen

pressure of 0.18mTorr and above the films exhibited monoclinic (ZrO_2) phase and below this pressure the composition of the film was ZrO.

Hembram et al [22] reported the electrical and structural properties of ZrO_2 films deposited by DC magnetron sputtering and they observed that the as deposited films were amorphous. After annealing at 600°C both the monoclinic and tetragonal phases were observed whereas the films annealed at 700°C showed only monoclinic phase. For the films annealed at 800°C, again both the tetragonal and monoclinic phases were observed. It was found that the films annealed at 600°C showed higher bandgap. With increase in annealing temperature, the films showed lower transmittance due to oxygen deficiency.

Briois et al [23] investigated the YSZ coatings from metallic targets in various reactive argon-oxygen mixtures by DC magnetron sputtering. They observed that with increasing Y content, the purely cubic and cubic-tetragonal phases were observed. With smaller concentration of Y, monoclinic and tetragonal phases were observed.

Zhao et al [24] reported the thickness dependent structural properties of ZrO_2 films by mid frequency magnetron sputtering. The films were deposited at 270°C and observed that both the tetragonal and monoclinic phases are present with increasing thickness of the film.

5.1.3 Literature review of thin film $ZrTiO_4$

$ZrTiO_4$ (ZT) and Sn modified $ZrTiO_4$ (ZST) are among the most promising microwave dielectric materials and in bulk form they find applications in phase shifters, oscillators and filters. $(Zr,Sn)TiO_4$ is also identified for DRAM applications apart from their use in optical thin film devices.

Chang et al [25] reported the structural and optical properties of RF sputtered $ZrTiO_4$ films at different substrate temperatures, starting from $ZrTiO_4$ ceramic target. They found that the films deposited below 300°C of substrate temperature were amorphous in nature and started crystallizing at 400°C. The refractive index and extinction coefficient increased with increase in substrate temperature where as the bandgap decreased. Viticoli et al [26] deposited the $ZrTiO_4$ and ZST films using pulsed laser deposition technique at different substrate temperatures. It was observed that in both the cases films were partially crystallised at 450°C and the crystallinity of the films was increased with increase in substrate temperature. Single-phase crystalline $ZrTiO_4$ and ZST films with dense columnar structure exhibited $\varepsilon_r \sim 38$ and

$\tan\delta \approx 1 \times 10^{-4}$ at 1 MHz. Padeletti et al [27] reported the dielectric properties of the $ZrTiO_4$ films prepared by MOCVD technique. It was observed that an increase in temperature causes an increase in roughness and formation of close packed columnar structures and the films deposited on platinum coated substrate showed $\varepsilon_r \sim 40$ at 1MHz. Kim et al [28] deposited the $ZrTiO_4$ films using DC magnetron sputtering at different deposition temperatures and annealed at 800°C. They found that as the deposition temperature increases, the dielectric loss and strain in the deposited films decreased. The films deposited at higher temperature and post annealed at 800°C showed $\varepsilon_r \sim 35 \pm 7$ and $\tan\delta \approx 0.005\text{-}0.034$ at 100 KHz. Victor et al [29] reported the structural, electrical and dielectric properties of $ZrTiO_4$ films by pulsed laser deposition technique. They observed that the films grown at 300°C were amorphous where as the films grown at higher substrate temperatures (>500°C) were highly oriented along (020) direction. A higher dielectric constant and higher leakage current were observed for highly oriented films compared to polycrystalline films.

5.1.4 Literature review of thin film $(Zr_{0.8},Sn_{0.2})TiO_4$ (ZST)

Nakagawara et al [30] deposited ZST films by pulsed laser deposition and studied the effect of crystallinity on the electrical and microwave dielectric properties. The films were crystallined between 500-700°C and the dielectric constant of 27 and 38 were obtained for the amorphous and crystalline films respectively, measured at 1-10 GHz.

Huang et al [31] reported the structural, electrical and dielectric properties of ZST films at different substrate temperatures by RF magnetron sputtering. The ZST target was prepared with 1wt% ZnO as a sintering aid. $\varepsilon_r \sim 42$ and $\tan\delta \approx 0.065$ at 10 MHz and leakage current density of 2×10^{-7} A/cm^2 was observed for films that were deposited at 450°C. Cheng et al [32] deposited ZST thin films using RF magnetron sputtering and the electric and dielectric properties were reported. The films deposited at 300°C and annealed at 650°C were crystallized and dielectric constant of 36.5 and a $\tan\delta$ of 0.0062 were observed at 100 KHz along with a current density lower than 10^{-7} A/cm^2. Yang et al [33] prepared the ZST thin films by sol gel method. The films were heated at 250°C during deposition and annealed at 700°C and found that the roughness is higher when they are annealed at higher temperatures and decreased for lower annealing temperatures. The deposited ZST film had a low effective dielectric constant of 16 due to the formation of an interface layer. The leakage current density

of ZST film was lower than 5.1×10^{-8} A/cm^2 up to an applied electrical field of 1 mV/cm at the measured temperature 50 °C. The dominant conduction mechanism of the crystallized ZST film annealed at 700 °C was suggested as the Frenkel–Poole emission. Nistor et al [34] deposited thin films of ZST were deposited using a pulsed electron beam source based on a channel-spark discharge for target ablation. An advanced degree of crystallization was obtained for the films deposited on alumina substrate post-annealed at 1000°C. The crystalline lattice constants of the films are very close to those of the target material, which confirms the same stoichiometry in the films as in the bulk.

5.1.5 Objectives of the present study

From a literature survey, it is clear that even though the ZST thin films were prepared by different methods by a few authors, there are no reports on the deposition of ZST thin films from a complex target (optimized ratios of Zr, Sn and Ti metals in the same cathode) by DC magnetron sputtering. The ambient temperature crystallization of these films as well as their deposition in the pure oxygen plasma has not been reported so far. A number of processing parameters starting from the deposition of individual metal oxides up to the deposition of ZST films has to be optimized to achieve better structural, optical, morphological, electrical and dielectric properties. Though only few research groups have deposited ZST films, these research groups did not study the sub oxides of ZST films such as TiO_2, ZrO_2 and $ZrTiO_4$ films using the same technique. Due to the variations in all the processing parameters by different groups there is a wide variation in all the properties reported. To overcome this difficulty, we carried out a comprehensive investigation in which all the sub oxides of ZST were deposited under similar conditions to understand their growth kinetics. The objective of this study is to deposit ZST films from a complex target using DC reactive magnetron sputtering and study their structural, optical, morphological, electrical and dielectric properties and to investigate their feasibility in different applications such as optical, high-k gate oxides etc.

The present study reports the following:

- Ambient temperature crystallization of the films in the $(Zr,Sn)TiO_4$ system.
- Deposition of $(Zr,Sn)TiO_4$ films in the pure oxygen (100%) DC plasma atmosphere.

- Deposition of $ZrTiO_4$ films from Zr and Ti metal targets and $(Zr,Sn)TiO_4$ films from a single target using DC reactive magnetron sputtering.
- Study the structural, optical, morphological, electrical and dielectric (both at low and at microwave frequencies) properties of the components in the $(Zr,Sn)TiO_4$ system.

5.1.6 Experimental details

The aim of this study is to deposit and to understand the growth kinetics of the $(Zr_{0.8},Sn_{0.2})TiO_4$ (ZST) thin films from a single cathode from Zr,Sn and Ti metals using DC reactive magnetron sputtering. To grow ZST thin films from DC reactive magnetron sputtering from a single cathode, we need to understand the growth kinetics of the sub oxides of the (ZST) system because the threshold cathode potentials of the TiO_2 and ZrO_2 films are different. The depositition conditions of the sub-oxides of ZST systemTiO_2, ZrO_2 and $ZrTiO_4$ are tabulated in table 5.1.I.

The thin film depositions were carried out in a COOKE Vacuum system (USA), and the cathode was purchased from Advanced Process Technology Pvt.Ltd, Pune, India. High purity argon (99.999%) and oxygen (99.999%) have been used as the sputtering and reactive gas respectively. The discharge characteristics have been controlled using a variable DC power supply (1KV and 1A). Pure titanium (99.99%) disc of 48mm diameter and 3 mm thickness has been used as sputtering target. The sputtering chamber was evacuated to a base pressure $5x10^{-6}$ Torr before admitting the reactive gases in to the system. In each experiment the target was pre sputtered in argon atmosphere until the surface oxide layer is removed from the target. The removal of oxide is characterized by the sudden change in the discharge characteristics and the change in the discharge color to blue from a pale pink.

In the case of TiO_2 & ZrO_2, the distance between the substrate to target distance (D_{s-t}) is optimized at D_{s-t} of 3.5 cm. In the case of $ZrTiO_4$ and ZST films the conditions when optimized, the films exhibited best results at the D_{s-t} of 3cm and the details are discussed in the later sections.

Optimized deposition conditions for TiO_2 & ZrO_2 films:

Power density : 1.0-1.5 W/cm^2

Substrate to target distance (D_{s-t}): 3.5 cm

Working pressure : 0.1 mTorr

Substrate temperature : Ambient

Optimized deposition conditions for $ZrTiO_4$ and ZST films:

Power density : 1.0-1.5 W/cm^2

Substrate to target distance (D_{s-t}): 3 cm

Working pressure : 0.1 mTorr

Substrate temperature : Ambient

Table 5.1.I: Deposition conditions for the compositions TiO_2, ZrO_2, $ZrTiO_4$ and ZST.

5.1.7 I-V characteristics of the sputter process of films in the system (Zr,Sn)TiO_4:

The I-V characteristics of the TiO_2 films deposited at 0.1mTorr as a function of oxygen mixing percentage (OMP) and the films deposited at different working pressures in the pure oxygen plasma are shown in figure 5.1.7a and 5.1.7b respectively. For ZrO_2 the variation in cathode current as a function of applied cathode potential, for deposition at different working pressures in the pure oxygen plasma are shown in figure 5.1.7c and 5.1.7d respectively. Similarly for $ZrTiO_4$ the variation in cathode current as a function of applied cathode potential and at different working pressures in the pure oxygen plasma are plotted in figure 5.1.7e and 5.1.7f respectively.

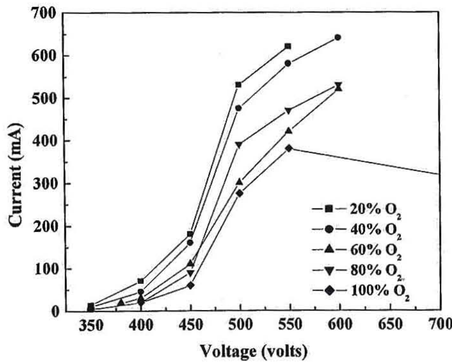

Figure 5.1.7a: I-V characteristics of the DC plasma for TiO_2 films at different OMPs.

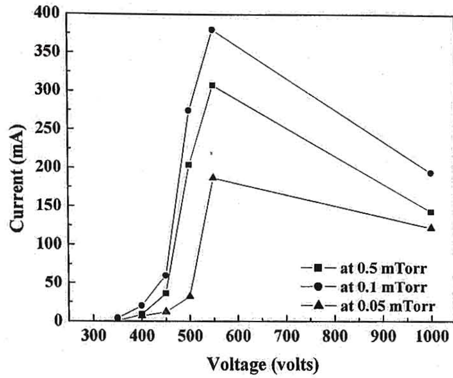

Figure 5.1.7b: I-V characteristics of the DC plasma for TiO_2 films deposited in pure oxygen plasma with different working pressures.

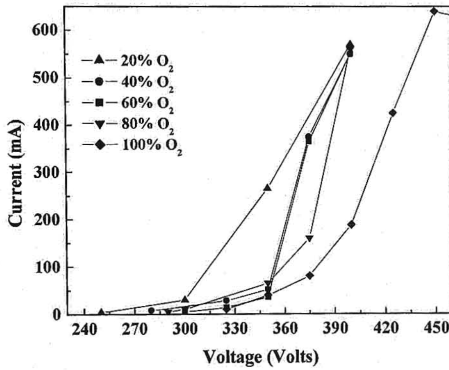

Figure 5.1.7c: I-V characteristics of the DC plasma for ZrO_2 films at different OMPs.

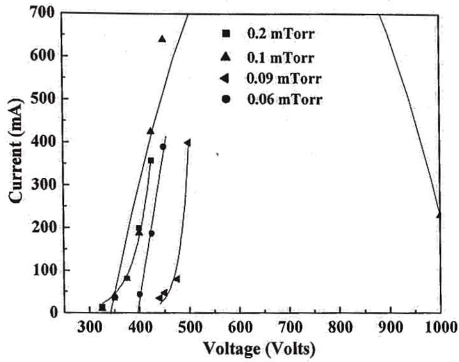

Figure 5.1.7d: I-V characteristics of the DC plasma for ZrO_2 films deposited in pure oxygen plasma with different working pressures.

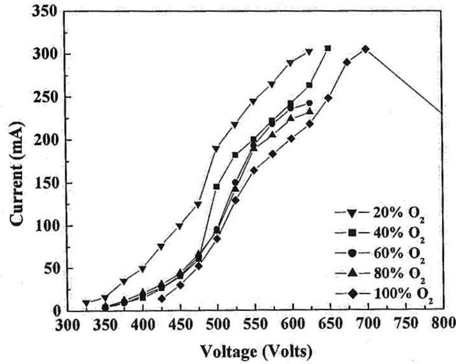

Figure 5.1.7e: I-V characteristics of the DC plasma for $ZrTiO_4$ films at different OMPs.

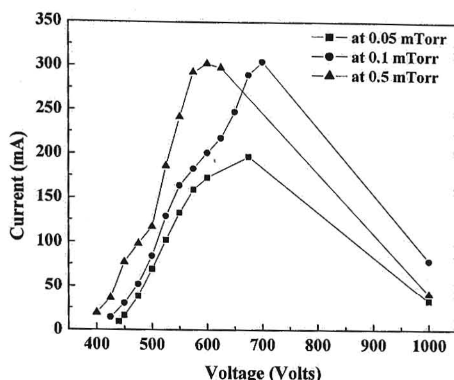

Figure 5.1.7f: I-V characteristics of the DC plasma for $ZrTiO_4$ films deposited in pure oxygen plasma with different working pressures.

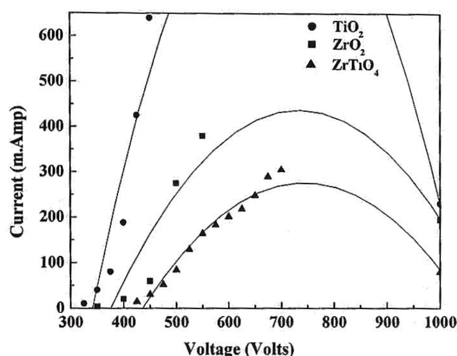

Figure 5.1.7g: Variation in cathode current as a function of cathode potential for the TiO_2, ZrO_2 and $ZrTiO_4$ films deposited at 0.1mTorr pressure in pure oxygen plasma.

In all the three cases it is observed that as the OMP increases, the threshold cathode potential also increases; also as the cathode potential increases the cathode current increases up to some critical cathode potential and after that, cathode current started decreasing. For the films deposited in pure oxygen plasma, as the working pressures increase (0.5, 0.1 & 0.05 mTorr) the cathode current increases up to 0.1 mTorr, and above that it starts decreasing. It is also found that the threshold cathode potential is lower at higher working pressures. In the case of films deposited in the pure oxygen plasma, initially cathode current increases with increase in cathode potential and then decreases with increase in cathode potential. The variation in

cathode current as a function of cathode potential for the TiO_2, ZrO_2 and $ZrTiO_4$ films deposited at 0.1mTorr in pure oxygen plasma is plotted in figure 5.1.7g. It is observed that the lower threshold cathode potential is for ZrO_2 and the $ZrTiO_4$ exhibited the highest, and in between comes that for TiO_2. The differences in the threshold cathode potentials can be attributed to the differences in the sputtering yields of the Ti and Zr. In all the cases it is observed that the I-V characteristics change drastically as the OMP increases. It has been reported [35] that the addition of even small quantity of oxygen causes an increase in ionization cathode current, as the pressure in the sputtering environment increased which resulted in higher cathode currents even at lower cathode potentials. These observations are in contrast to the generally observed behavior of I-V characteristics in oxygen and argon mixtures. Maniv and West wood [36] during reactive sputtering of Zn & ITO and Rizk et al [37] during reactive sputtering of copper, observed that the cathode potential required to achieve a particular cathode current decreased with the addition of oxygen. Rizk et al discussed I-V characteristics in an oxygen and argon mixture at 25% and 50% OMP. Though the cathode potential dropped at 25% OMP, the curve with 50% OMP showed very high potential. This behavior in the former case was attributed to the reduction in the drift velocity of electrons [38] but no explanation was offered for the later case.

The potential required for achieving 100mA cathode current as a function of OMP is plotted in figure 5.1.7h. In all the cases it is observed that as the OMP increases up to 40%, the cathode potential increases, while from 40-80% of OMP it is almost constant and at 100% of OMP the cathode potential again started increasing. The cathode potentials are higher for $ZrTiO_4$ and lower for ZrO_2, but TiO_2 falls between them. In the present case, the model proposed by Rao et al [39] can explain these results where the cathode potential required to achieve a particular current is plotted as a function of OMP. The figure represents the process in three stages. In the first stage (region I) the cathode potential increases beyond a certain critical OMP; it is constant in the second stage (region II) and in the third stage (region III) it again starts increasing. In the present study a similar trend is observed in all the three cases, which is shown in figure 5.1.7h.

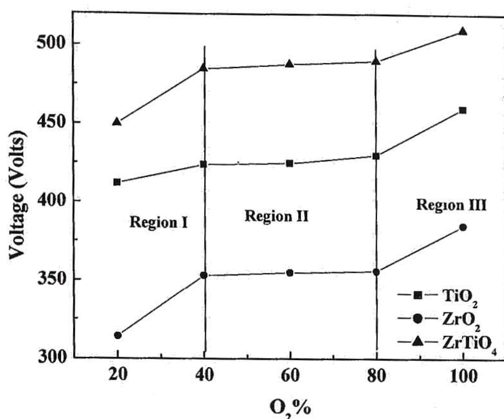

Figure 5.1.7h: The potential required for achieving 100mA cathode current as a function of OMP for TiO_2, ZrO_2 and $ZrTiO_4$ films deposited at 0.1mTorr in the pure oxygen plasma.

The increase in the first stage can be attributed to the negative ion formation [35-37, 40] during which some of the secondary electrons emitted by the cathode get attached to the oxygen atoms and hence depletion in the number of electrons takes place. This results in the higher cathode potentials to achieve the required cathode current, which is essentially positive argon ion current. In the second region the target poisoning starts and hence oxide layer building takes place up on the target surface. Since the oxide has the higher secondary electron emission [41] than its corresponding metal, both the total number of electrons as well as the ionization increases, resulting in a drop in the cathode potential. Incidentally, this drop in the deposition rate is because of the lower sputtering yield of the oxide. In all the three cases it is also observed that as the OMP increases in the sputtering environment, then reduction in rate of deposition takes place, which consequently results in a reduction in the thickness of the film takes place. This is discussed later. These results support the argument that the target poisoning starts taking place only when the reactive gas content exceeds the sputtered metal content near the cathode [40]. As the OMP increases in the sputtering environment, the oxide layer thickness on the target increases and results in a decrease in the conductivity of the target. The need for higher cathode potentials for breaking this insulating barrier is obvious (i.e. region III). Under these conditions the survival of glow discharge becomes difficult. Howson

et al [42] reported the observation of pressure instability in reactive magnetron sputtering.

The variation in rate of deposition of the components in the system (ZST) as a function of OMP is plotted in figure 5.1.7i. The rate of depositions of the TiO_2, ZrO_2, $ZrTiO_4$ and ZST films are found to be 3.9-6.3, 10.2-15.1, 5.9-10.4 and 3.1-5.7 nm/ min respectively. In all the cases it is observed that as the OMP increases in the sputtering environment, the rate of deposition decreases. The ZrO_2 films showed higher rate of depositions where as ZST films showed lowest, and the $ZrTiO_4$ exhibited higher rate of deposition compared to TiO_2. The differences in the rate of depositions can be attributed to the differences in the sputtering yields of Ti and Zr. In the case of ZST, films were deposited at a lower rate of deposition to avoid Sn metal melting because the Sn metal has a lower melting temperature. The reduction in rate of deposition with increase in OMP can be attributed to the target poisoning and hence to the oxide layer building up on the target surface.

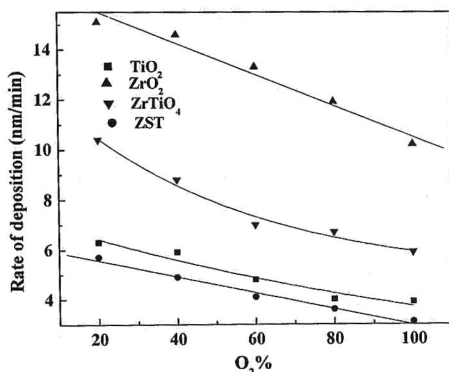

Figure 5.1.7i: Rate of deposition of the components in system (ZST) as a function of OMP

However for the first time this study demonstrated growth of TiO_2, ZrO_2, $ZrTiO_4$ and ZST films in pure oxygen plasma using DC reactive magnetron sputtering, which has not been reported earlier. It is interesting to know the variations in the rate of deposition as a function of substrate to target distance (D_{s-t}) in the pure oxygen plasma, which is not studied so far. So in the present study the variations in the rate of deposition of TiO_2 films in pure oxygen plasma are studied. Another objective was to see whether the sputtering took place with variations in working

pressure and D_{s-t}. The variation in rate of deposition as a function of D_{s-t} and the working oxygen pressure for TiO_2 films are plotted in figure 5.1.7j & k respectively. It is found that films deposited at lower working oxygen pressures showed higher rate of deposition and as the oxygen working pressure increases from 0.05-0.5 mTorr the rate of deposition decreased.

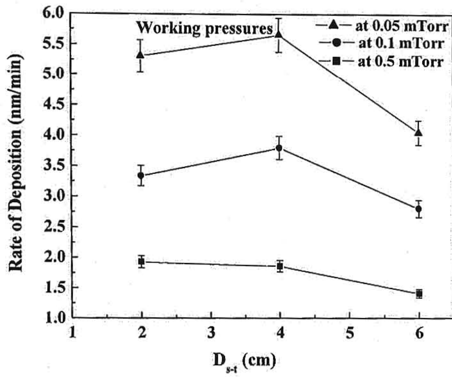

Figure 5.1.7j: Variation in rate of deposition of TiO_2 films as a function of D_{s-t} in pure oxygen plasma.

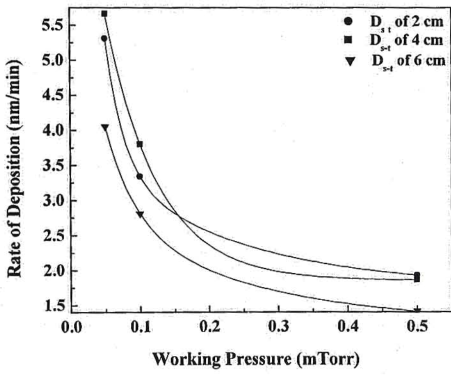

Figure 5.1.7k: Variation in rate of deposition of TiO_2 films as a function of working pressure, in pure oxygen plasma.

It is also observed that the rate of deposition increased with increase in D_{s-t} up to 4cm and above that it started decreasing. As the oxygen content in the plasma increases, the target surface becomes more oxidized and more negative oxygen ions will be produced in the plasma. The addition of oxygen in the sputtering environment

results in a decrease of the deposition rate due to the oxidation of the target surface, and also at higher OMP in the plasma, negative oxygen ion bombardment will preferentially sputter the oxygen atoms from the deposited layer. Significantly, however, the rate of deposition does not fall to zero at any pressure. At a D_{s-t} value of 6cms and a pressure of 0.05 mTorr, the rate of deposition is still of the order of 1 nm/min.

Structure and microstructure of the films in the system $(Zr,Sn)TiO_4$

5.2 Structure and morphology of TiO_2 films:

Titania thin films were deposited on glass and platinized silicon substrates as a function of OMP by DC reactive magnetron sputtering. The deposition of titania films in pure oxygen atmosphere was demonstrated for the first time.

The XRD patterns of the TiO_2 films deposited on glass, and on platinized silicon at the D_{s-t} of 3.5cm for different OMP are shown in figures 5.2.1a, b & c respectively. It is observed that the as deposited films got crystallized, but films below a thickness of 150nm did not show any evidence of crystallinity. It is interesting to note that as the OMP increases in the sputtering atmosphere, up to 30% of OMP only anatase phase is observed, and as the OMP increased further from 40% to 100%, both anatase and rutile phases are observed. It is also observed that as the OMP increases, the weight fraction of the rutile phase has increased.

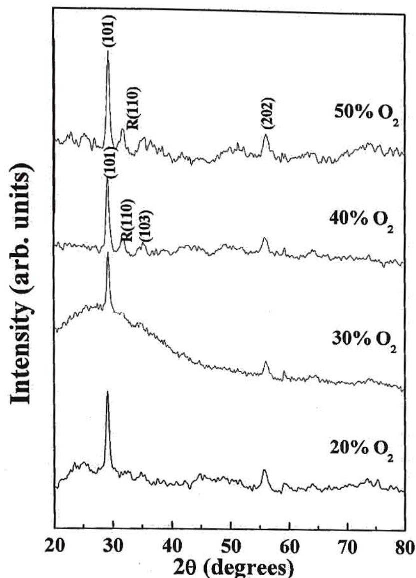

Figure 5.2.1a

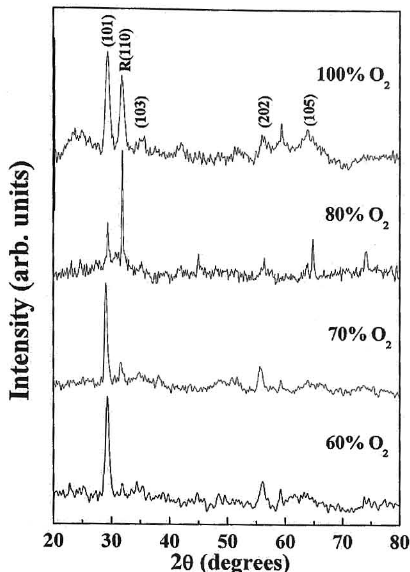

Figure 5.2.1b

Figure 5.2.1a & b: XRD patterns of TiO_2 films deposited on glass with different OMPs.

The weight ratios of anatase and rutile phases in their mixed phases are qualitatively analyzed using the following equation [13].

$$W_{an}= [1/\{1+1.265\ (I_{ru}/I_{an})\}]\ x100 \qquad (5.2.1.1)$$

where, W_{an}, I_{ru} and I_{an} denote the weight fraction of the anatase phase, the intensities of the strongest anatase and rutile reflections respectively. The intensities of (101) anatase peak and (110) rutile peak are taken. The weight fractions of the rutile and anatase phase are tabulated in table 5.2.I the rutile phase ranged between 35.4-67.7%.

	OMP					
Phase	40%	50%	60%	70%	80%	100%
Anatase	64.57	63.21	61.41	54.27	49.28	32.41
Rutile	35.43	36.8	38.6	45.73	50.72	67.69

Table 5.2.I: Weight fractions of the anatase and rutile phases calculatrd from XRD.

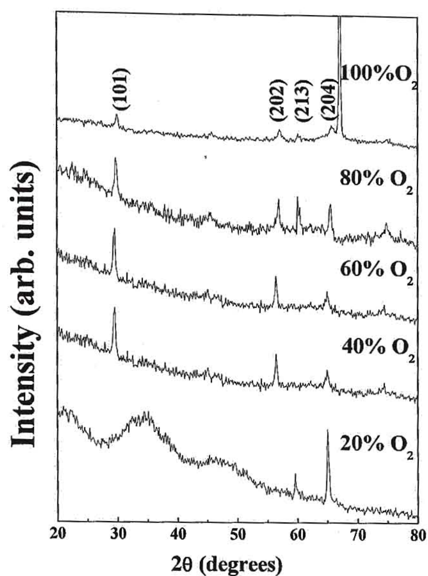

Figure 5.2.1c: XRD patterns of TiO_2 films deposited on platinized silicon with different OMPs.

The X-ray diffraction patterns of TiO_2 films deposited in the pure oxygen atmosphere at different D_{s-t} of 2, 4 & 6cms on glass at different working pressures are shown in figures 5.2.2a, 2b and 2c respectively. It is observed that as the D_{s-t} increases from 2cm to 4cm, the crystallinity of the films increases, and above that (at 6cms) it started decreasing, and also as the working pressure decreases from 0.5 mTorr to 0.05 mTorr the crystallinity of the films increased.

It is also interesting to note that the films deposited at 2cms are grown in the (200) direction. The films deposited at D_{s-t} of 4cms showed better crystallinity compared to other films deposited either at D_{s-t} of 2 or 6cms. Films deposited at D_{s-t} of 4cm on fused silica and silicon at different working pressures is shown in figure 5.2.2 d & e respectively.

Films deposited at 0.5 mTorr did not show any diffraction peak, indicating amorphous state or the presence of very small crystallites. As the working pressure decreases from 0.5 to 0.1 mTorr, appearance of the anatase (101) peak is observed.

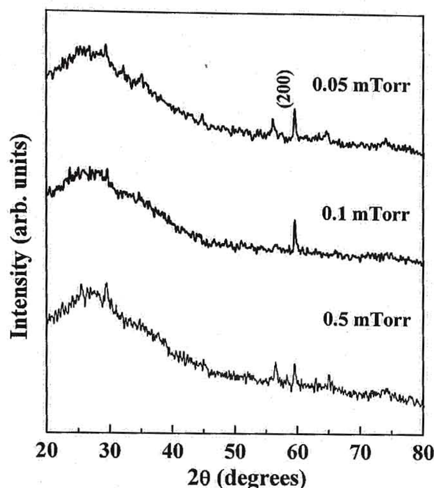

Figure 5.2.2a: XRD patterns of the TiO_2 films deposited at different oxygen working pressures at D_{s-t} of 2cms.

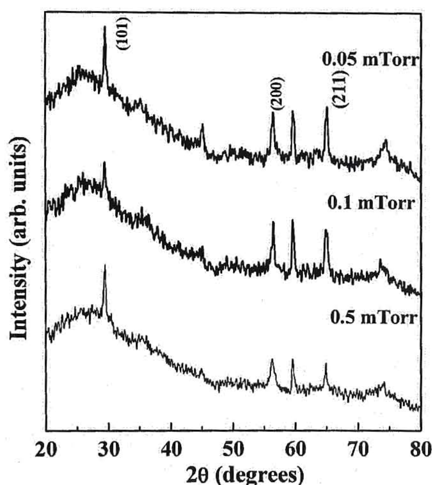

Figure 5.2.2b: XRD patterns of the TiO_2 films deposited at different oxygen working pressures at D_{s-t} of 4cms.

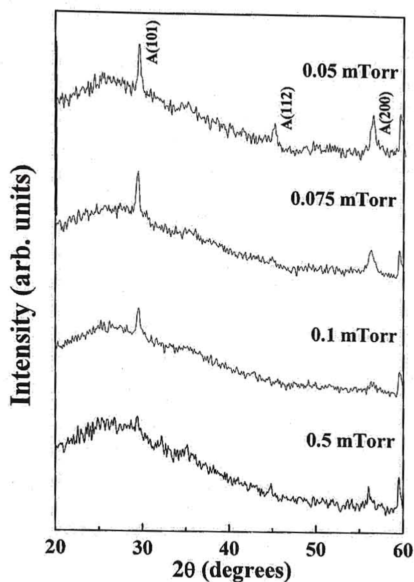

Figure 5.2.2c: XRD patterns of the TiO_2 films deposited at different oxygen working pressures at D_{s-t} of 6cms.

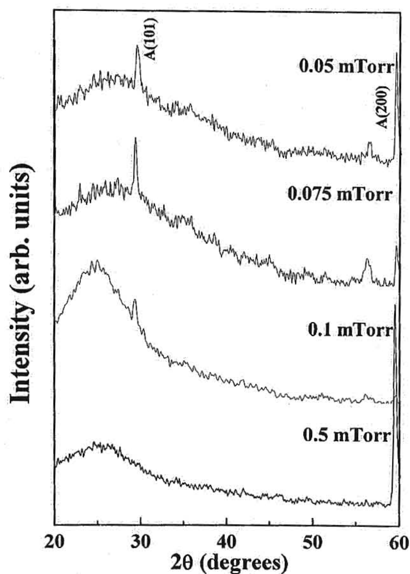

Figure 5.2.2d: Films deposited on fused silica at D_{s-t} of 4cm and at different working pressures.

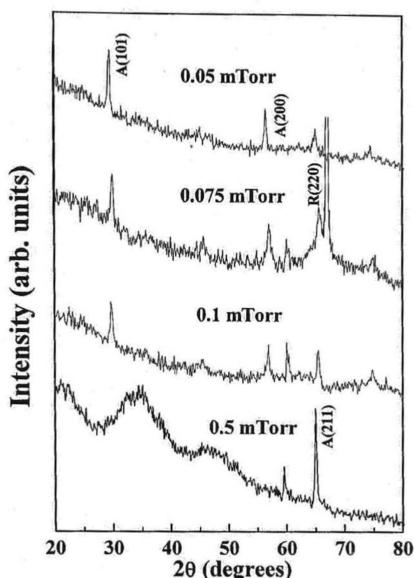

Figure 5.2.2e: Films deposited on silicon at D_{s-t} of 4cm and at different working pressures.

Further decrease in oxygen partial pressure from 0.1 to 0.075 and 0.05 mTorr resulted in the appearance of an additional anatase (200) peak. Significantly the films deposited at 0.075 mTorr on silicon showed a strong rutile (R) peak (220) at a D_{s-t} of 4 and 6cms. Anatase (A) (101) has the lowest surface energy and tends to grow preferentially [43] and the (200) plane can arise due to the channeling effect caused by the particle bombardment [44]. So, the film formed might exhibit growth competition between A (101) and R (220) orientation.

To calculate the weight fractions in this case, intensities of (101) anatase peak and (220) rutile peak are taken. It is found that W_{an} increased with increase in D_{s-t} from 4 to 6 cms. The weight fractions of the anatase phase are 11.7% and 69.4% at 4 and 6cms respectively. The presence of rutile phase appeared at 0.075mTorr deposited at D_{s-t} of 4 and 6cms; this can be attributed to the interaction between the positive ions accelerated from the plasma and the atoms on the substrate surface. Diffusion of the incident particles and the relaxation of the surface are also expected to be enhanced by the collision between the impacting ions and substrate atoms. The film deposited at a D_{s-t} of 2cms did not show any rutile peak which shows that apart

from working pressure, D_{s-t} also plays an important role in determination of the structure of the deposited films. The appearance of a mixed phase is not due to the phase transition from anatase to rutile but due to the growth competition that takes place between the two phases during the deposition process itself. The crystalline nucleation at low temperatures is probably governed by the kinetic energy of particle impinging on the surface of the growing film [13].

There are very few reports on the ambient temperature crystallization of titania thin films by DC magnetron sputtering although crystallization as a result of *in situ* heating and post-deposition annealing is very frequently reported for sputtered films. For example, Springer and Marius have reported crystalline TiO_2 films by heating at high temperatures during deposition [45,2]. Takahashi et al. observed partially crystalline films by varying the distance between target and substrate [3]. Aita et al. reported crystalline films after annealing at 700-1000^{0}C [4] and Ya-Qi et al. reported crystallinity in films annealed between 300-1100^{0}C [5]. Mardare et al. reported that as deposited films are amorphous and crystallized after annealing [6]. Zhang et al. also reported the partially crystalline TiO_2 films heated at 120^{0}C during deposition [7].

The crystallite sizes as estimated from the full width at half maximum (FWHM) for the A(101) peak was in the range of 25-50nm for the films deposited on glass and 23-35nm for the films on platinized silicon.

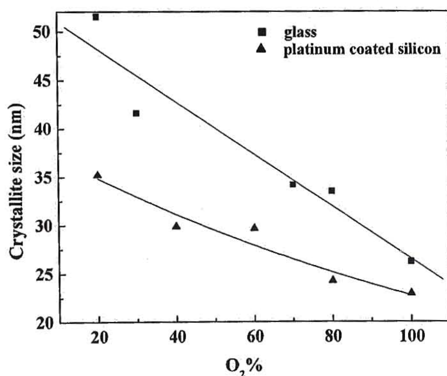

Figure 5.2.3a: Variation in crystallite size as a function of OMP for the films deposited on glass and on platinized silicon.

The variation in crystallite size as a function of OMP for the films deposited on glass and on platinized silicon is shown in figure 5.2.3a. It is also found that the

crystallite size decreases with increasing sputtering chamber pressure but at the same time it is independent of input power.

It is found that the films deposited on platinized silicon exhibited lower crystallite sizes compared to the films deposited on glass. It is also observed that the crystallite size decreases with increase in thickness of the film as shown in figure 5.2.3b.

To isolate the effects of thickness and rate of deposition, the crystallite size was plotted as a function of rate of deposition at 20% OMP. It is evident from figure 5.2.3c that the rate of deposition has a more profound effect on the crystallite size, exhibiting almost an exponential decrease with increase in rate of deposition. In other words, at a constant total pressure, the crystallite size decreases with increase in the thickness, rate of deposition as well as OMP.

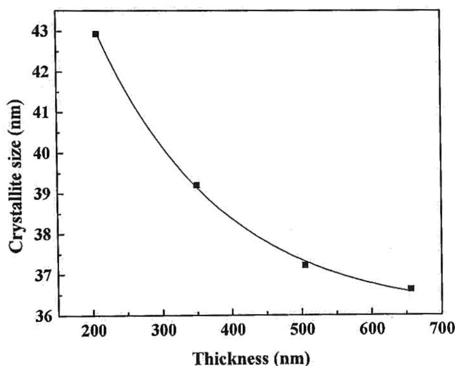

Figure 5.2.3b: Variation in crystallite size as a function of thickness of the films deposited on glass.

These results indicate that densification and crystallization are inter-related processes. Recent work on DC magnetron sputtered titania films starting from a Ti target has invoked the theory of charged clusters to explain the crystallization of titania thin films at ambient temperatures [9]. The grain sizes reported in that work are of the order of 2-3 nm which is substantially lower than those observed in the current study.

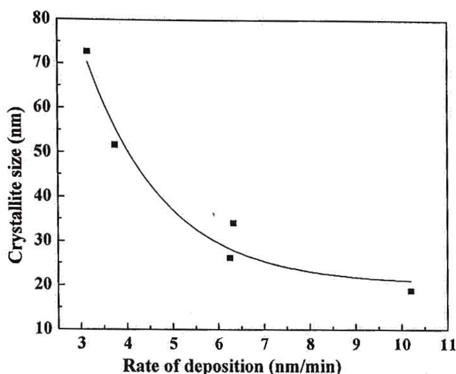

Figure 5.2.3c: Variation in crystallite size as a function of rate of deposition of the films deposited on glass.

The variation in crystallite sizes of the films deposited in pure oxygen atmosphere at different working oxygen pressures as a function of D_{s-t} is shown in figure 5.2.4. In all the cases the crystallite size is maximum at D_{s-t} of 4cm; above and below that it decreased. It is found that films deposited at 0.05 mTorr have showed the highest crystallite size at D_{s-t} of 4cm. The small crystallite sizes at a lower D_{s-t} of 2 cm may be due to the decrease in mean free path of the sputtered particles that lowers the rate of deposition, while the reduction in rate of deposition at higher D_{s-t} of 6cm is due to the reduction in the number of atoms that reach the substrate. The crystallite sizes ranged between 16-24, 35-45 and 21-31.6 for the films deposited at the D_{s-t} of 2, 4 and 6cms respectively.

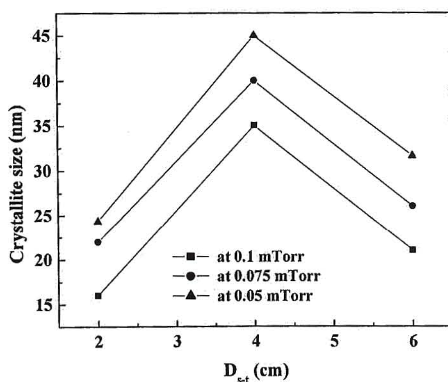

Figure 5.2.4: Variation in crystallite size as a function of D_{s-t} for the films deposited at different working pressures in pure oxygen plasma.

The Dynamic Force Microscope (DFM) images of the films deposited in 20% O_2 shown in figure 5.2.5a indicate that these crystallites aggregate in to large triangular grains of 100 nm size or greater and are three dimensional in nature. This would also imply triangular columnar growth. At 100% oxygen in the sputtering environment, the AFM image of figure5.2.5b shows that the grains are still triangular but the size has decreased. This correlates well with the x-ray diffraction data that reveals a smaller crystallite size for these films. Ya-Qi [5] et al. reported the columnar growth of TiO_2 films.

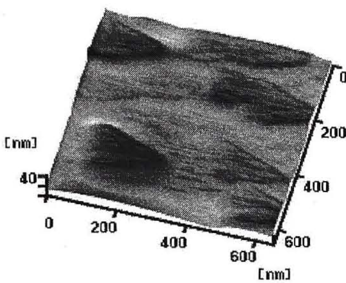

Figure 5.2.5a

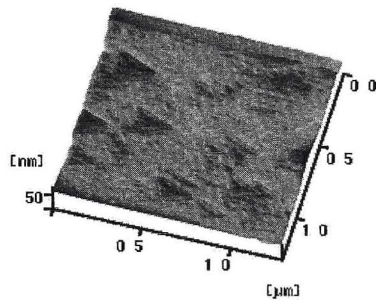

Figure 5.2.5b

Figure 5.2.5 a & b: DFM images of TiO_2 films deposited on glass at 20 and 100% OMP respectively.

The DFM images of the films deposited in pure oxygen atmosphere on fused silica at different working oxygen pressures of 0.05, 0.1 and 0.5 mTorr are shown in figure 5.2.6a-c respectively. It is observed that the grain size of the films increased with increase in working oxygen pressure and it is true for the samples deposited on glass and silicon. Films deposited on glass and silicon at 0.05 mTorr oxygen working pressure is shown in figure 5.2.6 d & e respectively. It is clearly observed that the microstructure of the films is affected with the substrate. The mean grain size of these films is found to vary with the distance (D_{s-t}) as well as the total pressure. For the films deposited at a D_{s-t} of 4cm, the grain size is smaller and optical packing density is higher compared to other films.

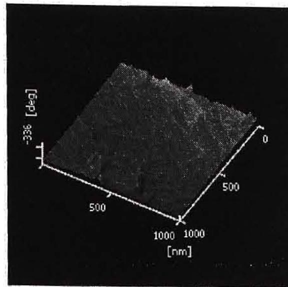

Figure 5.2.6a: DFM image of the film deposited on fused silica, at 0.05 mTorr in the pure oxygen atmosphere.

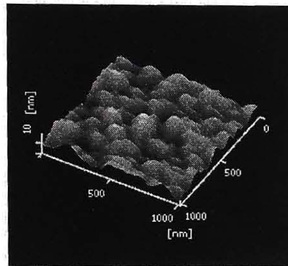

Figure 5.2.6b: DFM image of the film deposited on fused silica, at 0.1 mTorr in the pure oxygen atmosphere.

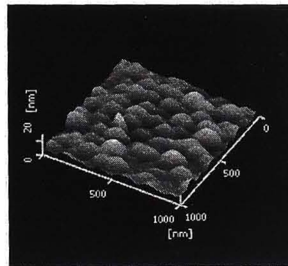

Figure 5.2.6c: DFM image of the film deposited on fused silica, at 0.5 mTorr in the pure oxygen atmosphere.

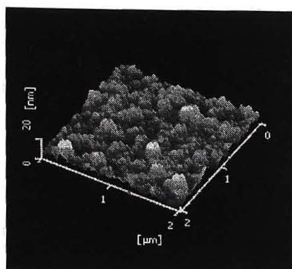

Figure 5.2.6d: DFM image of the film deposited on glass, at 0.05 mTorr in the pure oxygen atmosphere

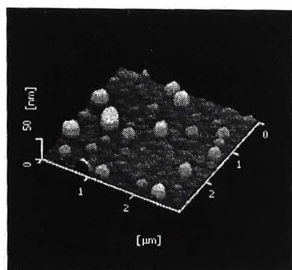

Figure 5.2.6e: DFM image of the film deposited on silicon, at 0.05 mTorr in the pure oxygen atmosphere.

Scanning Electron Micrographs of the films deposited on glass at 20, 50, 80 & 100% of OMP in the sputtering atmosphere are shown in figure 5.2.7a to d respectively. It is found that the film deposited around 50% OMP in the plasma shows maximum densification and porosity increases thereafter. The densification and porosity are related to the packing density of the thin film defined as the ratio of the solid part of the film (columns) to the total volume (columns+voids). A packing density of unity refers to a pore free film. SEM pictures reveal that there is an increase in packing density of the films up to 50% of OMP in the sputter gas causing an increase in dielectric constant as described in section 7.3.1 of chapter 7. The decrease in dielectric constant with increase in OMP beyond 50% may be due to lower packing densities, which are observed from SEM results.

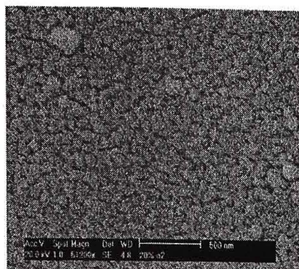

Figure 5.2.7a

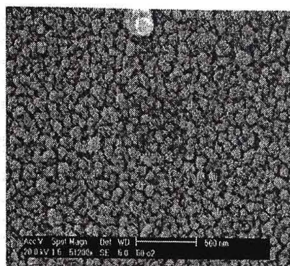

Figure 5.2.7b

Figure 5.2.7a & b: SEM pictures of TiO_2 films deposited at 20 & 50 % OMP respectively.

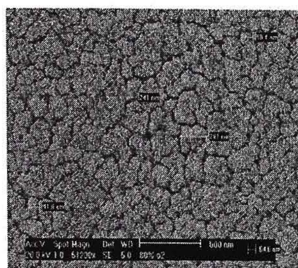

Figure 5.2.7c

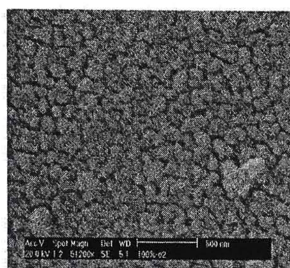

Figure 5.2.7d

Figure 5.2.7c & d: SEM pictures of TiO_2 films deposited at 80 & 100 % OMP respectively.

5.3 Structure and morphology of ZrO_2 films:

Zirconia films were deposited on to glass, fused silica and platinized silicon at different OMPs. The effect of processing parameters and substrates were investigated as a function of OMP. The X-ray diffraction patterns of the ZrO_2 films deposited on glass, fused silica and platinized silicon at different OMP (20, 40, 60, 80 and 100%) are shown in figure 5.3.1a, b and c respectively. In the case of films deposited on glass it is evident that the films are partially crystallized in a mixture of monoclinic and cubic phases with a strong glassy background. It is significant to note that the films are crystallized, although no external heating of the substrate was resorted to during the preparation. The as deposited films are found to be crystalline in monoclinic and cubic phases with the variation in OMP, and the films deposited with 20 and 100% of oxygen partial pressures showed monoclinic phase alone.

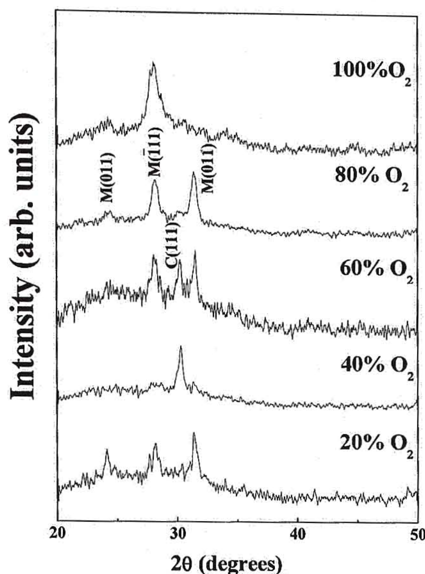

Figure 5.3.1a: XRD patterns of the ZrO_2 films deposited on glass with different OMPs.

Films deposited on fused silica and platinized silicon are also partially crystallized but only in monoclinic phase irrespective of the OMP in the sputtering gas.

We examine the role of strain in the low temperature formation of the cubic phase which is rather unusual. The crystallographic strain in the films deposited on glass and fused silica are plotted as a function of OMP in figure 5.3.2.

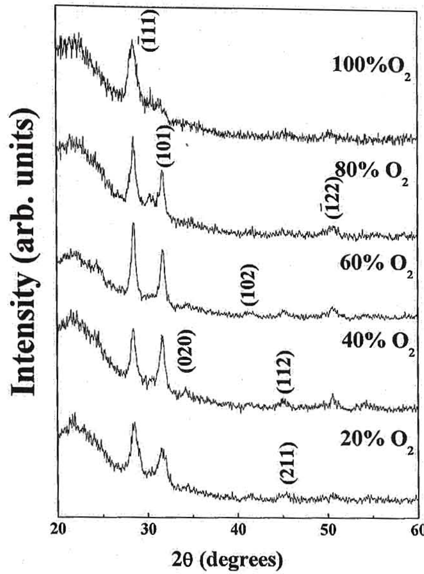

Figure 5.3.1b: XRD patterns of the ZrO_2 films deposited on fused silica with different OMPs.

It is observed that films deposited on fused silica crystallized only in monoclinic phase and exhibited tensile stress. For films deposited on glass, the monoclinic phase exhibited compressive stress whereas the cubic phase showed tensile stress. In the case of the films deposited on glass, the strain increased with increase in OMP and peaked at 40% of OMP and decreased thereafter. However, for the films deposited on fused silica, the strain increased up to 80% of OMP and decreased in pure oxygen atmosphere.

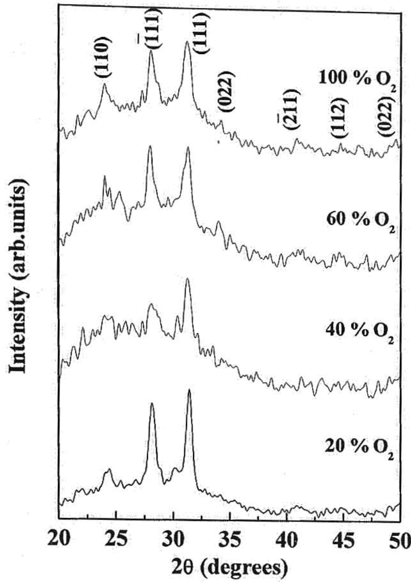

Figure 5.3.1c: XRD patterns of the ZrO_2 films deposited on platinized silicon with different OMPs.

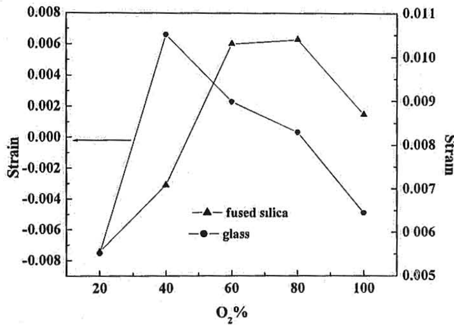

Figure 5.3.2: Variation in strain in the films deposited on glass and on fused silica as a function of OMP.

20%	40%		60%		80%		100%
Monoclinic	Cubic	Monoclinic	Cubic	Monoclinic	Cubic	Monoclinic	Monoclinic
-0.007 $(\bar{1}11)$	0.006 (111)	-0.003 (011)	0.002 (111)	-0.001 (011)	0.0003 (111)	-0.005 $(\bar{1}11)$	-0.001 (011)
-0.005 (111)		-0.001 $(\bar{1}11)$		-0.006 $(\bar{1}11)$		-0.002 (111)	-0.004 $(\bar{1}11)$
		-0.003 (111)		-0.003 (020)			-0.009 (111)
		-0.003(020)					

Table 5.3.I: Crystallographic strain in the films deposited on glass.

	20%	40%	60%	80%	100%
Δd/d	0.008 $(\bar{1}11)$	0.007 $(\bar{1}11)$	0.001 $(\bar{1}11)$	0.01 (011)	0.008 (011)
	0.005 (111)	0.006 (111)	0.001 (111)	0.005 $(\bar{1}11)$	0.004 $(\bar{1}11)$
	0.004 (211)	0.003 (020)	0.01 (102)	0.003 (111)	0.007 (111)
				0.002 (102)	

Table 5.3.II: Crystallographic strain in the films deposited on fused silica.
[Numbers in bracket indicate the Miller indices].

The details of the strain values are tabulated in tables 5.3.I & II for films deposited on glass and fused silica respectively. From the tables 5.3.I & II it is clear that strain energy is an important factor in the nucleation of the crystalline phase of the deposited films. In the films deposited on glass there is a competition between the tensile and compressive strain energies, which in turn determines the crystallization in to either the cubic or monoclinic phases or both.At the 40-80% of OMP, the large tensile stress aids the stability of the cubic phase and consequently at these OMPs the cubic phase is dominates over the monoclinic phase.

The weight ratios of monoclinic and cubic phases, in their mixed phases are qualitatively analyzed [13] using the following equation, for the films deposited on glass.

$$W_{mc}= [1/\{1+1.265\ (I_{cu}/I_{mc})\}]\ x100 \qquad (5.3.1.1)$$

where, W_{mc}, I_{cu} and I_{mc} denote the weight fraction of the monoclinic phase, the intensities of the strongest cubic and monoclinic reflections respectively. In this case intensities of $(\bar{1}11)$ monoclinic phase peak and (111) cubic phase peaks are taken. It is found that W_{mc} increased with increase in the OMP from 40-80%. The weight

fractions of the monoclinic phases are 29.5, 45 and 58.5% for the films deposited with 40, 60 & 80% OMP respectively in the sputtering environment. The presence of cubic phase appeared at 40, 60 & 80% of OMP can be attributed to the interaction between the positive ions accelerated from the plasma and the atoms on the substrate surface. Diffusion of the incident particles and the relaxation of the surface are also expected to be enhanced by the collisions between the impacting ions and substrate atoms. The films deposited at 20 and 100% OMP did not show any cubic peak, which shows that OMP plays an important role in determination of the structure of the deposited films. The appearance of a mixed phase is not due to the phase transition from monoclinic phase to the cubic phase but due to the growth competition that takes place between two phases during the deposition process itself.

It is well known that the deposition of thin films from the vapor phase is far away from the equilibrium state. Therefore the zirconia thin films deposited by DC magnetron sputtering without substrate heating are reported to be amorphous [14]. However, in the present study films are either in the pure monoclinic phase or in a mixture of both monoclinic and cubic phases. More significantly, the films are nanocrystalline in the as deposited state indicating plasma-assisted crystallization since the measured temperature rise during the deposition was only of the order of 100°C.

Two mechanisms have been proposed in literature, for the low temperature formation of the high temperature polymorphs of zirconia *i.e.* the tetragonal and cubic phases [46, 47].

1. Small value of grain and crystallite sizes
2. The presence of oxygen vacancies

In addition to these, the crystallographic texture and phase composition of thin films are in general also determined by the minimization of the following factors (apart from *in situ* and *ex situ* processing conditions) [48, 49].

1. Surface free energy
2. Interface energy and
3. Strain energy

The effect of these parameters is investigated in detail experimentally and by using analytical models and these results are widely reported. While the surface free energy and interface energy are relatively independent of processing conditions, the

strain energy is strongly dependent on processing conditions such as working pressure, power density and substrate temperature.

In the current study, the presence of cubic phase at 40-80% OMP in the sputtering gas can be attributed to a competition between the mechanisms listed above. The crystallite and grain sizes are uniformly small in our case, independent of processing parameters. Furthermore, since the film material and substrate have not been changed, the effect of surface and interface energies can also be neglected to a first approximation.

The stabilization of cubic phase in bulk occurs at temperatures >800°C, but in the present case the substrate temperature did not exceed more than 100°C. This suggests that the appearance of mixed phases is not due to the phase transition from monoclinic to cubic, but due to the competition between the presence of oxygen vacancies and strain energy minimization. It should be noted that the films at low OMP would have significant oxygen non-stoichiometry creating oxygen vacancies. Interestingly, formation of cubic phase is accompanied by an increase in the refractive index when the OMP is between 40 to 80%. It is known that the cubic phase of zirconia has the highest refractive index of the three polymorphs. As the OMP is further increased the non-stoichiometry evidently decreases and the strain increases, resulting in the formation of pure monoclinic phase.

The crystallite size of the films deposited on glass, fused silica and platinized silicon as a function of OMP is plotted in figure 5.3.3. It is observed that films deposited on glass showed larger crystallite sizes compared to the films deposited on fused silica and platinized silicon.

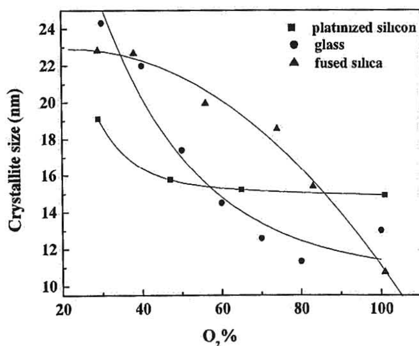

Figure 5.3.3: Variation in crystallite size of the films deposited on glass, fused silica and on platinized silicon.

It is observed that the crystallite size exponentially decreases as the OMP increases. The crystallite sizes as estimated from the full width at half maximum (FWHM) of the XRD peaks were in the range of 11-24, 10-13.9 and 14.9-19.12 nm for the films deposited on glass, fused silica and platinized silicon respectively. It is also found that crystallite size decreases with increasing sputtering pressure, but it is independent of input power. It is observed that the refractive index and crystallite size follow the same path as a function of OMP in the sputtering gas. It is well known that stoichiometric ZrO_2 naturally grows in the amorphous state unless activation energy is provided in the form of temperature or ion bombardment.

The DFM images of the films deposited on glass and fused silica with OMP in the sputtering process are shown in the figures 5.3.4a to d and figure 5.3.5a to d respectively. For the films deposited on glass it is observed that there is not much variation in grain size of the deposited films with the variation in OMP and ranged between 38-45nm.

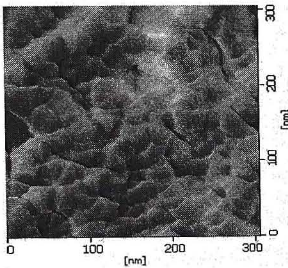

Figure 5.3.4a

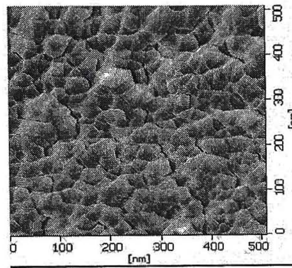

Figure 5.3.4b

Figure 5.3.4a& b: DFM images of the ZrO_2 films deposited on glass with 20 and 40% OMP respectively.

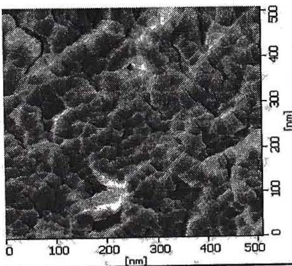

Figure 5.3.4c

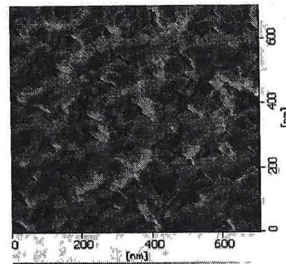

Figure 5.3.4d

Figure 5.3.4c& d: DFM images of the ZrO_2 films deposited on glass with 80 and 100% OMP respectively.

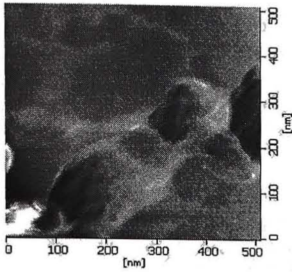

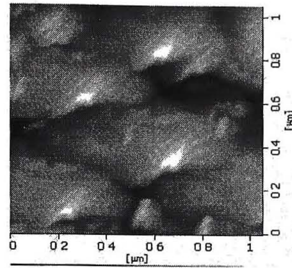

Figure 5.3.5a

Figure 5.3.5b (b)

Figure 5.3.5a& b: DFM images of the ZrO_2 films deposited on fused silica with 20 and 40% OMP respectively.

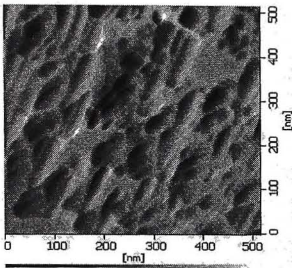

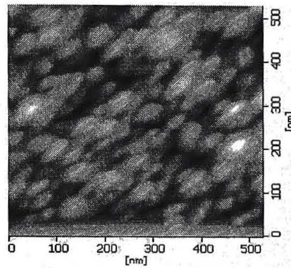

Figure 5.3.5c

Figure 5.3.5d

Figure 5.3.5c & d: DFM images of the ZrO_2 films deposited on fused silica with 80 and 100% OMP respectively.

The grains appear to grow in square shapes with significant porosity, which is reflected in the low refractive index values of the films discussed in chapter 6. But in the case of the films deposited on fused silica, the grain sizes are one order higher than for the films deposited on glass.

5.4 Structure and morphology of $ZrTiO_4$ (ZT) films:

$ZrTiO_4$ thin films were deposited on to glass, platinized silicon and fused silica substrates at different substrate to target distances (3, 5 &7 cms) as a function of OMP from Zr and Ti metal targets by DC reactive magnetron sputtering.

X-ray diffraction patterns of the films deposited on glass with different oxygen mixing percentages (OMP) of 20, 40, 60, 80 and 100%, at different substrate to target distances (D_{s-t}) of 3 and 5cms are shown in figure 5.4.1a & b respectively.

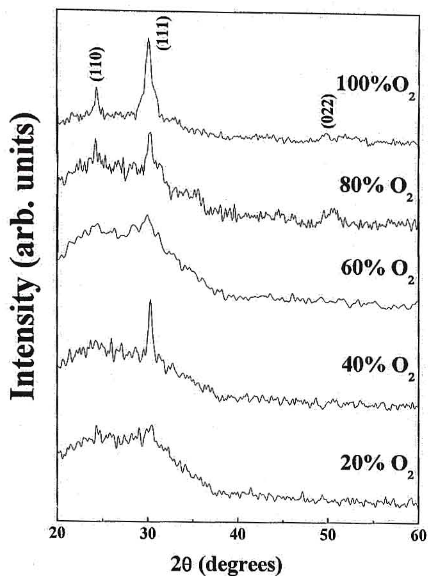

Figure 5.4.1a: XRD patterns of $ZrTiO_4$ films deposited on glass at a D_{s-t} of 3cm, with different OMPs.

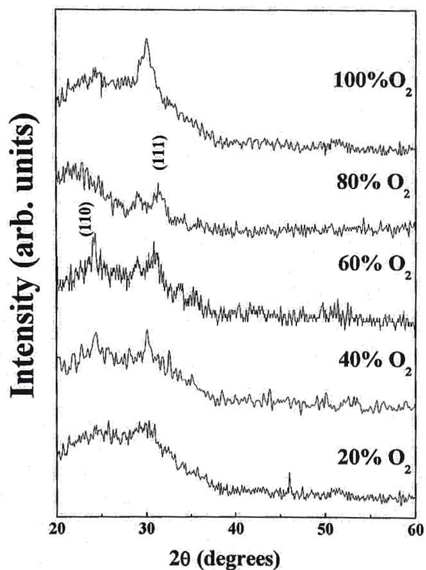

Figure 5.4.1b: XRD patterns of $ZrTiO_4$ films deposited on glass at a D_{s-t} of 5cm, with different OMPs.

It is evident that the films are crystallized in the orthorhombic phase with a strong glassy background. It is significant to note that the films were crystallized, although no external heating of the substrate was resorted to during the deposition.

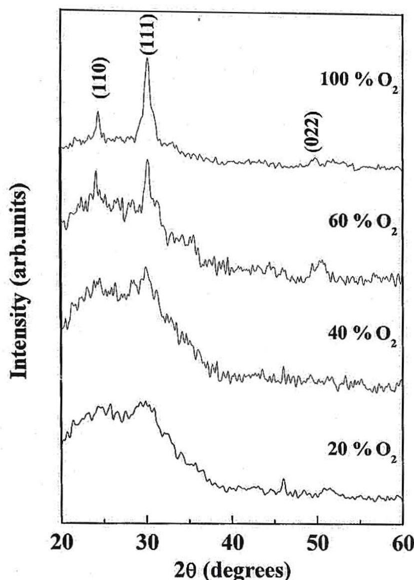

Figure 5.4.1c: XRD patterns of $ZrTiO_4$ films deposited on platinized silicon at a $D_{s\text{-}t}$ of 3cm, with different OMPs.

It is also observed that the (111) peak is broadening with decrease in OMP. The variation in crystallite size as a function of OMP for films deposited at different $D_{s\text{-}t}$ values of 3 and 5cms on glass substrates are shown in figure 5.4.2a, and the variation in crystallite size of the films deposited on platinized silicon as a function of OMP is shown in figure 5.4.2b. On both the substrates it is observed that the crystallite size decreases as the OMP increases.

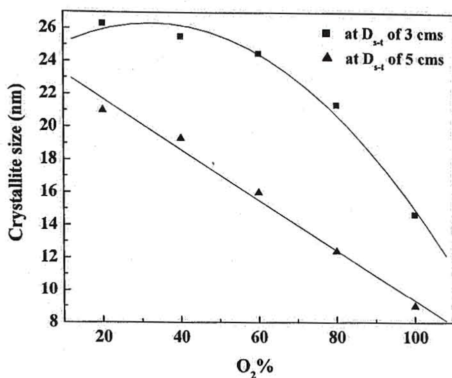

Figure 5.4.2a: Variation in crystallite size as a function of OMP for the films deposited on glass at D_{s-t} values of 3 and 5cms.

It is observed that the films deposited at D_{s-t} of 5cm showed lower crystallite sizes than the films deposited at D_{s-t} of 3cm; the films deposited at D_{s-t} of 7cm are found to be amorphous. The crystallite sizes of the films deposited on platinized silicon are ranged between 13-28nm. It is observed that $ZrTiO_4$ films deposited on fused silica are amorphous irrespective of the OMP and the D_{s-t}.

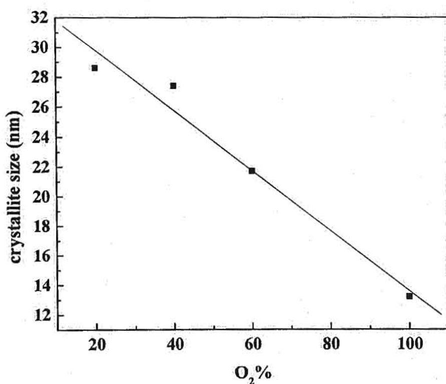

Figure 5.4.2b: Variation in crystallite size as a function of OMP for the films deposited on platinized silicon at D_{s-t} of 3 cm.

The small crystallite size at higher D_{s-t} of 5 cm compared to that of 3cm may be due to the reduction in the number of atoms that reaches the substrate. The increase in the crystallite size at D_{s-t} of 3cm can be attributed to the increase in rate of

deposition. It was found that crystallite size decreases with increasing sputtering pressure, but it is independent of input power density. Titania and Zirconia thin films deposited by DC magnetron sputtering without substrate heating have earlier been reported to be amorphous [42,43]. The as deposited films naturally grow in the amorphous state unless activation is provided to the process either in the form of temperature or ion bombardment.

The DFM pictures of the ZT films deposited on glass and fused silica at D_{s-t} of 3cm are shown in figures 5.4.3 (a-c) & 5.4.4 (a-c) respectively, where a, b and c corresponds to the films deposited with 20, 40 and 100% of OMP.

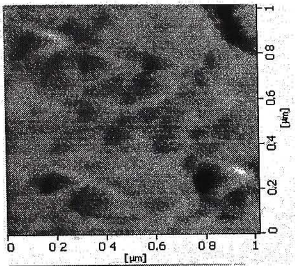

Figure 5.4.3a

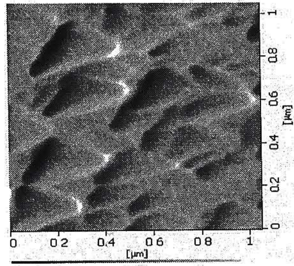

Figure 5.4.3b

Figure 5.4.3a & b: DFM images of $ZrTiO_4$ films deposited on glass with 20 and 40% OMP respectively at D_{s-t} of 3cm.

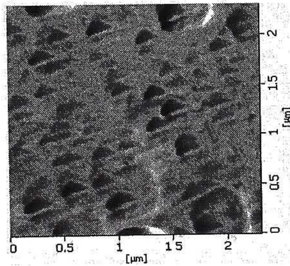

Figure 5.4.3c: DFM image of $ZrTiO_4$ film deposited on glass in pure oxygen plasma at D_{s-t} of 3cm.

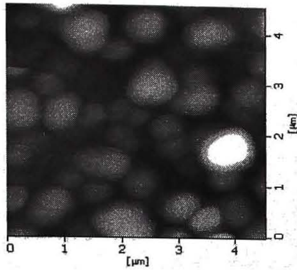

Figure 5.4.4a

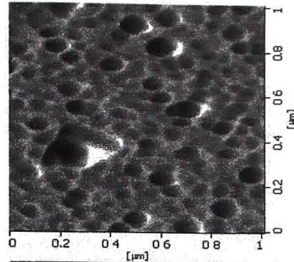

Figure 5.4.4b

Figure 5.4.4a & b: DFM images of $ZrTiO_4$ films deposited on fused silica with 20 and 40% OMP at D_{s-t} of 3cm.

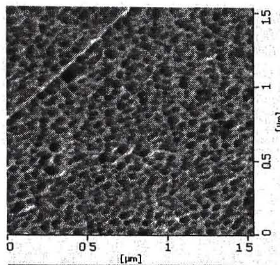

Figure 5.4.4c: DFM image of $ZrTiO_4$ film deposited on fused silica in pure oxygen plasma at D_{s-t} of 3cm.

It is observed that the films deposited on glass showed the triangular grains where as the films deposited on fused silica showed the spherical shape grains. In both the cases as the OMP in the sputtering atmosphere increases the grain size is decreased.

5.5 Structure and morphology of $(Zr,Sn)TiO_4$ (ZST) films:

Deposition of ZST thin films from the complex metal target (single cathode from Zr, Ti and Sn metals) by DC reactive magnetron sputtering was demonstrated. The films were deposited on to glass, platinized silicon and fused silica substrates with different OMPs.

X-ray diffraction patterns of the films deposited on glass with different oxygen mixing percentages (OMP) of 20, 40, 60, 80 and 100% are shown in figure 5.5.1.

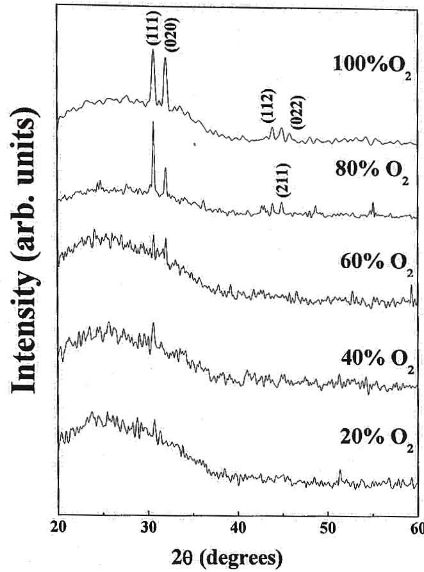

Figure 5.5.1: XRD patterns of the ZST films deposited on glass with different OMPs.

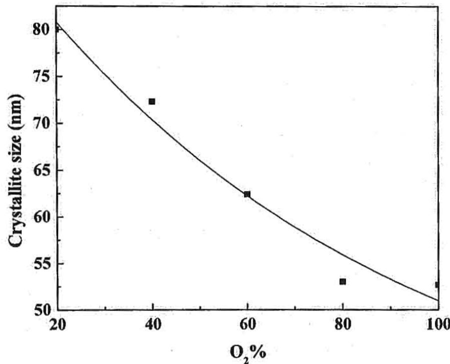

Figure 5.5.2: Variation in crystallite size as a function of OMP.

It is evident that the films are crystallized in the orthorhombic phase with a strong glassy background. It is significant to note that the films crystallized, although no external heating of the substrate was resorted to during the deposition. It is also observed that the (111) peak is broadening with increase in OMP. The variation in crystallite size as a function of OMP is shown in figure 5.5.2. It is observed that the

crystallite size decreases as the OMP increases. The crystallite sizes as estimated from the full width at half maximum (FWHM) of the XRD peaks were in the range 52-80 nm for all the films. It is observed that $(Zr_{0.8},Sn_{0.2})TiO_4$ (ZST) films deposited on fused silica and platinized silicon are amorphous irrespective of the OMP. It was also found that crystallite size decreases with increasing sputtering pressure, but it is independent of input power density. ZST thin films without substrate heating have earlier been reported to be amorphous [31, 32, 50].

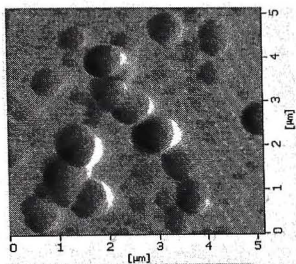

Figure 5.5.3a

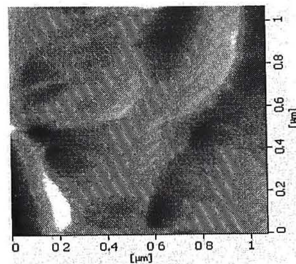

Figure 5.5.3b

Figure 5.5.3a & b: DFM images of ZST films deposited on fused silica with 20 and 40% OMP.

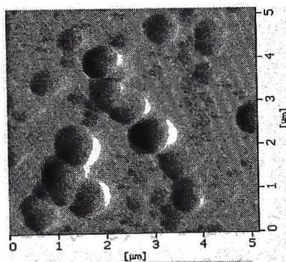

Figure 5.5.3c: DFM image of ZST film deposited on fused silica in pure oxygen plasma.

The DFM images of the ZST films deposited at different OMPs (20,40&100%) on fused silica and on glass are shown in figures 5.5.3a-c and 5.5.4a-c respectively. It was observed that all the films showed columnar growth. The spherical grains along with triangular grains were observed for the films deposited on fused silica where as the films deposited on glass showed only triangular grains. In both cases the films deposited at 40% of OMP showed higher grain sizes compared to the films deposited at other OMPs and the films deposited in pure oxygen plasma showed the smallest grains.

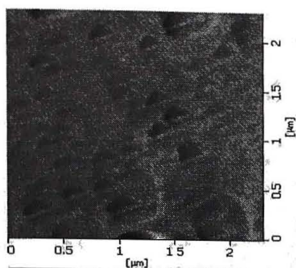

Figure 5.5.4a

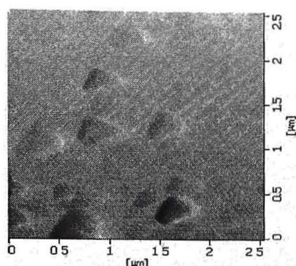

Figure 5.5.4b

Figure 5.5.4a & b: DFM images of ZST films deposited on glass with 20 and 40% OMP respectively.

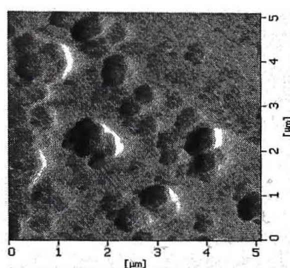

Figure 5.5.4c: DFM image of ZST film deposited on glass in pure oxygen plasma.

5.6 Discussion and conclusions:

The ability of sputtering Ti, Zr, $ZrTiO_4$ and ZST in a 100% oxygen atmosphere even with the accompanying problem of target poisoning is important. These observations correlates well with recent reports on the growth of TiO_2 films starting from TiO_{2-x} target by DC magnetron sputtering [51]. These studies indicate that as long as the target oxidation remains incomplete, sputtering will continue to occur even in a DC magnetron sputtering geometry.

It would therefore seem that, while charged clusters could be the nucleating centers or "seeds" for onset of crystallinity, the significant grain growth observed here is the result of plasma-assisted activation while the film is growing. Therefore, we believe, that the free energy of the substrate-film interface should also be taken in to consideration to explain the crystallinity. Thus, a combination of gas phase clustering and the surface conditions on the substrate would appear to control crystallinity or the lack of it in such environments.

- The structure and morphology of titania, zirconia, $ZrTiO_4$ and ZST films are studied systematically deposited as a function of OMP.
- Significantly, in all the cases, the as deposited films were crystallized without any external heating.
- The as deposited TiO_2 films on glass are crystallized in the anatase and rutile phases irrespective of the OMP where as the films deposited on to fused silica substrates showed anatse phase alone.
- The as deposited TiO_2 films in pure DC oxygen atmosphere are partially crystalline irrespective of the substrate used and the presence of rutile phase is observed for films deposited on Si.
- TiO_2 Films are deposited on to glass, fused silica and silicon in pure oxygen plasma at different D_{s-t} (2, 4 & 6 cm) and different working pressures (0.5, 0.1, 0.075 & 0.05 mTorr). It is observed that the films deposited at D_{s-t} of 4cm with 0.05 mTorr showed better properties compared to other deposition conditions.
- The morphology of TiO_2 films showed columnar growth and the grains are triangular in nature. For the films deposited in pure oxygen atmosphere growth is different.
- SEM pictures showed that the TiO_2 films deposited at 50% of OMP are more densified compared to other films.
- ZrO_2 films deposited on fused silica and platinized silicon showed only monoclinic phase irrespective of the OMP where as the films deposited on glass at 40-80% of OMP showed both monoclinic and cubic phases.
- ZrO_2 films deposited on glass, the monoclinic phase exhibited compressive stress whereas the cubic phase showed tensile stress.
- ZrO_2 films deposited on glass showed square particles with smaller grain size where as the films deposited on fused silica exhibited spherical grains.
- Deposition of $ZrTiO_4$ thin films from Zr and Ti metal targets by DC reactive magnetron sputtering is demonstrated.
- $ZrTiO_4$ thin films are deposited on to glass at a D_{s-t} of 3 and 5cms were crystallined irrespective of OMP where as the films deposited at a D_{s-t} of 7cm was amorphous.

- $ZrTiO_4$ films deposited on platinized silicon at D_{s-t} of 3cm are also partially crystalline where as the films deposited on fused silica was amorphous irrespective of OMP and D_{s-t}.
- Films deposited at D_{s-t} of 3cm exhibited better properties compared to the films deposited at D_{s-t} of 5 and 7cms.
- The DFM pictures of $ZrTiO_4$ films deposited on to glass showed triangular grains where as the films deposited on to fused silica showed spherical grains irrespective of the D_{s-t} and OMP.
- In all the cases the crystallite sizes of the deposited films were decreased with increase in OMP.
- ZST films deposited on glass were crystallized where as the films deposited on platinized silicon and fused silica were amorphous irrespective of variations in processing parameters.
- ZST films deposited on glass showed triangular grains where as the films deposited on fused silica showed spherical grains along with triangular grains.
- The deposition and the systematic study of titania, zirconia, $ZrTiO_4$ and ZST films in the pure oxygen atmosphere are reported for the first time.
- In all the cases it is observed that the processing parameters played an important role on the crystallization of the deposited films.

References:

[1] M.H.Suhail, G.Mohan Rao and S.Mohan, J.Appl.Phys., **71**, 1421 (1992).

[2] Marius D.Stamate, Appl. Surf. Sci., **205**,353 (2003).

[3] T.Takashi, H.Nakabayashi, Thin Solid Films, **420-421**,433 (2002).

[4] J.D.DeLoach, G.Scarel and C.R.Aita, J.Appl.Phys., **85**, 2377 (1999).

[5] Ya-Qi Hou, D-M. Zhaung, M. Zhao and M-S. Wu, Appl.Surf.Sci., **218**, 97 (2003).

[6] D. Mardare and A. Stancu, Mater. Res. Bull., **35**, 2017 (2000).

[7] W.Zhang, Y. Li, S. Zhu and F. Wang, Surf. Coat. Technol., **182**,192 (2004).

[8] K.Takamura, Y.Abe and K.Sasaki, Vacuum, **74**, 397 (2004).

[9] M. C.Barnes, S. Kumar, L. Green, N-M Hwang and A. R. Gerson, Surf. Coat. Technol., **190**,321 (2005).

[10] S.B.Amor, G.Baud, J.P.Besse and M.Jacquet, Mater.Sci.Eng.B, **47**, 110 (1997).

[11] Y. Tachibana, H. O. Hayashi, A. Mitsui and Y. Hayashi, Vacuum, **59**, 836 (2000).

[12] H.Tomaszewski, H.Poleman, D.Depla, DPoelman, R.Gryse, L.Fiermans, M. F. Reyniers, G Heynderickx, and G B. Marin, Vacuum, **68**, 31 (2003).

[13] T.Asanuma, T.Matsutani, C.Liu, T.Mihara, and M.Kiuchi, J.Appl.Phys., **95**, 6011(2004).

[14] M.H.Suhail, G.Mohan Rao, and S.Mohan, J.Vac.Sci.Technol.A, **9**, 2675 (1991).

[15] S. B. Amor, B. Rogier, G. Baud, M. Jacquet and M. Nardin, Mater.Sci.Eng.B, **57**, 28 (1998).

[16] P. Gao, L. J. Meng, M. P. dos Santos, V. Teixeira and M. Andritschky, Vacuum, **56**, 143 (2000)

[17] S.H.Jeong, I.S.Bae, Y.S.Shin, S.B.Lee, H.T.Kwak and J.H.Boo, Thin Solid Films, **475**, 354 (2005).

[18] K.Goedicke, J-S Liebig, O.Zywitzki and H.Sahm, Thin Solid Films, **377-378**, 37 (2000).

[19] S. Collard, H. Kupfer, W. Hoyer and G. Hecht, Vacuum, **55**, 153 (1999).

[20] S.Venkataraj, O.Kappertz, Ch.Liesch, R.Detemple, R.Jayavel, and M.Wuttig, Vacuum, **75**, 7 (2004).

[21] M.S.Wong, W.J.Chia, P.Yashar, J.M.Schneider, W.D.Sproul, and S. A. Barnett, Surf.Coat.Technol., **86-87**, 381 (1996).

[22] K.P.S.S Hembram, G.Dutta, V.Umesh, G.Waghmare and G.Mohan Rao, Physica B, **399**, 21 (2007).

[23] P.Briois, F.Lapostolle, V.Demange, E.Djurado and A.Billard, Surf.Coat.Technol., **201**, 6012 (2007).

[24] S.Zhao, F.Ma, Z.Song and K.Xu, Optical Materials, xxx (2007).

[25] D-A.Chang, P.Lin and T-Y. Tseng, J.Appl.Phys., **77**, 4445 (1995).

[26] M. Viticoli, G. Padeletti, S. Kaciulis, G.M. Ingo, L. Pandolfi and C. Zaldo, Mater.Sci.Eng.B, **118**, 87 (2005).

[27] G. Padeletti, A. Cusmà, M. Viticoli, G. M. Ingo, A. Mezzi and B. Watts, Mater.Sci.Eng.B, **109**, 104 (2004).

[28] T.Kim, J.Oh, B.Park and K.S.Hong, Appl.Phys.Lett., **76**, 3043 (2000).

[29] P. Victor, S. S. N. Bharadwaja, J. Nagaraju and S. B. Krupanidhi, Solid State Commun., **120**, 379 (2001).

[30] O.Nakagawara, Y.Toyota, M.Kobayashi, Y.Yoshino, H.Tabata and T.Kawai, J.Appl.Phys., **80**, 388 (1996).

[31] C-L. Huang and C-H. Hsu, J.Appl.Phys., **96**, 1186 (2004).

[32] W.X. Cheng, A.L.Ding, P.S.Qiu, X.Y.He and S.S.H.Zheng, Appl.Surf.Sci., **214**,136 (2003).

[33] R-Y.Yang, Y-K. Su, M-H. Weng and Y-S.Ho, Appl.Surf.Sci., **253**, 2203 (2006).

[34] M. Nistor, F. Gherendi, M. Magureanu, N.B. Mandache, A. Ioachim, M.G. Banciu, L. Nedelcu, M. Popescu, F. Sava and H.V. Alexandru, Appl. Surf. Sci., **247**, 169 (2005).

[35] L.Maissel: "Handbook of Thin Film Technology" (McGraw-Hill, New York) 1970.

[36] S.Maniv and W.D.Westwood, J.Vac.Sci.Technol. **17**, 743 (1980).

[37] A.Rizk, S.B.Youssef and S.K.Habib, Vacuum, **38**, 93 (1988).

[38] S.Maniv, J.Appl.Phys., **59**, 66 (1986).

[39] G.M.Rao and S.Mohan, J.Appl.Phys., **69**, 6652 (1991).

[40] J.Heller, Thin Solid Films, **17**, 163 (1973).

[41] J.L.Vosen and J.J.Cuomo, "In Thin Film Processes" (Academic, New York) 1978.

[42] R.P. Howson, A.G.Spencer, K.Oka, and R.W.Lewin, J.Vac.Sci.Technol.A, 7, 1230 (1989).

[43] M.Lazzeri, A.Vittadini, and A.Selloni, Phys.Rev. B, **63,** 155409 (2001).

[44] F.Zhang, Z.Zheng, Y.Chen, D.Liu, and X.Liu, J.Appl.Phys., **83,** 4101 (1998).

[45] S.G.Springer, P.E.Schmid, R.Sanjines and F.Levy, Surf. Coat. Technol., **151 152,** 51 (2002).

[46] J.D.DeLoach, C.R.Aita, and C-K.Loong, J.Vac.Sci.Technol.A, **20**, 1517 (2002).

[47] S.Fabris, A.T.Paxton, and M.W.Finnis, Acta Materialia, **50**, 5172 (2002).

[48] C.V.Thompson, J.Mater.Res., **14**, 3164 (1999).

[49] K.Barmak, J.Kim, C-S. Kim, W.E.Archibald, G.S.Rohrer, A.D.Rollett,

[50] D.Kinderleherer, S.Tasan, H.Zhang, and D.J.Srolovitz, Scripta Materialia, **54**, 1059 (2006).

[51] D-A.Chang, P.Lin, and T-Y.Tseng, J.Appl.Phys., 77, 4445 (1995).

[52] Y.Tachibana, H.Ohsaki, A.Hayashi, A.Mitsui and Y.Hayashi, Vacuum, **59**, 836 (2000).

Chapter-6

Optical and Electrical Studies of Films in the $(Zr,Sn)TiO_4$ System

The best materials for optical thin film applications have been found to be the dielectric oxides like Al_2O_3, CeO_2, HfO_2, SiO_2, TiO_2, ZrO_2 etc. Hence most of the work on optical thin films has been concentrated on these materials, their deposition and properties. Selenides, fluorides and sulphides also have found use in optical films but the oxides are decidedly superior due to their hardness, better durability in adverse environments, high refractive index and low optical losses.

Most of the optical devices use multilayer structures for improved performance and efficiency. This would normally mean a stack of high index and low index films coated alternatively, the sequence being decided by the final device requirement. The failure of any such determined mainly by the failure of any one of the layers and the degradation in its properties. Consequently a study of single layers of these materials is as important as the study of the multilayer. In the present study four high refractive index and large bandgap materials such as TiO_2, ZrO_2, $ZrTiO_4$ and $(Zr,Sn)TiO_4$ films have been prepared by DC reactive magnetron sputtering and studied their optical properties systematically.

6.1 Optical properties of TiO_2 films:

The transmittance spectra of the TiO_2 films deposited on glass at different Oxygen Mixing Percentages (OMP) is shown in figure 6.1.1a and the films deposited on fused silica at 0.05mTorr with different substrate to target distance (D_{s-t}) in the presence of pure oxygen atmosphere are shown in figure 6.1.1b. The transmittance of the films deposited on glass is around 80% when the OMP is varied, and it is around 90% in the case of pure oxygen atmosphere is in the region above the band gap. The films, which deposited at higher partial pressures of oxygen, show higher transmittance. The band gap region indicated by the wavelength at which transmittance of the films decreases to 50% is between 330-360nm indicating that the films deposited are uniform.

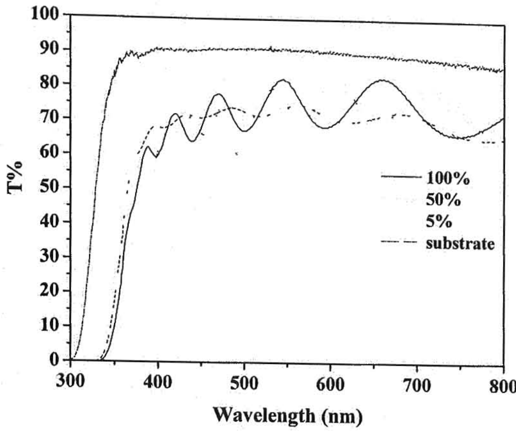

Figure 6.1.1a: Transmittance spectra of TiO_2 films deposited on glass at different OMPs.

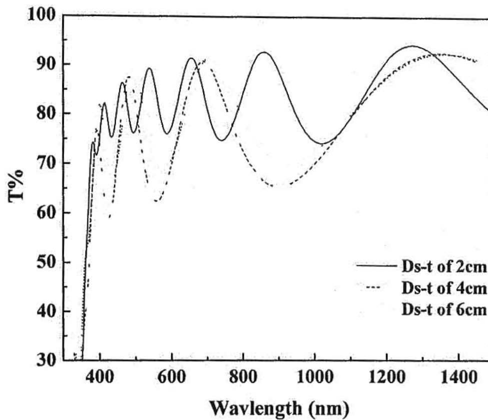

Figure 6.1.1b: Transmittance spectra of TiO_2 films deposited on fused silica at 0.05 mTorr at different D_{s-t} in pure oxygen plasma.

The variation in refractive index of the TiO_2 films deposited on glass as a function of OMP is shown in figure 6.1.2a and the variation in refractive index of the films deposited on fused silica in pure oxygen atmosphere at different working oxygen pressures as a function of D_{s-t} are shown in figure 6.1.2b. It is observed that for the films deposited on glass the refractive index is high at lower OMP and decreases as the oxygen partial pressure increases, and varies between 1.88-2.17 as OMP decreases from 100 to 20%.

In the case of the films deposited in pure oxygen atmosphere the values of the refractive index ranged between 1.9-2.32 at a wavelength of 600nm. The films deposited at 0.05 mTorr showed higher values, which decreased with increase in working pressure and increase in D_{s-t}.

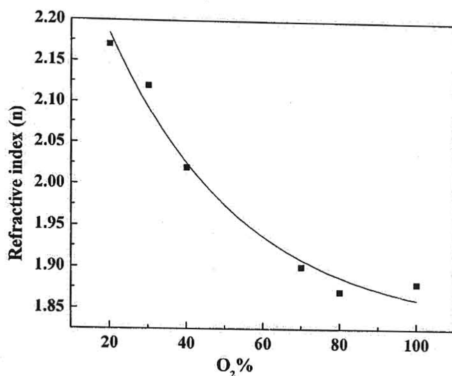

Figure 6.1.2a: Variation in refractive index of TiO_2 films deposited on glass as a function of OMP.

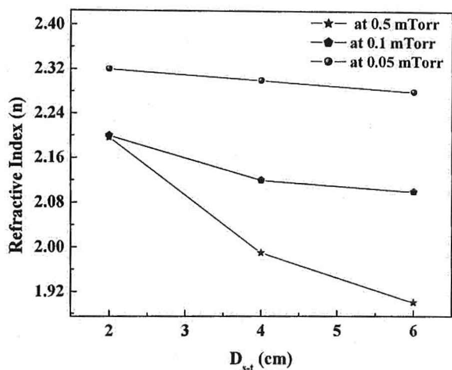

Figure 6.1.2b: Variation in refractive index of TiO_2 films deposited on fused silica at different oxygen working pressures as a function of D_{s-t} in pure oxygen plasma.

The relatively low values of n observed in the present study may partly be due to low packing density, partial crystallinity of the films and low adatom mobility of the films at ambient temperature. The increase in refractive index at 0.05 mTorr can be attributed to the increase in crystallinity and packing density of the films. The decrease in n value with higher working oxygen pressure is due to the low deposition

rates. Dannenberg et al. reported that refractive index of DC sputtered TiO_2 films range from 2.4-2.6 [1], Mardare et al. reported a range of refractive index between 2.19-2.4 [2] and Suhail et al. reported the refractive index of films as between 2.24-2.46 [3]. Tanemura et al. reported a refractive index of 2.65 for RF sputtered TiO_2 films [4]. Zywitzki et al. reported the refractive index of reactive pulsed magnetron sputtered films in the range of 2.45-2.68 [5]. The refractive index and crystallite size follow the same path as a function of OMP.

The variation in extinction coefficient (k) of the films deposited on glass as a function of OMP and the variation in extinction coefficient of the films deposited on fused silica in pure oxygen atmosphere at different working oxygen pressures as a function of D_{s-t} are shown in figure 6.1.2c & 2d respectively.

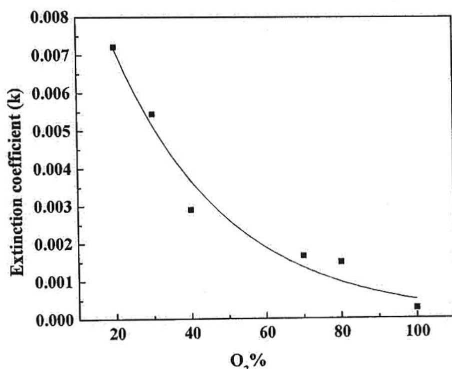

Figure 6.1.2c: Variation in extinction coefficient of TiO_2 films deposited on glass at different OMPs.

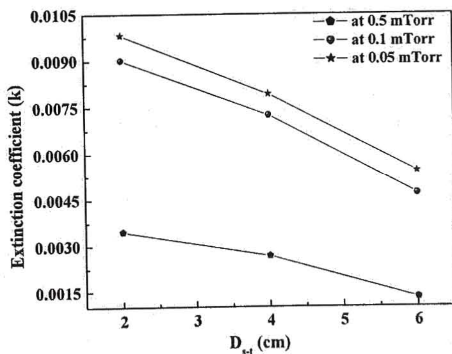

Figure 6.1.2d: Variation in extinction coefficient of TiO_2 films deposited on fused silica at different oxygen working pressures as a function of D_{s-t} in pure oxygen plasma.

It is observed that the variation in extinction coefficient has followed a similar trend as that of refractive index Vs OMP, since as the OMP increases the extinction coefficient decreases. But in the case of the films deposited in pure oxygen atmosphere, extinction coefficient values are lower for the films deposited at 0.5 mTorr and as the working pressure decreases from 0.5 to 0.05 mTorr the extinction coefficient values have increased.

The variation in packing density of the TiO_2 films as a function of OMP and the corresponding variation for films deposited in pure oxygen atmosphere at different working oxygen pressures at various values of $D_{s\text{-}t}$ are shown in figure 6.1.2e &2f respectively.

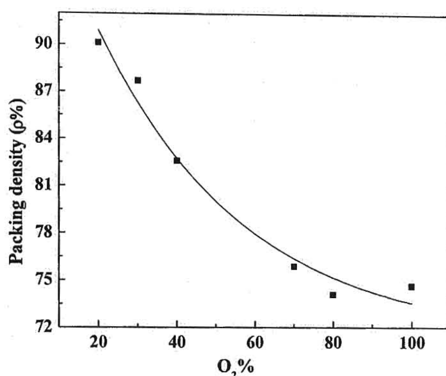

Figure 6.1.2e: Variation in packing density of TiO_2 films deposited on glass as a function of OMP.

The packing density of the thin film is defined as the ratio of the solid part of the film (columns) to the total volume (columns+voids). A packing density of unity refers to a pore free film. It is found that the variation in packing density vs. OMP followed a similar trend as that of refractive index n vs. OMP. It is observed that the packing densities of the films deposited on glass are lower than that of the films deposited on fused silica. The differences in the packing densities can be attributed to the surface free energies of the substrates, which influence the adatom mobility in the films. This would explain the reason for the lower values of n for the films deposited on glass and the increase in n values for films deposited on fused silica. It is observed that higher the packing density higher is the refractive index.

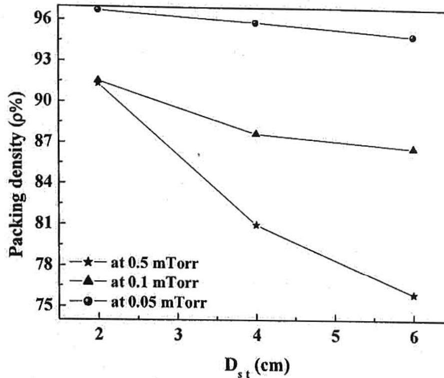

Figure 6.1.2f: Variation in packing density of TiO_2 films deposited on fused silica at different oxygen working pressures as a function of D_{s-t} in pure oxygen plasma.

Also it can be seen that the packing density is inversely proportional to the total working pressure. The films coated at lower working pressures showed higher packing density.

The optical bandgap values were calculated for films deposited on glass at different OMPs and it is shown in figure 6.1.3a while that for films deposited on fused silica in pure oxygen atmosphere at different working pressures and at different D_{s-t} is plotted in figure 6.1.3b. The optical bandgap values are a good qualitative estimate of stoichiometry. It was observed that the films showed bandgap values in between 3.2-3.5 eV. The bandgap for anatase TiO_2 is 3.20 eV [7], which indicates that the films in this case are well oxidized. The value of bandgap as a function of OMP is plotted and it is observed that as the OMP increases the bandgap also increases. In the case of films deposited in pure oxygen atmosphere, it is observed that the bandgap value increases with O_2 working pressure.

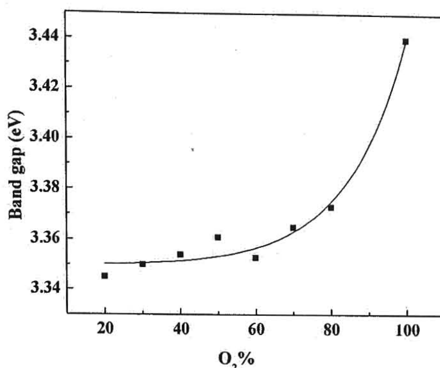

Figure 6.1.3a: Variation in bandgap of TiO_2 films deposited on glass as a function of OMP.

The bandgap values decreased with decrease in working pressure and increase in D_{s-t}. The increase in the bandgap can be attributed to the reduction in the oxygen vacancies with increase in the total working pressure [6]. It is observed that the bandgap increases from 3.2 – 3.5 eV as a function of OMP and working pressure where as over the same range the crystallite size decreases from 50 to 31 nm in pure oxygen atmosphere. The dependence of bandgap of films deposited on fused silica in pure oxygen atmosphere at the D_{s-t} of 4cm on the crystallite size is in figure 6.1.3c. There is a wide scatter in the reported values of optical bandgap of TiO_2 films ranging from 3.2 - 3.8 eV [1, 4, 7].

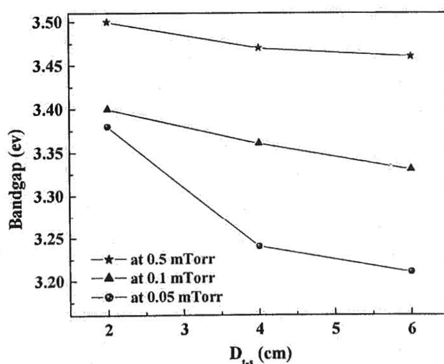

Figure 6.1.3b: Variation in bandgap of TiO_2 films deposited on fused silica at different working pressures as a function of D_{s-t} in pure oxygen plasma.

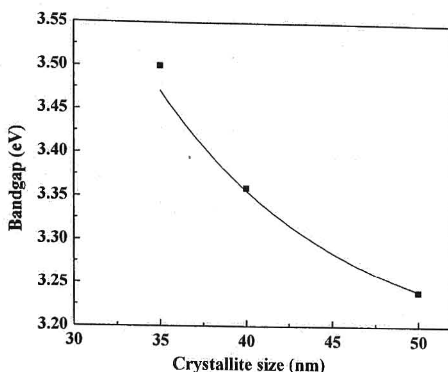

Figure 6.1.3c: Variation in bandgap of TiO_2 films deposited on fused silica at D_{s-t} of 4cm as a function of crystallite size in pure oxygen plasma.

As demonstrated in a number of other materials, the bandgap decreases with increase in crystallite size exhibiting approximately $1/d^2$ dependence, where d is the crystallite diameter [8]. It has been shown earlier [7] that the films deposited at higher working pressures are found to be amorphous and the bandgap tends to increase. Bandgap values of up to 3.70 eV have been reported for the amorphous phase [9].

It is clear from the results presented that the refractive index and crystallite size decrease with an increase in the percentage of oxygen in the sputtering environment. This is accompanied by an increase in the bandgap. More significantly the films are nanocrystalline in the as deposited state, indicating plasma-assisted crystallization since measured temperature rise during the deposition was only of the order of 100°C. It is well documented that stoichiometric TiO_2 naturally grows in the amorphous state unless activation energy is provided to the process either in the form of heat or ion bombardment. The band gap shows the expected increase with decrease in crystallite size, which is frequently deemed to indicate the onset of quantum confinement effects. Extensive XPS studies done on the growth of TiO_2 films by reactive sputtering shows that the deviation in oxygen stoichiometry is not very large even at low oxygen working pressures [10, 11]. However, when a crystalline phase of TiO_2 is embedded in a largely amorphous matrix of TiO_2 film, there are large deviations in optical band gap of the films from bulk values [7]. This would explain the situation in the current study appropriately.

6.2 Optical properties of ZrO_2 films:

The spectral transmittance of the films deposited on fused silica at different OMP is shown in figure 6.2.1. The transmittance of all the films is around 90% in the region above the band gap. The films which deposited at higher oxygen percentages show higher transmittance. The band gap region indicated by the wavelength at which transmittance of the films decreases to 50% is between 250-320nm.

The variation in refractive index of ZrO_2 films deposited on glass and fused silica as a function of OMP are shown in figure 6.2.2a. In both the cases the refractive index is high at lower OMPs in the sputtering gas and decreases as the OMP increases. The refractive index ranged between 1.69-1.85 and 1.99-2.15 at 600nm for the films deposited on glass and fused silica respectively. Films deposited on fused silica showed higher values.

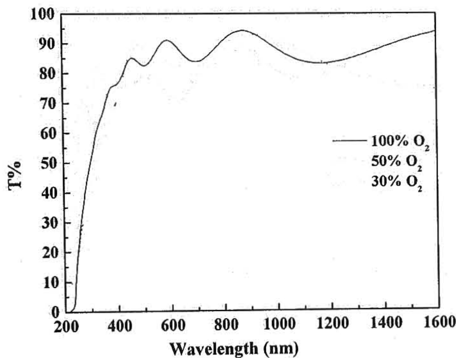

Figure 6.2.1: Transmittance spectra of ZrO_2 films deposited on fused silica at different OMPs.

Pengtao et al [12] reported 1.66-1.96, Amor et al [13] reported 1.65-2.15 for the films deposited on glass by RF magnetron sputtering; Venkatraj et al [14] reported 2.11-1.81 for films deposited on Si and Suhail et al [15] reported 2.15-1.9 for films deposited on fused silica by DC magnetron sputtering. The extinction coefficients of the films deposited on fused silica as a function of OMP are shown in Figure 6.2.2b. It is observed that as the OMP increases the extinction coefficient decreases.

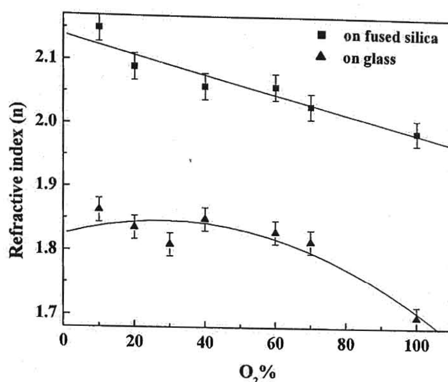

Figure 6.2.2a: Variation in refractive index of ZrO_2 films deposited on fused silica and on glass as a function of OMP.

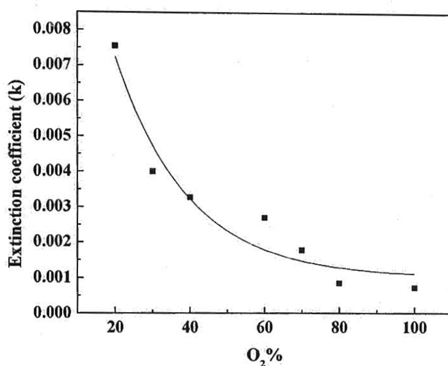

Figure 6.2.2b: Variation in extinction coefficient of ZrO_2 films deposited on fused silica as a function of OMP.

The n values of the films deposited on glass are relatively lower than those reported for annealed sputtered films. The low values of n deposited on glass observed in the present study may partly be due to partial crystallinity of the films and low adatom mobility in the films at ambient temperatures.

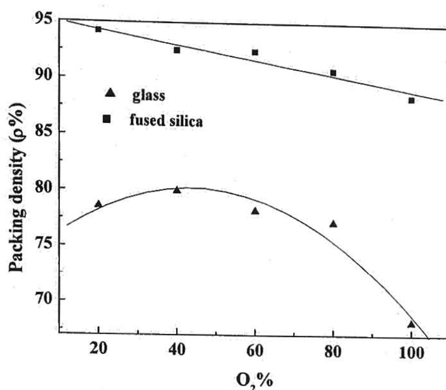

Figure 6.2.2c: Variation in packing density of ZrO_2 films deposited on fused silica and on glass as a function of OMP.

The lower n values can also be attributed to the lower packing densities (68-80%). The annealing of the sputtered films may be resulting in densification leading to higher refractive index in the cases quoted from literature. The slight increase in n at 40, 60 and 80% of OMP for the films deposited on glass can be attributed to the presence of cubic phase, and also at these oxygen percentages the films may have become more stoichiometric. The films deposited on glass showed lower refractive index values, while that for the films deposited on fused silica are comparable to the reported values. The lower values of n for the films on glass can also be attributed to the presence of mixed phases, which could cause the optical losses as well as to the lower packing densities (68-80%) and the higher values of n for films deposited on fused silica can be attributed to the higher packing densities (88.5-94.2%) that are shown in figure 6.2.2c. It is observed that higher the packing density higher is the refractive index and the increase in n in the case of films deposited on glass between 40-80% OMP is supported by the presence of cubic phase. The differences in the packing densities may be attributed to surface free energies of the substrates and to the observation from DFM images of the films surfaces that deposited on glass are porous while the films deposited on fused silica are dense. It is interesting to note that the optical packing densities are governed by the microstructure of the films.

The optical bandgap values and crystallite sizes are calculated for films deposited on fused silica at different OMPs and have been plotted in figure 6.2.3a. It

is observed that the films showed values of bandgap in between 5.5-5.7 eV. The value for ZrO_2 is 5eV indicating that the films in this case are well oxidized. The value of bandgap as a function of OMP is plotted and it is observed that as the OMP increases the bandgap increases.

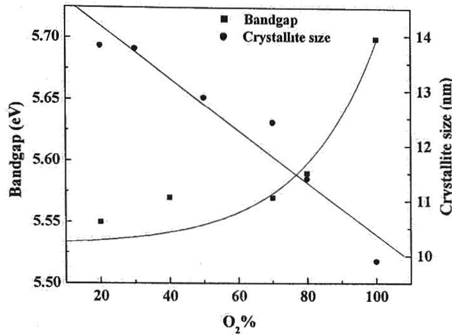

Figure 6.2.3a: Variation in bandgap and crystallite size of the ZrO_2 films deposited on fused silica as a function of OMP.

From figure 6.2.3a it is observed that the bandgap increases from 5.5-5.7eV as a function of OMP in the sputtering atmosphere, where as over the same range the crystallite size decreases from 13.9 to 10nm.

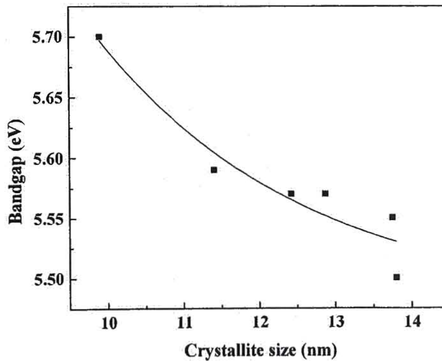

Figure 6.2.3b: Variation in bandgap of ZrO_2 films deposited on fused silica as a function of crystallite size.

It is found that crystallite size decreases with increasing sputtering pressure but it is independent of input power. The dependence of bandgap on crystallite size is shown in figure 6.2.3b, and the variation of square of the absorption coefficient as a

function of photon energy for the films deposited at different OMP is shown in figure 6.2.3c.

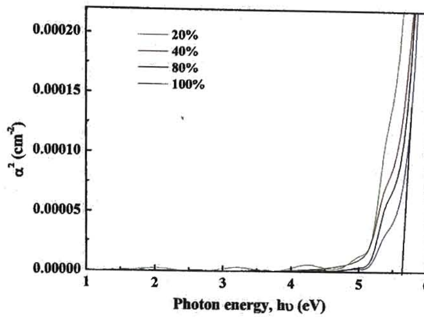

Figure 6.2.3c: Absorption coefficient of ZrO_2 films deposited on fused silica at different OMPs as a function of photon energy.

It is clear from the results presented that the refractive index and crystallite size decreases with increase in OMP in the sputtering environment. This is accompanied by an increase in the bandgap. As demonstrated in a number of other materials the bandgap decreases with increase in crystallite size exhibiting approximately $1/d^2$ dependence, where d is the crystallite diameter. The bandgap shows the expected increase with decrease in crystallite size, which frequently seemed to indicate the onset of quantum confinement effects. When a nanocrystalline phase of ZrO_2 is embedded in a largely amorphous matrix of ZrO_2 film there are large deviations in optical bandgap of the films from bulk values. This would explain the situation in the current study appropriately rather than the use of the effective mass approximation. The ability of sputtering Zr in a 100% oxygen atmosphere even with accompanying problem of target poisoning is important. The observation correlates well with reports on the growth of ZrO_2 films starting from ZrO_{2-x} target by DC magnetron sputtering [16].

6.3 Optical properties of $ZrTiO_4$ films:

Thin films of $ZrTiO_4$ are deposited on glass and on fused silica at different D_{s-t} (3, 5 and 7cms) to identify optimized D_{s-t} value and it were found that the films deposited at a D_{s-t} of 3cm showed better properties compared to other films. The spectral transmittance of the films deposited on fused silica at different OMP and at a

D_{s-t} of 3cm is shown in figure 6.3.1. The transmittance of all the films is around 90% in the region above the band gap. The films which deposited at higher OMPs showed higher transmittance. The band gap region indicated by the wavelength at which transmittance of the films decreases to 50% is between 320-340nm.

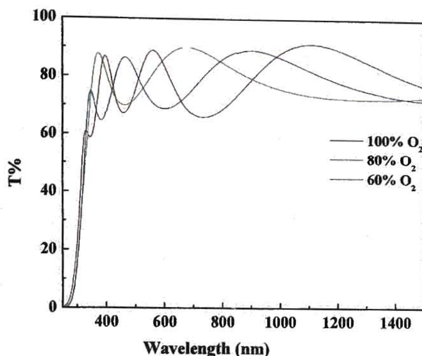

Figure 6.3.1: Transmittance spectra of $ZrTiO_4$ films deposited on fused silica at different OMPs and at a D_{s-t} of 3cm.

The refractive index (n) of the films deposited on glass and on fused silica at different OMPs and D_{s-t} values are shown in figure 6.3.2 a & b respectively. In both the cases it is observed that refractive index decreased with increase in OMP. For the films deposited on glass as well as on fused silica, refractive index decreased with increase in D_{s-t}. The films deposited on fused silica showed higher values of n compared to the films deposited on glass.

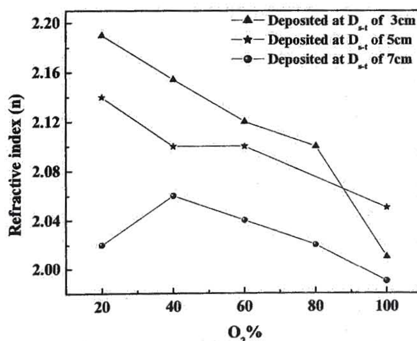

Figure 6.3.2a: Variation in refractive index of $ZrTiO_4$ films deposited on glass at different D_{s-t} values as a function of OMP.

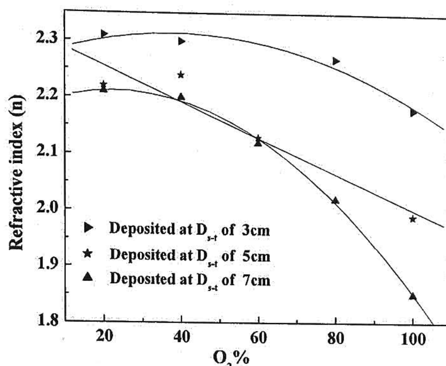

Figure 6.3.2b: Variation in refractive index of $ZrTiO_4$ films deposited on fused silica at different D_{s-t} values as a function of OMP.

The values of n ranged between 1.99-2.19 and 1.85-2.31(at 600nm) in the dispersion free region for the films deposited on glass and fused silica respectively. These values are comparable with the one reported for RF sputtered films deposited at room temperature, and the increase in n is observed with increase in deposition temperature [17]. The variation in packing density for films deposited on fused silica and that for films on glass as a function of OMP is shown in figure 6.3.2c & d respectively.

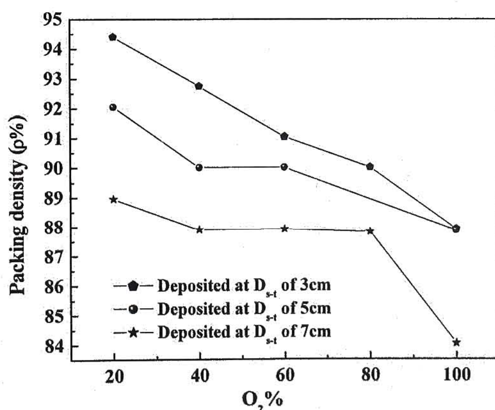

Figure 6.3.2c: Variation in packing density of $ZrTiO_4$ films deposited on glass at different D_{s-t} as a function of OMP.

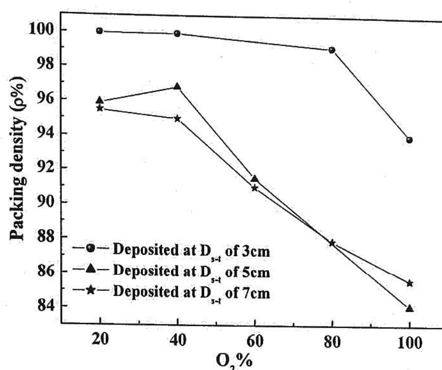

Figure 6.3.2d: Variation in packing density of $ZrTiO_4$ films deposited on fused silica at different D_{s-t} as a function of OMP.

It is observed that the films deposited on fused silica showed higher optical packing densities than the films deposited on glass. In both the cases the films deposited at the D_{s-t} of 3 cm showed higher values compared to the films deposited at 5 and 7cms of D_{s-t}. The packing density of the films supported the refractive index values and also it is observed that the films deposited on glass are porous compared to the films deposited on fused silica. The optical packing density values were ranged between 84-94.4 and 86-99.9 for the films deposited on glass and fused silica respectively. The low values of n observed in the present study may also be partly due to partial crystallinity of the films and low adatom mobility in the films at ambient temperatures. From this study it was observed that the refractive index values were strongly dependent on packing densities.

The extinction coefficient of the films deposited on glass and fused silica are shown in figure 6.3.2e & f respectively. In both the cases it is observed that higher the refractive index, higher is the extinction coefficient and as the OMP increases the extinction coefficient decreases.

The optical bandgap values of $ZrTiO_4$ films deposited on fused silica at different D_{s-t} values and as a function of OMP deposited are shown in figure 6.3.3a. It is observed that the bandgap increased with increase in OMP. The values of bandgap of the films ranged between 3.81-3.96eV and is in the same range as that of the values reported for films deposited by RF magnetron sputtering [17].

Figure 6.3.2e & f: Variation in extinction coefficient of $ZrTiO_4$ films deposited on glass and fused silica respectively at different D_{s-t} as a function of OMP.

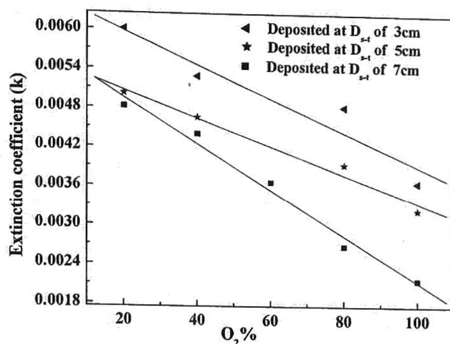

Figure 6.3.2e

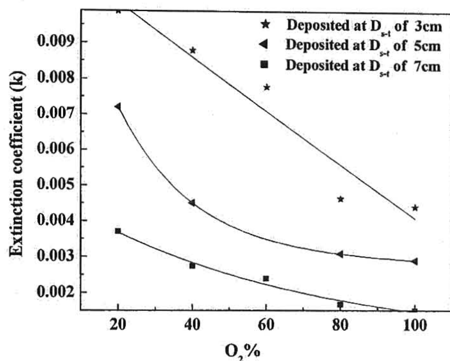

Figure 6.3.2f

The optical bandgap value for bulk $ZrTiO_4$ is not available in the literature. The increase in bandgap for the films on fused silica can be attributed to the reduction in oxygen vacancies with increase in OMP and it is well known that the films grown in the amorphous phase exhibits higher bandgap values.

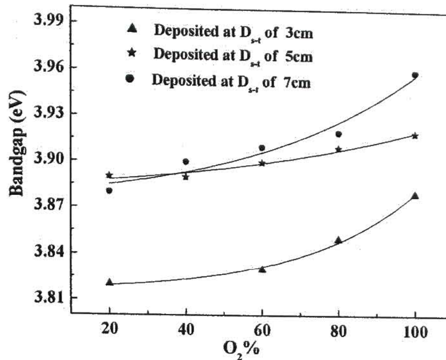

Figure 6.3.3a: Variation in bandgap of $ZrTiO_4$ films deposited on fused silica at different D_{s-t} and as a function of OMP.

But in the case of the films on glass they were partially crystalline and hence lower bandgap values. To get the required composition the ratios of Zr and Ti are varied and optimized, also the author has studied the growth kinetics of TiO_2 and ZrO_2 thin films individually. The ability of sputtering of Zr &Ti in a 100% oxygen atmosphere even with the accompanying problem of target poisoning is important. The observation correlates well with the reports on the growth of TiO_2 and ZrO_2 films starting from TiO_{2-x} and ZrO_{2-x} targets from DC magnetron sputtering. These studies indicate that as long as the target oxidation remains incomplete, sputtering will continue even in DC magnetron sputtering geometry.

6.4 Optical properties of ZST films:

Thin films of ZST are deposited on to glass and on fused silica substrates at a D_{s-t} of 3cm. A D_{s-t} of 3cm is chosen because at this D_{s-t} better crystallinity, structural and optical properties were exhibited. The optical transmittance spectra of the films deposited on fused silica at different OMP are shown in figure 6.4.1. It is observed that the films deposited at higher OMP showed higher transmittance. The transmittance of all the films is around 85% in the region above the band gap. The band gap region indicated by the wavelength at which transmittance of the films decreases to 50% is between 300-340nm.

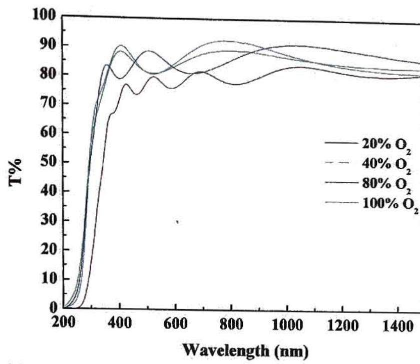

Figure 6.4.1: Transmittance spectra of ZST films deposited on fused silica at different OMPs.

The refractive index (n) of the films deposited on glass and on fused silica at different OMPs is shown in figure 6.4.2a. In both the cases it is observed that refractive index decreases with increase in OMP. The films deposited on fused silica showed higher values of n compared with the films deposited on glass. The values of n ranged between 1.59-1.79 and 1.6-1.85 (at 600nm) in the dispersion free region for the films deposited on glass and on fused silica respectively. These values are lower compared to those reported for RF sputtered films deposited at room temperature. An increase in n is observed with increase in deposition temperature [17-20]. The low values of n observed in the present study may partly be due to partial crystallinity of the films, low adatom mobility and lower packing densities of the films at ambient temperatures.

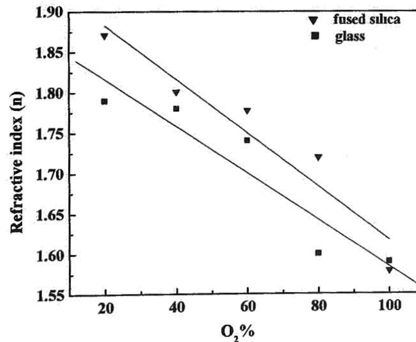

Figure 6.4.2a: Variation in refractive index of ZST films deposited on glass and fused silica as a function of OMP.

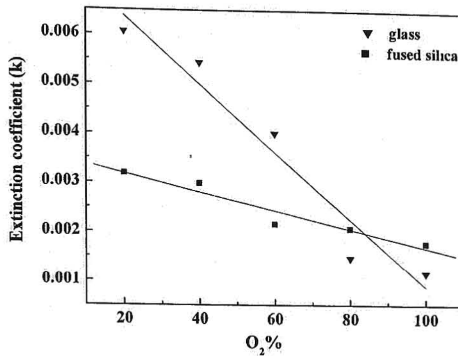

Figure 6.4.2b: Variation in extinction coefficient of ZST films deposited on glass and fused silica as a function of OMP.

The extinction coefficients of the films deposited on both glass and fused silica are shown in figure 6.4.2b. It is observed that extinction coefficient values of films on fused silica are higher compared to that of films on glass, but in both cases the values decreases with decrease in OMP. The extinction coefficient values ranged between 0.0032 to 0.0012 and 0.006 to 0.0012 for the films deposited on glass and fused silica respectively.

The optical bandgap values of $(Zr_{0.8},Sn_{0.2})TiO_4$ films deposited on glass and fused silica as a function of OMP are shown in figure 6.4.3a. In both cases it is observed that the bandgap increased with increase in OMP.

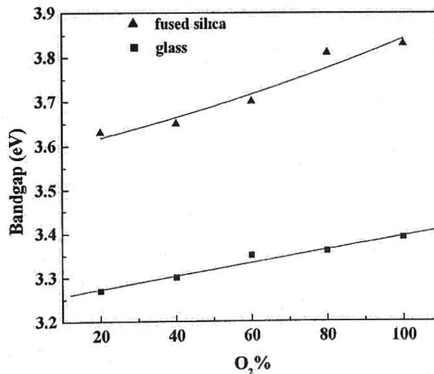

Figure 6.4.3a: Variation in bandgap of ZST films deposited on glass and fused silica as a function of OMP.

The value of bandgap of the films is ranged between 3.27-3.34eV and 3.63-3.83eV for the films deposited on glass and fused silica respectively. These values are equally comparable with the values reported for the films deposited by RF magnetron sputtering and with films prepared by sol-gel process [17-20].

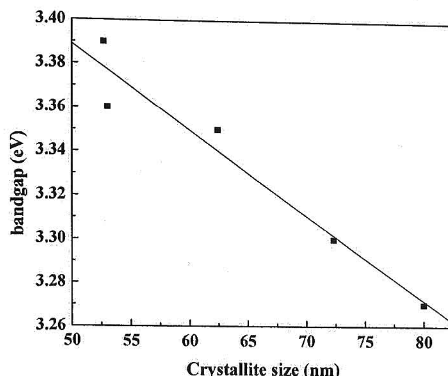

Figure 6.4.3b: Variation in bandgap of ZST films deposited on glass as a function of crystallite size.

The optical bandgap value for bulk $(Zr_{0.8},Sn_{0.2})TiO_4$ is not available in the literature are in agreement with other reports [17-20]. It is well known that the optical bandgap values are a good qualitative estimate of the stoichiometry of the deposited films. The increase in bandgap can be attributed to the reduction in oxygen vacancies and partially crystalline nature of the films with increase in OMP.

To get the required composition, initially the present authors studied the growth kinetics of TiO_2 and ZrO_2 thin films individually and then to deposit $ZrTiO_4$ films, the ratios of Zr and Ti are optimized. The ability of sputtering from Zr, Ti & Sn targets in a 100% oxygen atmosphere even with the accompanying problem of target poisoning is important. This study indicates that as long as the target oxidation remains incomplete, sputtering will continue even in a DC magnetron sputtering geometry. The dependence of bandgap on crystallite size is shown in figure 6.4.3b, the bandgap decreases with increase in crystallite size exhibiting approximately $1/d^2$ dependence.

6.5 Electrical properties of the films in the $(Zr,Sn)TiO_4$ system:

In the present study we have measured the current density of TiO_2, ZrO_2, $ZrTiO_4$ and ZST films as a function of applied voltage. The measurements were performed with MIM structures. The Metal-Insulator-Metal (MIM) capacitor structures are formed with TiO_2, ZrO_2, $ZrTiO_4$ and ZST films deposited at different Oxygen Mixing Percentages (OMP). Platinum coated silicon was used as the substrate. Silver electrodes of thickness 300 nm and area 0.5 x 0.5 mm were deposited as top electrodes using DC magnetron sputtering. The thickness of the oxide layer is about 200nm. The leakage current measurement is carried out with a Precision Materials Analyzer of Radiant technology, USA.

The current density of the films of TiO_2 and ZrO_2 deposited at different OMP are shown in figure 6.5.1a & b as a function of applied voltage. It is observed that the films coated at 100% OMP are having a lower break down voltage compared to the films deposited at lower OMPs. Films deposited with 40% OMP exhibited lowest leakage currents. For TiO_2 films, the leakage current density varied from $3.5x10^{-9}$ A/cm^2 to $2.9x10^{-8}$ A/cm^2 corresponding to 40% OMP and 100% OMP respectively. The calculated resistivity values for TiO_2 films deposited at four OMP values are displayed in figure 6.5.1c. Again the the highest resistivity is exhibited by films deposited at 40% OMP. In most of the ceramic thin films the leakage current is attributed to the Schottky barrier limited current flow [21,22]. For this mechanism, the charge carriers are thermally excited over an energy barrier at metal ceramic interfaces. This barrier is created by equilibration of the energies of charge carriers in the metal and ceramic and its value at zero applied fields is modified by a field dependent lowering of the barrier resulting from the image forces. This is called Schottky effect [23]. An interfacial Schottkey barrier can primarily limit the leakage current through these films where properties depend on the interfaces and microstructure. The current densities started increasing with an applied electric field from 7.5 MV/m and 14.55 MV/m TiO_2 and ZrO_2 films respectively. These values are their respective breakdown field strengths.

The dependence of resistivity and breakdown field strength of these films with OMP can be explained in terms of the oxygen vacancies present in the films. The oxygen vacancies are known to have an important role to play in the resistance degradation of oxide thin films [24]. Films with fewer oxygen vacancies will have

high resistance than that having more oxygen vacancies. The oxygen vacancies are created in a material system as per the following equation.

$$O_O = 1/2O_2 + V_o + 2e^{-} \quad (6.5.1.1)$$

Figure 6.5.1a & b: Variation in current densities of TiO_2 and ZrO_2 films as a function of applied voltage.

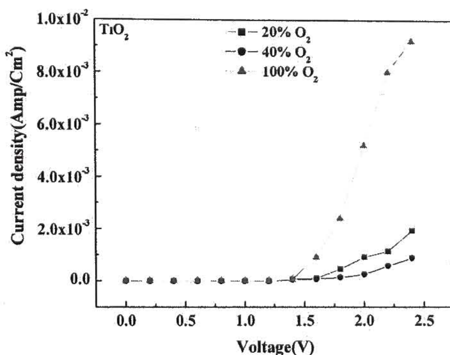

Figure 6.5.1a

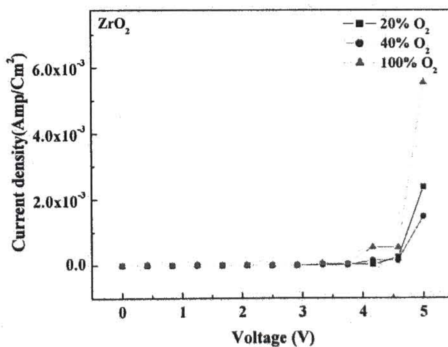

Figure 6.5.1b

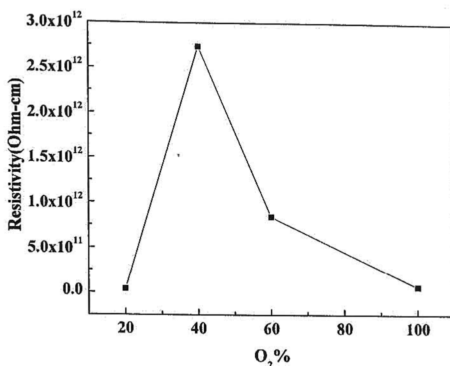

Figure 6.5.1c: Variation in resistivity of TiO_2 films as a function of OMP.

These reactions show that the number of oxygen vacancies could strongly dependent on OMP. Along with the electro neutrality condition, this will determine the defect concentration and the conductivity mechanism of the thin films.

At higher oxygen partial pressures there is a possibility of reduction of Ti & Zr through reverse oxygen sputtering resulting in the formation of TiO_{2-x} and ZrO_{2-x}, followed by a chemical segregation to the grain boundaries. This could affect the dielectric and the conduction behavior of TiO_2 and ZrO_2 films at the higher OMPs. In the TiO_2 and ZrO_2 films excess Ti and Zr accommodation is possible by the combination of the following reactions [25,26],

$$AO_2 \rightarrow A \quad + 2O_i'' \qquad (6.5.1.2)$$

Or

$$AO_2 \rightarrow A \quad + 4e' + O_2 \qquad (6.5.1.3)$$

where A=Ti or Zr and A +4e' → A

The variation in current density of $ZrTiO_4$ and ZST films deposited at different OMP are shown in figure 6.5.2a & b as a function of applied voltage. In both the cases it is observed that the films deposited at 40% OMP showed lowest leakage current density while films deposited in 100% OMP exhibited higher values. The magnitude of current densities is 9.03×10^{-7} and 9.72×10^{-7} Amp/cm^2 at 1.25 Volt/m are observed for $ZrTiO_4$ and ZST films respectively. The breakdown field strenght of the $ZrTiO_4$ and ZST films at 40% OMP are found to be 8 MV/m and 16.55 MV/m. Again

it was found that at other OMP values, the breakdown starts from lower field strengths for both films.

Figure 6.5.2a & b: Variation in current density of $ZrTiO_4$ and ZST films as a function of applied voltage.

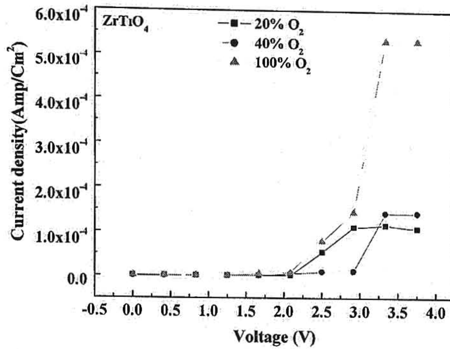

Figure 6.5.2a

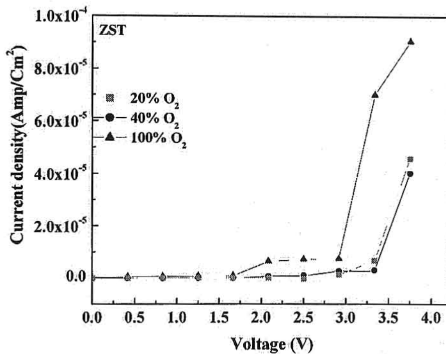

Figure 6.5.2a

In general the poly crystalline samples exhibit a lower leakage current than highly oriented films [27]. The leakage current is influenced by the grain size, crystallinity and surface morphology because of the presence of electrostatic barriers at the grain -grain interfaces which arise from the donor acceptor type traps localized at the grain boundaries [27]. Surface and grain boundaries introduce additional electronic states in the band gap because of the unsaturated bonds, which arise from

the disruption of the periodical crystal lattice. Hence these grain boundaries act as charge carrier trap sites. Due to the presence of grain boundary space charge layer which is formed eventually, the flow of charges gets limited. As the microstructure contains many grains and grain boundaries the leakage current will be lesser in these polycrystalline films. From this study, it is clear that by optimizing the processing parameters we can reduce the leakage current density and increase the breakdown field strength. The values obtained in this study for all the film compositions shows that they can be used in integrated circuits and the films deposited at 40% OMP gave the best results in all cases.

Conclusions:

- Titania and zirconia thin films are deposited by DC reactive magnetron sputtering on glass and fused silica substrates at different OMPs.
- $ZrTiO_4$ films are deposited from Zr and Ti metal targets using DC reactive magnetron sputtering on to borosilicate and fused silica substrates at different OMPs in the sputtering atmospheres. The distance between target and substrate (D_{s-t}) is varied (3, 5 and 7cms) to identify the suitable D_{s-t} and found that D_{s-t} of 3cm gave best properties among them.
- For the first time, ZST films are deposited from a composite metal target of Zr, Sn and Ti by DC reactive magnetron sputtering.
- The systematic study of the optical properties such as refractive index, extinction coefficient and bandgap of the TiO_2, ZrO_2, $ZrTiO_4$ and ZST films are carried out with the variation in OMP.
- For the first time TiO_2, ZrO_2, $ZrTiO_4$ and ZST films are deposited in pure oxygen plasma and their optical properties are reported.
- The optical properties TiO_2 films deposited in pure dc oxygen plasma are studied as a function of distance between target and substrate and at different working pressures.
- TiO_2 films deposited in pure oxygen plasma exhibited better properties at D_{s-t} of 4cm with a working pressure of 0.05 mTorr.
- In all the cases the transmittance of the films is higher with increase in OMP.
- Films deposited on fused silica showed higher transmittances compared to the films deposited on glass.

- In all the cases both refractive index and extinction coefficient of the films decreased with increase in OMP.
- The variation in refractive index values are attributed to the packing densities and partial crystallinity of the films.
- The bandgap decreases with increase in crystallite size exhibiting approximately $1/d^2$ dependence.
- Films deposited at higher working pressures showed higher bandgap values.
- The films deposited on fused silica exhibited higher bandgap values than the films deposited on glass and is attributed to the fact that the films grown in the amorphous phase exhibits higher bandgap values.
- In all the cases the bandgap values have increased with increase in OMP indicating that the films are well oxidized with increasing OMP.

References:

[1] R. Dannenberg and Phil Greene, Thin Solid Films, **360**,122 (2000).

[2] D. Mardare and A. Stancu, Mater. Res. Bull., **35**, 2017 (2000).

[3] M.H.Suhail, G.Mohan Rao and S.Mohan, J.Appl.Phys., **71**, 1421 (1992).

[4] S.Tanemura, L.Miao, P.Jin, K.Kaneko, A.Terai and N.N.Gabain, Appl.Surf.Sci., **212-213**, 654 (2003).

[5] O.Zywitzki, T.Modes, H.Sham, P.Frach, K.Goedicke and D.Glob, Surf. Coat. Technol., **180-181**,538 (2004).

[6] N.Martin, C.Rouselot, C.Savall, and F.Palmino, Thin Solid Films, **287**, 154 (1996).

[7] J.D.DeLoach, G.Scarel and C.R.Aita, J.Appl.Phys., **85**, 2377 (1999).

[8] M.G.Krishna and A.K.Bhattacharya, Inter. J.Moder. Phys. B, **15**, 191 (2001).

[9] S.Mohan and M.G. Krishna, Vacuum, **46**, 645 (1995).

[10] Y. Tachibana, H. O. Hayashi, A. Mitsui and Y. Hayashi, Vacuum, **59**, 836 (2000).

[11] H.Tomaszewski, H.Poleman, D.Depla, D.Poelman, R.Gryse, L.Fiermans, M. F. Reyniers, G.Heynderick, and G B. Marin, Vacuum, **68**, 31 (2003).

[12] G.Pengtao, L.J.Meng, M.P.dos Santos, V.Teixeira, and M.Andritschky, Thin Solid Films, **377-378**, 557 (2000).

[13] S.B.Amor, B.Rogier, G.Baud, M.Jacquet and M.Nardin, Mater.Sci.Eng.B. **57**, 28 (1998).

[14] S.Venkataraj, O.Kappertz, Ch.Liesch, R.Detemple, R.Jayavel, and M.Wuttig, Vacuum, **75**, 7 (2004).

[15] M.H.Suhail, G.Mohan Rao, and S.Mohan, J.Vac.Sci.Technol.A. **9**, 2675 (1991).

[16] M.S.Wong, W.J.Chia, P.Yashar, J.M.Schneider, W.D.Sproul, and S.A.Barnett, Surf.Coat.Technol., **86-87**, 381 (1996).

[17] D-A.Chang, P.Lin and T-Y. Tseng, J.Appl.Phys., 77, 4445 (1995).

[18] R-Y.Yang, Y-K.Su, M-H.Weng and Y-S.Ho, Appl.Surf.Sci. **253**, 2203 (2006).

[19] C-L. Huang and C-H. Hsu, J.Appl.Phys. **96**, 1186 (2004).

[20] W.X. Cheng, A.L.Ding, P.S.Qiu, X.Y.He and S.S.H.Zheng, Appl.Surf.Sci. **214**,136 (2003).

[21] G.W.Dietz, M. Schumacher, R. Waser S. K. Streiffer, C. Basceri, and A.I.Kingon, J.Appl.Phys., **82**, 2359 (1997).

[22] R. Waser, Integr.Ferroelectrics, **15**, 39 (1997).

[23] G.W.Dietz and R. Waser, Integr.Ferroelectrics, **9**, 317 (1995).

[24] K .P. Jayadevan, C-Y. Liu, and T-Y. Tseng, J.Am.Ceram.Soc., 88, 2456 (2005).

[25] D.M.Smyth, J.Solid State Chem., **20**, 359 (1976).

[26] R.K.Sharma, N-H.Chan and D.M.Smyth, J.Am.Ceram.Soc., **64**, 448 (1981).

[27] L-J.Wu and J-M.Wu, J.Phys. D: Appl.Phys., 40, 4948 (2007).

Chapter-7

Dielectric Properties of Thin Films in the $(Zr,Sn)TiO_4$ System

The present chapter describes the dielectric properties of thin films in the system $(Zr,Sn)TiO_4$. The dielectric properties have been measured both at low (100 KHz to 10 MHz) and at microwave (8.2 to 12.4 GHz) frequency range. The details of measurement techniques have been discussed in section 2.7 of chapter 2. In the present study the thin films of $ZrTiO_4$ were deposited from single cathode using Zr and Ti metal targets and ZST films were also deposited from the single cathode (from Zr, Ti & Sn metal targets). However, the dielectric properties of TiO_2, ZrO_2, $ZrTiO_4$ and ZST films as a function of Oxygen Mixing Percentage (OMP) have not been studied systematically both at lower and at microwave frequencies.

7.1 Dielectric properties of films in the system $(Zr,Sn)TiO_4$ at low frequencies

The Metal-Insulator-Metal (MIM) capacitor structures of the TiO_2, ZrO_2, $ZrTiO_4$ and ZST films are deposited on platinized silicon at different OMP. Silver electrodes of thickness 300 nm and size 0.5 x 0.5 mm were deposited as top electrodes using DC magnetron sputtering. The thickness of the oxide layer is about 200nm.

7.1.1 Low frequency dielectric properties of TiO_2 films:

The variation in dielectric constants and dielectric loss of the films deposited at different OMP as a function of frequency are shown in figure 7.1.1a & b respectively. It is observed that as the frequency increases the dielectric constant of the films decreased. It is also observed that the dielectric constant of the films increased with increase in OMP up to 40% and thereafter started decreasing. Films deposited with 40% OMP exhibited high dielectric constants (56 to 70.6) compared to the films deposited at other OMP and the films deposited in pure oxygen atmosphere showed lower values.

The dielectric constants of these films are found to be varying from 70.6 to 54.73 over a frequency range of 100 KHz to 10 MHz. All these films show a clear frequency dispersion of dielectric constant. The dielectric loss of the films increased

with increase in frequency as well as with increase in OMP except for the film deposited at 40% OMP.

Figure 7.1.1a & b: Dielectric constant and tanδ of TiO_2 films deposited at different OMP as a function of frequency.

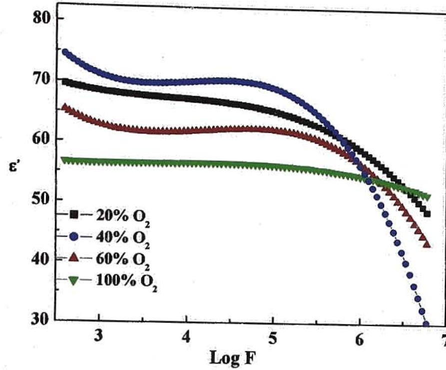

Figure 7.1.1a

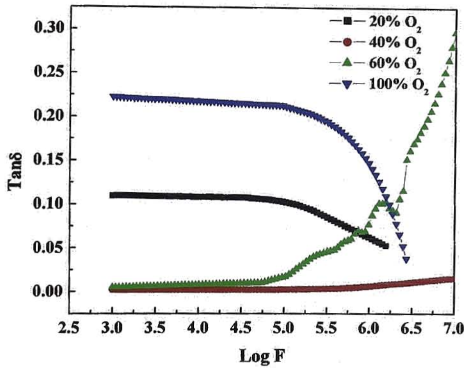

Figure 7.1.1b

In the lower frequency region, the dielectric loss tangent is slightly higher compared to that of at higher frequencies. This variation in loss at lower frequencies may be due to the contributions from metal electrode and the electrode interfaces. The defects present in these thin films could constitute local defect oriented polarization centers and these defects oriented dipoles could try to align themselves in the

direction of the field. Hence the observed variation of dielectric constant and loss tangent of these films can be explained in terms of the dipolar theory of dielectrics. The dielectric dispersion in these TiO_2 thin films could partly be caused by a compositional heterogeneity in a local level. The main cause for this suspected compositional heterogeneity is oxygen vacancies. The oxygen vacancies can get connected with locally frozen cation vacancies or an external field can reorient impurities. This could constitute the orienting dipoles in these systems. The dielectric constant and loss of the films measured at 5 MHz are tabulated in table 7.1.I. The systematic study of the dielectric properties of these films with variation in OMP is not reported earlier.

Alexandrove et al [3] reported the value of dielectric constant (ε') of TiO_2 films at 1 KHz and found to vary between 30 to 60 where as for the same films measured at 1MHz the values were found to be between 16 and 52.

OMP	**20%**	**40%**	**60%**	**100%**
ε'	49.6	51.08	43	33.9
Tanδ	0.213	0.051	0.26	0.33

Table 7.1.I: Dielectric constant and tanδ of TiO_2 films measured at 5 MHz.

Various values for the ε' of TiO_2 thin films have been reported for different methods of deposition and crystalline phases by various authors. Examples are, $\varepsilon' = 4$-40 (amorphous and rutile) [4], $\varepsilon' = 5$-80 (amorphous and mixed anatase+rutile) [5], $\varepsilon' = 42$ (amorphous and anatase) [6] and $\varepsilon' = 58.5$-77(rutile) [7].

7.1.2 Low frequency dielectric properties of ZrO_2 thin films:

The variation in dielectric constant and loss of ZrO_2 films as a function of frequency for the films deposited at different OMP are shown in figure 7.1.2a & b respectively. It is observed that as the OMP increases from 20% to 40% the dielectric constant increased and thereafter it started decreasing, where as the dielectric loss is lowest for the film deposited at 40% of OMP.

Figure 7.1.2a & b: Dielectric constant and tanδ of ZrO_2 films deposited at different OMP as a function of frequency.

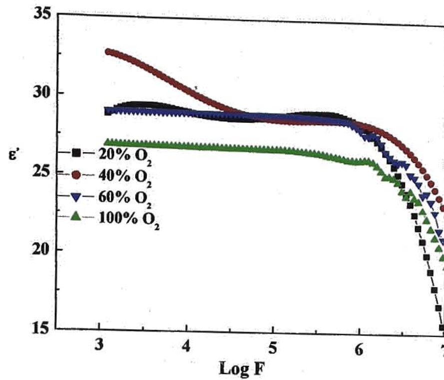

Figure 7.1.2a

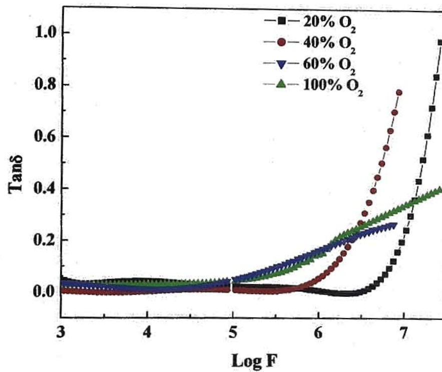

Figure 7.1.2b

The dielectric constants of the films decreased with increase in frequency while the loss increased with increase in frequency. Interestingly, the films deposited at 40% of OMP showed higher dielectric constants with lower loss. It is well known that the processing conditions can cause the variations in stoichiometry and oxygen vacancies, resulting in differences with the dielectric constants. The obtained values in this study at 5 MHz are tabulated in table 7.1.2.I.

OMP	20%	40%	60%	100%
ε'	21.65	24.5	18.93	15.6
Tanδ	0.055	0.029	0.11	0.18

Table 7.1.2.I: Dielectric constant and tanδ of ZrO_2 films measured at 5 MHz.

Jeong et al [8] reported that the dielectric constant for YSZ and ZrO_2 RF sputtered films are 24 and 21.6 respectively, when measured at 1MHz; Vrejoiu et al [9] reported that for laser ablated ZrO_2 films, the dielectric constant is 12 when measured at 2MHz.

7.1.3 Low frequency dielectric properties of $ZrTiO_4$ thin films:

The variation in dielectric constant and loss of $ZrTiO_4$ films deposited at different OMP as a function of frequency are shown in figures 7.1.3a & b respectively. It was observed that as the OMP in the sputtering atmosphere increases from 20% to 40%, the dielectric constants of the films increased and thereafter it started decreasing with increase in OMP. It was found that the films deposited with 40% of OMP exhibited higher dielectric constant and lower losses. The dielectric constant of these films did not show much dependence on frequency whereas the loss is higher at lower frequency region and can be due to the metal electrode and its interface. At higher frequency region, the loss tangent remained constant. The loss of the films deposited above and below 40% of OMP was higher. The films deposited in pure oxygen atmosphere showed lowest dielectric constant and highest losses.

The dielectric constant and loss of the $ZrTiO_4$ films measured at 5 MHz were tabulated in table 7.1.3.I. Viticoli et al [10] reported a dielectric constant of 41 and tanδ of 3.1×10^{-4} at 1MHz for the films deposited by PLD at 550°C and Padeletti et al [11] reported a dielectric constant of 40 at 1MHz for the films deposited by MOCVD at 600°C.

Kim et al [12] reported a resonance in the dielectric response of $ZrTiO_4$ film is about 1MHz and in the present study such a response was found above 18 MHz. It could will be the effect of test fixture as it is known that a test fixture could give a resonance depending on the stray capacitances and inductances associated with it. Therefore dielectric constant and loss are measured till the onset of this resonance. It

is relevant to note that the resonance type relaxation appears in a paraelectric material usually in the far infrared and optical range of frequencies [13].

Figure 7.1.3a & b: Dielectric constant and tanδ of $ZrTiO_4$ films deposited at different OMP as a function of frequency.

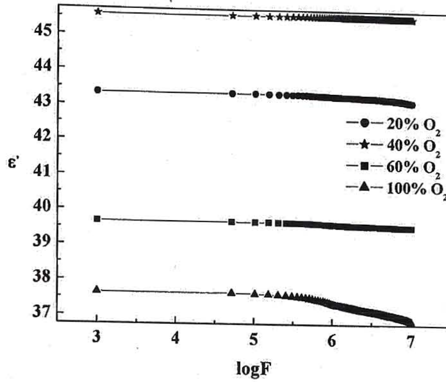

Figure 7.1.3a

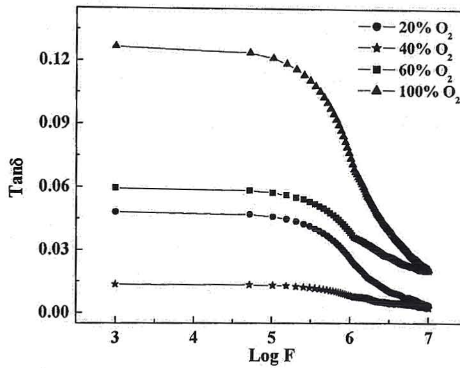

Figure 7.1.3b

OMP	20%	40%	60%	100%
ε'	43.23	46.55	39.56	37.0
Tanδ	0.007	0.004	0.023	0.03

Table 7.1.3.I: Dielectric constant and tanδ of $ZrTiO_4$ films measured at 5 MHz.

7.1.4 Low frequency dielectric properties of ZST thin films:

The variation in dielectric constant and dielectric loss of ZST films deposited at different OMPs as a function of frequency are shown in figure 7.1.4a & b respectively. It was observed that as the OMP increases the dielectric constant increased up to 40% and thereafter started decreasing. At lower frequencies film deposited at 20% OMP showed higher dielectric constant values compared to the film deposited at 40% OMP above that the dielectric constant of the film deposited at 20% OMP is decreased with increase in frequency. It was also observed that the dielectric loss was slightly higher at the low frequency region. The films deposited in pure oxygen plasma showed higher loss with lower dielectric constants where as the films deposited at 40% OMP exhibited higher dielectric constant with lower loss.

Cheng et al [14] reported a dielectric constant of 36.6 and tanδ of 0.0069 for the RF sputtered ZST films measured at 100 KHz, while the corresponding values reported by Viticoli et al [11] for the pulsed laser deposited ZST films measured at 1MHz is 38 and 0.0055. Huang et al [15] reported that the dielectric constant for the RF sputtered ZST films deposited at 450°C and measured at 10 MHz is 51.

Figure 7.1.4a & b: Dielectric constant and tanδ of ZST films deposited at different OMP as a function of frequency.

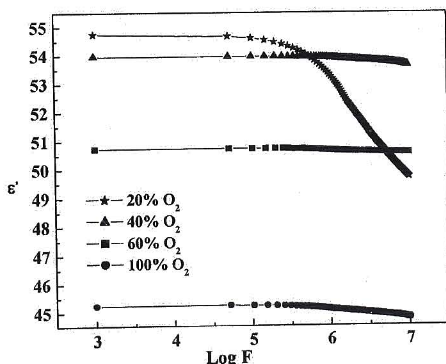

Figure 7.1.4a

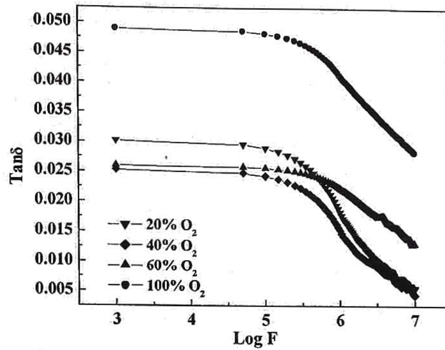

Figure 7.1.4b

The dielectric constant and loss of ZST films measured at 5 MHz are tabulated in table 7.1.4.I.

OMP	20%	40%	60%	100%
ε'	50.74	53.7	50.6	44.9
Tanδ	0.008	0.0075	0.016	0.03

Table 7.1.4.I: Dielectric constant and tanδ of ZST films measured at 5 MHz.

Conclusions:

- The MIM structures of TiO_2, ZrO_2, $ZrTiO_4$ and ZST thin films were fabricated at different OMP.
- The dielectric properties of these films were measured at low frequencies. In the case of TiO_2 and ZrO_2 films the dielectric constant decreased with increase in frequency where as the dielectric loss increased with increase in frequency.
- In the case of $ZrTiO_4$ and ZST films, there is not much change in dielectric constant with increase in frequency where as the dielectric loss of the films decreased with increase in frequency.
- In all the cases, films deposited around 40% OMP showed highest dielectric constant and lowest dielectric losses compared to the films deposited at other OMP.

- It is found that at lower frequencies all the films in the $(Zr,Sn)TiO_4$ system exhibited dielectric constant values comparable to that of their bulk counterparts.
- It is observed that the OMP in sputtering atmosphere played an important role on the dielectric properties of films in the $(Zr,Sn)TiO_4$ system.

7.2 Microwave dielectric properties of films in the $(Zr,Sn)TiO_4$ system:

The microwave dielectric constant and dielectric loss of the thin films in the $(Zr,Sn)TiO_4$ system, deposited on borosilicate glass substrates has been measured at some spot frequencies in the X-band frequency range (8.2-12.4 GHz). The spot frequencies are selected from the available resonances of the cavity used in the measurement. At the selected resonance frequencies of the cavity, the sample is at the maximum E field position.

7.2.1 Effect of frequency variation on microwave dielectric constant and on loss of films in the $(Zr,Sn)TiO_4$ system:

The variation of dielectric constant and tanδ of TiO_2 films deposited at various OMP on glass as a function of frequency are shown in figure 7.2.1a & b. The frequency dependence of the microwave dielectric properties of the films deposited on glass in pure oxygen atmosphere at different working pressures at a Ds-t of 4cm is shown in figure 7.2.1.c & d. For ZrO_2 films deposited on glass at various OMP, the variation of dielectric constant and loss as a function of frequency are shown in figure 7.2.1e & f respectively. Similarly the variation in dielectric constant and loss for $ZrTiO_4$ and ZST films deposited on glass are shown in figures 7.2.1g & h and 7.2.1i & j respectively.

In all the cases it is observed that the dielectric constant slightly decreased with increase in frequency, where as the dielectric loss increased with increase in frequency. This variation in dielectric constant indicates the presence of a weak dipolar relaxation in the films of TiO_2, ZrO_2, $ZrTiO_4$ and ZST around this frequency range. Since oxygen partial pressure is the processing variable in these samples, it is quiet possible that dipoles associated with oxygen non-stoichiometry are responsible for this weak relaxation. To highlight the influence of OMP on the microwave dielectric properties of these films, the data presented in this section are plotted as a

function of OMP, in the next section. It is interesting to note that as in the case of low frequencies, the dielectric properties of films prepared near 40% of OMP gave better result, indicating the key role played by oxygen stoichiometry in the dielectric properties of these films.

Figure 7.2.1a & b: Dielectric constant and tanδ of TiO_2 films deposited at various OMP on glass as a function of frequency.

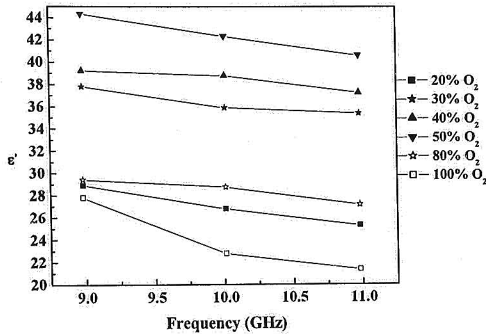

Figure 7.2.1a

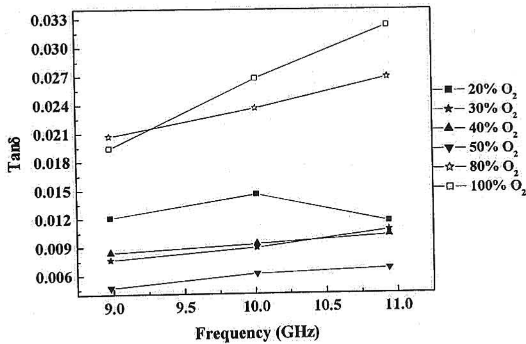

Figure 7.2.1b

Figure 7.2.1c & d: Dielectric constant and tanδ of TiO_2 films deposited on glass in pure oxygen atmosphere at various working pressures, plotted as a function of frequency.

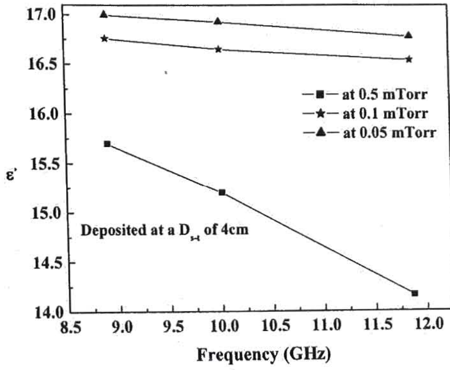

Figure 7.2.1c

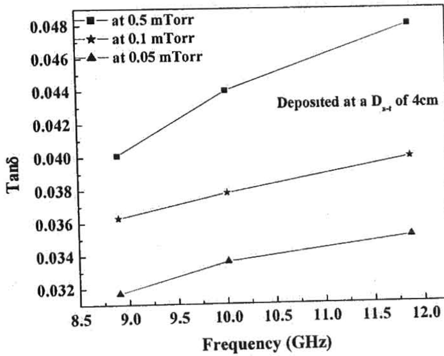

Figure 7.2.1d

Figure 7.2.1e & f: Dielectric constant and tanδ of ZrO_2 films deposited at various OMP on glass as a function of frequency.

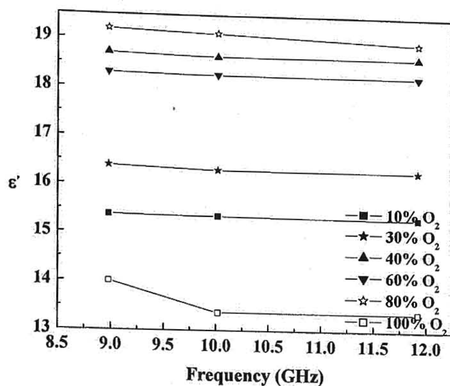

Figure 7.2.1e

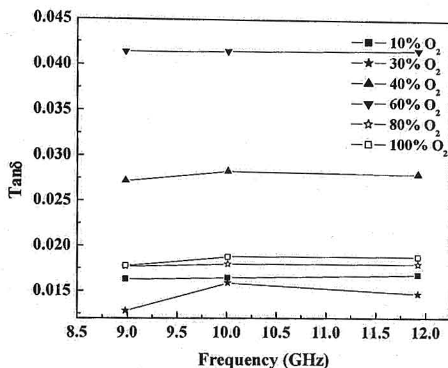

Figure 7.2.1f

It is also important to note that at low frequencies the measurement required a capacitor structure while the as deposited films could be used in the microwave frequencies. In that way, measurements at microwave frequencies are loss influenced by extraneous factors like a buried metal electrode, top electrode and the associated interface effects. However the number of data points in the microwave frequencies is few compared to the lower frequency measurements using an impedance analyzer.

Figure 7.2.1g & h: Dielectric constant and tanδ of $ZrTiO_4$ films deposited at various OMP at various OMP on glass as a function of frequency (lines are only a guide to eye).

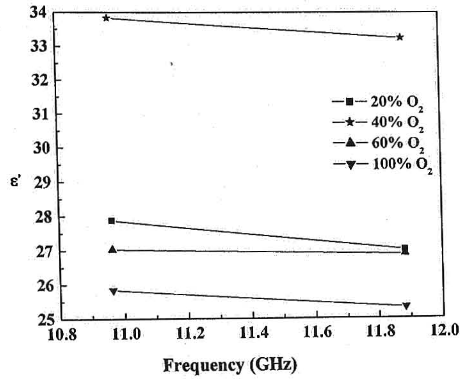

Figure 7.2.1g

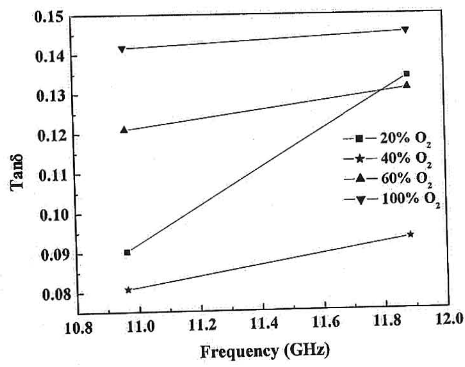

Figure 7.52.1h

Figure 7.2.1i & j: Dielectric constant and tanδ of ZST films deposited at various OMP on glass as a function of frequency (lines are only a guide to eye).

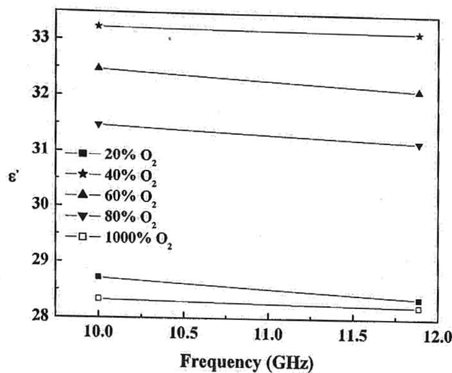

Figure 7.2.1i

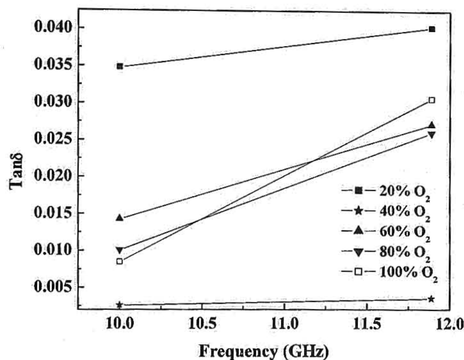

Figure 7.2.1j

7.3 Effect of OMP on microwave dielectric constant and tanδ of films in the (Zr,Sn)TiO_4 system:

7.3.1 TiO_2 thin films:

The dependence of the dielectric constant and loss (Tanδ) as a function of OMP is shown in figure 7.3.1a & b respectively. The value of the dielectric constant obtained for TiO_2 thin films is found to increase initially as the OMP increases. It

achieves a maximum value around 50% of OMP for all the three measurement frequencies. Further increase of the OMP causes the dielectric constant to decrease and the loss factor to increase. The dielectric constant increases from 21 at 20% OMP to 44 at 50% OMP and decreases beyond this value.

The film deposited at 50% of OMP showed better densification compared to the other films and are observed from the Scanning Electron Micrograph (SEM) pictures which are shown in the discussion of structure and morphology of TiO_2 films in chapter 5 section 5.2.7. At the same OMP (i.e. 50%), the dielectric loss shows a minimum in its value, increasing thereafter. The variation of dielectric constant and loss at different OMP may be the result of stoichiometric changes resulting from the variation of OMP.

SEM pictures also indicate that the densification is maximum around 50% OMP and porosity increases thereafter. This could cause the increase in dielectric constant near 50% OMP, and partly explain the reduction in dielectric constant beyond 50% OMP as they showed higher porosities with lower grain sizes at these OMPs.

Figure 7.3.1a & b: Dielectric constant and tanδ of TiO_2 films deposited on glass as a function of OMP.

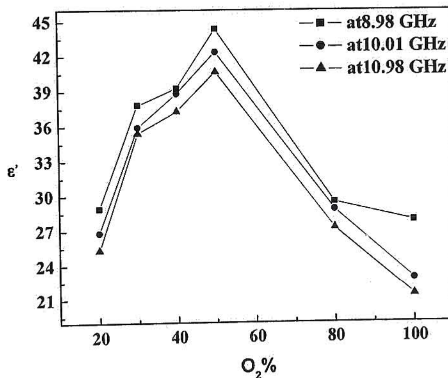

Figure 7.3.1a

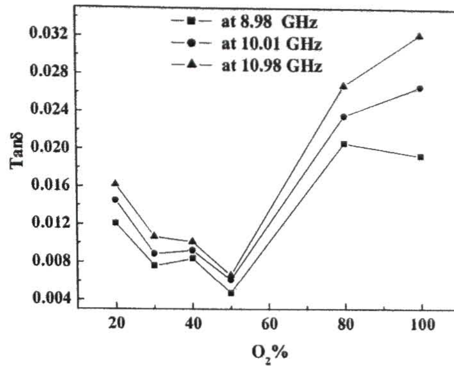

Figure 7.3.1b

Figure 7.3.1c & d: Dielectric constant and tanδ of TiO_2 films deposited on glass at various working pressures in pure oxygen atmosphere as a function of D_{s-t}.

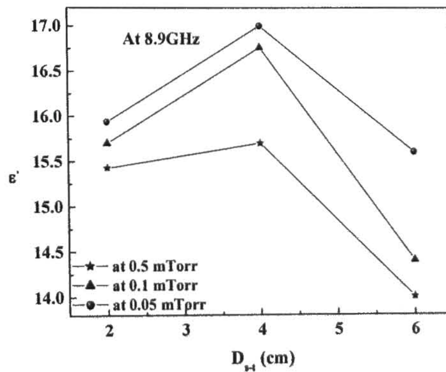

Figure 7.3.1c

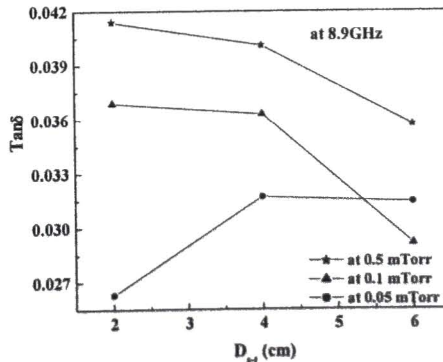

Figure 7.3.1d

Figure 7.3.1c & d shows the variation of dielectric constant and loss of TiO_2 films deposited on glass at different working oxygen pressures in pure oxygen atmosphere, plotted as a function of distance between substrate to target (D_{s-t}). Interestingly, the variation in crystallite size vs. D_{s-t} also followed a similar trend (section 5.2.1, figure 5.2.4 of chapter 5). It is found that dielectric constant decreased with increase in working pressure and showed maximum values for films deposited at a D_{s-t} of 4cm. In all the cases dielectric constant peaked at a D_{s-t} of 4cm irrespective of working pressure. It can also be noted from figure 7.3.1c that at a D_{s-t} of 4cm the crystallite size of these films are maximum irrespective of the working pressure. The maximum dielectric constant value is found to be 17 for the films deposited at 0.05 m.Torr working pressure at a D_{s-t} of 4cm and measured at 8.9GHz. The dielectric loss is also found to be low for films deposited at lower working pressures (0.05 mTorr) irrespective of the D_{s-t}. The increase in dielectric loss at higher working pressures coincides with occurrence of lower packing densities and smaller grains.

7.3.2 ZrO_2 thin films:

The microwave dielectric constant and dielectric loss of ZrO_2 films deposited as a function of OMP on glass and fused silica measured at different frequencies are shown in figure 7.3.2a & b and 7.3.2c & 2d respectively. For the films deposited either on glass or fused silica, there is not much variation in dielectric constant with increase in frequency. For the films deposited on glass, it is observed that as the OMP increases the dielectric constant increased up to 80% and above that it decreased. The maximum dielectric constant is found to be 19.2 measured at 11.92GHz for the films deposited at 80% OMP. The dielectric constant values ranged from 13-19.2. The dielectric loss is found to be lower for the films deposited at 30% OMP.

Figure 7.3.2a & b: Dielectric constant and tanδ of ZrO_2 films deposited on glass as a function of OMP.

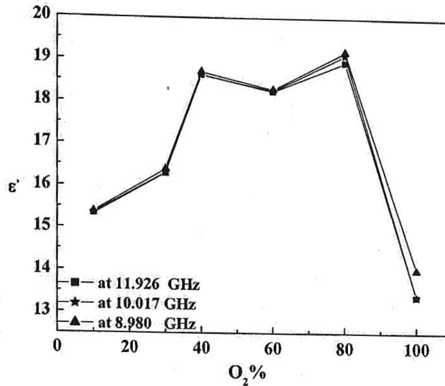

Figure 7.3.2a

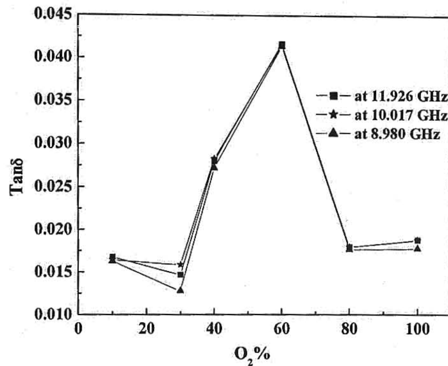

Figure 7.3.2b

For the films deposited on fused silica the dielectric constant decreased with increase in OMP. The maximum dielectric constant of the deposited films observed is 22.3 measured at 8.24 GHz and the values ranged from 12.16 to 22.3. It is observed that the dielectric loss is lower for the films deposited at 20% OMP. The dielectric loss of the films deposited on glass and fused silica peaked at 60% and 40% of OMP respectively. The increase in dielectric constant of the films deposited on glass with increase in OMP up to 60% can be attributed to the presence of cubic phase and to the possible variations in stoichiometry of the films. One of the reasons for the lower

dielectric constant values at 100% OMP could be the lower optical packing density (68.6%).

Figure 7.3.2c & d: Dielectric constant and tanδ of ZrO_2 films deposited on fused silica as a function of OMP.

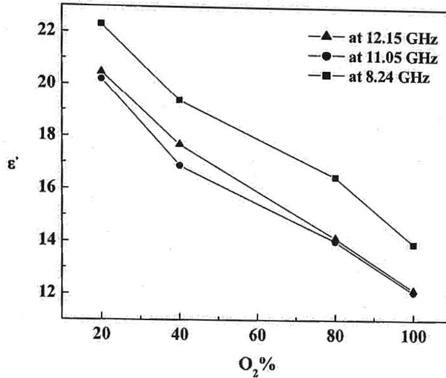

Figure 7.3.2c

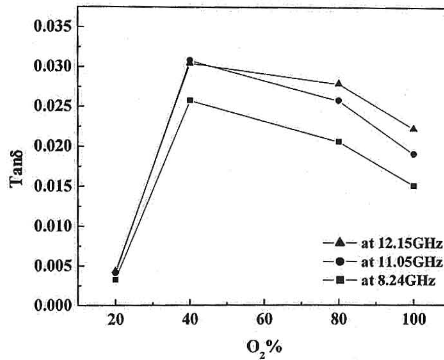

Figure 7.3.2d

The increase in dielectric constant for the films deposited on fused silica compared to that on glass could partly be attributed to the higher optical packing densities (88.5-94.2%) similarly, corresponding to the reduction in dielectric constant with OMP, a decrease in optical packing density could be observed (section 6.2, figure 6.2.2c of chapter 6). In addition, the defects in the crystal lattice will contribute

to dielectric losses, which could set off electrostriction about the defects that excite acoustic vibrations in the medium, which tend to dissipate the energy of the microwave field [13].

7.3.3 $ZrTiO_4$ thin films:

The variation in microwave dielectric constant and loss of $ZrTiO_4$ films deposited on glass as a function of OMP is shown in figure 7.3.3. It is found that as the OMP increases the dielectric constant increased up to 40% of OMP and above that it started decreasing whereas the dielectric loss is lower at 40% OMP, with higher values above and below that. The maximum value of dielectric constant is 33.84 and minimum value of loss is 0.081 at 10.96 GHz observed for films prepared at 40% OMP. The reduction in dielectric loss at 40% of OMP can be partly attributed to the larger grain size, which is clearly observed from the DFM pictures (chapter 5, section 5.4.3).

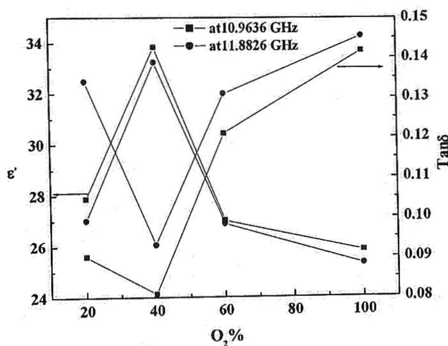

Figure 7.3.3: Dielectric constant and tanδ of $ZrTiO_4$ films deposited on glass as a function of OMP.

The specimen with large grain is expected to have a lower dielectric loss because the grain growth decreases the grain boundary area. The dielectric constant and loss values are ranged between 25.84-33.84 and 0.08-0.141 at 10.96 GHz respectively. Dielectric properties of $ZrTiO_4$ films at microwave frequencies are reported for the first time.

7.3.4 ZST thin films:

The dependence of the dielectric constant and loss (Tanδ) of ZST films deposited on glass as a function of OMP is shown in figure 7.3.4. The value of the dielectric constant obtained for ZST thin films is found to increase initially as the OMP increases. It achieves a maximum value around 40% of OMP for both the measurement frequencies. Further increase of the OMP causes the dielectric constant to decrease and the loss factor to increase. The dielectric constant increases from 28.71 at 20% of OMP to 33.23 at 40% OMP and decreases beyond this value.

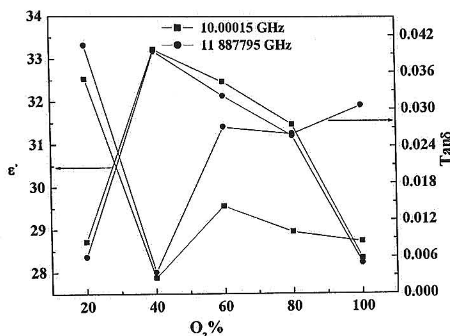

Figure 7.3.4: Dielectric constant and tanδ of ZST films deposited on glass as a function of OMP.

At the same OMP the dielectric loss shows a minimum in its value, increasing there after. The reduction in loss at 40% OMP coincides with the increase in uniform grain size which was observed from the DFM (chapter 5, section 5.5.4) images and the increase in dielectric loss at other OMPs coincides with the smaller grain sizes.

7.4 Effect of crystallite size and bandgap on microwave dielectric properties of films in the (Zr,Sn)TiO_4 system:

7.4.1 TiO_2 thin films:

The microwave dielectric constant and tanδ of TiO_2 films deposited on glass are plotted as a function of their respective crystallite size and are shown in figures 7.4.1a & b respectively. It is observed that as the crystallite size increases the dielectric constant increased up to 37.6 nm and above that it started decreasing with

further increase in crystallite size. The dielectric loss is higher at lower crystallite sizes and decreased with increase in size. Beyond a size of 37.6nm, the dielectric loss also started increasing with further increase in crystallite size and with increase in frequency. The dielectric constant and dielectric loss shows a clear dependence on the crystallite size and the microstructure. The observed changes in the microwave dielectric properties of these thin films can be directly attributed to the observed changes in the microstructure as clearly seen in the DFM images (chapter 5, section 5.2.5).

Figure 7.4.1a & b: Dielectric constant and tanδ of TiO_2 films deposited on glass plotted as a function of crystallite size.

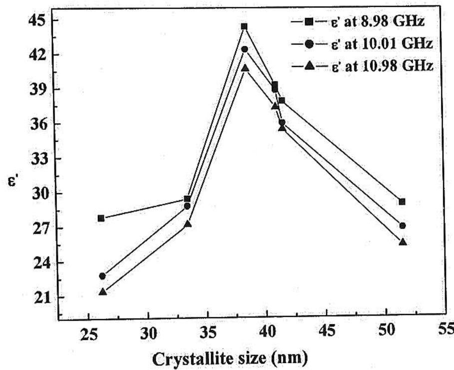

Figure 7.4.1a

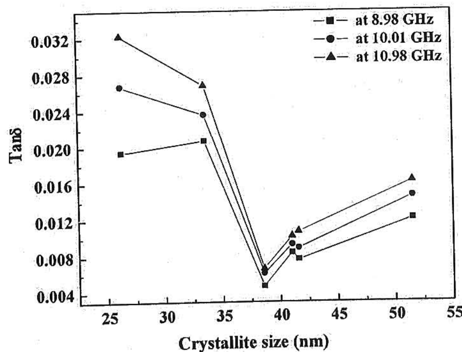

Figure 7.4.1b

Figure 7.4.1c & d: Dielectric constant and tanδ of TiO_2 films deposited on glass plotted as a function of their bandgap.

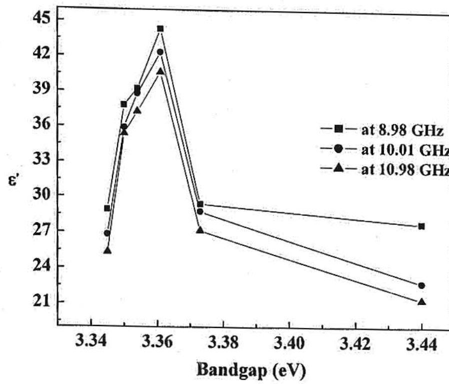

Figure 7.4.1c

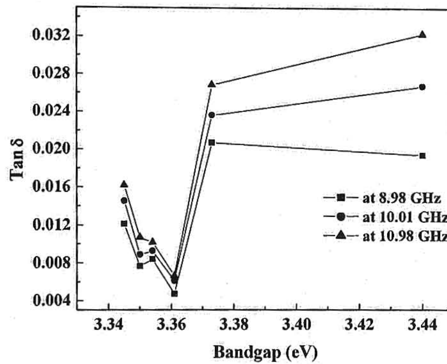

Figure 7.4.1d

Figure 7.4.1c & d shows the variation of microwave dielectric constant and loss of TiO_2 films deposited on glass plotted as a function of the bandgap of these films. The dielectric constant increases with increase in bandgap up to 3.36 eV corresponding to 50% OMP and decreases thereafter. The dielectric loss decreases with increase in bandgap up to 3.36 eV and increases with further increase in bandgap.

A more microscopic reason for the observed variation could be that lower OMP can cause the reduction of Ti^{4+} to Ti^{3+} and the resulting oxygen vacancies can

cause donor action and hence the release of electrons. These electrons cause hopping conduction, which could cause the high dielectric loss in the films. As the OMP increases the films become well oxidized, which means a reduction of oxygen vacancies and hence reduction in loss. This trend is observed up to 50% of OMP. As the OMP increases beyond 50%, the increase in loss can be attributed to the porosity and decrease in particle and crystallite sizes. The SEM pictures clearly show the reduction in grain size above 50% of OMP. It is observed that at 50% of OMP the grain size is uniform and higher compared to other films.

The variation of the dielectric constant with the crystallite size may be explained as follows. The defect sites in the TiO_2 lattice can induce defect-oriented polarization to the neighboring defect free cells in the crystal lattice. This defect-oriented polarization could possess short range ordering inside the lattice contributing to the total polarization of the TiO_2 lattice and therefore the total dielectric constant of TiO_2 films. The growth of the microscopic polar regions will be restricted due to the constraints of a small crystallite size. As the crystallite size increases it enhances the growth of microscopic polar regions inside the crystallites and hence the dielectric constant. With further increase of crystallite size, the relative number of microscopic polar regions may be reduced due to the larger crystallite sizes or it may be due to the loss of short range ordering due to the larger crystallite sizes. The observed variation of dielectric constant with crystalline size indicates a competition between number of microscopic polar regions and their size. The growth of microscopic polar regions may be reaching their maximum limit where the dielectric constant is found to be maximum.

7.4.2 ZrO_2 thin films:

Figure 7.4.2 a & b shows the variation in dielectric constant and dielectric loss of ZrO_2 films deposited on quartz as a function of crystallite size and bandgap respectively. It is found that the dielectric constant increased with increase in crystallite size, where as the dielectric loss peaked around when the crystallite size of 12nm.When it comes to bandgap dependence, it is observed that the dielectric constant decreases with increase in bandgap and the dielectric loss peaked around 5.57eV.

Figure 7.4.2a & b: Dielectric constant and tanδ of ZrO_2 films deposited on quartz as a function of crystallite size and bandgap.

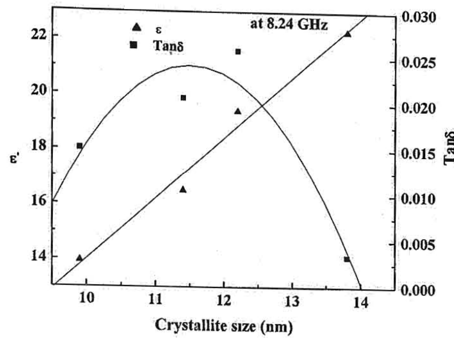

Figure 7.4.2a

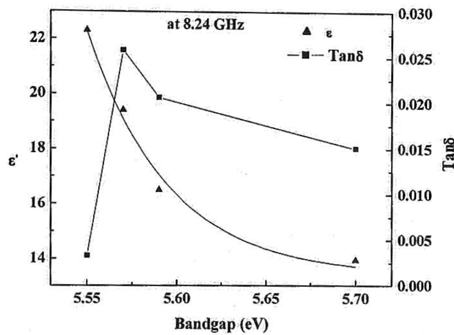

Figure 7.4.2b

7.4.3 $ZrTiO_4$ thin films:

Figure 7.4.3a shows the variation of microwave dielectric constant and loss of $ZrTiO_4$ films deposited on glass as a function of crystallite size at two spot frequencies. It was observed that the dielectric constant went through a peak at a crystallite size of 25.4nm and the dielectric loss showed an exactly opposite response. As the crystallite size increases the loss decreases up to 25.4nm thereafter it is increased. The variation of microwave dielectric constant and loss of the $ZrTiO_4$ films at 11.88 GHz with bandgap is shown in figure 7.4.3b.

Figure 7.4.3a & b: Dielectric constant and tanδ of $ZrTiO_4$ films deposited on glass as a function of crystallite size and bandgap respectively.

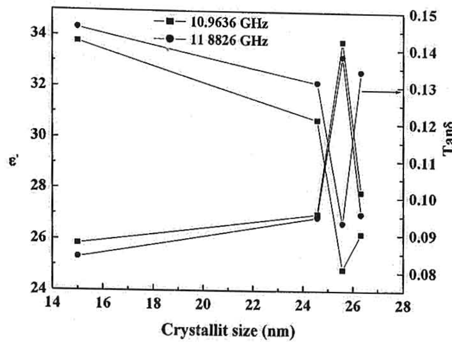

Figure 7.4.3a

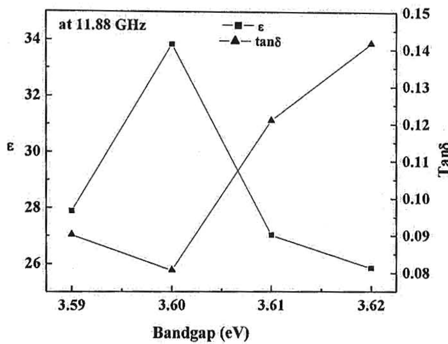

Figure 7.4.3b

The dielectric constant increases with increase in bandgap up to 3.6 eV corresponding to 40% OMP and above, which the dielectric constant decreases with further increase in bandgap. The dielectric loss also decreases with increase in bandgap up to 3.6 eV and increases with further increase in bandgap.

7.4.4 ZST thin films:

The variation of microwave dielectric constant and loss of ZST films deposited on glass as a function of crystallite size are shown in figures 7.4.4a & b

respectively. It is observed that as the crystallite size increases the dielectric constant increases up to 72.3nm and above that it started decreased. The dielectric loss goes through a minimum at the same crystallite size. The variation of microwave dielectric constant and loss of ZST films deposited on glass as a function of bandgap is shown in figures 7.4.4c. The dielectric constant increases with increase in bandgap up to 3.3 eV corresponding to 40% OMP and above that it decreases while the loss goes through a minimum at the same bandgap value. At higher bandgap values the films became more lossy at 11 GHz compared to 10 GHz.

It can be noted that the microwave dielectric properties of these films are quite similar and the discussion on TiO2 films given in section 7.4.1 holds good for other films in the $(Zr,Sn)TiO_4$ system also.

Figure 7.4.4a & b: Microwave dielectric constant and tanδ of ZST films deposited on glass plotted as a function of crystallite size.

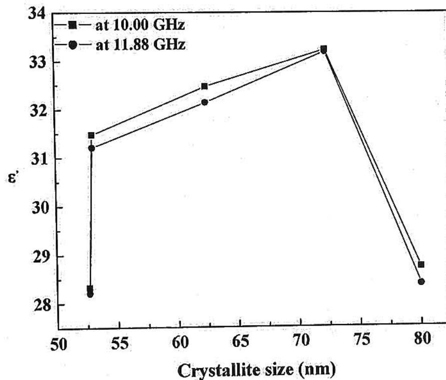

Figure 7.4.4a

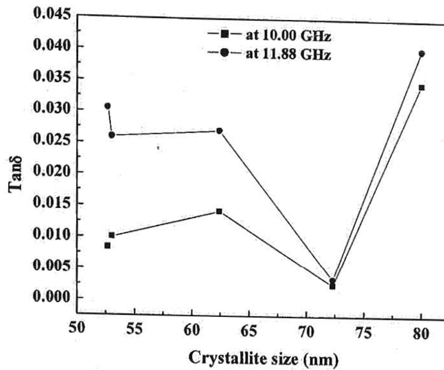

Figure 7.4.4b

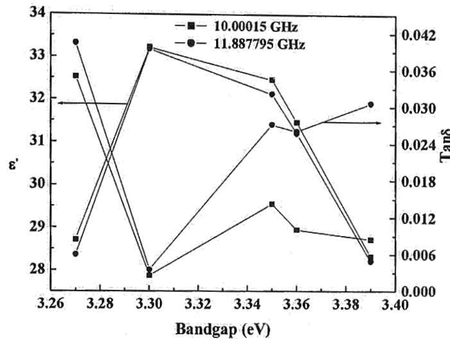

Figure 7.4.4c: Microwave dielectric constant and tanδ of ZST films deposited on glass plotted as a function of bandgap.

Discussion

The dielectric properties of TiO_2, ZrO_2 and $ZrTiO_4$ thin films at microwave frequencies are not previously reported. For ZST films, Nakagawara et al [18] reported that the value of dielectric constant for RF sputtered ZST films deposited at higher substrate temperatures (500-700°C) and measured at 10GHz is 38. Significantly, ZST films in the current study have been deposited at ambient temperatures and exhibit a maximum dielectric constant value of 33, indicating a porosity driven reduction in dielectric constant.

In the present study, the microwave dielectric properties of ZST are also studied in bulk form. In bulk ZST also it is found that large grains give lower tanδ

because grain growth decreases the grain boundary area (section 4.6 of chapter 4). Simultaneous occurrence of higher dielectric constant and lower loss at 40% OMP and the observation of large grains in the same film (section 5.2 of chapter 5) are significant. In an oxide, observation of high dielectric constant with low dielectric loss is possible when the structure gets favorably disposed towards higher dielectric constant and the vibration of polar optic phonons are within their harmonic limits. However, oxygen stoichiometry is known to play a key role as it heavily influences the occurrence of many extrinsic loss mechanisms. It is also observed that the dielectric constant slightly decreased with increase in frequency, where as the dielectric loss increases with increase in frequency. This variation indicates the presence of dipolar relaxation in ZST films around this frequency region, which is absent in their bulk counterparts. This again highlights the role of oxygen stoichiometry in these films, as it is known that oxygen deficiency could lead to defect based dipole formation, which could exhibit a dipolar relaxation [19] influencing the dielectric properties heavily.

7.5 Effect of strain on microwave dielectric loss of films in the $(Zr,Sn)TiO_4$ system:

The variation in crystallographic strain of TiO_2, ZrO_2, $ZrTiO_4$ and ZST films deposited on glass as a function of OMP and $\tan\delta$ are shown in figures 7.5.1 a-d respectively. Interestingly, in each composition of the system, it is found that the dielectric loss and crystallographic strain in the deposited films followed a similar trend as a function of OMP. In all cases the increase or decrease in the microwave dielectric loss is accompanied by the same in crystallographic starin at the same or near by OMP values. This is a preliminary indication that these two are correlated even in this type of linear dielectrics as opposed to polar dielectrics where such correlations are known to exist. That is, the strain in the deposited films influences the microwave dielectric loss. In general, reduction in strain and increase in crystallinity occur for the films deposited at higher temperatures but in the present case the films are deposited at ambient temperatures. The crystalline defects represented by local strain could cause anharmonic lattice vibrations leading to the high dielectric losses [16].

Figure 7.5.1a- d: Strain and tanδ of TiO_2, ZrO_2, $ZrTiO_4$ and ZST films deposited on glass as a function of OMP.

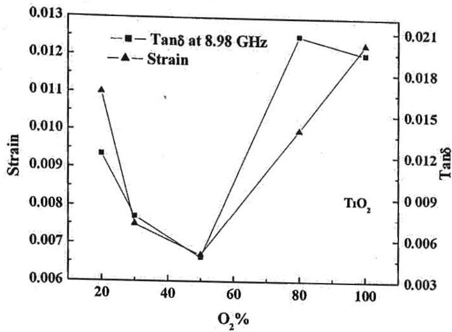

Figure 7.5.1a

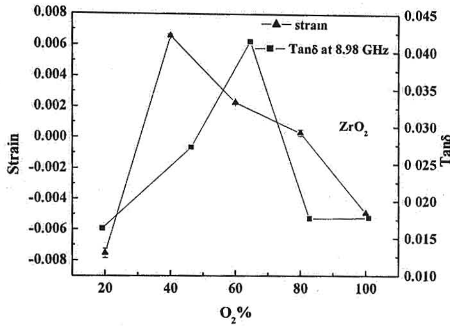

Figure 7.5.1b

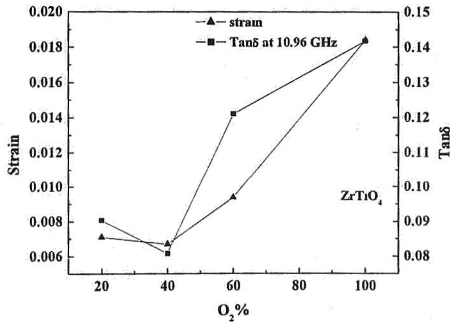

Figure 7.5.1c

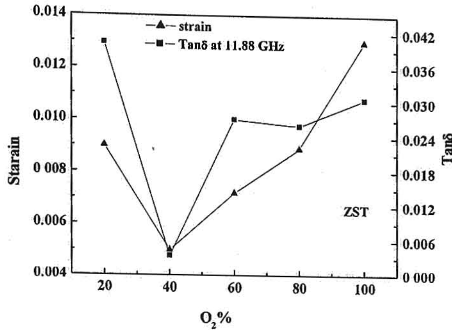

Figure 7.5.1d

The low dielectric losses in the case of bulk TiO_2, ZrO_2, $ZrTiO_4$ and ZST materials with large grains is attributed to the reduction in the strain of the crystallites in ceramics prepared at higher sintering temperatures. In the presence of applied electric field the depolarization fields generally appear at grain boundaries, which influence the fields inside the grains and the dielectric response of the changes. On the other hand, the grain boundary regions are interconnected in all directions and their properties may dominate or severely influence the effective dielectric response of the whole system even if their volume concentration is very small [17]. The DFM pictures (section 5.2 of chapter 5) showed that as the OMP increases in the sputtering atmosphere the average grain size of the films decreases with significant porosity, which plays an important role in the dielectric loss of the films.

7.6 Effect of processing parameters on dielectric properties:

The dielectric properties of TiO_2, ZrO_2, $ZrTiO_4$ and ZST are measured both at lower (100 KHz-10 MHz) and at microwave frequencies (8.2-12.2 GHz). In both the frequency regions films deposited with 40% OMP showed higher dielectric constants with lower loss. Above that, with increase in OMP, the dielectric constants decreased where as the dielectric loss increased. The variation in dielectric constant and dielectric loss also follow the variation in rate of depositions as a function of OMP except at 40% of OMP. Interestingly the grain size of all the films with 40% OMP are higher compared to the films deposited at other OMPs. It was observed that the dielectric properties of all these films are dependent on microstructure.

The dependence of optical and dielectric properties on the OMP appear to follow similar trends. It is known that oxygen stoichiometry can affect optical bandgap as well as dielectric properties. It is seen that OMP changes the rate of deposition, microstructure, crystallite size, optical packing density and thereby porosity as well as crystallographic strain. However, from the current study it is not possible to unambiguously establish, which of these variables is dominant in determining the observed variations in physical properties over the frequencies. Of particular interest is the critical behavior in dielectric properties at 40% OMP. It correlates well with morphological changes such as grain size and also crystallite size. Although, stoichiometry variations may be one of the causes for the variations in dielectric and optical observed, role of morphological changes can not be underestimated. A more detailed study is required to establish the exact causes for the observed dielectric properties. It may be noted that studies with microwave dielectric properties of thin films are not widespread in these type of linear dielectrics.

References:

[1] D.C.Gronemeyer, Phys.Rev., **113**, 1222 (1959).

[2] L.J Berberich and M.E Bell, J.Appl. Phys., **11**, 681 (1940).

[3] P.Alexandrov, J.Koprinarove and D.Todorov, Vacuum, **47**, 1333 (1998).

[4] W.D.Brown and W.W.Granneman, Solid State Electron., **21**, 837 (1978).

[5] M.Takeuchi and H Nagasaka, Thin solid films, **51**, 83 (1978).

[6] T.Fuyuki and H. Matsunami, Jpn J.Appl.Phys., **25**, 1288 (1986).

[7] G.P.Burns, J.Appl.Phys., **65**, 2095, (1989).

[8] S.H.Jeong, I.S.Bae, Y.S.Shin, S-B.Lee, H -T.Kwak and J-H.Boo, Thin Solid Films, **475**, 354 (2005).

[9] I.Vrejoiu, D.G.Matei, M.Morar, G.Epurescu, A. Ferrari, M.Balucani, G.Lamedica, G.Dinescu, C.Grigoriu, and M.Dinescu, Material Science in Semiconductor Processing **5**, 253 (2003).

[10] G.Padeletti, A.Cusma, M.Viticoli, G.M.Ingo, A.Mezzi and B.Watts, Mater.Sci. & Eng.B, **109**, 104 (2004).

[11] M.Viticoli, G.Padeletti, S.Kaciulis, G.M.Ingo, L.Pandolfi and C.Zaldo, Mater.Sci. & Eng.B, **118**, 87 (2005).

[12] T.Kim, J.Oh, B.Park and S.Hong, Appl.Phys.Lett., **76**, 3043 (2000).

[13] B.Tareev, "Physics of dielectric materials" (Mir Publishers, Moscow) 1975.

[14] W.X. Cheng, A.L.Ding, P.S.Qiu, X.Y.He and S.S.H.Zheng, Appl.Surf.Sci., **214**,136 (2003).

[15] C-L. Huang and C-H. Hsu, J.Appl.Phys., **96**, 1186 (2004).

[16] W.Chang, C.M.Gilmore, W.J.Kim, J.M.Pond, S.W.Kirchoefer, S.B.Qadri, D.B.Chirsey and J.S.Horwitz, J.Appl.Phys., **87**, 3044 (2000).

[17] J.Petzelt and I.Rychetsky, Ferroelectrics, **316**, 89 (2005).

[18] O.Nakagawara, Y.Toyota, M.Kobayashi, Y.Yoshino, H.Tabata and T.Kawai, J.Appl.Phys., **80**, 388 (1996).

[19] M.A.Leschenko, Y-M.Poplavko and V.P.Bovtan, Ferroelectrics, **131**, 213 (1992).

Chapter-8

Conclusions and Future Scope of the Work

8.1 Conclusions:

In summary, dielectric resonators (DR) of $(Zr_{0.8},Sn_{0.2})TiO_4$ (ZST) composition have been prepared by solid state reaction method. The effect of various additives, their concentrations and processing parameters on structure, microstructure and on microwave dielectric properties are studied. Successful efforts were made to reduce the sintering temperature from 1650 to1150°C without affecting the microwave dielectric properties of the ZST ceramics by reducing the initial particle size and adding different type of additives. 1wt% ZnO is added as a sintering aid every time and by reducing the initial particle size up to 220nm, the samples showed better sinterability at 1350°C.

It is well known that the addition of liquid phase sintering aids reduces the sintering temperature without affecting the microwave dielectric properties. For that purpose, in the present study different amount (0.5, 1.0 & 1.5 wt%) of CuO was added as a sintering aid along with 1wt% ZnO. Then the powders were milled for 1, 5 & 7 hours and found that the samples densified at 1300°C itself and exhibited improved microstructure and dielectric properties. Among the above 3 batches, samples milled for 5 hours gave good microstructure and microwave dielectric properties. The microwave dielectric properties for the samples milled for 5 hours and added with different wt% of CuO and for the sample added with 1wt% ZnO alone were measured at cryogenic temperatures (15-290K). Samples added with CuO exhibited less dependence on temperature than for the sample without CuO.

The effect of various additives such as alkaline earth metal oxides (BaO, SrO & MgO), pentavalent oxides (Ta_2O_5, Nb_2O_5 & V_2O_5), rare earth oxides (Sm_2O_3, Nd_2O_3 & CeO_2) up to 1.5 wt% and glass additives (B_2O_3, ZnO-B_2O_3 & 5ZnO-2B_2O_3) up to 1wt% along with 1wt% ZnO have been added to ZST ceramics and studied their effect on structure, microstrucre and on the microwave dielectric properties. In all the cases it is found that the dielectric constant and temperature coefficient of resonant frequency are not affected much where as the Q factor changed drastically. The improvements in Q factor are attributed to the improvements in density, increase in uniform grain size and reduction in oxygen vacancies. The impedance spectroscopy of

the samples added with CuO and without CuO were carried out and found that this material do not have any other loss generating mechanism at low frequencies except the temperature dependent generation of charge carriers.

Thin films of $(Zr_{0.8},Sn_{0.2})TiO_4$ have been deposited by dc reactive magnetron sputtering from Zr, Sn and Ti metal targets using a single cathode in oxygen atmosphere. Initially to understand the growth kinetics of these films, we have studied the films of the sub oxides in the ZST system such as TiO_2, ZrO_2 and $ZrTiO_4$. The processing parameters such as substrate to target distance, working pressure, Oxygen Mixing Percentage (OMP) and power density etc were optimized to get best structural, microstructural, optical, electrical and dielectric properties. For the first time all these films were deposited in pure oxygen plasma. Significantly, as deposited films were partially crystallized indicating plasma assisted crystallization even though the substrates were not heated during deposition. The crystallite sizes of the films decreased with increase in OMP. The microstructure of these films shown columnar growth and films deposited on glass substrates shown triangular shaped grains where as the films deposited on fused silica exhibited spherical shaped grains.

The optical properties of the films in the $(Zr,Sn)TiO_4$ system has been studied. It was observed that as the OMP increases both the refractive index and extinction coefficient are decreasing where as the bandgap got increased. The bandgap decreased with increase in crystallite size exhibiting an approximately $1/d^2$ dependence. The electrical properties of the films were measured and found that the films with optimized conditions showed lower leakage currents. The leakage currents were dependent on processing parameters, crystallinity and microstructure.

The dielectric properties of TiO_2, ZrO_2, $ZrTiO_4$ and ZST films were measured both at low frequency and at microwave frequencies. At lower frequency range, for TiO_2 both the dielectric constant and loss decreased with increase in frequency but for ZrO_2 films dielectric constant decreased with increase in frequency while the losses are increased. But in the case of $ZrTiO_4$ and ZST films both the dielectric constant and loss are found to decrease with increase in frequency. At microwave frequencies the dielectric constant values decreased with increase in frequency and the loss values increased. The dielectric constant and loss showed enormous dependence on OMP and the resulting variation in crystallite size and bandgap. Interestingly the dielectric loss of the films showed profound dependence on crystallographic strain in the

deposited films. For many of these films, the microwave dielectric properties are reported for the first time.

In the present study DRs and thin films of zirconium tin titanate have been prepared by solid state reaction method and dc reactive magnetron sputtering respectively. In bulk form dielectric constant of 38.9, Qxf_o of 49,600 and τ_f of 2 ppm^{o}C^{-1} were observed for the sample sintered with 1wt% ZnO at 1350°C where as in thin film form dielectric constant of 33.23 and Tanδ= 0.0035 were observed at 10 GHz. The microwave dielectric properties of thin films were inferior compared to that of bulk. The reduction in strain and increase of crystallinity occurs for the films when deposited at higher temperatures giving rise to lower dielectric loss, but in the present case the films are deposited at ambient temperatures. The lower values of observed dielectric constant of ZST films can be attributed to the partial crystallinity, smaller grains and porosity in the deposited films.

8.2 Future scope of the work:

The effect of initial particle size of the ZST ceramics can be studied further systematically to try and reduce the sintering temperature further. We have added different types of additives to reduce the sintering temperature and to improve the microwave dielectric properties. During this process the microstructure of the ZST ceramics changes. To find out whether these additives entered in to the matrix of ZST or remained at the grain boundary, a composition analysis across the microstructure with a facility like Electron probe Micro Analysis (EPMA) will be useful. We have focused on to reduce microwave dielectric losses that are extrinsic in nature by process optimization. We have not studied the intrinsic loss mechanisms and that could be studied with far IR reflectivity spectroscopy.

In the case of thin films, since the crystallinity and microstructure are playing an important role on optical, electrical and microwave dielectric properties, a systematic study of the films by varying the substrate temperature during deposition will be beneficial. A detailed compositional analysis of $ZrTiO_4$ and ZST films deposited at different are needed to explain the loss mechanisms of the films. Films deposited with same OMP but having different microstructures can be obtained by annealing or heating during deposition. A detailed compositional analysis with independent control over microstructure will help in interpreting the observed variations in optical and dielectric properties with changes in OMP during deposition.

An accurate determination of crystallographic strain using X- Ray reflectivity measurements will help in establishing the observed correlations between crystallographic strain and tanδ at microwave frequencies. In addition, it is interesting to see whether instrumented indentation measurements using a nanoindentor throws more light in to the observed possible correlation between strain in the films and the microwave dielectric loss in these linear dielectrics.

The dielectric properties of these films are measured only at a few spot frequencies in the microwave range. It is interesting to do a broad band measurement of dielectric constant and tanδ of these films spanning over a few bands to ascertain the loss mechanisms in these films at such frequencies.

List of Publications

International Journals:

1. "Ambient temperature growth of nanocrystalline titanium dioxide thin films" **D.Pamu**, M.Ghanashyam Krishna, K.C.James Raju and Anil K Bhatnagar, Solid State Communications, **135**, 7 (2005).
2. "Microwave dielectric behavior of nanocrystalline Titanium dioxide thin films". **D.Pamu**, K.Sudheendran, M.Ghanashyam Krishna, K.C.James Raju and Anil K Bhatnagar, Vacuum, **81**, 686 (2007).
3. "Cryogenic microwave dielectric properties of sintered ($Zr_{0.8}$,$Sn_{0.2}$)TiO_4 doped with CuO and ZnO"
   M.V. Jacob, **D.Pamu**, K.C.James Raju, Journal of American Ceramic Society **90**, 1511 (2007).
4. "Effect of particle size and ZnO addition on the microwave dielectric properties of nanocrystalline ZST ceramics"
   D.Pamu, G. Lakshminarayana Rao, K.C.James Raju, accepted in Advances in Applied Ceramics, **108**, xxx (2007).
5. "Effect of CuO on the sintering and cryogenic microwave characteristics of addition on the microwave dielectric properties of ($Zr_{0.8}$,$Sn_{0.2}$)TiO_4 ceramics"
   D.Pamu, G. Lakshminarayana Rao, K.C.James Raju, and M.V. Jacob, Science and Technology of Advanced Materials **8**, 469 (2007).
6. "Ambient temperature stabilization of crystalline zirconia thin films deposited by dc magnetron sputtering"
   D.Pamu, K.Sudheendran, M.Ghanashyam Krishna, K.C.James Raju and Anil K Bhatnagar, accepted in Thin Solid films (Press).
7. "Effect of Sm_2O_3/ ZnO on the microstructure and microwave dielectric properties of nanocrystalline ZST ceramics"
   D.Pamu, G. Lakshminarayana Rao and K.C.James Raju, Ceramics International (In Press).
8. "Crystallographic texture, morphology, optical and microwave dielectric properties of nanostructured zirconia thin films"
   D Pamu, K. Sudheendran, M Ghanashyam Krishna and K C James Raju, Journal of Vacuum Science and Technology A, **26**, xxx (2008).

International & National Conferences:

1. "Microwave dielectric properties of $(Zr_{0.8},Sn_{0.2})TiO_4$"
   D.Pamu, G. Lakshminarayana Rao, K.C.James Raju, M.Ghanashyam Krishna and Anil K Bhatnagar, Presented in 13th National Seminar on Ferroelectrics and Dielectrics Conference, New Delhi, 2004, India.
2. "Determination of the Microwave Dielectric Permittivity of thin films using the Extended Cavity Perturbation Technique"
   K.Sudheendran, **D.Pamu**, K.C.James Raju, M.Ghanashyam Krishna and Anil K Bhatnagar, Presented in Asian Pacific Microwave Conference, New Delhi, 2004, India.
3. "Varactor tuned filter using cylindrical dielectric resonator"
   G.Lakshminarayana Rao, **D.Pamu**, K.C.James Raju, M.Ghanashyam Krishna and Anil K Bhatnagar, Presented in Asian Pacific Microwave Conference, pp. 257-258, New Delhi, 2004, India.
4. "Effect of ball milling on the microwave dielectric properties of ZST"
   D.Pamu, G. Lakshminarayana Rao, K.C.James Raju and Anil K Bhatnagar, Presented at Materials for Electrical, Electronic and Magnetic Applications (MEEMA)-2005, DMRL Hyderabad, India.
5. "Effect of particle size and ZnO addition on the microwave dielectric properties of ZST",
   D.Pamu, G. Lakshminarayana Rao and K.C.James Raju, presented at National Seminar on Advances in Electro Ceramics (NSAE-2006), DRDO Centre for Piezoelectroceramics, Pune, India.
6. "Effect of microstructure on the microwave characteristics of $Ba(Zn_{1/3}Ta_{2/3})O_3$ Ceramics for dielectric resonator applications"
   D.Pamu, G. Lakshminarayana Rao and K.C.James Raju, presented at National Seminar on Advances in Electro Ceramics (NSAE-2006), DRDO Centre for Piezoelectroceramics, Pune, India.
7. "Effect of BaO, SrO and MgO addition on the microwave dielectric properties of nanocrystalline ZST ceramics"
   D.Pamu, G. Lakshminarayana Rao and K.C.James Raju, Presented in 14th National Seminar on Ferroelectrics and Dielectrics, IIT Karaghpur 2006, India.
8. "The effect of Al_2O_3 on the microstructure and on the microwave dielectric Properties of BZT"

D.Pamu, G. Lakshminarayana Rao and K.C.James Raju, Presented in 14th National Seminar on Ferroelectrics and Dielectrics, IIT Karaghpur 2006, India.

9. "Nanocrystalline microwave dielectric properties of BST and TiO_2 thin films" K.Sudheendran, **D.Pamu**, K. Venkata Saravanan, K.C.James Raju, Ghanashyam Krishna and Anil K Bhatnagar, Presented in 14th National Seminar on Ferroelectrics and Dielectrics, IIT Karaghpur 2006, India.
10. "Size dependent microwave dielectric properties of nanostructured oxide films" K.Sudheendran, **D.Pamu**, K. Venkata Saravanan, K.C.James Raju, Ghanashyam Krishna and Anil K Bhatnagar, Presented in International Conference NANO 2006 at IISc, Bangalore, India.

Communicated: -

1. "Determination of dielectric constant and loss of high-K thin films in the microwave region by the extended cavity perturbation technique" K.Sudheendran, **D.Pamu**, K.C.James Raju and M.Ghanashyam Krishna.
2. "Zirconium Tin Titanate thin films with high dielectric constant and low dielectric loss in the microwave region" **D.Pamu**, K.Sudheendran, M.Ghanashyam Krishna and K.C.James Raju.
3. "Demonstration of nanocrystalline titania thin films in pure oxygen atmosphere" **D.Pamu**, K.Sudheendran, M.Ghanashyam Krishna and K.C.James Raju.
4. "Effect of microstructure on the microwave dielectric properties of CeO_2 and Nd_2O_3 doped ZST ceramics" **D.Pamu**, G. Lakshminarayana Rao and K.C.James Raju.
5. "Effect of CuO on microstructure and microwave dielectric properties of ZST" **D.Pamu**, G. Lakshminarayana Rao and K.C.James Raju.
6. "Effect of pentavalent oxides on the microwave dielectric properties of ZST ceramics" **D.Pamu**, G. Lakshminarayana Rao and K.C.James Raju.
7. "Effect of glass additives on the microstructure and on the microwave dielectric properties of ZST ceramics" **D.Pamu**, G. Lakshminarayana Rao and K.C.James Raju.
8. "Effect of BaO, SrO and MgO addition on the microwave dielectric properties of ZST ceramics" **D.Pamu**, G. Lakshminarayana Rao and K.C.James Raju.

9. “Ambient temperature deposition of $ZrTiO_4$ films from Zr and Ti metal targets using DC magnetron sputtering”
   D.Pamu, M.Ghanashyam Krishna and K.C.James Raju.